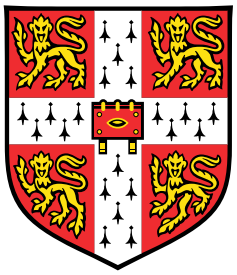

Geochemical records in travertine veins at the Green River CO_2 seeps (Utah)

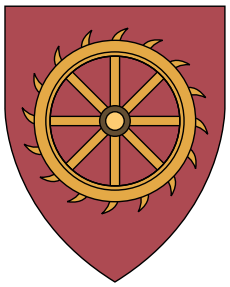

Peter Malcolm Scott

Department of Earth Sciences
University of Cambridge/ British Geological Survey (NIGL)

This dissertation is submitted for the degree of
Doctor of Philosophy

St Catharine's College July 2018

This thesis is dedicated to my granny, Greta Scott who passed away earlier this year.

Declaration

This dissertation is the result of my own work and includes nothing which is the outcome of work done in collaboration except where specifically indicated in the text. This work has not been submitted in whole or part towards any other qualification at this, or any other university. The total length does not exceed the 275 numbered page limit prescribed by the Department of Earth Sciences Degree Committee, including 225 pages of text, illustrations and bibliography.

Peter Malcolm Scott
July 2018

Acknowledgements

I would like to take this opportunity to thank everyone who has helped me out over the course of this PhD. First of all, thanks to Mike Bickle, Dan Condon and Niko Kampman for their wisdom and witticisms. I appreciate the support and advice you have all offered over the course of this project. I would particularly like to thank Aleksey Sadekov, Matt Horstwood, Diana Sahy, Steve Noble, Hazel Chapman, Mervyn Greaves, James Rolphe and Sammbuddha Misra for help with analyses and teaching me the ins-and-outs of labs and mass spectrometry. Also thanks to Andy Howell, Christoph Gruetzner, James Jackson and Alex Copley for the training, data processing and use of their drone. Massive thanks to the numerous others in the department who've assisted me by discussing work, music, philosophy and politics over coffee or stronger beverages.

To those who've dealt with my peripheral chaos; thanks Andy, Madeleine, Alex, Victoria, Alex, Nick & Tom. You've been very understanding, supportive and tolerant individuals, particularly regarding storage of double basses, speakers/sound gear, bikes, homebrew and allotment equipment. Also thanks to all of you, for interesting and useful scientific conversations. Running the 'exclusive' Happy Hour stash wasn't half bad.

I am very grateful as well, to those at Shell Global Solutions who hosted me for a 6-month internship. The use of reservoir-scale numerical models really helped put some of the challenges of CCS in perspective for me. It is a shame not to include some of this work in this thesis. Thanks to Niko, Jeroen, Kevin and the rest of the Subsurface Storage team.

Second to last, I'd like to thank all of the musicians who've I've played with over the last few years. The gigs have been enjoyable, and some delightfully surreal: a Swiss mountain, a free masonry hall, a 15th century palace and a series of Earth Science departments... I hold you all responsible for the condition of my sanity. Finally, I'd like to thank Mum, Dad, Doug, Marion & Bernard. I'm eternally grateful to all of you for helping me through this long journey.

Abstract

Geological Carbon Storage is necessary for reduction of anthropogenic carbon dioxide (CO_2) emissions. CO_2 is captured at 'point sources' (i.e. heavy industries, where large, concentrated volumes of CO_2 are produced) and subsequently purified, compressed and transported. Some CO_2 can be used for other processes, but excess CO_2 can be injected into geological formations where it can be securely stored as either a gas, supercritical fluid or dissolved in formation fluids. Understanding the interactions of CO_2 within the subsurface is important for risk characterisation. The long-term storage of CO_2 at reservoir scales involves fluids close to equilibrium, which is better characterised using natural analogues than laboratory experiments.

At the Green River CO_2 seeps in Utah, CO_2 saturated brines migrate up two fault systems: the Little Grand and Salt Wash faults. Modern springs, a man-made cold water geyser (Crystal Geyser), and fluid sampling during drilling at Little Grand in 2012 constrain current fluid compositions adjacent to and along the 10km of fault. Tufa/travertine ($CaCO_3$) deposits form at modern springs, and historic deposits form along both faults. Fossil travertine veins can be dated by U-Th chronology and preserve chemical signatures of the fluids they form from: trace metals, $\delta^{234}U_i$ and $^{87}Sr/^{86}Sr$. Laser ablation methods were developed to analyse these samples, allowing for rapid, high spatial resolution analysis. The techniques are accurate and show external precision of $\pm 42 \times 10^{-6} (2\sigma)$ for $^{87}Sr/^{86}Sr$, $7 \times 10^{-7} (2\sigma)$ for $^{230}Th/^{238}U$ and $\pm 1.3 \times 10^{-6} (2\sigma)$ for $^{234}U/^{238}U$. Session uncertainties are propagated using an excess variance approach, giving typical age uncertainties of 20 ± 1.8kyr and 120 ± 4kyr, and $\pm 40‰$ for $\delta^{234}U_i$. Individual vein samples grow over <5kyr, and localised vein networks may form for up to 15kyr.

$^{87}Sr/^{86}Sr$ & $\delta^{234}U_i$ show limited variability within samples, and much larger variability between sample localities. At Salt Wash, these trends can be interpreted using an analytical reactive transport model for flow in the Navajo sandstone. This model is calibrated using spring fluid samples, and applied to interpret vein samples. Trends in $\delta^{234}U_i$ are more easily interpreted spatially, due to increased residence times inferred from α-recoil inputs. This is counter to previous interpretations at this field area, where trends were interpreted as purely

temporal. However, samples on the Little Grand fault do not fit either model well. Next to Crystal Geyser, one vein has clear annual layering. Trace metal trends show similarity to mixing patterns observed during geyser eruptions. There is a tentative link that the draining of the Navajo responds to seasonal changes in crustal stress, prior to man-made geysering activity.

Table of contents

List of figures

List of figures

List of tables

Chapter 1

Introduction

1.1 Climate change

Carbon dioxide (CO_2) plays a key role in the regulation of climate. It is a greenhouse gas which prevents the escape of long wavelength radiation emitted by our planet. Combined with solar irradiance this regulates the temperature of our planet (alongside other gases, notably CH_4 and H_2O). The evidence for rising atmospheric CO_2 concentrations and global average temperature since the start of the industrial revolution is unequivocal, and the burning of fossil fuels such as coal, oil and gas for industrial and domestic energy and transportation is responsible (IPCC et al., 2014) (figure 1.1). Much of the CO_2, and the majority of energy has been accommodated by global oceans, mitigating forcing thus far. However, some feedbacks within the climate and ocean systems can act to positively enforce this warming and some are still relatively poorly understood. Increased temperatures, increased sea level, modified hydrologic cycles, variable extreme weather risks and lower oceanic pH and oxygenation have direct and indirect consequences to human society. Examples include, but are not limited to, coastal flooding, population displacement, disrupted food chains and water shortages in addition to loss of delicate environmental ecosystems. Any impacts will be felt disproportionately in poorer countries. There is global agreement that CO_2 emissions must be reduced ('mitigated') to prevent further warning, with ambitions to limit warming to 2°C above pre-industrial levels by 2100 (Paris COP, 2015). Current emissions are not on track to achieve such a scenario (Raftery et al., 2017).

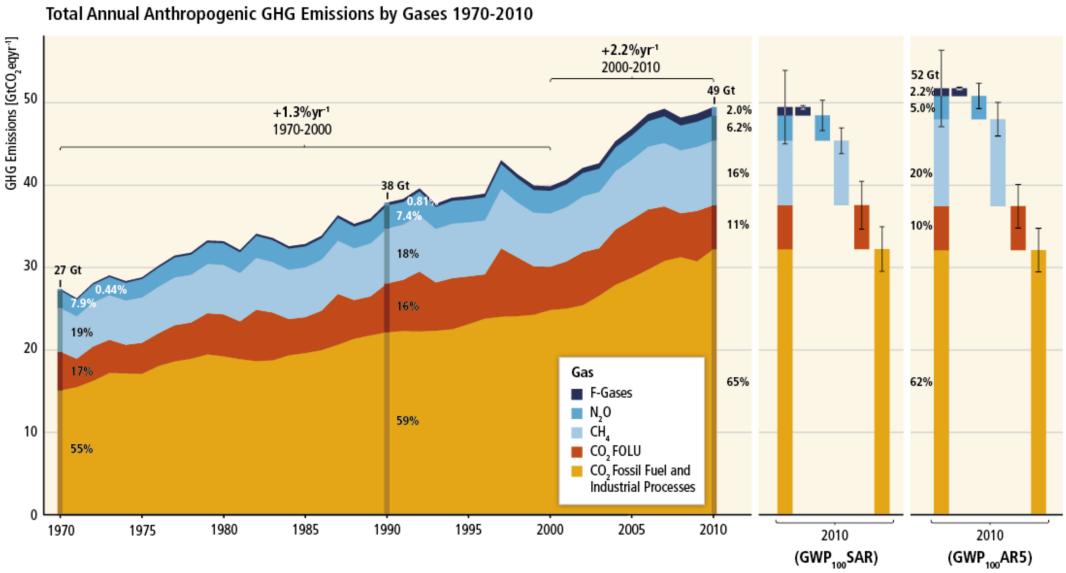

Fig. 1.1 From (IPCC et al., 2014); Global Greenhouse gas emissions and their sources. *"Total annual anthropogenic greenhouse gas (GHG) emissions (gigatonne of CO_2-equivalent per year, $GtCO_2$-eq/yr) for the period 1970 to 2010 by gases: CO_2 from fossil fuel combustion and industrial processes; CO_2 from Forestry and Other Land Use (FOLU); methane (CH4); nitrous oxide (N2O); fluorinated gases covered under the Kyoto Protocol (F-gases). Right hand side shows 2010 emissions, using alternatively CO_2-equivalent emission weightings based on Second Assessment Report (SAR) and AR5 values. Unless otherwise stated, CO_2-equivalent emissions in this report include the basket of Kyoto gases (CO_2, CH4, N2O as well as F-gases) calculated based on 100-year Global Warming Potential (GWP100) values from the SAR (see Glossary). Using the most recent 100-year Global Warming Potential values from the AR5 (right-hand bars) would result in higher total annual greenhouse gas emissions (52 $GtCO_2$-eq/yr) from an increased contribution of methane, but does not change the long-term trend significantly."*

1.1.1 CO_2 mitigation strategies

The last IPCC report on climate change presents a range of emissions scenarios and predicted temperature changes (IPCC, 2015). In all but the 'business-as-usual' scenario, some form of carbon reduction technology is invoked. The timing of implementation and the extent of it vary between the scenarios. This excludes the natural sinks of CO_2 (chemical weathering and burial of organic material), which act too slowly to mitigate current emissions.

Substantial changes are required to reduce sources emitting CO_2 (figure 1.2). Fossil fuels are burned in a range of different environments; either at dispersed sources such as transportation or point sources such as heavy industries. Additionally, chemical processes such as cement production and setting, or coke used in steel manufacturing produce sizeable emissions. Transitioning towards CO_2 free energy sources (wind, wave, hydro, solar, nuclear) is possible, but is a gradual process. Similarly transportation can transition from petrol/diesel towards electric cars which centralises energy production. Issues such as continuity of energy supply and ability to deal with variable energy demand mean that even in a 'low-carbon' economy some energy generated by burning of fossil fuel is likely necessary without the implementation of grid scale energy storage. For energy security, a more diverse range of energy sources is preferable. Therefore processes such as Carbon Capture, Utilisation and Storage (CCUS) are necessary, as they can be retrofitted to these 'point' emission sources and to new schemes. Bioenergy combined with CCS (BeCCS) is suggested as a method of using biological productivity to capture CO_2 from the atmosphere, but is criticised as as an inefficient use of land area and potential drain on soil fertility.

As a last option for climate change mitigation, there are geoengineering approaches. These are currently considered prohibitively expensive, and it is difficult to quantify the consequences of such actions for example reducing incident incoming radiation. In the worst case scenario, where CO_2 emissions targets are massively overshot, direct capture from air may be necessary. The CO_2 still requires to either be used, and any excess stored. The current scale of CO_2 emissions, and the limited utilisation of CO_2, require that the majority of CO_2 is sequestered.

1.2 Carbon Capture, Utilisation & Storage (CCUS or CCS)

Carbon Capture, Utilisation & Storage, involves the process of stripping CO_2 from exhaust flue gases, purifying, compressing and then transporting this CO_2 so that it can be used for other processes or stored. There are a series of challenges to be solved at each step: for

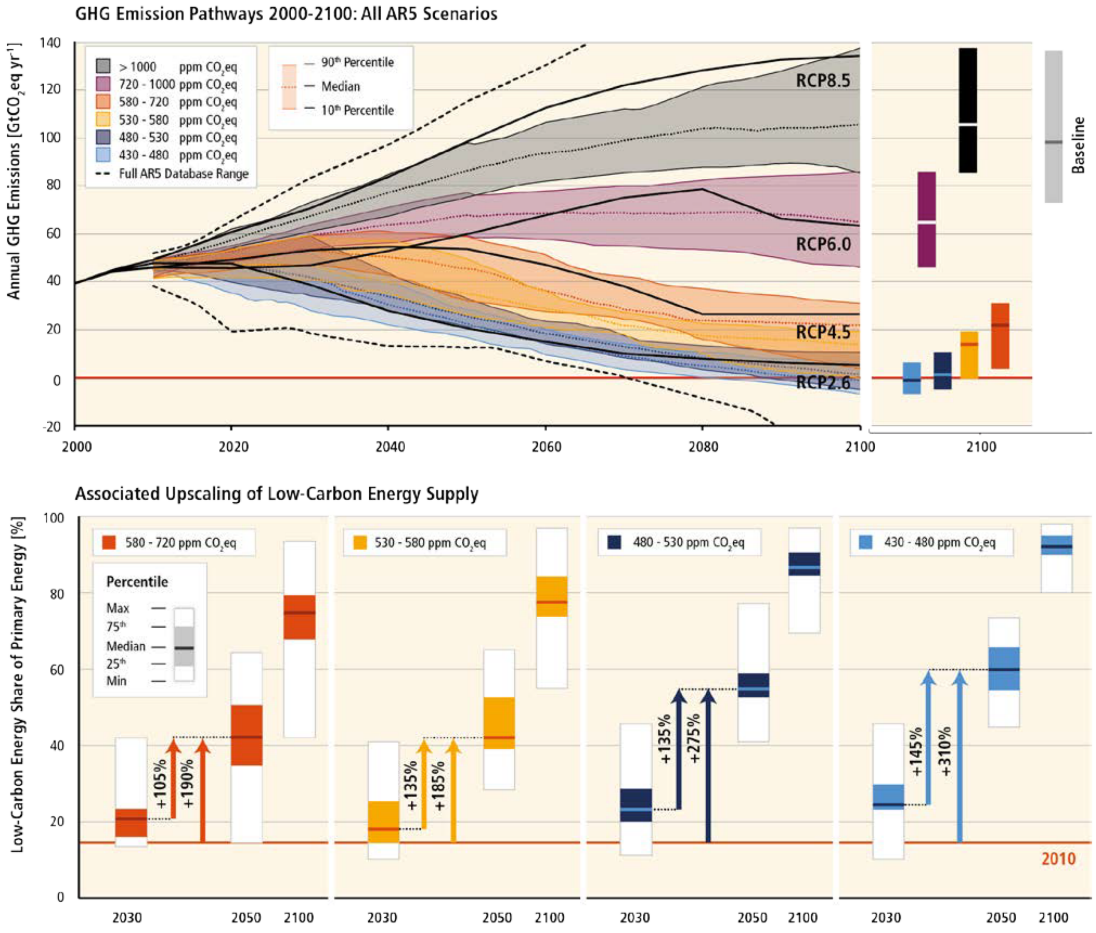

Fig. 1.2 Greenhouse gas emission scenarios and the required change in energy supply for each of these scenarios IPCC et al. (2014). Within models of energy supply, emissions limiting CO_2 to the lowest (430ppm) scenario cannot be achieved without including CCS; and it is a very useful technology for reducing emissions in the other scenarios. The current trajectory of emissions places us between scenario RCP8.5 and RCP6.

example ensuring efficient, inexpensive purification, safe transportation and secure storage. Following capture, compressed CO_2 must be transported using either tankers or pipelines. Some of this CO_2 can be used in other chemical or biological processes. Current demand for CO_2 is low compared to the volumes generated, therefore storage of this excess CO_2 is necessary. There are two main global options for storage: depleted oil and gas fields and saline reservoirs. There are advantages and disadvantages to each. Depleted oil and gas fields have existing infrastructure. If this is of sufficient quality, then it is easy to retrofit the field. However the reservoir may be underpressured due to historical extraction, and may also have lots of drill holes which can present risks if poor quality cement was used or the seal is incomplete. Saline aquifers are the most common global reservoir (Bachu, 2015) but may not have proven structural seals, though these seals will be perforated fewer times. The oil and gas sector has considerable experience of handling CO_2 from years of using it in mature fields for enhanced oil recovery operations (EOR). However, there is limited information on migration and monitoring of the injected CO_2 at this scale, and the history of extraction modifies reservoir pressures.

Globally there are a number of different CO_2 injection experiments. To date four fields continue to inject power plant scale CO_2 emissions (approx 0.5-5Mtpa CO_2) and are dedicated only to storage; Sleipnir, Snøhvit (Norway), QUEST (Canada) and Illinois Industrial CCS (USA); Gorgon (Australia) is currently in construction (Global CCS institute, 2017). Many smaller scale experiments have been carried out, and several large projects use CO_2 injection for EOR. Some of these are summarised in Bickle (2009); Kampman et al. (2014a). The UK currently has 98 operational fossil fuel power plants (DUKES, May 2017). Upscaling capture technology to power plant scale is currently in progress, but current estimates suggest that CCS increases energy costs by 20-30% (BEIS, 2017). This is currently considered an unfeasible price hike for government, industry or tax-payers. There is limited support for CO_2 taxation, which may increase feasibility. The total storage of the Norwegian sector of the North Sea is 5.5Gtpa (Halland et al., 2014); total UK emissions are $\approx$370Mtpa of which $\approx$110Mtpa is from energy (BEIS, 2017) and the UK sector of the North Sea is larger, so there is potential to store at least 50 years of current energy emissions. As many fields on the UK shelf are approaching maturity and decommissioning, CCS activities make sense for maintaining jobs and using this infrastructure whilst it exists. Unfortunately however, the funding for the two UK schemes (the Shell Peterhead project and the Capture Power White Rose project) was withdrawn: *"the £1 billion ring-fenced capital budget for the Carbon Capture and Storage (CCS) Competition is no longer available"* (Government statement to London Stock Exchange, 25th November 2015).

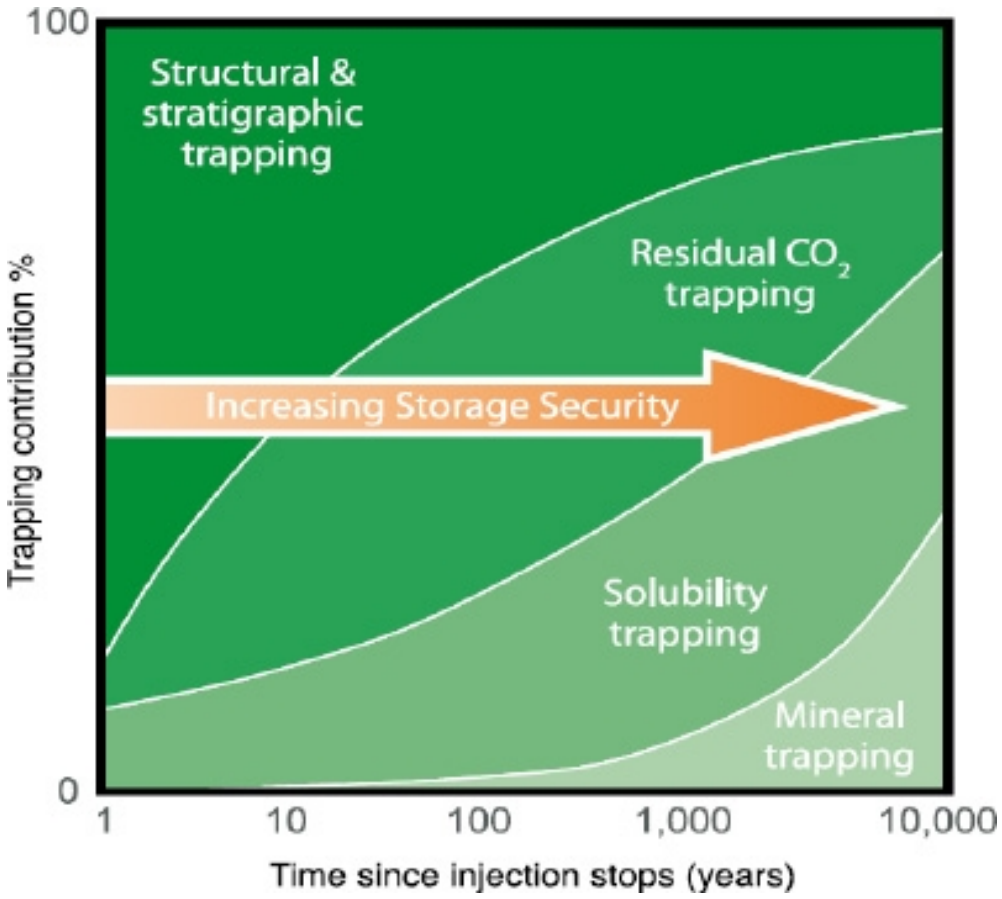

Fig. 1.3 From IPCC (2005); relative importance of different CO_2 storage mechanisms with time. The transitions between these different forms of storage is schematic, but the transition from structural trapping of a buoyant CO_2 phase to other forms of trapping reduces the mobility of the CO_2 making storage more secure. The relative contributions of each form of storage will be reservoir specific.

A concern with CCS is the security of storage and perhaps more importantly public perceptions of subsurface activities. Storage can take several forms, depending upon which phase CO_2 is stored in. Within a reservoir injected CO_2 will initially exist as a free phase; either a gas, liquid or supercritical fluid depending upon pressure and temperature. Most proposed reservoirs are >600-800m therefore CO_2 is a supercritical fluid. As CO_2 migrates, some of it will be trapped by capillary forces in pores, and some of the CO_2 will partition into reservoir fluids, for example dissolving in brines and decreasing their pH. This also increases fluid densities, and can lead to fluid convection. Finally these CO_2-bearing fluids may react with reservoir minerals, leading to precipitation of carbonate minerals. These different forms of trapping are considered to offer increasing storage security. However, the integrity of mud/siltstone caprocks in contact with CO_2 is maintained over at least 0.5Ma so the consequences of CO_2 storage over human timescales are limited (Kampman et al., 2016; Maskell et al., 2017).

1.2.1 Multiphase CO_2 properties

The migration of CO_2 within the subsurface is controlled by its multiphase flow properties through porous media. CO_2 is less dense than reservoir brines (in most P-T space), and therefore rises buoyantly within reservoirs. Microscopic interactions between minerals and fluids influence the macroscopic properties of flow. Flow properties are therefore experimentally determined for given units, to give relative permeabilities or capillary entrance pressures. This averages properties such as mineral wettability at ≈3cm scale typical of the experiments. Traditionally measurements are performed for gas-water or oil-water, but can be scaled for three phases i.e. gas-oil-water. The properties of each phase vary with P-T-X. For CO_2, most experiments explore the properties between supercritical CO_2 and brines; there are currently no published determinations for gaseous CO_2-water relative permeabilities (Burnside and Naylor, 2014).

Importantly for CO_2 storage, there is a phase transition around 600-800m depth (at hydrostatic conditions). At most reservoir temperatures this is a gradual transition from supercritical CO_2 to gaseous CO_2. However, if the geothermal gradient is lower (or surface temperatures cooler) then it is possible to form liquid CO_2. This phase change has an associated jump in physical properties such as density and viscosity. Models have shown that Joule-Thompson cooling (cooling during decompression) is sufficient to drive fluid temperatures through the phase transition zone despite an initial hydrothermal gradient which does not intersect the transition. In the numerical simulations this creates cyclical variation

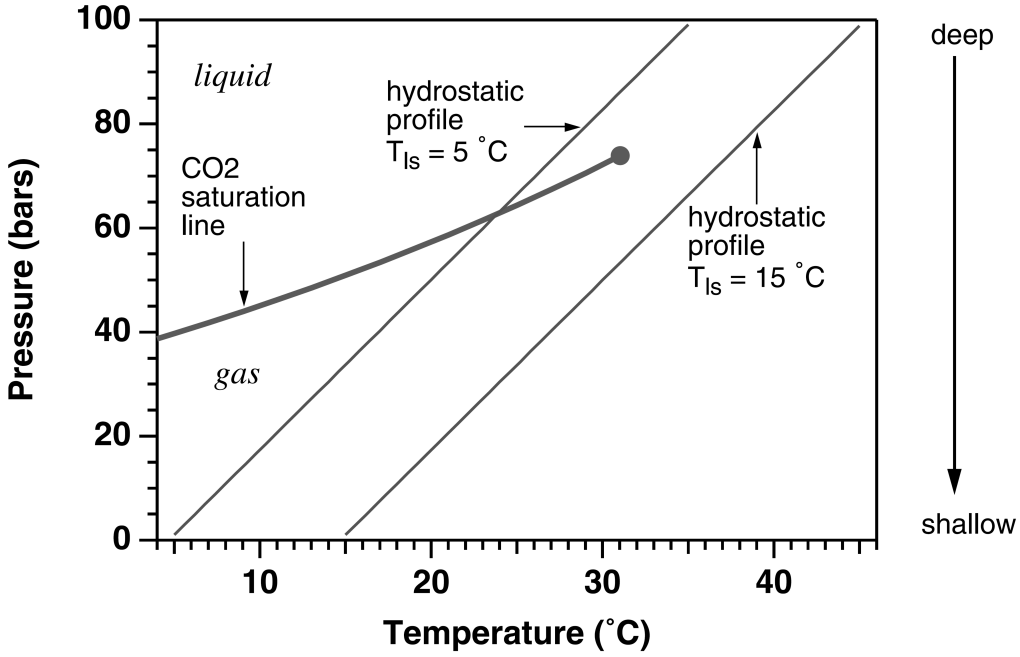

Fig. 1.4 Phase behaviour of CO_2 in the upper ≈1000m from Pruess (2005). At pressures and temperatures greater than triple point of 31°C, 73 bar, CO_2 exists as a supercritical state. At lower pressures CO_2 is a gas, and at lower temperatures it is a liquid. Two typical hydrothermal gradients (30°C/km) with differing surface temperatures are shown. In the lower temperature scenario, this intersects the phase change between CO_2(g) and CO_2(l), and a corresponding large jump in physical properties.

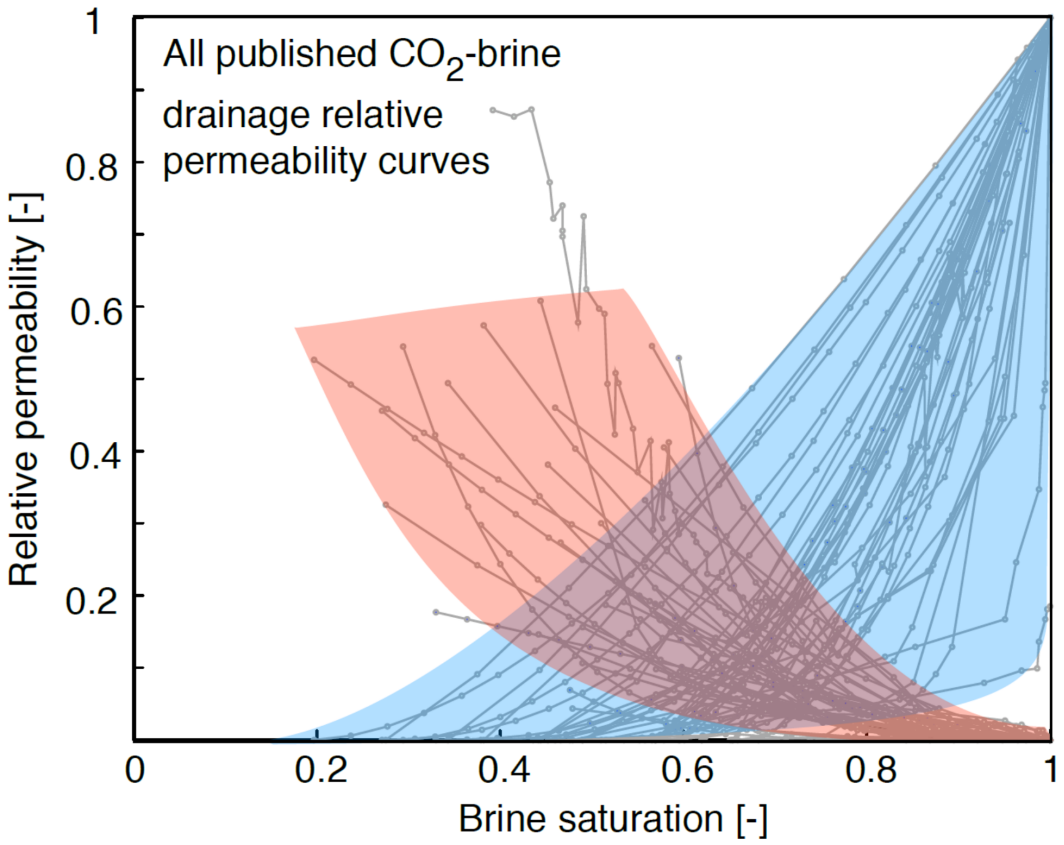

Fig. 1.5 Compiled CO_2(sc)-brine relative permeabilities for sandstones from Benson et al. (2013b). The permeability of a sandstone to CO_2 at maximum saturation is lower than it is to brine, and the pore space maintains connate water concentrations (i.e. water held by capillary forces) of at least 20%. The flow of CO_2 into a reservoir will decrease the brine saturation and the permeability of the sandstone to brine, whilst the permeability to CO_2 increases.

generating stagnant three-phase regions which are dispersed as heat diffusion from the rock matrices 'boils' away the liquid CO_2 (Pruess, 2005). This effect may be an artefact of spatial discretisation. Significant cooling may occur around CO_2 injectors, and these thermal effects may in turn influence geomechanical rock properties. Also, around the injectors H_2O partitioning into the CO_2 can reduce volumes of connate water and lead to precipitation of mineral phases (i.e. 'salting out').

1.2.2 CO_2 fluid-rock interactions

The interaction of CO_2 with reservoir and cap rocks is important in determining the longterm storage of CO_2. The dissolution of CO_2 in reservoir fluids gives a mildly acidic solution through carbonate speciation shown in equation 1.1:

$$CO_2(aq) + H_2O \longleftrightarrow H_2CO_3 \longleftrightarrow H^+ + HCO_3{}^- \longleftrightarrow 2H^+ + CO_3{}^{2-} \quad (1.1)$$

this decrease pH but can be buffered by other solution properties such as alkalinity (where total alkalinity is defined as capacity of the solution to neutralise an acid). Alkalinity is defined by all charged species within a solution. It is convenient to calculate solution chemistry numerically, using software such as PHREEQC to calculate solution chemistry and speciation. The quality of these results depend upon the input of thermodynamic databases; variable data quality and omission of some chemical species may subtly skew these results. Most thermodynamic data is determined in dilute solutions, and activity models have to be adapted at higher ionic strengths. Such databases are even more limited, requiring additional parameters for either Deybe-Huckel or Pitzer models. Numerical models also allow calculation of mineral saturation indexes, and can include relationships for equilbrium or kinetic dissolution/precipitation behaviour which can be made to feedback onto porosity and permeability.

Dissolution rates of minerals, in particular silicates present in sandstone reservoirs (alkali and plagioclase feldspars) have been determined at a range of scales (Brantley et al., 2008). The equation for incongruent weathering of plagioclase is:

$$CaAl_2Si_2O_8 + 2H^+ + H_2O \longrightarrow Ca^{2+} + Al_2Si_2O_5(OH)_4 \quad (1.2)$$

and results in the deposition of clay minerals. It also supplies important cations to the solution. Carbonate minerals may then precipitate by equation:

$$(Ca, Mg, Fe)^{2+} + 2HCO_3{}^- \longrightarrow (Fe, Ca, Mg)CO_3 + H_2O + CO_2(g) \quad (1.3)$$

Dissolution rates appear to be slower at reservoir scale than in experiments (Kampman et al., 2009; Zhu, 2005). Field scale injection experiments such as CarbFix show fast dissolution rates of glasses (Kelemen and Matter, 2008; Matter et al., 2016), confirming that reservoir composition and proximity of minerals to equilibrium is important. Dissolution/precipitation reactions can modify the permeability of a unit. In extreme cases, for example in carbonates, dissolution of $CaCO_3$ increases permeability and flow in this region, in turn increasing dissolution. This positive feedback between transport and reaction leads to formation of 'worm-holes' (Snippe et al., 2017). Conversely, precipitation of secondary minerals can reduce permeability. It is important to understand the governing processes responsible to predict the severity of CO_2 leaking in the unlikely event integrity of a storage site is compromised.

1.3 Assessing storage security

Active storage sites for CO_2 can be monitored in a range of ways. Pressures and fluid compositions at well heads (and potentially in reservoirs with the right sampling equipment) can inform about fluid breakthrough. Otherwise, geophysical sensing methods can be used such as seismic surveys, surface deformation/ or remote sensing techniques (Verkerke et al., 2014). These methods are useful over the timescale of injection experiments, and where appropriate reference baseline measurements are available. However, to understand the consequences of storing CO_2 on longer timescales, we have to look at natural accumulations of CO_2. Green River in Utah is an example of such a site, but leaks because it is cut by two fault systems. However stratigraphic models predict that these fault zones should have very low permeabilities, similar to faults observed offshore (Shipton et al., 2004). Fault bounded reservoirs are common within oil and gas fields, and can divide a reservoir into multiple isolated (or semi-isolated) compartments. The faults at Green River are of similar scale to fault bounded oil and gas reservoirs.

1.4 Objectives of this thesis

This project aims to use travertine vein records at Green River, Utah to understand historical CO_2 leakage from reservoirs up fault systems and the interaction of these fluids with reservoir and fault zone rocks. Low resolution vein records were presented in Kampman et al. (2012) and observed a wide range of variation in different isotopic proxies. This variability was attributed largely to glacial-interglacial forcing driving vertical migration of CO_2 and in turn causing dissolution of silicate minerals (predominantly feldspars). Modern fluid spring samples have also been used to show increasing dissolution of silicate minerals with distance along the fault fault zone (Kampman et al., 2009). Therefore there are several questions which can be addressed:

- What do high resolution records within the veins record? Do any samples capture the glacial-interglacial transitions? Are the distinct signals observed at low resolution preserved?
- Can reactive transport modelling be used to compare fluid flow rates during glacial and interglacial periods? What is the impact of temporal and spatial variation of deposits?
- Can rates of silicate dissolution and carbonate/clay precipitation into/from CO_2 rich fluids be better constrained? How might these vary with proximity to equilibrium?

1.5 Outline of this thesis

To address these objectives, the thesis takes the following outline:

Chapter 2 describes the geology around Green River in Utah. It briefly introduces the regional and local geology, and describes the modern and historical evidence for CO_2 seeping up two fault networks. It includes drone mapping of fracture networks in one of the fault footwalls.

Chapter 3 presents the development of laser ablation methods for rapid analysis of $^{87}Sr/^{86}Sr$, and $^{234}U/^{238}U$-$^{230}Th/^{238}U$ for U-Th dating. The methods have to deal with isobaric interferences and low count rates respectively. Methods are then applied to aragonite veins.

Chapter 4 shows proxy records measured in different veins, at a range of scales. It starts with discussion of previous records presented at fault scale and then presents records at cm to mm scale, and mm to μm scale. This includes results using methods presented in Chapter 3. The internal variability of samples is small, compared to the variability between samples.

Chapter 5 derives an analytical reactive transport modelling to explain spatial variability in $^{87}Sr/^{86}Sr$ and $^{234}U/^{238}U_i$ isotope compositions as a function of dissolution and α-recoil with distance along a one-dimensional flow path. The parameters in this model are calibrated using spring fluid samples dispersed along the fault. The model is then applied to travertine samples, explaining isotopic variation as a function of space rather than time.

Chapter 6 summarises the findings of this thesis.

Finally, three appendices are included providing information on A) the collection of drone data, B) compiled tables of raw data presented and C) solutions to reactive transport equations.

Chapter 2

Geology of Green River, Utah

This chapter introduces the field area, Green River (Utah) which is a natural, leaking, CO_2 accumulation. It covers the geologic history of the region, field relationships and observational evidence for CO_2 mediated reactions and leakage. It is one of the best studied natural analogues for CO_2 sequestration, with very few comparable sites worldwide. The stratigraphy of the region is well constrained from USGS mapping of the extensive outcrops across the state, oil and gas exploration wells and hydrologic surveys of regional aquifers (Doelling, 2002; Doelling et al., 2015; Hood and Patterson, 1984). Over recent years a number of PhD projects have focussed on: the spring water chemistry (Kampman, 2011), travertine 'mound' ages (Burnside, 2010), fault zone structures (Dockrill, 2006), haematite bleaching reactions (Wigley, 2012), cap rock reactions from core sampled by fault zone drilling (Maskell, 2016), and vein cross cutting relationships (Frery, 2013). This chapter will focus on the geologic processes leading to carbonate mineralisation hosted in faults and fractures, which are the focus of later analyses.

2.1 Regional geology and stratigraphy

2.1.1 Colorado plateau CO_2 accumulations

The areas within and around the Colorado plateau (covering the states of Utah, Arizona, New Mexico and Colorado) host multiple accumulations of CO_2 in structural traps (figure 2.1). Many of the deposits, for example Mc Callum Dome are interpretted to have securely stored CO_2 for up to 50Ma (Gilfillan et al., 2008). Such reservoirs are often exploited for use in Enhanced Oil Recovery (EOR) in Texas, or to strip out noble gases within the CO_2. At Green River (Utah), CO_2 saturated brines and CO_2(g) leak to the surface up

two fault systems (figures 2.2 and 2.3) within the Paradox Basin (Jung et al., 2015). The Paradox basin is bound by four major uplifted regions; the San Raphael Swell to the north-west, the Uncompahgre Uplift to the north-east, the San Juan dome to the east, and the Monument Uplift to the south. In the uplifted regions units as young as Jurassic age can lie unconformably upon pre-Cambrian basement. The Paradox basin is perhaps best well known for a thick evaporite succession (the Paradox Formation) which formed during the Pennsylvanian. Surrounding the edge of the Colorado plateau are younger (Cenozoic) intrusions. These are commonly considered to be the source of CO_2, based upon carbon and noble gas isotopes ratios ($CO_2/^3He$ and $^{20}Ne/^{36}Ar$) of the gas phase (Gilfillan et al., 2008). There is, however, some ambiguity in interpretation of these results due to probable fluid-gas exchange during CO_2 migration (a minimum of 100km to Green River). Microbial sulphate respiration at Green River produces minor volumes of H_2S, though these inputs are not large enough to significantly modify either the $\delta^{34}S$ or the $\delta^{13}C$ isotope systems (Chen et al., 2016a; Kampman et al., 2009; Maskell et al., 2017).

2.1.2 Stratigraphy of the Paradox Basin (south-east Utah)

The stratigraphy of south-east Utah is well constrained due to extensive exposure from river incision forming deep canyons, and from oil and gas exploration wells (Dockrill and Shipton, 2010). Figure 2.4 shows units from the mid-Mississippian ($\approx$ 350Ma) through to the mid-Cretaceous ($\approx$80-90 Ma). In 2012, a site on the Little Grand Wash Fault near Green River was drilled by the continental drilling program (DOSECC). This drill core provides excellent local constraint on the stratigraphy of shallower units and data on fracturing in the damage zone of the fault (Kampman et al. (2014b) & Maskell, (2016)). Unfortunately, drilling could not proceed further than the mid-Jurassic Navajo sandstone, and therefore the deeper Wingate and White Rim sandstones (and their corresponding seals) were not sampled. The transmissive units, which are predominantly sandstones (figure 2.4), all have the potential to store CO_2 as either a gas, or dissolved in formation fluids. The surface exposure of these units is very extensive can be seen in figure 2.3. Around Green River, these units form a shallowly northward plunging anticline (maximum dip 10-15°), with most units bedded near horizontal (0-5°).

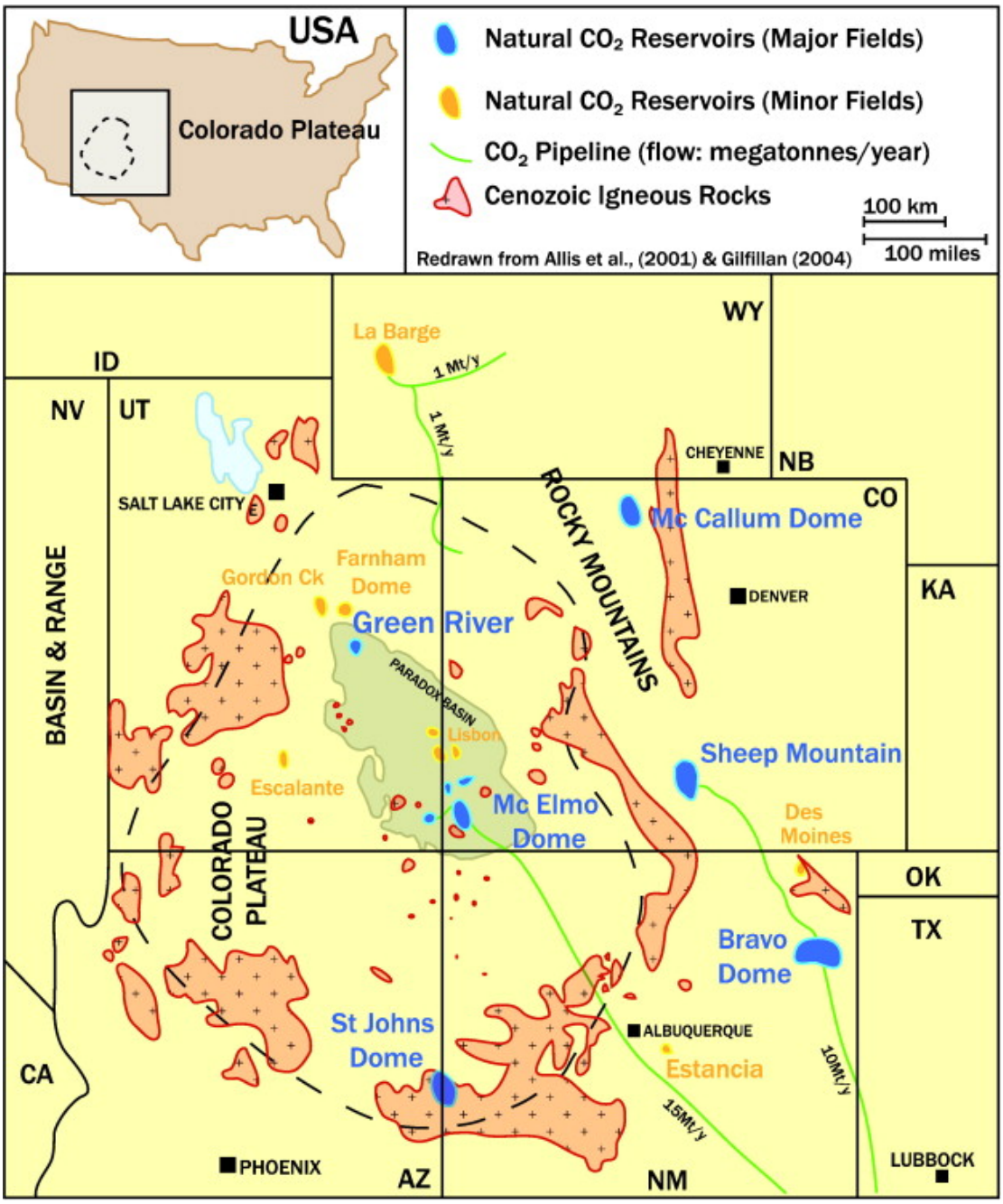

Fig. 2.1 Figure from Kampman et al. (2013a) redrawn after Allis et al. (2001) and Gilfillan et al. (2008). The Colorado plateau is outlined by a dashed line, and roughly follows a ring of cenozoic instrusions, which are inferred to be the source of CO_2. Structural traps around the plateau have stored this CO_2 for up to 50Ma. Green River is within the Paradox basin, and is unique as CO_2 seeps to the surface up two faults and a number of abandoned exploration and water wells.

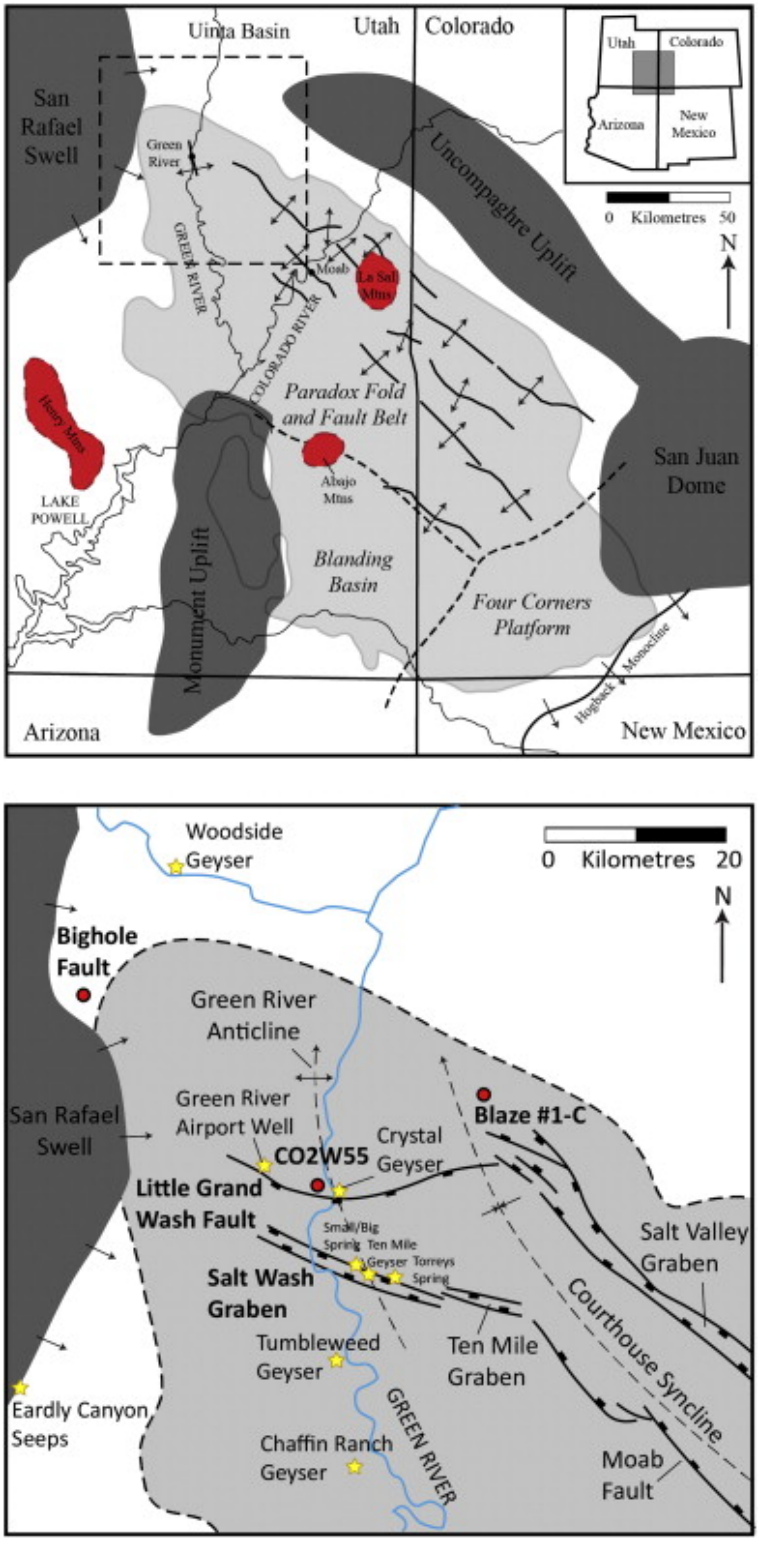

Fig. 2.2 Figure from Kampman et al. (2014b). (Top) spatial extent of the Paradox basin (light grey shading), uplifted basement (dark grey shading), anticline hinges, intrusions (red) and (Bottom) general structure at Green River. Spring samples presented in Kampman et al. (2009) are indicated by yellow stars. The Salt Valley Graben to the North of Moab is interpreted to have formed due to salt dome collapse. Known igneous intrusions are all >100km from Green River. The red circles on the lower panel show core localities used for comparisons in Kampman et al. (2014b).

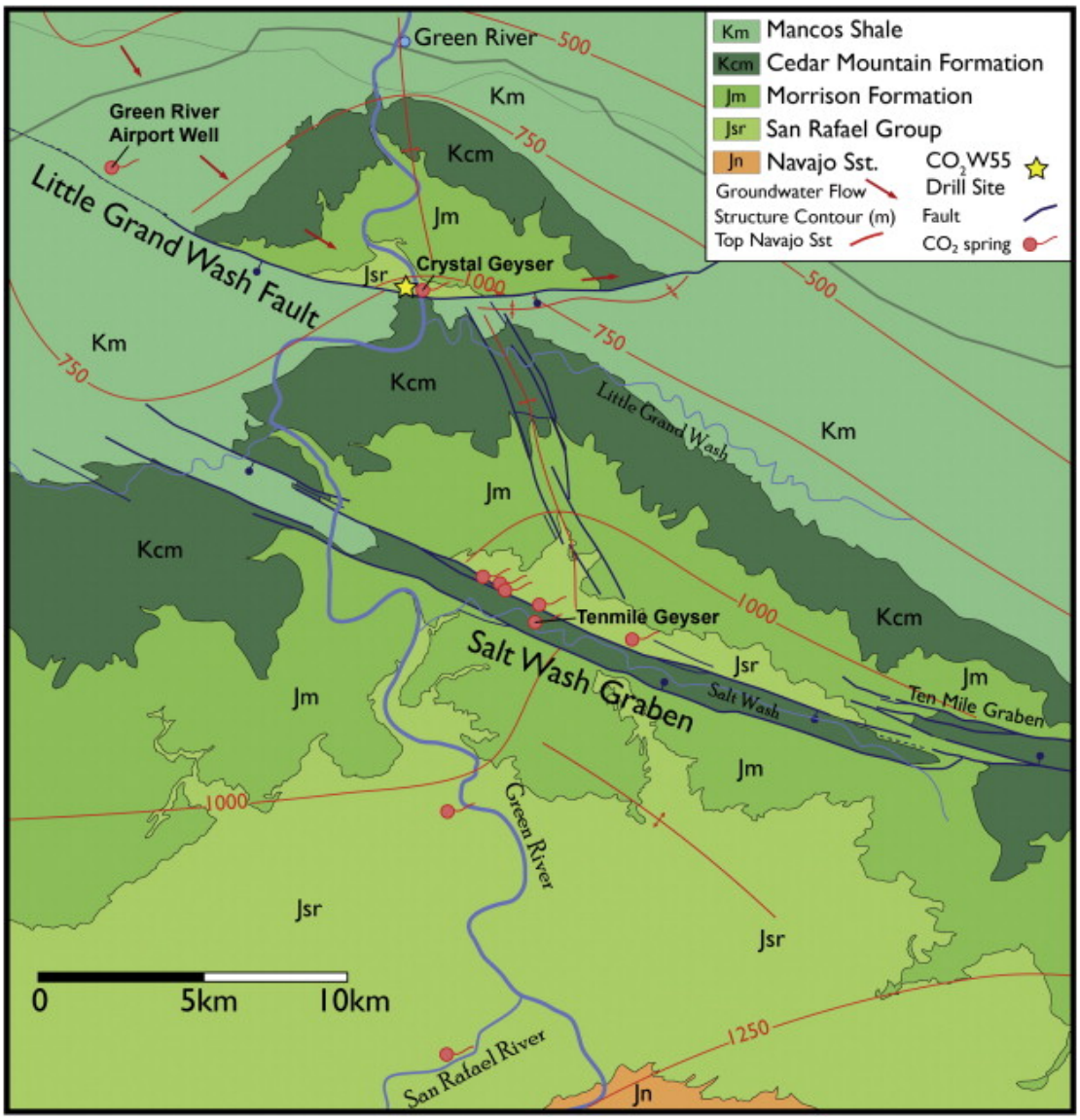

Fig. 2.3 Distribution of spring samples around the fault system, Kampman et al. (2014b), redrawing of Kampman et al. (2009). Spring samples are indicated by red points. Red contours show the depth to the top of the Navajo sandstone. The reservoir is predominantly water saturated in this region, so these contours define a potentiometric surface which dictates regional groundwater flow.

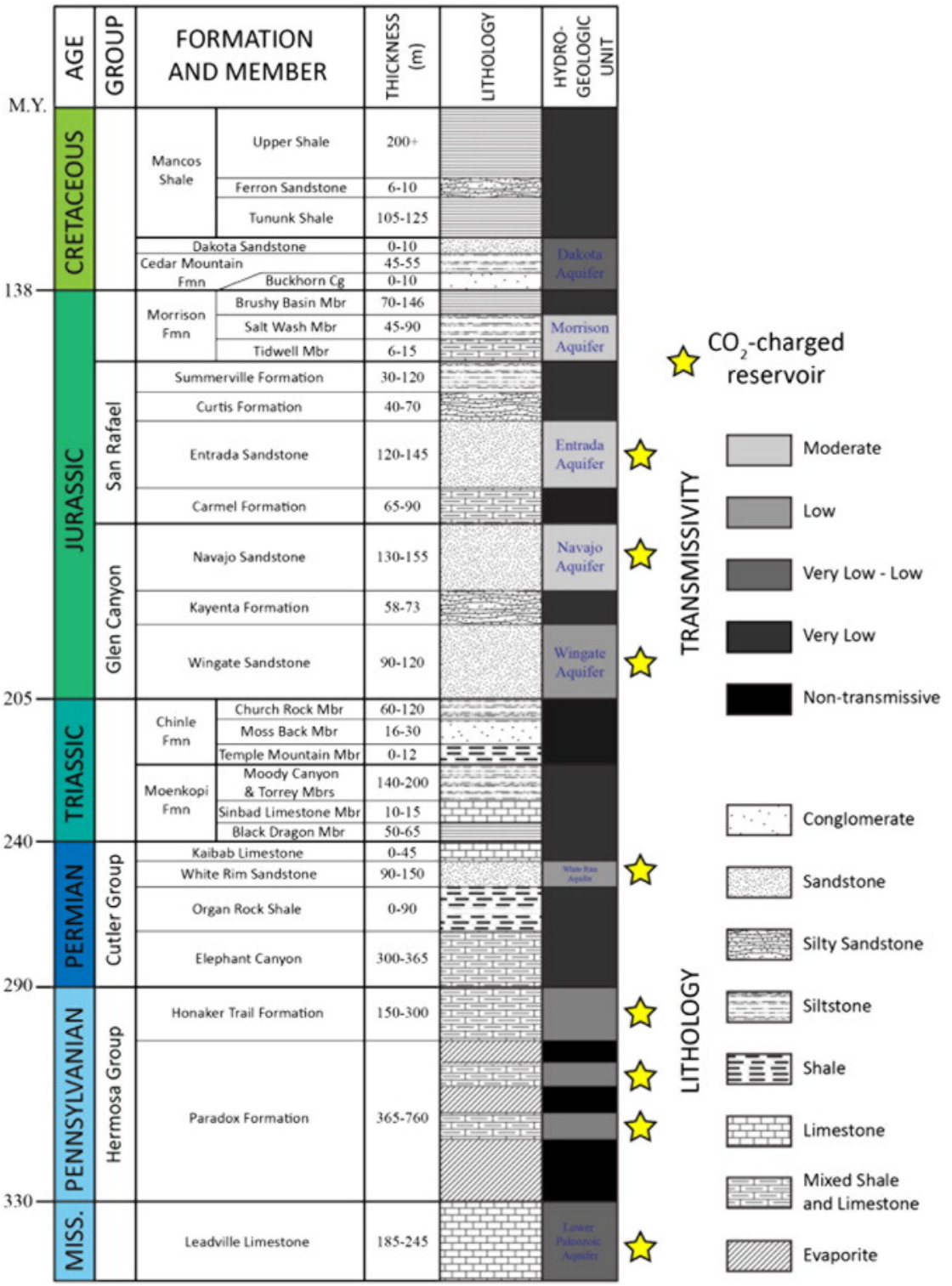

Fig. 2.4 Stratigraphy at Green River, from Kampman et al. (2014b), based upon well logs, local drilling and regional mapping. Potential CO_2 reservoirs are indicated by yellow stars, and have low high transmisvity. Reservoirs of Permian age and younger are siliciclastic, and prior to that are interbedded shale and limestone or limestone. Shale successions in the Cretaceous, Triassic and Permian are thicker than fault throws, and therefore faults core in these units should be relatively impermeable. The Morrison Formation (Jurassic-Cretaceous boundary) hosts roll-front U-V deposits, which were exploited in the San Raphael Swell, the aquifer recharge region. The Paradox Formation (Pennsylvanian) also hosts potash deposits. The Navajo sandstone hosts Mn deposits, to the South of Green River.

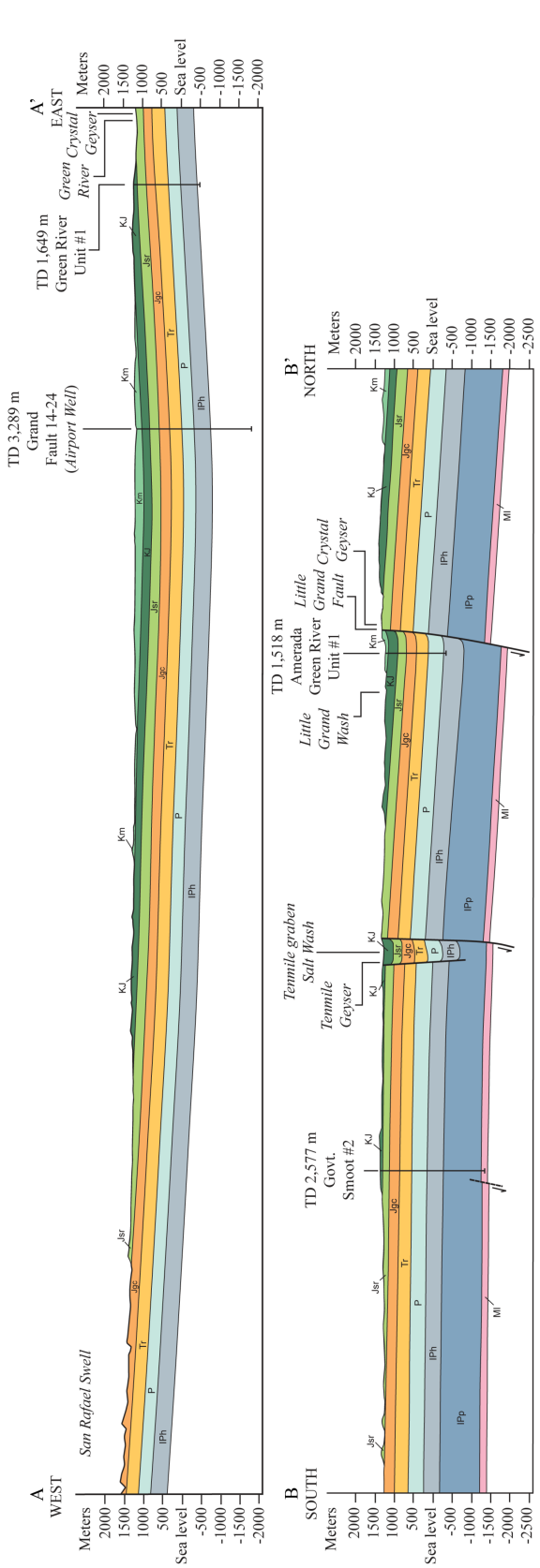

Fig. 2.5 Cross sections from (A) the San Rafael Swell to Green River and (B) along the Green River anticline, from (Doelling, 2002; Doelling et al., 2015; Kampman et al., 2009). Constraints are from surface mapping, and from exploration wells (as indicated), the geometry of fault zones is based upon Dockrill and Shipton (2010). CO_2 migrates vertically along these fault zones, and the predominant groundwater aquifers flow from their recharge zones in the San Rafael Swell towards Green River in the South East.

2.1.3 Fault zone geometries

The two fault zones trend between WNW-ESE and W-E. Both faults have maximum throws >250m so would be visible on seismic surveys, which by traditional methods have vertical resolution equivalent to a wavelet $\approx$ 25m. The internal properties of the fault zone are dependant upon the deformation mechanism of lithological units, examples of which are shown in figure 2.6. The permeability structure of fault zones can be separated into two zones: the fault core, and the surrounding fault damage zone (Caine et al., 1996). The development of these dictate whether the fault is a barrier or a conduit to flow.

Shales tend to deform in a ductile manner, and can be injected into the fault core ('clay smearing'), acting to reduce permeability in the fault core. More highly cemented units, such as sandstones, will deform in a brittle manner allowing fracture networks to develop in the fault damage zone (panel b in figure 2.6). The permeability of fracture networks is highly dependant upon pressure, which dictates the magnitude of fracture apertures. The density of fractures, and their apertures, can be higher towards the tips of faults where units are in tensile stress without surpassing a threshold for brittle fracture. Fractures are less likely to be maintained in units which deform in a ductile fashion. Cataclasistic deformation of sandstones will reduce permeability within the fault core, relative to the neighbouring reservoir. The properties of the fault core can be predicted by proxies such as the shale-gouge ratio or clay smear potential, which are functions of the lithology. Such models were created for Salt Wash and Little Grand Wash faults by Dockrill and Shipton (2010). High values for both proxies along each fault suggest that cross fault fluid flow is minimal over the central 10-15km of the faults. At small throws towards the fault tips, reservoir self-juxtaposition occurs and allows cross fault flow. This also limits the storage of buoyant phases, and is termed the spill point. There is no direct evidence of recent movement on the fault; at a single locality on Little Grand Wash there are cemented breccias with clasts of veins of ages $\approx$ 120ka (sample 'FB' in appendix B). Otherwise, minor earthquakes (< magnitude 2.5) were observed within 2km of Crystal Geyser in 2006 and 2010 (Han et al., 2017). Modern fluid flow is unrelated to seismic activity, and as there is no distinctive evidence of fault movement in the last 120ka it is unlikely that seismic pumping is responsible for fluid flow (and this process is restricted to much larger faults (Sibson et al., 1975)).

Little Grand Wash Fault

The Little Grand Wash Fault is the northerly of the two faults, and is a listric fault dipping steeply to the south. It is composed of several southward dipping fault splays. It is therefore

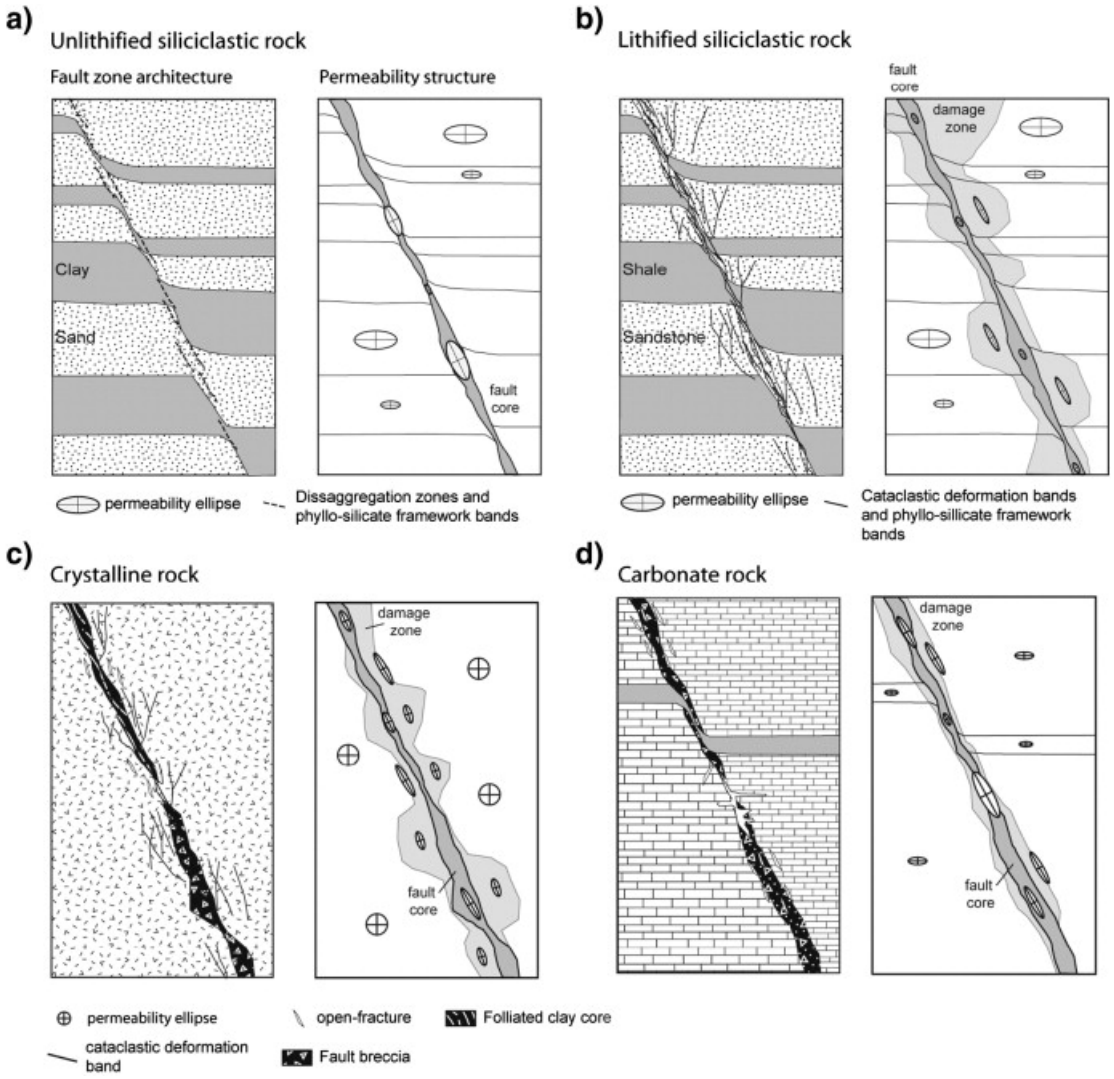

Fig. 2.6 Fault zone deformation processes from Bense et al. (2013). Directional permeability is represented by an ellipse. Each panel shows typical shallow (<1km depth) deformation of a) unlithified siliciclastic sediments b) lithified siliciclastic sediments c) crystaline rocks and d) carbonate rocks. At Green River panel b) is most relevant; the width of the damage zone (light grey) is wider in these lithified sandstones, due to fracture formation.

Fig. 2.7 Siltstone bleaching reaction in fractured block, Little Grand Wash Fault (38.9363°N, -110.1152°E). Iron reduction must be mediated by a reductant in the fluid, likely CH_4 or H_2S. Lens cap diameter ≈65mm.

difficult to distinguish the core of the fault. The maximum throw of the fault is ≈ 260m, which is centred around the anticline hinge (Dockrill and Shipton, 2010). The hanging wall of the fault is composed of (downthrown) Mancos Shale, therefore the surface exposure in the fault zone is very clay/shale rich. Fractured red siltstone blocks within the fault zone show evidence of iron reduction around fracture networks (figure 2.7), and cataclastic bands are present within sandstone blocks (figure 2.8). At a single locality along the fault hydrocarbons (oil) seep to the surface (displayed in figure 2.12).

Next to the Green River, at the centre of the anticline hinge, a partially sealed abandoned exploration well (drilled in the 1930's) forms Crystal Geyser, a cold-water geyser. Cold-water geysering has only been observed in unrestricted conduits, and are therefore predominantly man-made (Han et al., 2013). Solubility of CO_2 within solution decreases as fluid decompresses, and the exsolution of CO_2 is the driving force for Geyser eruptions (Assayag et al., 2009; Duan et al., 2006; Dubacq et al., 2013). The interaction of the evolving gas phase with brine dictates the multiphase flow properties and the manner of eruption, with the major styles being dispersed, bubble or plug flow. Degassing is thought to initiate at ≈120m depth in the unconfined borehole (Assayag et al., 2009). CO_2 saturated fluids were recovered from the Navajo Formation during drilling (Kampman et al., 2014b).

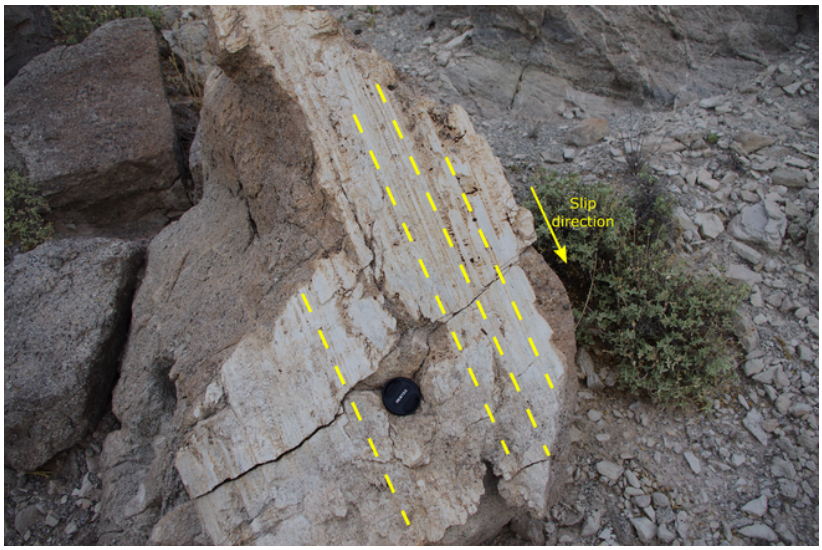

Fig. 2.8 Surface of cataclastic band between fault splays at Little Grand Wash Fault (38.9356°N, -110.1158°E). These bands act to reduce the permeability of fault cores composed of sandstone units. Lens cap diameter ≈65mm.

Salt Wash Graben

To the south of the field area is the Salt Wash graben, which is composed of two faults. The northern, southern dipping fault, has a maximum throw of 366m, and the southern, north-dipping fault has a throw of 210m. The southern fault shows no evidence that it is transmissive to fluids and is assumed to pinch out onto the northern fault (Jung et al., 2015). The maximum throw on both faults is to the east of the anticline hinge (Dockrill and Shipton, 2010). There is a relay ramp to the eastern end of the fault, where it begins to overlap with the next graben, Ten-Mile graben which is filled with gypsum precipitates. Associated with the gypsum is Manganite (MnO(OH)) and Rancieite ($(Ca, Mn)Mn_4O_9 \cdot 3\,H_2O$), which are probably surface alteration products.

Compared to Little Grand Wash Fault, there are fewer fault splays, which may be the result of lithological control. Within the fault zone at Salt Wash, there are extensive gypsum veins, upto 15m thick, and at one locality sheared gypsum is cross cut by laminar gypsum veins within the fault zone (figure 2.9). A TOUGHREACT-2 modelling study by Patil et al. (2017), shows that gypsum precipitation can occur when calcite nucleation is inhibited, but aragonite saturation is not met. They erroneously note there is no evidence of gypsum precipitation at Green River.

Fig. 2.9 Cross cutting sheared gypsum veins from within the northern fault at Salt Wash (38.8562°N, -110.0752°E; looking west). Sheared gypsum is cut by laminar gypsum. Gypsum can flow, and therefore is not a reliable shear sense indicator.

Entrada bleaching at Salt Wash

The exposed footwall at Salt Wash is composed of the Entrada sandstone. The formation has a very pronounced red colour from haematite grain coatings on (mostly) quartz. Where CO_2 and a reductant (CH_4, or more likely H_2S) flow through the sandstone this leads to a 'bleaching' reaction, where haematite dissolves turning the sandstone white. These reaction fronts mobilise trace metals from the bleached zone and redeposit them beyond the front (Wigley et al., 2013). Bleaching of the Entrada is extensive around the anticline hinge at Salt Wash, but can also be observed up to 6km away to the south east (towards Ten Mile Graben). The lower sections of exposed Entrada show bleaching which follows bedding, and where permeability heterogeneity exists because of dune interbedding, the bleaching occurs in the more permeable layers. Around the anticline, where the Entrada is highly fractured, the fractures are bleached due to vertical fluid transport. Bleached cores of fractures at the surface weather preferentially to unbleached fractures, with potential geomechanical implications (if these reactions occur within the reservoir). The cores of some fractures are sealed by gypsum (or celestine) precipitates. These fractures are on the same strike as local faults. This is shown in figure 2.11, which is a composite image produced from a Unmanned Aerial Vehicle (UAV/ drone) survey carried out to the east of the anticline hinge at Salt Wash in September 2016. Collection of this data is discussed in appendix A.

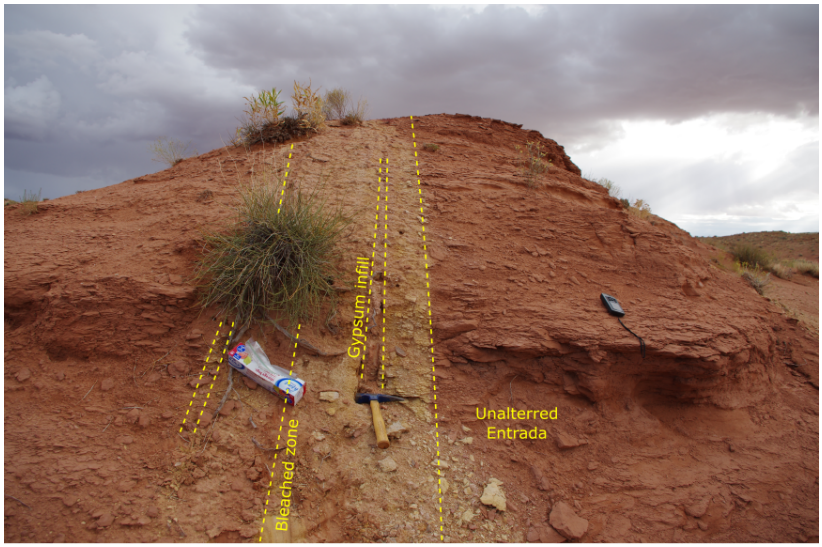

Fig. 2.10 Weathered bleached fracture with gypsum in the core in fracture networks east of the anticline hinge at Salt Wash (38.8624°N, -110.0882°E)

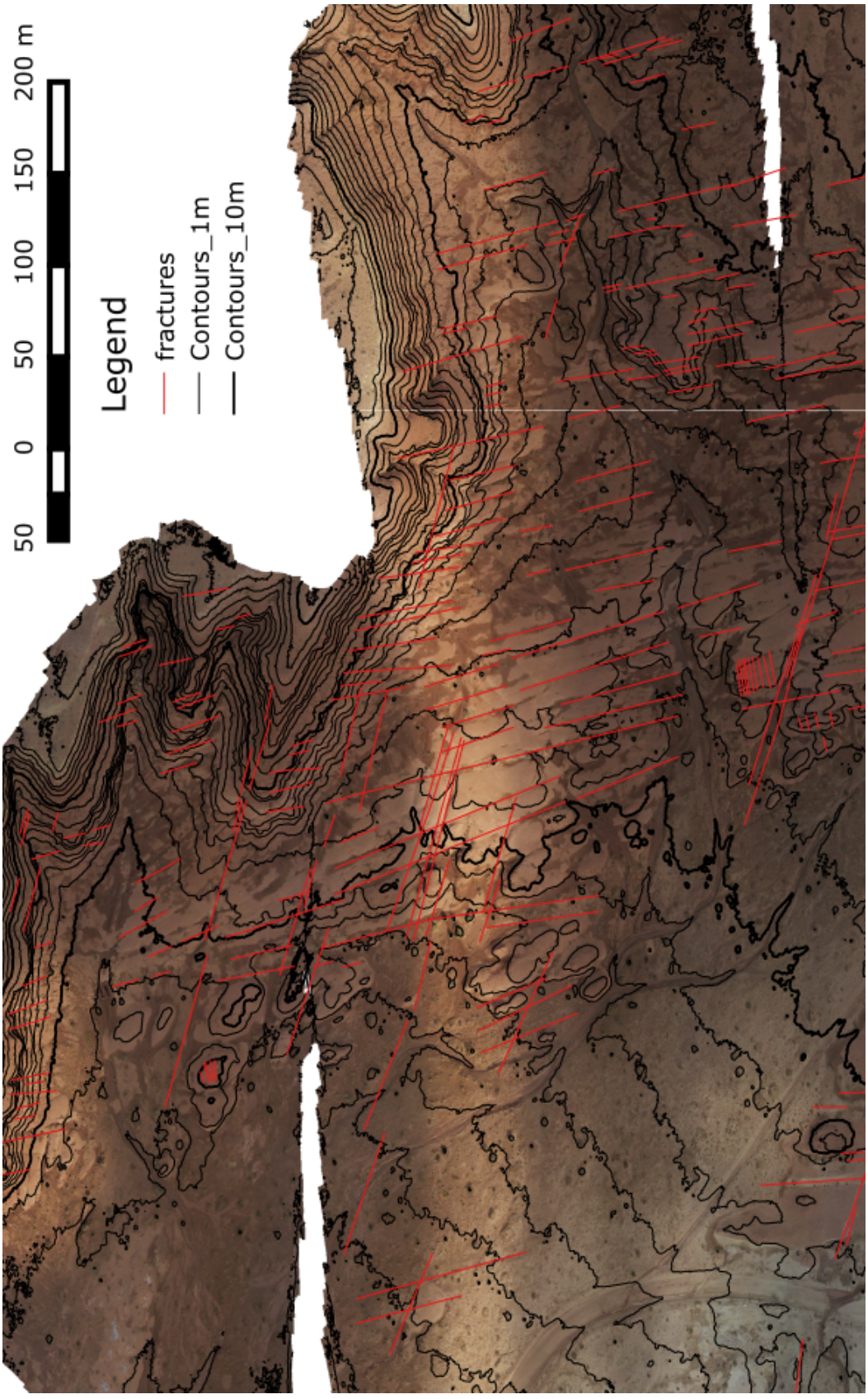

Fig. 2.11 Map of fracture networks in the Entrada sandstone in the footwall of the Salt Wash fault, 1km east of the anticline hinge. Contours derived from a calculated digital elevation model (DEM), are shown in black, and fracture networks are shown in red. Vertical flow of fluids is predominately mediated through these networks.

NNW-SSE graben between Little Grand Wash and Salt Wash

Between the two major normal faults is a small graben structure with faults either side of the anticline hinge axis. These faults appear not to be transmissve to fluids, and show much smaller throw. They may slightly alter groundwater flow patterns in shallow units, acting to channel flow parallel to the anticline hinge axis and at an angle to the potentiometric surface. Fracture networks at Salt Wash have the same strike as this pair of faults.

2.1.4 Regional groundwater flow and springs

All units above the White Rim sandstone are exposed in the San Raphael Swell to the North-West of Green River (figures 2.2 and 2.4). Aquifers are partially saturated and can recharge in this region (Kampman, 2011). The depth of the most shallow aquifer, the Navajo sandstone, increases to the south-east (indicated by red contours in figure 2.3). This unit is known to supply fluid to Crystal Geyser, and is thought to be the main fluid supply to springs along the fault (Kampman et al., 2009). The decrease in hydraulic head to the south-east away from the San Raphael Swell drives regional groundwater flow in the Navajo (Hood and Patterson, 1984). Recharge in the aquifer, and therefore fluid pressures, may change as local precipitation patterns vary. The extent of glacial lakes and mountain glaciers have fluctuated with glacial-interglacial climate patterns. Glacial Lake Bonneville, for example, occupied an area larger than the modern Salt flats (Laabs et al., 2009), and prior to this two other glacial lakes occupied the region; Cutler Dam and Little Valley (Kampman et al., 2012). Lake Bonneville drained North along the Snake River plain (Idaho) (Malde, 1968), and the palaeoshore of the lake is $\approx$ 120-150km to the northwest of the San Raphael swell. The glacial hydrologic cycle is therefore more intense (wetter) than the present day, and the large glacial lake is thought to have maintained glacier cover in the Uinta mountains between Utah and Wyoming. Glacial melt and higher precipitation could therefore contribute to greater aquifer recharge. Deeper units are slightly overpressured (up to 15bar, a maximum of $\approx$ 10% relative to hydrological pressure), which drives vertical migration of fluids through permeable zones (i.e. in fracture networks) (Kampman et al., 2014b). An important question is how fluids leak through fault zones such as at Green River, where thick shale successions are juxtaposed on faults forming low permeability fault cores and narrow damage zones (Shipton et al., 2004).

2.1.5 Fault zone drilling

Fault zone drilling was undertaken by DOSECC in July 2012 and is discussed thoroughly in Kampman et al., (2013,2014) and Maskell, (2016). The drilling site was on the western bank of the Green River on the Little Grand Wash fault. The recovered core section intersects through one of the fault splays around the anticline hinge. The core logs are shown in appendix B. Fractures are preserved in the Entrada, Carmel and Navajo Formations, with the highest density of fractures in the Carmel. Some of these fractures are sealed with gypsum precipitates (Chen et al., 2016a), and fractures and cap-rock contacts show bleaching reactions requiring mildly reducing fluids (Maskell et al., 2017). Drilling was paused at varying reservoir depths in order to collect reservoir fluids in-situ (i.e. pressurised) using a custom fluid sampling device (Kampman et al., 2014b, 2013b). Degassing of fluids was observed in some units of the Entrada, and the entirety of the Navajo. The downhole fluids show that fluids are CO_2 saturated within the Navajo. Mixing trends suggest a minimum of three end-members, one for each formation; fault zone brines, Carmel Formation fluids and meteoric fluids from the Entrada. This will be discussed more thoroughly in chapter 4.

2.2 Secondary mineralisation: Tufa/Travertine deposits

Along the length of the Little Grand Wash and Salt Wash faults there is abundant carbonate mineralisation, and as previously mentioned sparse sulphate mineralisation. Carbonates occur in a range of morphologies but come under the definition of tufa (low temperature carbonates) or travertine. These terms are used interchangeably in the literature, though technically travertine should be reserved for high temperature carbonates with low porosity (Pentecost, 2005). The positions of the deposits are shown in figure 2.12. The largest deposits occur on Little Grand Wash (Burnside et al., 2013), and occur at fault splay intersections where fracture permeabilities are inferred to be higher. All the deposits are east of the anticline hinge. At Salt Wash the deposits are more evenly spread along the fault, with localities either side of the anticline hinge. There is a slightly higher density of deposits around the anitcline hinge axis. The following sections describe each of the carbonate morphologies; ‘mounds’, layered ‘mats’, cemented gravels, ‘feeder’ veins, box-work veins and speleothems. All are indicators of past movements of carbonate oversaturated fluids.

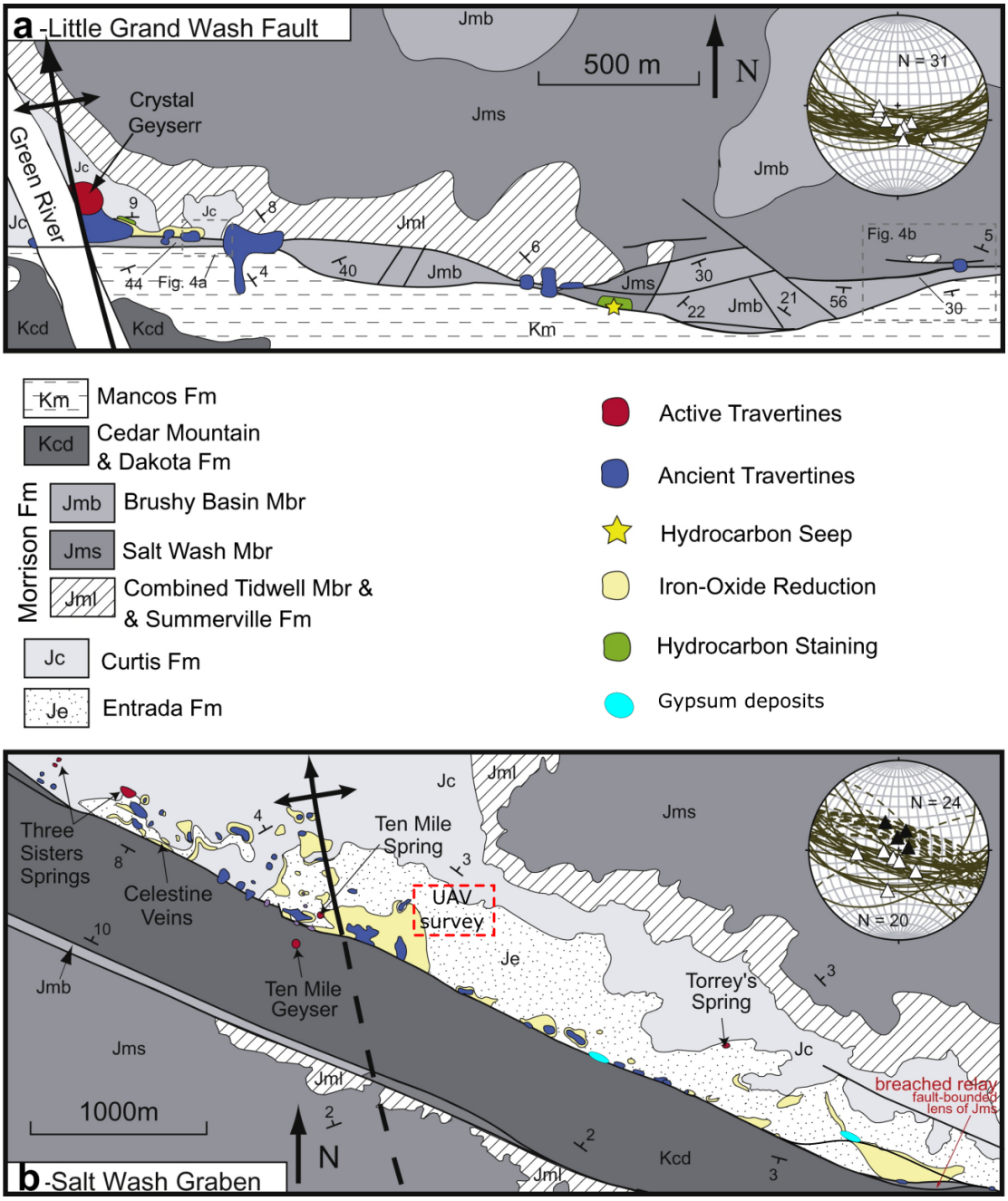

Fig. 2.12 Travertine deposit locations modified from Dockrill and Shipton (2010). Active springs are shown in red, carbonate deposit locations in blue, and a single locality at Little Grand Wash where there is hydrocarbon staining is shown in green. At Salt Wash haematite bleaching of the Entrada is indicated by cream. Gypsum localities are shown in light blue, and the area mapped by UAV outlined by the red dashed box. Equal angle stereonets show the orientation of lineations within the fault zone.

Fig. 2.13 Exposed vein with porous surface travertine 'mat' growing on top; Salt Wash (38.8558°N, -110.0736°E). Lens cap diameter ≈65mm.

Travertine 'mounds', 'mats' and cemented gravels

The term 'mounds' is used to describe any exposed locality with carbonate mineralisation. They are exposed at relative topographic highs in the footwalls of both the Little Grand Wash and Salt Wash faults. The top of many (but not all) mounds posses layered mat deposits, and this is thought to protect them against erosion (Burnside, 2010). Modern layered mats form from overflowing borehole fluids at Crystal Geyser. The deposits are porous, entrain local sediment and show evidence of microbial activity (Barth and Chafetz, 2015). As such, these carbonate mats are difficult to date by U-series due to high detrital contamination. The historic deposits are thought to be 'fed' by fluid flow up fractures networks, where vein deposits form (discussed in the next section). An example of a 'feeder' vein (discussed in the next section), with a layered mat on top of it is shown in figure 2.13.

At some localities there are carbonate cemented gravels. This was interpreted as in-situ mineralisation of stream gravel beds, and these deposits form a series of palaeo-river terraces. This relationship was used to infer incision rates, though ages were determined on feeder veins rather than directly on the cements (Burnside, 2010).

Travertine 'feeder' veins

Mounds are eroded by river incision, revealing cross sections of aragonite vein networks. These are typically <5m below the cemented mats or river gravels, suggesting formation in the shallow subsurface. These are assumed to form in feeder conduits to the surface carbonate

Fig. 2.14 Cemented gravels; Salt Wash/Ten Mile (38.8480°N, -110.0366°E)

deposits. The veins exploit weaknesses in the rocks, following existing fractures or bedding planes. Gratier et al. (2012) suggest that sudden exsolution of CO_2 from oversaturated solutions could induce fracturing, which is later held open by aragonite crystallisation. Veins crystallise inwards from the outer-walls of the fracture. They often form coarse radiating crystals, up to 5cm long, suggesting continuous growth within a fluid filled cavity. The thickness of veins varies widely, from 1cm up to 3m at 'Universal Mound' on Little Grand Wash fault (Burnside et al., 2013). Most samples display some form of growth banding, suggesting pulsed growth. The significance of this is discussed in chapter 4. At some localities multiple generations of veins are observed in cross cutting relationships, for example next to Crystal Geyser, and are interpreted to represent episodic fluid migration related to fault sealing (Frery et al., 2015). In thin section, individual crystals up to 200μm long are observed. Twins and crystal boundaries often accommodate detrital phases. Calcite veins are observed in the hanging wall at Little Grand Wash (within the Mancos Shale) but exposure is extremely poor: locations could only be found by drift mapping and digging through deposits.

The large veins are excellent targets for U-series chronology, because of low detrital contamination. Therefore, the largest veins at multiple localities were analysed as they are thought to result from the largest fluid fluxes up the fault system. Some of the veins show evidence of growth haitus' where dendritic iron-oxide structures form. Secondary electron microscopy (SEM) images (figure 2.15) show bud-like structures which may be biogenic in origin (similar to those observed in surface deposits by Barth and Chafetz (2015)). Just below this feature in one sample is interstitial celestine within aragonite (figure

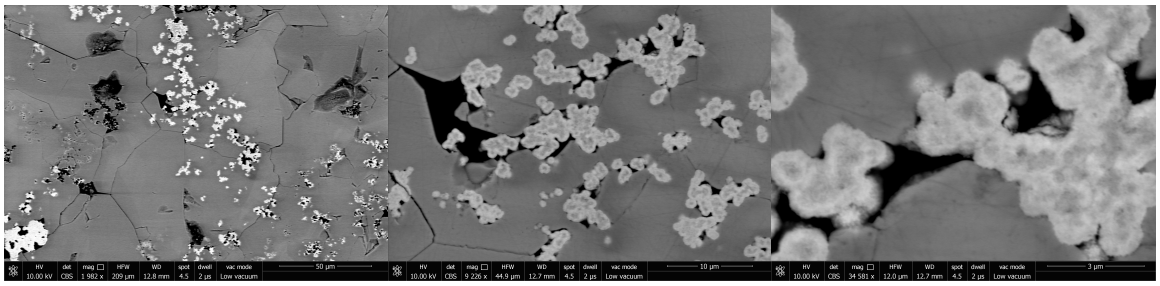

(a) 50μm (b) 10μm (c) 3μm

Fig. 2.15 Electron back scatter images of interstitial Fe-oxyhydroxides within aragonite vein sample SW/06/25C. Bud-like structures suggest biogenic origins, field of view marked beneath each figure.

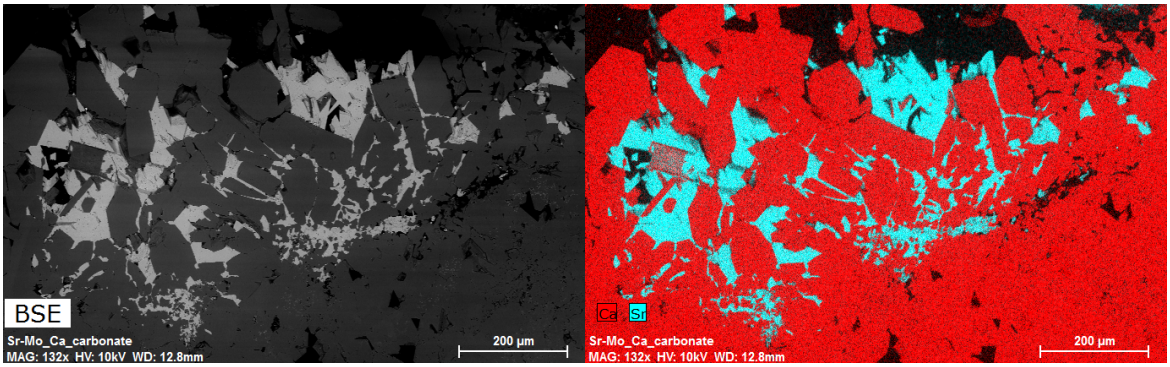

(a) BSE image (b) EBSD image

Fig. 2.16 Interstitial sulphates within aragonite vein sample SW/06/25C. (a) Electron backscatter (BSE) image shows celestine in lighter greys, and (b) electron back-scatter diffraction (EBSD) image shows the abundance of Ca (red) and Sr(blue), which differentiates the aragonite and celestine.

2.16). Celestine has been observed in the area before, but has always formed pure veins (Dockrill and Shipton, 2010). Previously this was interpreted as mixing of a Sr and SO_4 bearing fluid (Dockrill and Shipton, 2010), but inter-grown aragonite and celestine makes a single fluid source more likely. The presence of celestine could complicate interpretation of geochemical trends, for example of Sr or Ba: there is complete solid solution between celestine and barite ($SrSO_4 - BaSO_4$)). This may cause a bias in measurement of systems such as $^{87}Sr/_{86}Sr$ because fractionation factors for$\delta^{88}Sr$ depend upon this solid-solution composition (Widanagamage et al., 2014). These biases are discussed more thoroughly in chapter 3, and may also apply to other isotopic or trace metal tracers.

Fig. 2.17 Boxwork veining; Little Grand Wash (38.9364°N, -110.1088°E)

'Box-work' veins

'Box work' veining is observed within silty/shaley units at Little Grand Wash Fault, and forms mm to cm scale, cross cutting vein structures (figure 2.17). It has been suggested that these occur in regions with highest fluid fluxes (Burnside, 2010), but the limitation to two localities with fine grained units make lithological control more likely. Subsets of these veins have reduction halos surrounding them (figure 2.18). These fracture sets therefore have accommodated reduced fluids.

Speleothems

Open voids in some of the vein systems exist, mostly on Little Grand Wash, and these voids have speleothems growing within them (stalagmites, stalactites and flow stones; figure 2.19). To form, these voids must have been aerated to allow for CO_2 degassing from a descending carbonate saturated fluid. The carbonate is coloured yellowish-brown, with thin rust coloured layers, suggesting high Fe or Mn concentrations. Such structures indicate mixing of meteoric fluids and groundwaters. The speleothems remain vertical, suggesting no large movements on the fault since their formation.

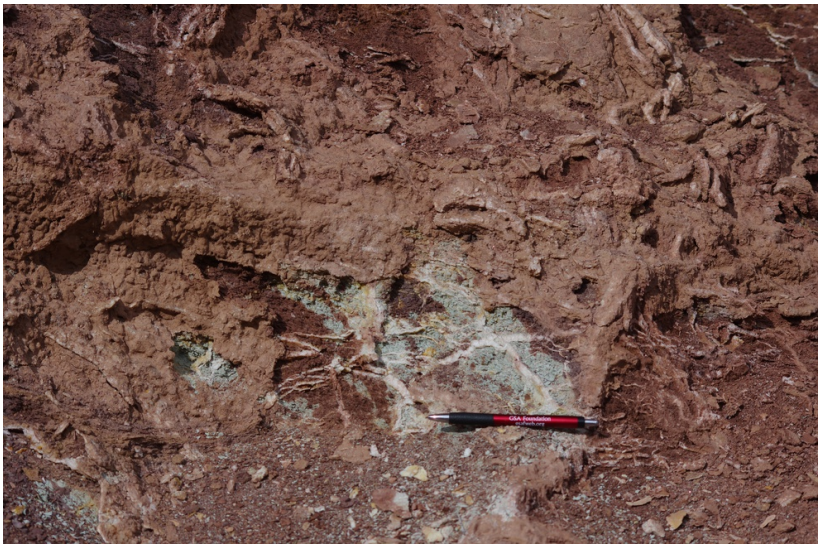

Fig. 2.18 Siltstone iron reduction associated with boxwork veins; Little Grand Wash (38.9364°N, -110.1088°E)

Fig. 2.19 Speleothems; Little Grand Wash (38.9364°N, -110.1088°E)

2.3 Conclusions

This chapter has introduced the regional and local geology of the field area Green River (Utah). It has briefly covered the stratigraphy of the Paradox basin in south-east Utah, and the structure of the faults zones at Green River. CO_2-rich springs, a man-made Geyser and higher soil gas CO_2 fluxes indicate contemporary CO_2 seeps. Carbonate deposits indicate histroic flux of carbonate oversaturated, and thus CO_2-rich, fluids. The deposits have a range of morphologies, but with the exception of speleothem structures indicate fluxes of fault derived fluids. Flow is most likely accommodated by fracture networks within the damage zone of faults, and carbonate veins are largely restricted to the fault footwall. The thicker aragonite 'feeder' veins are targeted in the following chapters of this thesis, as they represent the largest fluid fluxes. The presence of other accessory phases within aragonite (celestine and iron-oxyhydroxides) may impact concentrations of trace metals, with implications for isotope and trace metal measurements presented in chapters 3, 4 and 5. Sulphate deposits within the fault are discussed briefly, though their significance to fluid migration is not yet fully understood.

Chapter 3

Laser ablation Sr and U isotopes

This chapter presents the laser ablation methods developed for analysis of Sr and U isotopes by inductively coupled plasma mass spectrometry (ICP-MS). Analysis focuses on carbonates, as the methods are applied to the aragonite feeder veins collected from Green River. However, to demonstrate the advantage of medium instrumental resolution for analysis of Sr isotopes, NIST glasses are measured. The chapter is split into three main sections; a brief introduction to laser ablation mass spectrometry, the Sr isotope method in Cambridge, and the U isotope method at the British Geological Survey National Isotope Geochemistry Lab (BGS/NIGL). The data collected by these methods, and their modelling, is presented in the following chapters 4 and 5.

3.1 Laser Ablation Mass spectrometry

Laser ablation is a form of sample introduction to an ICP-MS. A laser pulse hits the sample, leading to disaggregation of the sample into particles and plasma, which may subsequently condense (Wu et al., 2017). The particle size distribution is particularly important, as this influences transport properties towards the plasma torch (Guillong and Gunther, 2002). Once in the plasma torch, particles disaggregate (also a function of size), elements volatilise and then ionise. Comparisons of nano-second (ns) and femto-second (fs) lasers show that shorter laser pulses create more uniform particle sizes, and reduce elemental fractionation (Zheng et al., 2017). However a disadvantage of laser ablation is that there is no chemical separation of elements from the sample matrix, so elemental and polyatomic isobaric interferences can cause significant issues. As such, both the laser and mass spectrometer must be tuned to minimise the impact of interferences. A higher resolving power may be used to 'avoid'

Table 3.1 Terminology definitions

Term	Description
Accuracy	Measured value relative to a reference value.
Error	Offset from a reference value, can be systematic (a bias) or random.
Precision	Also reproducibility or repeatability; a measure showing the extent that repeat measurements give the same result.
Uncertainty	Range of values, encompassing the 'true' value.
Confidence Interval	An uncertainty, quantified relative to a statistical distribution. It is common in geochronology to quote to 2σ[1]which is approximately a 95% confidence interval for a univariate distribution, or a 86% for a bivariate distribution
Date	A number calculated using isotope ratios and a decay equation.
Age	An interpreted date, normally given geological significance.

[1] strictly this should be s, rather than σ, as analysis is performed on a set of subsamples rather than the entire population

interferences, at the expense of sensitivity; another isotope of the interfering element can be used to make a correction; or a collision/reaction cell can be used to remove interferences.

3.1.1 Accuracy, precision, error and uncertainty

The performance of any analytical technique is judged on several criteria: accuracy, precision, error and uncertainty. In keeping with other geochronological conventions, we use the same terminology as Schoene et al., (2013) regarding 'accuracy', 'precision', 'error', 'uncertainty', 'date' and 'age'. These are discussed with reference to metrology terminology in Horstwood et al. (2016), and summarised in table 3.1. A note on units: ppm on a Sr isotope ratio is used as shorthand for $\times 10^{-6}$ on the absolute value, rather than expressing a relative uncertainty. However, % and ‰ remain used as relative uncertainties.

Mean Squared Weighted Deviation (MSWD)

The Mean Squared Weighted Deviation (MSWD, or reduced chi-squared test in non-geological disciplines) is a measure of data point uncertainties relative to data dispersion. It is calculated by the following formula:

$$MSWD_u = \frac{1}{N-1} \cdot \sum_{i=1}^{N} \frac{(x_i - \bar{x})^2}{\sigma_{x_i}^2} \tag{3.1}$$

It is a comparison of the scatter from repeats $(x_i - \bar{x})$ to analytical uncertainties σ_{x_i}, and is commonly used in geochronology (McLean et al., 2016; Wendt and Carl, 1991; York, 1969). The weighted mean (and standard deviation) of the whole population is used as a reference value ($\bar{x}$). If MSWD = 1, calculated σ matches that expected from known analytical errors; MSWD » 1 shows that data points are over-dispersed so data point uncertainties are underestimated; MSWD « 1 shows data are under-dispersed, so uncertainties are overestimated. MSWD > 1 can result from underestimating analytical errors or from sample/standard heterogeneity. A larger MSWD can be acceptable at small numbers of repeat analyses (Spencer et al., 2016; Wendt and Carl, 1991).

3.2 Strontium isotopes

3.2.1 Introduction

Radiogenic strontium isotopes ($^{87}Sr/^{86}Sr$) are used to address a diverse range of scientific questions, acting as tracers of: silicate/carbonate weathering (Bickle et al., 2005; Edmond, 1992; Tipper et al., 2006), sediment origins (Hemming et al., 1998; Revel et al., 1996), migration patterns and ecosystem processes (Capo et al., 1998; Font et al., 2007; Hobson, 1999; Hodell et al., 2004; Kennedy et al., 2002), magmatic processes (Doe et al., 1982; Zindler et al., 1981, 1979); or as a geochronological tool in marine sediments using isotope stratigraphy (Diener et al., 1996; Elderfield, 1986; Hodell et al., 1989; McArthur et al., 2001; Palmer and Elderfield, 1985). Variation in $^{87}Sr/^{86}Sr$ is caused by the preferable partitioning of Rb (relative to Sr) into solid phases during partial melting and crustal differentiation and the subsequent β-decay of ^{87}Rb to ^{87}Sr ($t_{1/2} \approx 4.961 \times 10^{10}$years). Additionally, stable Sr isotopes ($^{88}Sr/^{86}Sr$, often expressed as $\delta^{88}Sr$) are known to fractionate between fluids and minerals (AlKhatib and Eisenhauer, 2016a,b; Krabbenhöft et al., 2010; Raddatz et al., 2013; Stevenson et al., 2014; Widanagamage et al., 2014) and in the planetary sciences $^{84}Sr/^{86}Sr$ is used to trace nucleosynthetic processes(Andreasen and Sharma, 2007).

Traditionally Sr is chemically separated from the sample matrix by solution chemistry and analysed by thermal ionisation mass spectrometry (TIMS) or Multiple Collector Inductively Coupled Plasma mass spectrometry (MC-ICPMS). During chemical processing, a subsample is dissolved and the resulting solution is passed through a cation exchange column, separating elements by their adsorption properties. The resulting mono-elemental Sr solution can then be prepared for mass spectrometry. Precision of ± 0.000010 (10ppm, 2σ) is routinely achieved for $^{87}Sr/^{86}Sr$ using these methods, and can be improved up to ± 0.000002 (2ppm, 2σ, Yobregat et al. (2017)). However, the chemical separation process requires clean laboratory facilities and is both labour and time intensive. Additionally, physical subsampling may have limited spatially resolution, damages or wastes samples, and has a risk of contamination during handling of very small samples.

Laser Ablation Multi-Collector Inductively Coupled Mass Spectrometry (LA-MC-ICPMS) is an alternative method for precise and accurate $^{87}Sr/^{86}Sr$ measurements of geological samples (Christensen et al., 1995). LA-MC-ICPMS has several compelling advantages; it has high spatial precision (10-100μm), causes minimal sample damage, and is rapid compared to solution methods. However, the lower precision from short collection times, and the lack of chemical separation raise analytical challenges, particularly from isobaric interferences (ions or polyatomic molecules with the same mass/charge ratio as Sr isotopes (Woodhead et al., 2005)). The interferences reduce accuracy and can decrease or apparently (misleadingly) increase precision. They are highly dependent upon the sample composition. Four possible approaches exist for dealing with interferences: correction, resolution, minimisation and collision/reaction. Interferences such as REE^{++} and Rb^{+} can be corrected through measurement of their other isotopes, whilst stable interferences such as Kr^{+}, which is introduced as in impurity with He, can be corrected for as instrumental background (Horstwood et al., 2008; Irrgeher et al., 2016; Woodhead et al., 2005). However, implicit in these corrections are assumptions of REE & Rb isotopic compositions and their modification by instrumental fractionation. The accuracy of corrections for REE^{++} may be assessed using $^{84}Sr/^{86}Sr$ as an independent check. The minor isotopic abundance of ^{84}Sr and the presence of calcium/argon polyatomic interferences in carbonate and apatite make this ratio difficult to measure, though these interferences are not observed in all analytical setups (Yang et al., 2011).

Instrumental tuning can be used to minimise the impact of interferences, if Sr sensitivity is not an issue; or increased instrumental resolution can be used to avoid specific interferences. This has been shown using (pseudo-) medium resolution on Sector Field ICP-MS to avoid calcium phosphate polyatomics in apatite (Irrgeher et al., 2016). More complex analytical setups where collision cells (Schmidberger et al., 2003), custom interfaces (Lewis et al.,

2014), or reaction cells with CH_3F, O_2 or N_2O have also been used to minimise interferences, but such analyses have currently only been performed on quadrupole-MS (Balcaen et al., 2015; Bolea-Fernandez et al., 2016a,b; Hogmalm et al., 2017; Zack and Hogmalm, 2016).

In this work, we revisit different approaches to laser ablation $^{87}Sr/^{86}Sr$ measurements and suggest that use of medium resolution to avoid REE^{++} interferences on a MC-ICP-MS can simplify and improve existing $^{87}Sr/^{86}Sr$ methods. We use a range of terrestrial carbonates and NIST glasses to demonstrate improved accuracy. The latter are a particularly difficult matrix to analyse, due to high concentrations of multiple elements which form interferences (Jochum et al., 2011). As medium resolution reduces signal intensities, an approach is proposed which optimises precision as a function of sample volume. A comparison of data reduction procedures is presented which tests direct linear response, standard-sample bracketing and internal mass normalisation.

3.2.2 LA-ICP-MS analysis

Sample and standard preparation

Four carbonates with a range of Sr concentrations and isotopic compositions were selected as standards (Calcite: Oka, NCC and eBlue; Aragonite: PAr). Oka calcite is from the Oka carbonatite complex in Quebec Chen and Simonetti (2013); Grünenfelder et al. (1986); NCC is a vein carbonate from Norman Cross, supplied to us by Tony Dickson; eBlue is of unknown online origin, provided by Aleksey Sadekov; and PAr is a subsample of aragonite vein sample 2/4 from Green River, Utah (Frery et al., 2016; Kampman et al., 2012) and is presented in figure 4.8 of chapter 4. Subsamples of each carbonate standard were taken for repeat analyses of $^{87}Sr/^{86}Sr$ and Sr concentrations by TIMS[1] and ICP-OES[2] using methods described in Bickle et al. (2003) and Villiers et al. (2002) (on a VG Sector 54 TIMS and Varian Vista ICP-OES, respectively). These solution based techniques are typically precise to ± 0.000025 (25ppm, repeats of NBS 987 2003-2016) for $^{87}Sr/^{86}Sr$ and ± 0.01 for Sr/Ca (both 2σ). The crystals for standards were mounted in epoxy and polished using diamond paste to a finest grade of 0.25µm. Major elements were analysed by electron microprobe, and give reasonable agreement with the ICP-OES data (see table 3.2). Notably NCC has $\approx$1wt% Fe, and Par and Oka are $\approx$1wt% Sr.

[1] Thermal Ionisation Mass spectrometry

[2] Inductively Coupled Plasma Optical Emission Spectrometry, also referred to as ICP-AES Atomic Emission Spectroscopy

Table 3.2 Electron probe data major element composition data for carbonate standards

Element	Oka ppm	2σ	eBlue ppm	2σ	Par ppm	2σ	NCC ppm	2σ
Na	170	248	52	216	2125	674	150	276
Si	64	178	54	100	29	100	55	140
Fe	94	280	50	116	115	388	14696	4230
Mn	1640	90	167	378	138	350	1820	814
Ca	374258	8298	386162	12842	371663	6604	362902	10520
S	27	82	24	44	914	514	60	72
Sr	15722	2214	958	242	7290	2384	988	426
Al	67	166	20	56	31	94	52	154
Mg	314	68	137	218	0	0	2287	888
P	61	76	70	40	116	78	155	118

The unknown samples are predominantly aragonite veins from Green River, Utah. These samples have been used to understand fluid sourcing and silicate reactions in a natural leaking CO_2 reservoir (Kampman et al., 2009, 2012). Additionally, some other limestone, foraminifera and barite samples were also measured. Prior to analysis all samples are rinsed in Milli-Q[3], dried overnight, and dusted with an Ar jet to remove any remaining loose particles. Where possible, samples are polished to a provide a flat surface for focusing, though to a coarser grade than the standards.

Analysis setup

Analyses were performed using a Photon Machines G2 193nm excimer laser system coupled to a Thermo-Fischer Neptune+ MC-ICPMS. Samples are placed in the two-volume laser cell which is purged and left flushing He for a few hours to ensure complete removal of air. The He gas flow from the laser, which carries suspended particles from the ablation, is blended with Ar using a 'squid' manifold. The 'squid' also smooths laser pulses at low repetition rates (Eggins et al., 1998; Fehrenbacher et al., 2015). The blended gases then enter the plasma torch, where particle disaggregation, volatilisation and ionization occurs.

Eight faraday detectors are used in a single static collector configuration, given in table 3.3. Five of these collectors are necessary for Sr and Rb isotopes: ^{84}Sr, ^{85}Rb, ^{86}Sr, ^{87}Sr & ^{87}Rb, ^{88}Sr. The additional three are for tuning, quality control and monitoring purposes: $^{82.5}$Ho^{++}, ^{83}Kr, ^{89}Y. Y is often considered as as a proxy for Rare Earth Element (REE) concentrations due to their very similar chemical characteristics. Both Y and Ho are mono-

[3] 18.2mΩ

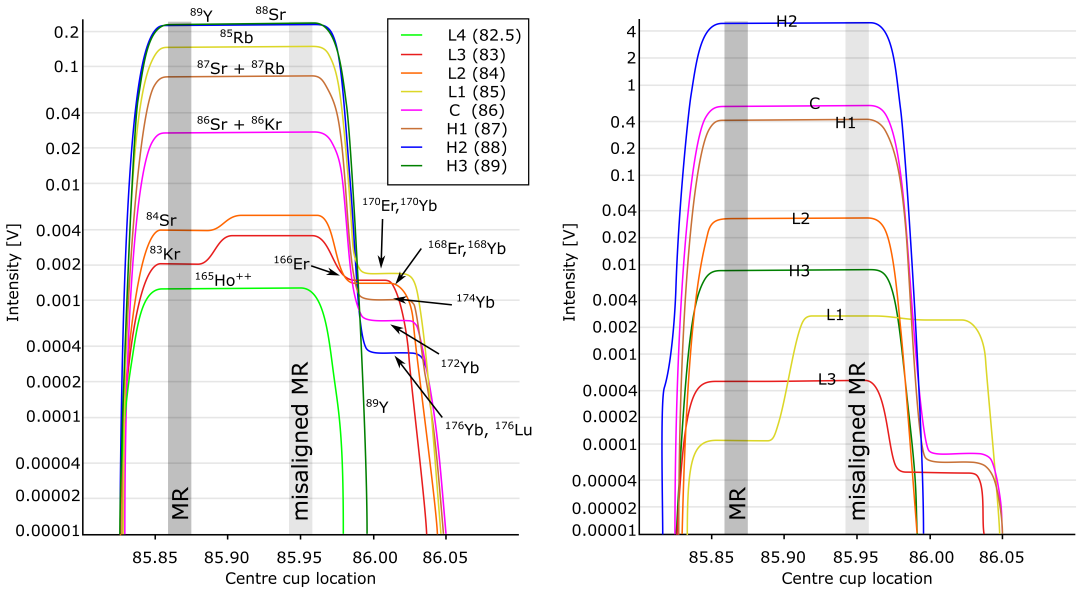

Fig. 3.1 Cup alignment, with interference in NIST 612 (left) and Oka carbonate (right)

isotopic, with similar ionisation energies, so the ratio of Ho^{++}/Y^{+} is a good approximation for REE^{++} formation rates. In NIST glass, which contains significant REE concentrations, it was possible to reduce the $^{82.5}Ho^{++}/^{89}Y^{+}$ ratio from 4% to 0.1% through tuning the MC-ICPMS. Analysis is performed in medium resolution (MR) and data is collected on the REE interference-free left plateau, shown in figure 3.1. We also report results for low resolution (LR) 'misaligned' MR (the combination of REE and Sr signals) in comparison. A short integration time of 0.524s is used to capture transient signals, which can be excluded during data processing. This is particularly important for samples with minor inclusions, such as occluded clay or Fe-Mn oxyhydroxide particles in carbonates, which are heterogeneously distributed and may contribute interferences. Gas and torch parameters can be tuned to minimise either oxide or double-charged ion formation. Double charged ions are resolved in MR, and Zn, Ga and Ge which form interfering oxides are uncommon in carbonates allowing tuning for maximum Sr sensitivity rather than maximum Sr/interference ratios. Zn, Ga and Ge may cause significant interferences during analysis of NIST glasses, which are discussed in detail later. However these are unusual in most samples. Typical analysis settings are summarized in table 3.4.

Analysis procedure

Square spots are pre-ablated for 10 shots with a larger spot than the main ablation, typically 120µm and 100µm. Pre-ablation removes contaminants in the near surface that escape earlier

Table 3.3 Cup configuration and potential interferences on Sr isotopes

Detector	L4	L3	L2	L1	C	H1	H2	H3
Mass	82.5	83	84	85	86	87	88	89
Amplifier	10^{11}	10^{12}	10^{11}	10^{11}	10^{11}	10^{11}	10^{11}	10^{11}
Isotope of interest			^{84}Sr		^{86}Sr	^{87}Sr	^{88}Sr	
Monitored Interferences	$^{165}Ho^{++}$	^{83}Kr	^{84}Kr	^{85}Rb	^{86}Kr	^{87}Rb		^{89}Y
Double charged Interferences		$^{166}Sr^{++}$ $^{168}Yb^{++}$	$^{168}Er^{++}$ $^{170}Yb^{++}$	$^{170}Er^{++}$ $^{172}Yb^{++}$	$^{174}Yb^{++}$	$^{176}Yb^{++}$ $^{176}Lu^{++}$ $^{174}Hf^{++}$	$^{176}Hf^{++}$	$^{178}Hf^{++}$
Argides		$^{43}Ca^{40}Ar^{+}$	$^{44}Ca^{40}Ar^{+}$	$^{45}Sc^{40}Ar^{+}$	$^{46}Ca^{40}Ar^{+}$ $^{46}Ti^{40}Ar^{+}$	$^{47}Ti^{40}Ar^{+}$	$^{48}Ca^{40}Ar^{+}$ $^{48}Ti^{40}Ar+$	$^{49}Ti^{40}Ar^{+}$
Dimers		$^{43}Ca^{40}Ca^{+}$	$^{44}Ca^{40}Ca^{+}$		$^{46}Ca^{40}Ca^{+}$		$^{48}Ca^{40}Ca^{+}$	
Phosphates		$^{36}Ar^{31}P^{16}O^{+}$		$^{38}Ar^{31}P^{16}O^{+}$		$^{40}Ca^{31}P^{16}O^{+}$ $^{40}Ar^{31}P^{16}O^{+}$		$^{42}Ca^{31}P^{16}O^{+}$
Oxide Interferences		$^{67}Zn^{16}O^{+}$ $^{51}V^{16}O_2{}^{+}$	$^{68}Zn^{16}O^{+}$ $^{52}Cr^{16}O_2{}^{+}$	$^{69}Ga^{16}O^{+}$ $^{53}Cr^{16}O_2{}^{+}$	$^{70}Zn^{16}O^{+}$ $^{70}Ge^{16}O^{+}$ $^{54}Cr^{16}O_2{}^{+}$ $^{54}Fe^{16}O_2{}^{+}$	$^{71}Ga^{16}O^{+}$ $^{55}Mn^{16}O_2{}^{+}$	$^{72}Ge^{16}O^{+}$ $^{56}Fe^{16}O_2{}^{+}$	$^{73}Ge^{16}O^{+}$ $^{57}Fe^{16}O_2{}^{+}$

Table 3.4 Operating conditions

Laser settings	**Photon machines G2 193nm**
Spot size	50 - 130μm (100μm typical)
Fluence	2.4 J/cm^2
Repetition rate	4-10 Hz (6 Hz typical)
Number of shots	200 shots (depth $\sim$ 30µm)
Ablation time	$\approx$ 30 seconds
Cell type	Two volume
He flow	1L/min (split: 0.3 cell and 0.7 cup)
N2 flow	6mL/min
Mass Spec. settings	**Neptune+ MC-ICPMS**
Forward RF power	1400W
Interface cones	X-cones (Ni)
Injector	Platinum
Mass resolution	MR (m/Δm $\approx$4000)
Integration time	0.524s
Cooling Gas	14.9 L/min
Auxiliary Gas	0.9 L/min
Sample Gas	0.8 L/min

cleaning routines. Where possible, all samples are measured in triplicate within the same run to check concordance. The main ablation is limited to 200 shots to avoid laser induced fractionation with increasing depth, which has been observed in other elements (Paton et al., 2010). Over the depths sampled ($< 30\mu m$) Sr signal intensities decrease ≈10%, but isotopic fractionation is not observed. Baselines are collected for a minimum of 30 seconds between the pre-ablation and ablation, with 90% of the Sr signal washing out within 1.5s (3 integrations). Assuming a cuboid ablation pit at 100µm spot size and a depth of $30\mu m$, ≈1 µg of carbonate is consumed. For material such as Oka, which has the highest Sr concentration at ≈15,000ppm, ≈15ng of Sr is consumed per ablation. Typically, such an ablation gives ≈1V on ^{87}Sr and ≈11.8V on ^{88}Sr.

Data processing

Methods for processing laser ablation Sr isotopes have been widely discussed (Horsky et al., 2016; Horstwood et al., 2008; Vroon et al., 2008). We use Iolite v2.5, a mass spectrometry and laser ablation data processing package (Paton et al., 2011). Similarly to previous studies, the following order of corrections are applied:

1) Baseline/background correction

Instrumental background comes mainly from Kr gas interferences and from blank/washout of Sr and Rb. Background time periods are selected between pre-ablation and ablation of every spot, and post ablation prior to the next spot. Iolite fits a polymodal spline through the background data (as a function of time) which is applied to samples and standards.

2) Mass fractionation

ICP-MS is well known to impart a mass fractionation during analysis, where transmission of heavier ions is greater than lighter ions. This is empirically described through an exponential law, and given the symbol β (Albarède et al., 2015). The magnitude of this fractionation is assessed relative to a known isotope ratio (i.e. ^{88}Sr/^{86}Sr), shown in equation 3.2.

$$\beta_{Sr} = Ln\left(\frac{^{88}Sr}{^{86}Sr}\right)_n / \left(\frac{^{88}Sr}{^{86}Sr}\right)_m / Ln\left(\frac{M_{88}}{M_{86}}\right) \tag{3.2}$$

Where ^{88}Sr/^{86}Sr$_n$ is the assumed natural ratio of 8.37520938, ^{88}Sr/^{86}Sr$_m$ is the raw measured ratio, and M_{88} and M_{86} are the masses of each respective isotope. β_{Sr} is then used to correct the measured ratio as follows:

$$\left(\frac{^{87}Sr}{^{86}Sr}\right) = \left(\frac{^{87}Sr}{^{86}Sr}\right)_m (M_{87}/M_{86})^{\beta_{Sr}} \tag{3.3}$$

Where ^{84}Sr or ^{85}Rb can be substituted for ^{87}Sr. β varies with instrumental setup, and may drift during analysis. It is assumed that $\beta_{Rb} \approx \beta_{Sr}$ is reasonable in materials with Rb/Sr ratios < 0.01; this assumption is tested and discussed later.

3) Rb correction

The ^{87}Sr/^{86}Sr ratio is corrected for ^{87}Rb using the ^{85}Rb signal, assuming an unfractionated ^{87}Rb/^{85}Rb value of 0.3857558 and correcting that for the measured Sr fractionation factor.

4) Standard-sample bracketing routines (optional)

Standard-sample bracketing routines can be used to correct instrumental biases, and where an ^{88}Sr/^{86}Sr ratio is not assumed, δ^{88}Sr can be determined. A correction factor is calculated from bracketing standards and applied to samples as a function of time. Standards must be run frequently to characterise drift. However, fluctuations at higher frequency than standard-sample repeat time, for example short term variation in mass fractionation, will not be resolved. Ideal standards are isotopically homogenous and compositionally similar to the samples. If Rb is present then an assumption (or calibration) of the $\beta_{Rb} \approx \beta_{Sr}$ relationship is required. Sr concentrations are determined by bracketing the signal intensity of ^{88}Sr. Assuming that the standard and sample are compositionally similar, comprising a similar stoichiometric abundance of Ca, this is an approximation to Sr/Ca ratios. However, precision and accuracy are limited by concentration heterogeneity of the standard.

An alternative data reduction strategy used by Fietzke et al. (2008) (direct linear response) reports higher precision relative to 'standard' routines. Processing by this method requires a regression of raw signal intensities and the resulting gradient is the isotope ratio of interest. This is tested and discussed below.

Uncertainties & MSWD

Uncertainties are calculated by the program Iolite, and are quoted as two standard errors (2SE) for individual analysis spots. 2σ outlier rejection is included, but points are rarely excluded from the calculation (typically 1 in 60 integrations). Unless otherwise stated, data is processed using mass fractionation correction, taking the sample ^{88}Sr/^{86}Sr ratio to be the accepted value (8.37520938) and standard-sample bracketing is used only for the estimate

of concentration. Signal to electronic noise and counting statistics are the limitations on precision. Long-term reproducibility relative to data point uncertainties is described by the mean squared weighted deviations (MSWD, or reduced-chi-squared) statistic.

3.2.3 Results & Discussion

Interferences and strategies to minimize them

Isobaric interferences are ions or polyatomic molecules with the same mass to charge ratio as a measured isotope which therefore contribute to the measured signal. Potential interferences for Sr isotopes have been discussed in (Horstwood et al., 2008; Irrgeher et al., 2016; Vroon et al., 2008). Interferences on an isotope may have a slightly different masses, and as instrumental mass resolution increases peaks can be separated and distinct. The 10% mass valley definition power (m/Δm) is the theoretical mass resolving power (m/Δm) necessary to separate two peaks of equal height with a valley that is 10% of the height of the peaks (IUPAC, 1997). Low resolution on the NEPTUNE is m/Δm ≈300, medium resolution ≈4,000 and high resolution ≈10,000. Values for each interference are given in the following discussion.

Potential interferences can be minimised by instrumental tuning, resolved using higher instrumental resolution, corrected by monitoring an independent (interference free) isotope, corrected as a background (if present in the injection system rather than the sample), or collided/reacted in a collision cell. The impact of an interference depends upon its concentration distribution in the mineral, and chemical behaviour (relative to Sr) during ablation, particle disaggregation/volatilisation and ionisation in the plasma. These factors may make corrections difficult, especially when multiple interferences are involved. The impact of different interferences is summarised in figure 3.2 for standard bracketing analyses and 3.3 for internally normalised samples.

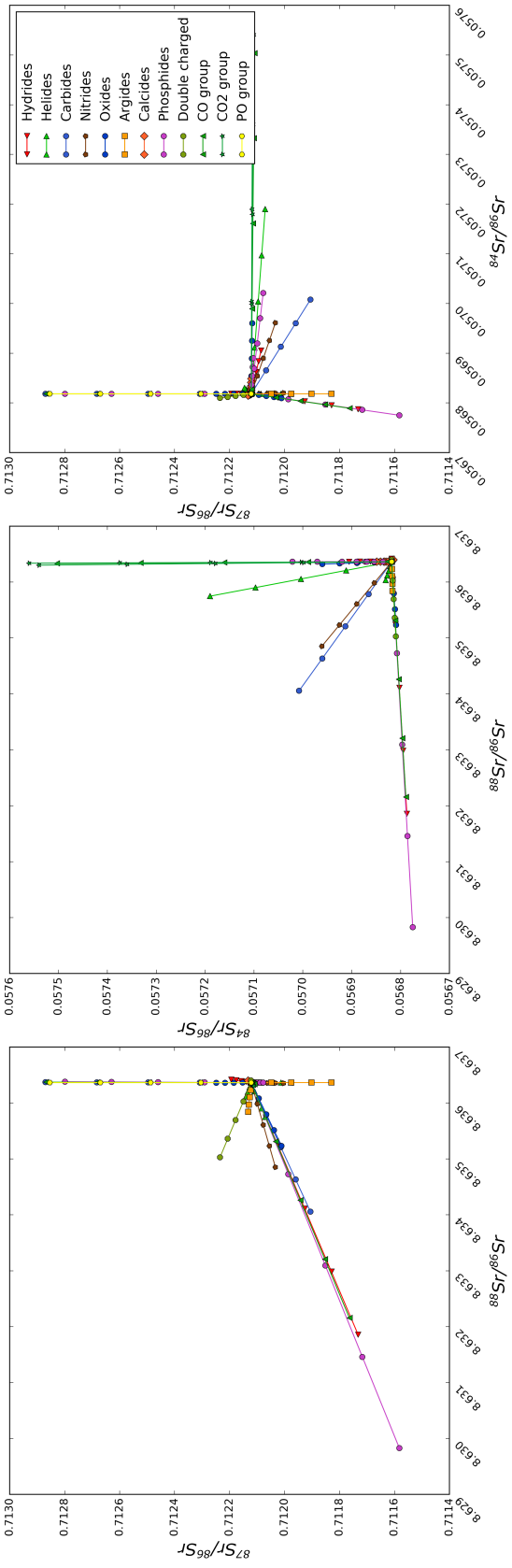

Fig. 3.2 The offsets on raw isotope ratio measurements caused by different interferences. This is representative of the offsets caused by uncorrected interferences during standard-sample bracketing

Rubidium (Rb)

m/Δm ≈ 308,000 (^{87}Rb)
Rubidium has two isotopes: ^{87}Rb and ^{85}Rb. It cannot be resolved from ^{87}Sr even at high resolution but the ^{87}Rb contribution to ^{87}Sr signal can be corrected using ^{85}Rb. This relies on the ^{85}Rb signal being interference free, the ^{85}Rb/^{87}Rb isotope composition known, and the assumption that the mass fractionation of Rb is sufficiently similar to that of Sr. However, as Sr more readily undergoes secondary ionisation this is not completely robust (Luo et al., 2015; Paton et al., 2010; Woodhead et al., 2005) but empirical relationships of the offset on ^{87}Sr/$_{86}$Sr against ^{87}Rb suggest they are within ≈ 5% (Zhang et al., 2018). Natural variation in ^{85}Rb/^{87}Rb is currently constrained to ±1‰ (Teng et al., 2017). Therefore, the majority of studies are constrained to low Rb/Sr materials. Recent advances using CH_3F as a reaction gas in a collision cell, separating Rb from Sr by measuring the resulting SrF^+ are promising (Bolea-Fernandez et al., 2016a,b; Tanner et al., 2002), though low Sr concentrations, small spot sizes and the current measurements on a quadrupole limits precision to ≈±200ppm at best, and typically nearer to ≈±400ppm. Balcaen et al. (2015) note that reaction cell approaches will also avoid interferences such as REE^{++}.

Krypton (Kr)

m/Δm ≈ 44,000 (^{84}Kr); 64,000 (^{86}Kr)
Krypton has six isotopes, two of which fall on Sr isotope masses (^{84}Kr and ^{86}Kr) and others (^{82}Kr and ^{83}Kr) which can be monitored. It also cannot be avoided in medium resolution, but as it is sourced from the Ar or He gasses used (Woodhead et al., 2005), Kr presents a stable background signal and may be corrected by the background measurement. During analyses, backgrounds of ^{84}Kr + ^{84}Sr were typically ≈1.5-3mV, ^{86}Kr + ^{86}Sr ≈0.6-1.2mV and ^{83}Kr ≈0.3-0.6mV. Kr signal intensities would rise as He cylinders were emptied, and would drop rapidly when He flow rate was reduced.

Double charged rare earth elements (REE) and Hafnium (Hf)

m/Δm ≈ 1,340-1,600
The even isotopes of the REE and Hf undergo secondary ionisation, leading to interferences on Sr (REE^{++} and Hf^{++}). This has previously been corrected in low resolution by monitoring the 'half masses' of the double charged odd isotopes (Horstwood et al., 2008; Paton et al., 2007; Ramos et al., 2004). The uncorrected interference can produce offsets of ≈+0.00800 to ^{87}Sr/^{86}Sr ratios measured in apatites.

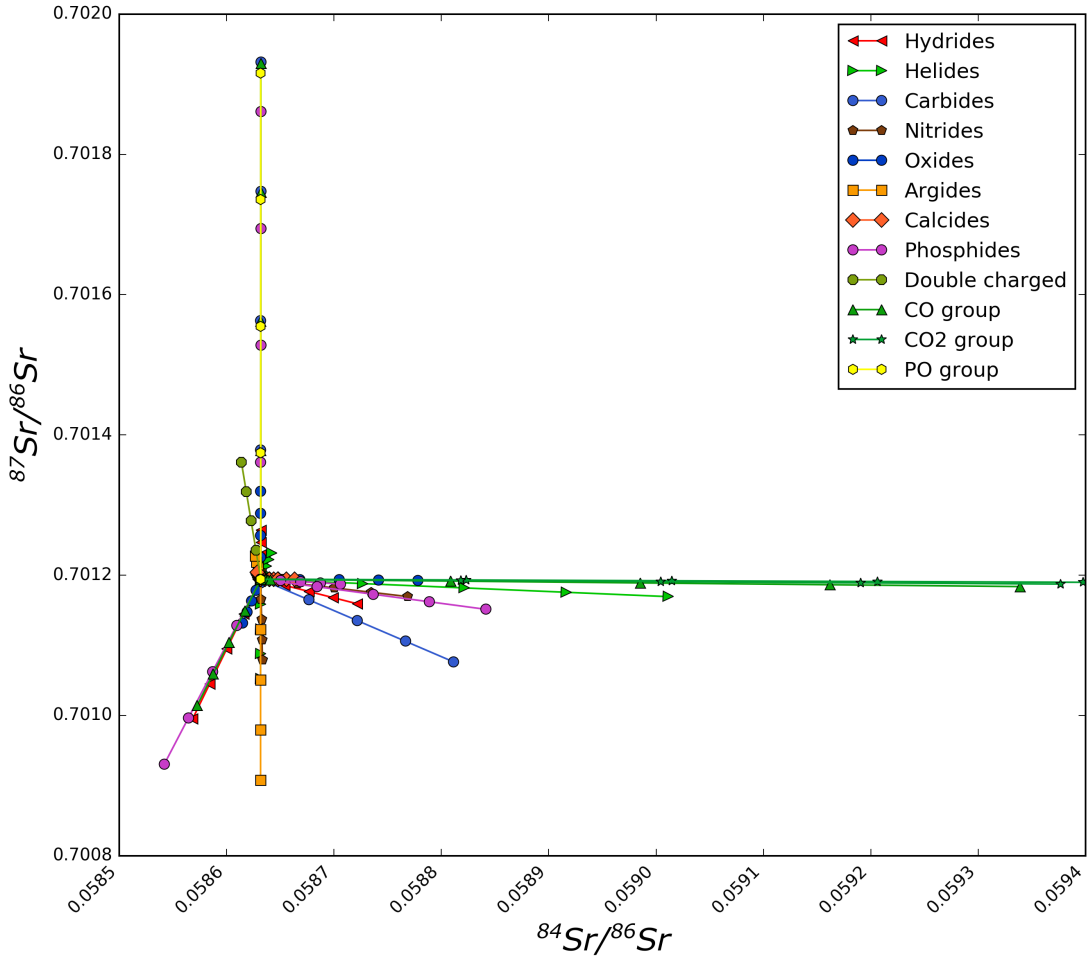

Fig. 3.3 Propagated effect of interferences using mass normalisation correction. This figure shows the combined impact of interferences, when corrected using internal mass normalisation to a $^{88}Sr/^{86}Sr$ ratio. Assumes that all elements have the same β value as Sr (or a miscalculation of that value). This is comparable to the third panel of figure 3.2, which does not include the mass fractionation correction.

Again, assumptions of isotopic composition, and mass fractionation behaviour (β_{REE}) during secondary ionisation are necessary to use monitoring of the 'half masses' for correction. The accuracy of analyses of $^{84}Sr/^{86}Sr$ is commonly used as validation of this method, but the lower precision of the $^{84}Sr/^{86}Sr$ ratio and additional interferences leave some ambiguity.

In our analytical setup, REE^{++} and Hf^{++} interferences are both avoided by using medium instrumental resolution. This is illustrated in figure 3.1, where the REE^{++} interferences are seen on the right (higher mass) shoulder. The medium resolution slits supplied with the NEPTUNE operate at m/Δm≈4000, however with use this mass resolution degrades. Whilst m/Δm remains >1,600 REE interference will be resolved, and increased transmission at this degraded resolution can result in improved precision for a short while. In an ideal world, a custom slit with a mass resolution m/Δm ≈2,000 would balance sensitivity and mass resolution.

Oxides

m/Δm ≈ 7,100-13,100

Vroon et al. (2008) discuss the interference of Zn, Ga and Ge oxides on Sr isotopic masses. In carbonates, concentrations of these elements are generally too low to need corrections. Ramos et al. (2004) performed experiments with Zn and Ga spiked Sr solutions in low resolution and found that they had little influence on measured $^{87}Sr/^{86}Sr$ ratios at Sr/Ga (10-20) and Sr/Zn (1-5) ratios typical of geological materials (Vroon et al., 2008). (Schmidberger et al., 2003) suggested that FeO_2 may be an issue in clinopyroxenes but these are resolved out in their collision cell. By similar arguments Mn, Cr, V and Ti may all form O_2 species, which could only be resolved at m/Δm ≈ 3,500-4,600. However, in our analyses of carbonates (including NCC with 1wt% Fe) we found no evidence of interfering oxides on either $^{87}Sr/^{86}Sr$ or $^{84}Sr/^{86}Sr$. Oxides are discussed later with regards to NIST glass where they may be problematic.

Argides and Calcium 'dimers'

m/Δm ≈ 9,200 – 20,000

Calcium and Argon are in abundant supply during ablation of carbonates, and $CaCa^+$ or $CaAr^+$ dimers interfere on Sr isotopes. The largest abundance dimer falls on ^{84}Sr ($^{44}Ca^{40}Ca^+$ or $^{44}Ca^{40}Ar^+$) and causes positive offsets on the $^{84}Sr/^{86}Sr$ ratio. The other Ca and Ar dimers are at least 50 times smaller (i.e. $^{44}Ca^{44}Ca^+$) and fall on larger Sr isotopes which are at least 10 times larger, so have a much smaller impact. Dimer interferences also fall on ^{82}Kr

($^{42}Ca^{40}Ca^{+}$) and ^{83}Kr ($^{43}Ca^{40}Ca^{+}$), which allows for monitoring. Irrgeher et al. (2016) infer the presence of these interferences through changes in the $^{82}Kr/^{83}Kr$ ratio (from a background value of 1 to a ratio ≈4.7 expected for dimers with no mass fractionation). Horstwood et al. (2008) and Woodhead et al. (2005), attribute signals of 51mV to 127mV on ^{82}Kr to dimers (Yang et al., 2011). This corresponds to ≈3.3mV-8.2mV at ^{83}Kr. During our analyses, ^{83}Kr remains constant between ablation/non-ablation implying that $CaCa^{+}$ or $CaAr^{+}$ formation rates are undetectable within electronic noise of $10^{11}\Omega$ amplifiers. Theoretically, Sc and Ti may form interfering argides but these elements are present at concentrations too low in carbonates to impact observed $^{87}Sr/^{86}Sr$ ratios.

Argon and Calcium ('polyatomics')

$m/\Delta m \approx 3{,}500 - 4{,}300$

During analysis of phosphates offsets of $^{87}Sr/^{86}Sr$ have been attributed to $ArPO^{+}$ or $CaPO^{+}$ interferences. These interferences are problematic, as $^{40}Ar^{31}P^{16}O^{+}$ comprises 99.361% of all $ArPO^{+}$ species, and $^{40}Ca^{31}P^{16}O^{+}$ is 96.712% of all $CaPO^{+}$ species making monitoring at other masses difficult. There is debate about the existence of these species, with Müller and Anczkiewicz (2016) observing no sign of this interference in pseudo-high resolution mass scans, and Irrgeher et al. (2016) observing, and suggesting they can be resolved in medium resolution. Horstwood et al. (2008) suggest that these interferences form when CaP^{+} becomes oxidised. As this work is focused on carbonates we cannot comment further on the existence of these species.

Hydrides, Helides, Nitrides, carbides and carbon-oxygen polyatomics

A range of other interferences are possible, but are generally considered too small to be of importance. Hydrides ($m/\Delta m \approx 7{,}700$-$12{,}700$), helides ($m/\Delta m \approx 8{,}500$-$15{,}000$), carbides ($m/\Delta m \approx 5{,}500 - 9{,}700$), and nitrides ($m/\Delta m \approx 4{,}400 - 5{,}700$) can potentially form within the mass spectrometer, but there is no discussion of these in the literature. Hydrides can be problematic during solution analysis, but as laser setups run in dry plasma, supply of H^{+} is limited (unless collision cells are used, but then such interferences are suppressed). Helides are considered as unreactive, but the major problematic helide would be with ^{84}Kr which would be present as a stable background. Similarly, nitrides should be small due to low reactivity, even though tiny volumes of N_2 (≈ 0.4% of the torch gas mix) are added to improve sensitivity. More complex carbon-oxygen breakdown products in carbonates could form in a similar manner to $CaPO^{+}$ interferences in apatites, but have not been observed to

Table 3.5 Comparison of medium resolution (MR) and low resolution (LR) analyses in Oka carbonate and NIST 610 and 612 glasses. Reference values for $^{87}Sr/^{86}Sr$ on are OKA: 0.703297±7, NIST610: 0.708363±14, NIST612: 0.709063±15, and for $^{84}Sr/^{86}Sr$ are assumed to be 0.05649 Woodhead et al. (2005). Concentration of Sr in NIST 610 is 525ppm Sr and NIST 612 is 78ppm Sr Jochum et al. (2011). A significant movement towards more accurate numbers in both NIST glasses for both isotope ratios compared to LR, but have still have offsets in MR for NIST610.

	MR				**Reference values**		
	$^{87}Sr/^{86}Sr$		$^{84}Sr/^{86}Sr$		$^{87}Sr/^{86}Sr$	$^{84}Sr/^{86}Sr$	**[Sr]**
Sample	Mean[1]	$\pm 2SE$[1,2]	Mean[1]	$\pm 2SE$[1,2]			
Oka	0.703332	36	0.056498	14	0.703297 ± 7	0.05649	15800
NIST 610	0.712663	1008	0.056673	348	0.708363 ± 14	0.05649	525
NIST 612	0.708917	3233	0.057200	2350	0.709063 ± 15	0.05649	78
	LR						
Oka	0.703323	17	0.056505	8	0.703297 ± 7	0.05649	15800
NIST 610	0.748080	430	0.085538	185	0.708363 ± 14	0.05649	525
NIST 612	0.719723	925	0.073567	860	0.709063 ± 15	0.05649	78
	MR$_m$[3]						
Oka	0.703293	33	0.056508	14	0.703297 ± 7	0.05649	15800
NIST 610	0.780885	960	0.102973	430	0.708363 ± 14	0.05649	525
NIST 612	0.728433	3200	0.084283	2350	0.709063 ± 15	0.05649	78

[1] n = 6
[2] Precision $\times 10^{-6}$
[3] Misaligned medium resolution

date. $^{x}Ca^{12}C^{16}O_2{}^{+}$ could fall on all Sr masses, but most heavily on ^{84}Sr. Such interferences have not been observed, but would be resolved at m/Δm ≈ 2,000-2,200.

Effect of MR on accuracy of $^{87}Sr/^{86}Sr$ measurement in NIST glasses

As discussed above, REE interferences are avoided in medium resolution. To test this approach, NIST glasses were analysed as they contain high Rb, Zn, Ga, Ge, Ti, REE and Hf concentrations, with ratios to Sr approaching unity (Jochum et al., 2011). REE^{++} fall on the high mass plateau, the central plateau is the combination of REE^{++} and Sr, and the left plateau is Sr and Rb. The right panel of figure 3.1 shows no interference shoulder associated with $CaCa^{+}$ or $CaAr^{+}$ on m/z=84 in carbonates. This is counter to observations by Irrgeher et al. (2016).

Low resolution and medium resolution analyses are compared in table 3.5 for NIST 610, NIST 612 and Oka carbonate. The $^{87}Sr/^{86}Sr$ isotope ratios of NIST glasses are given by

(Woodhead and Hergt, 2001), and Oka was analysed by TIMS in Cambridge (Table 3.6). In low resolution, spot size is reduced to 60µm to give ^{88}Sr signals around 8-10V. Except for the zoom optic settings and centre cup location, tuning parameters remain identical. Medium resolution analyses are performed in two locations; on the interference free left plateau and on the central plateau where interferences have maximum impact (termed 'misaligned' MR). The results in low resolution are not a direct comparison to REE corrected analyses of (Horstwood et al., 2008; Vroon et al., 2008).

Oka carbonate is accurate for ^{87}Sr/^{86}Sr and ^{84}Sr/^{86}Sr in MR and LR resolutions, and precision is higher in the LR case due to the larger signal. This is due to the combination of low concentrations of interfering elements and high Sr concentrations. Both NIST glasses are most accurate in MR, and LR is more accurate than 'misaligned' MR (due to 'smoothing' across the peak). The improvement from LR to MR is due to resolution of REE^{++}: ^{87}Sr/^{86}Sr improves by ≈35000 ppm in NIST 610 and by ≈11000ppm in NIST 612; ^{84}Sr/^{86}Sr accuracy is improved by ≈29000ppm and ≈16000ppm. However, there remains a systematic offset from the TIMS values determined by Woodhead and Hergt (2001). ^{87}Sr/^{86}Sr is offset by +4300 (±1000) ppm in NIST610, and +145 (±3200) ppm in NIST 612; ^{84}Sr/^{86}Sr is offset by +183 (±250) ppm and +710 (±2350) ppm, respectively. Due to lower Sr concentrations (NIST610: 515ppm, NIST612 78ppm; Jochum et al. (2011)), ^{84}Sr/^{86}Sr is within uncertainty of the 'true' value illustrating the limitation of this ratio as a validation of method accuracy.

The positive offset on ^{87}Sr/^{86}Sr can be explained in 2 ways: either Rb interferences are undercorrected when assuming $\beta_{Rb} \approx \beta_{Sr}$, or interferences such as oxides or argides are responsible. NIST 610 has both higher Rb/Sr ≈0.79 and Ga/Sr, Ge/Sr, Zn/Sr ranging from 0.84 to 0.90, whilst NIST 612 has Rb/Sr ≈0.40 and Ga/Sr, Ge/Sr, Zn/Sr in range 0.46-0.50. If the offset on ^{87}Sr/^{86}Sr is attributed to differences in $\beta_{Rb} \approx \beta_{Sr}$, then during these analyses β_{Rb} must be 5% larger than β_{Sr} to achieve ^{87}Sr/^{86}Sr matching the TIMS analyses (where β_{Sr} = -1.558 and β_{Rb} = -1.635). However, the signal on ^{83}Kr is 0.4mV and 2.8mV higher than baselines during ablation of NIST 612 and 610, suggesting the presence of non-resolved interferences such as ^{67}Zn^{16}O^{+} (which can account for raised ^{84}Sr/^{86}Sr). Assuming $\beta_{Zn} \approx \beta_{Sr}$ and natural Zn isotope composition allows estimation of ^{67}Zn^{16}O^{+} formation rates, which are ≈25% in both NIST glasses. This is very high (almost unreasonably so; these rates should be nearer to 0.1-1%) and can be minimised through MC-ICPMS tuning. Other interfering oxides present in NIST glasses (GaO^{+} and GeO^{+}) should therefore also be present and responsible for offsets on ^{87}Sr/^{86}Sr. Individually, ZnO^{+} increases the ^{84}Sr/^{86}Sr ratio, GaO^{+} increases ^{87}Sr/^{86}Sr, and GeO^{+} reduces both ^{84}Sr/^{86}Sr and ^{87}Sr/^{86}Sr. The net effect at concentrations typical of NIST glasses is to increase both ^{84}Sr/^{86}Sr and ^{87}Sr/^{86}Sr, but

this combined effect is difficult to judge accurately (see figure 3.3) because of ionisation and mass fractionation differences. Therefore, it is likely that the offset of β_{Rb} and β_{Sr} is <5%, because - as mentioned earlier - an oxide correction would act to reduce $^{87}Sr/^{86}Sr$. Decoupling the effects of oxides and $\beta_{Rb} \approx \beta_{Sr}$ is difficult though, as the effects could act to mask one another. It is worth noting that NIST glasses have higher Ga/Sr than most silicate geological matrices and larger than the Ga or Zn spiked Sr solutions in (Ramos et al., 2004). Carbonate matrices have much lower Ga, Zn and Ge and much higher Sr.

3.2.4 Optimization of Sr isotopes measurements

Accuracy of LA-MC-ICPMS methods in comparison with TIMS

Table 3.6 Comparison of TIMS and Laser data for carbonate standards. 2σ uncertainty is smaller than point sizes.

Standard material	Sr conc.		**LASER:**								**TIMS**	
			$^{87}Sr/^{86}Sr$				$^{84}Sr/^{86}Sr$				$^{87}Sr/^{86}Sr$	
	mmol/mol	ppm	Mean	Internal 2SE[1]	External 2SD[1]	MSWD	Mean	Internal 2SE[1]	External 2SD[1]	MSWD	Mean	External 2RSE[1]
eBlue	1.0	960	0.705939	215	268	1.68	0.056492	181	250	3.88	0.705939	7
NCC	1.0	990	0.708235	224	295	1.74	0.056459	186	323	2.62	0.708065	10
Par	9.9	7290	0.713018	49	73	2.15	0.056485	26	36	2.08	0.713035	7
Oka	14.4	15800	0.703297	38	42	1.61	0.056488	18	25	3.26	0.703297	7

[1] Precision $\times 10^{-6}$

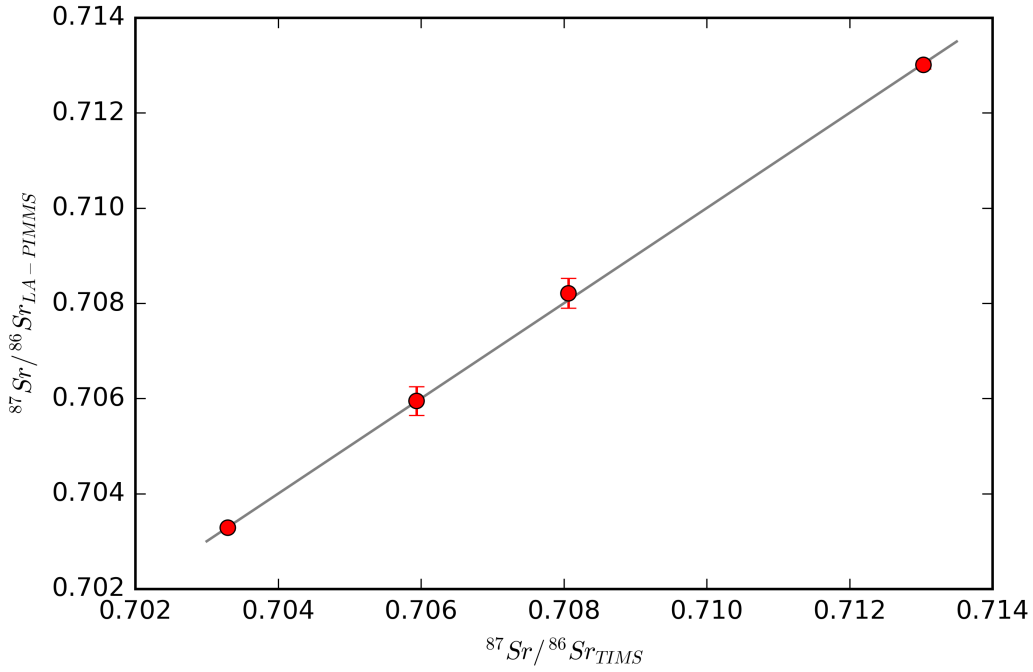

Fig. 3.4 Comparison of laser ablation and TIMS for carbonate standards

The ^{87}Sr/^{86}Sr ratio from TIMS and LA analyses of all carbonate standards are within uncertainty of each other, and ^{84}Sr/^{86}Sr ratios are within uncertainty of 0.056494 (see table 3.5). These results are from 11 different analytical sessions over the course of one year, including parameter sensitivity testing in the first five sessions. Each data point is the mean of 60 integrations and uncertainties are quoted at ±2SE. The uncertainty on low concentration carbonates (eBlue ≈ 960ppm, and NCC ≈ 990ppm) are typically ±220ppm for ^{87}Sr/^{86}Sr and are smaller on the higher concentration Par and NCC at ≈±45ppm. Par and NCC are offset by -17ppm and +170ppm relative to TIMS, offsets within the combined uncertainties of the LA and TIMS analyses. The offsets for eBlue (24 ppm) and Oka (0 ppm) are smaller than the external reproducibility of the LA analyses (73 and 42 ppm). ^{84}Sr/^{86}Sr ratios are within uncertainty of 0.056494, and again the high concentration carbonates are more precise (±22ppm) compared to lower concentration materials (±185ppm). These internal uncertainties are smaller than the long-term scatter in the data points, expressed as the 'External' 2σ uncertainty. This can be seen in the MSWD values which range from 1.61 to 2.15 for ^{87}Sr/^{86}Sr and 2.08 to 3.88 for ^{84}Sr/^{86}Sr, showing that data are marginally over-dispersed. Some of this overdispersion can be accountable to heterogeneity, which is discussed in the δ^{88}Sr section.

The mass of Sr analysed in each ablation is 0.5 - 15ng, comparable in size to the smallest masses measured by TIMS (e.g (Font et al., 2007)) which achieve external 2σ precision of $\pm$13ppm for $^{87}Sr/^{86}Sr$ and $\pm$12ppm for $^{84}Sr/^{86}Sr$. Individual analyses can have precision nearer to $\pm$2ppm for up to 500ng Sr (i.e. (Yobregat et al., 2017)). Relative to TIMS analyses, our laser ablation analyses are accurate, and have precision up to $\pm$40ppm for similar masses of Sr. Precision is dependent on signal size, which is discussed in following sections.

Effect of laser fractionation on $^{87}Sr/^{86}Sr$ measurements

The impact of different laser settings were tested. Spot sizes and repetition rates were varied from 25-130µm and 2-10Hz at a constant fluence. These tests investigate the physical effect of ablation on samples (Wang et al., 2006), laser induced fractionation during ablation and plasma induced fractionation/ matrix loading effects (Fietzke and Frische, 2016; Kosler et al., 2002; Kroslakova and Günther, 2007; Kuhn and Günther, 2003; Luo et al., 2015).

The analytical results show variation which is smaller than external repeatability during the range of operating conditions tested. No difference in mass fractionation behaviour was observed during these tests, and the instrument drifts in a stable fashion independent of the tests. Therefore, the effects of Ca ionisation do not appear to influence Sr ionisation. Neither varying spot sizes nor repetition rates impacted the accuracy of measurements for either $^{87}Sr/^{86}Sr$ or $^{84}Sr/^{86}Sr$, though precision improves with larger Sr signals at larger spot sizes or repetition rates. This is particularly pronounced in the lower Sr carbonates; eBlue and NCC. The precision of $^{84}Sr/^{86}Sr$ improves at larger spot sizes, for example in sessions 2 and 4 in figure 3.5 as discussed in following section.

Optimizing sample volume and collection time for precision

Signal intensity and collection time limits the precision that can be achieved during analysis. To investigate the interplay of these two factors and to optimize analysis for precision, data is reprocessed to simulate shorter ablation periods. This is particularly important during analysis of thin samples (i.e. thin sections) or small samples (i.e. foraminifera) where spot sizes are restricted. All samples and standards from sessions from November 2015 until January 2016 (8 sessions) are used in this calculation, so that a wide range of signal intensities are sampled. Processed data is exported from Iolite, and the mean and standard error for each analysis recalculated at different collection lengths. The original data are 60 integrations long, and at a repetition rate of 6Hz the collection is $\approx$ 30 seconds long. In figure 3.6, these data are represented by the black data points. These data are then truncated to 30 integrations

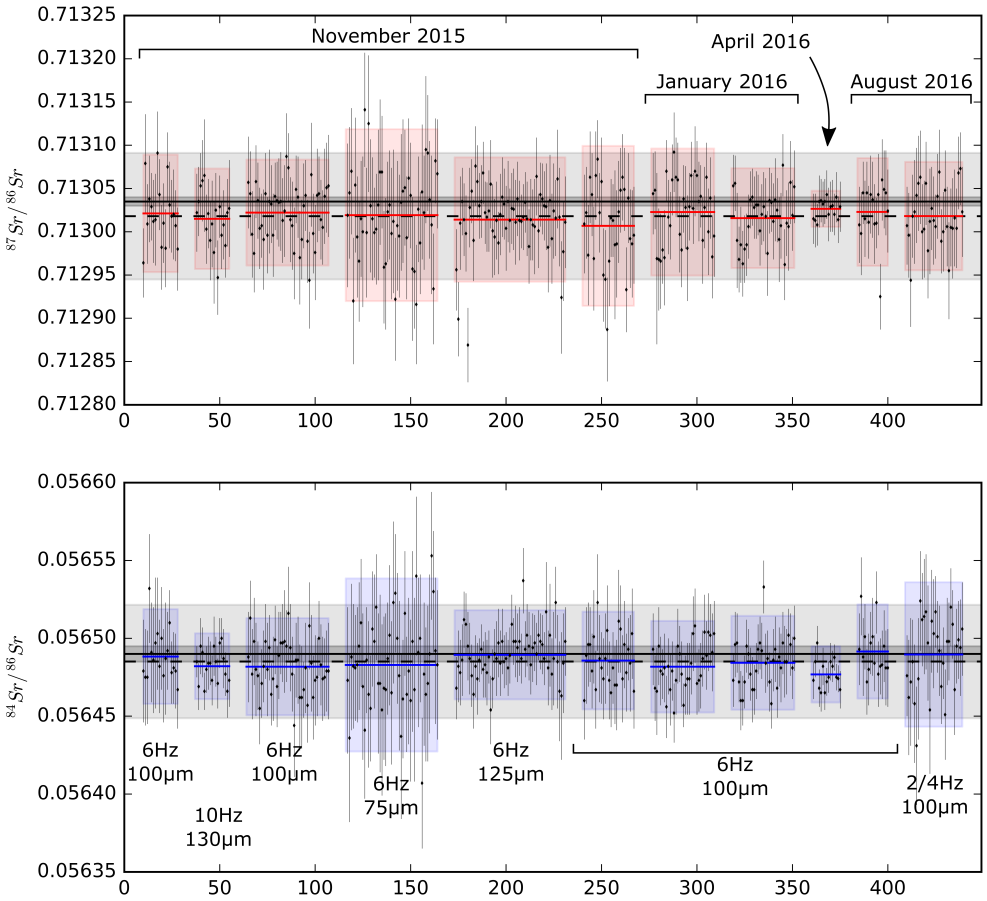

Fig. 3.5 Long term reproducibility of ^{87}Sr/^{86}Sr and ^{84}Sr/^{86}Sr over 9 months of analyses for our standard Par, including laser parameter sensitivity tests. Individual analyses are black points ±2SE; analysis session averages are solid coloured lines and colour shaded regions are $\pm 2\sigma$. The dashed black line is the average of all individual analyses and the light grey region is $\pm 2\sigma$, and the solid black line and dark grey shaded region are the TIMS analysis values ±2RSD. The data are marginally, but not significantly, overdispersed.

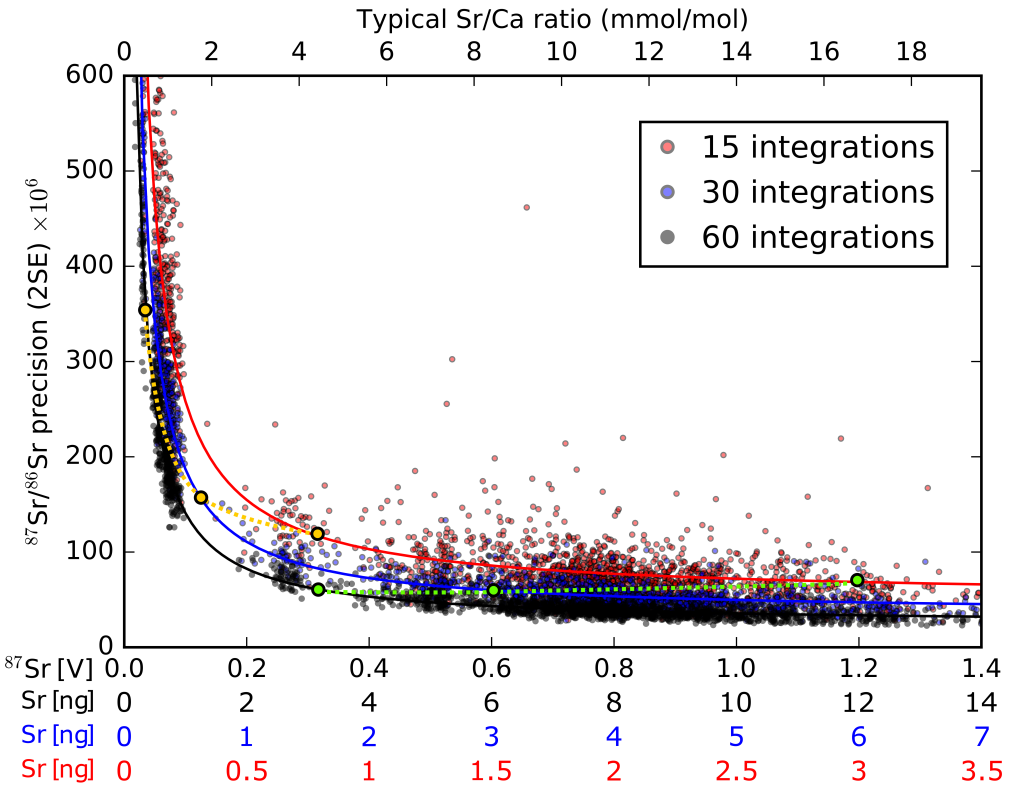

Fig. 3.6 Sensitivity experiment to assess the impact of shorter collections on internal data precision and accuracy on multiple samples. The Black data is full collection (60 integrations, ≈30seconds), blue is half this size (30 integrations), and red half again (15 integrations). The secondary axes show the mass of Sr analysed for these shortened collections. Subsampling strategies are shown for 2 samples (in orange and green), joining points of equal Sr analysed. The orange points show that precision can be improved through higher signal intensities for a shorter length of time. The green points show the opposite; that increasing signal intensity lowers precision once above this critical threshold. These are related to signal-noise ratios and counting statistics during analysis.

(blue) and 15 integrations (red). The solid lines are the least squares regression of precision against signal intensity, assuming a relationship y=a/bx + c.

The precision of $^{87}Sr/^{86}Sr$ rapidly improves as ^{87}Sr signal intensities increase towards 0.2V (≈2.5V ^{88}Sr), and begin to plateau beyond 0.4V ^{87}Sr. Within the plateau region, the full collection data improves in precision from ±100ppm at 0.4V to ±35ppm at 1.2V. The same shape of plateau is observed for the shortened collections but has higher uncertainties. The accuracy is assessed relative to the results with 60 integrations as independent TIMS analyses are not available for these samples. The offsets for the shorter analysis times are shown as histograms in figure 3.7, with results split for <0.4V and >0.4V. The offset in

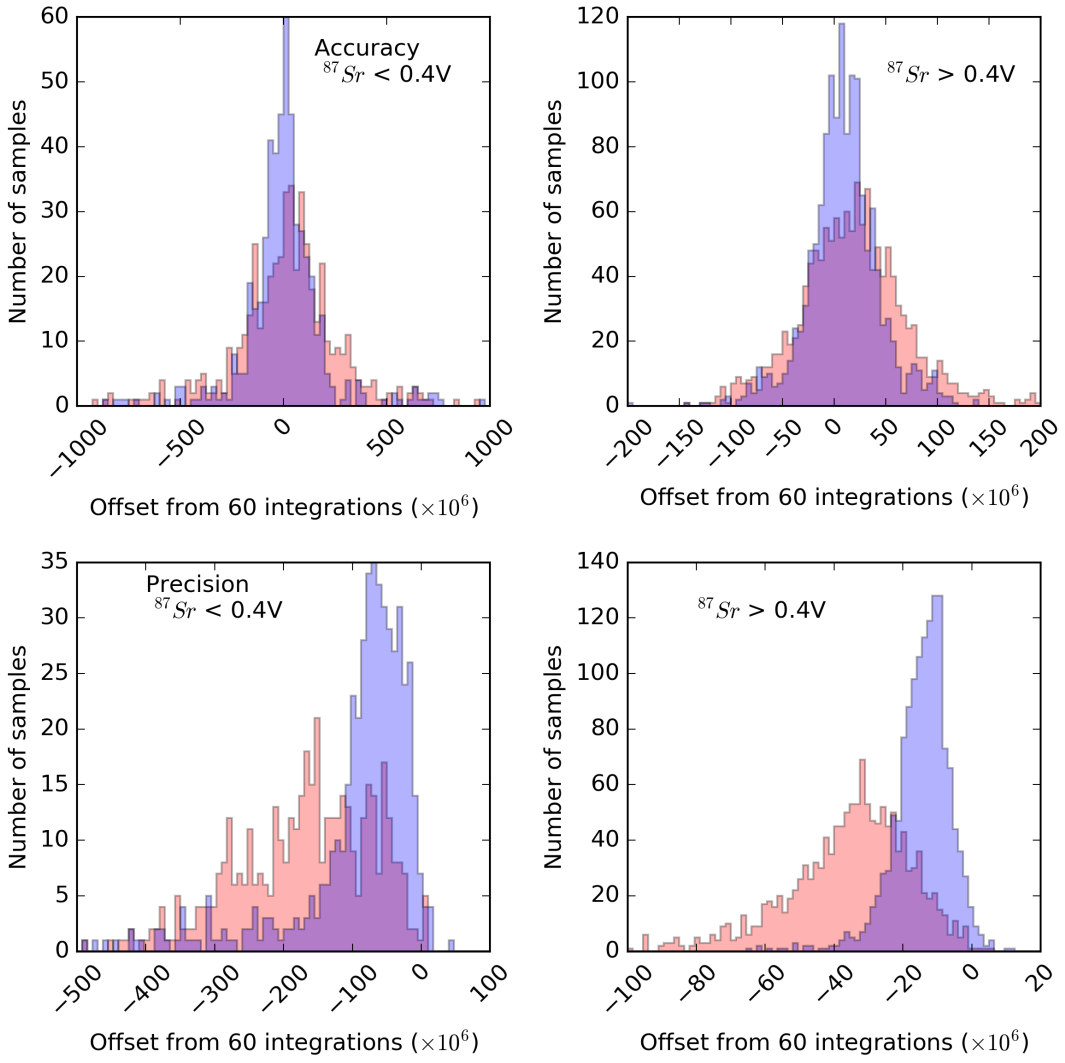

Fig. 3.7 Histograms showing the difference between the 60 and 30 (blue) and 60 and 15 (red) data for accuracy (top row) and precision (bottom row), for voltages <0.4V (left) and >0.4V (right).

accuracy forms a Gaussian distribution centred around zero. The source of scatter is therefore random, and as the offsets are smaller than internal uncertainties, no systematic offset is detectable. However, the offsets in precision show a more skewed Poisson distribution; at 30 integrations precision is ≈20-30ppm lower and at 15 integrations is ≈40-50ppm lower at >0.4V and ≈80ppm and ≈150ppm at <0.4V.

These short collections are limited by counting statistics. If for a given ablation a sample signal is <0.4V, then laser parameters can be adjusted to increase the Sr signal, given that the analytical setup is insensitive to the laser settings. Such a strategy is shown for the orange points in figure 3.6, which consume the same volume of material and mass of Sr. This allows sufficient signal-to-noise ratio in the system, likely arising from Boltzman-Johnson noise in the electronics. The ^{87}Sr and ^{86}Sr signal voltages are similar in size so jointly become limiting with regards to counting statistics.

Conversely, if a sample is already >0.4V it is preferable to collect at a lower signal voltage for a longer time, as indicated by green points in figure 3.6. Most studies target Sr signal intensities in the range 2-8V ^{88}Sr (0.16 - 0.65V ^{87}Sr) (Fietzke et al., 2008; Müller and Anczkiewicz, 2016; Yang et al., 2011), but the lower end of this range would be considered sub-optimal in our analysis. It is worth noting, that this scheme does not account for additional effects such as plasma shielding at high repetition rates, which may modify the matrix and can act to reduce gains in signal intensity (Vadillo et al., 1999). This optimisation can be applied to interference free materials at low resolution.

Precision can also be improved by increasing the stability of background interferences. When Kr intensities are higher, particularly as He cylinders empty, the precision decreases slightly. This effect is also seen after analysis of materials with high Rb, such as NIST glass. Washout of Rb signal takes several hours, with precision marginally increasing as washout proceeds. Given that signal intensity is the main control on precision it is likely that newly developed $10^{13}\Omega$ amplifiers will provide superior precisions for signals below 0.5V on $10^{11}\Omega$ resistors. This brings separate challenges as signal decay times (τ) need to be carefully considered, especially where concentration heterogeneities exist.

Long term stability

Long term stability for analyses of the standard Par is shown in figure 3.5, and given in table 3.6. For high concentration materials (Oka), the external reproducibility is ±42ppm for ^{87}Sr/^{86}Sr and ±25ppm for ^{84}Sr/^{86}Sr. Using these uncertainties gives a MSWD of 1. Par, which also has high concentrations, shows lower repeatability (±73ppm and ±36ppm for ^{87}Sr/^{86}Sr and ^{84}Sr/^{86}Sr) due to isotopic heterogeneity, probably related to growth bands

which are visually present in this carbonate. Triplicate measurements allow identification of regions where heterogeneity may be present, and allow further averaging of variation. The external reproducibility compares well to the ±53ppm 4 year external reproducibility (across 7 sessions) of Müller and Anczkiewicz (2016).

Comparisons of data reduction protocols and their effect on $^{87}Sr/^{86}Sr$ ratio

All results presented up to this point have been calculated assuming a constant ratio of $^{86}Sr/^{88}Sr$ for correction of instrumental mass biases, and is commonly accepted procedure (Horsky et al., 2016). The standards which have been used to verify instrumental accuracy are compared to TIMS measurements based upon the same mass bias assumptions. In this section, other data reduction approaches are discussed.

Standard-sample bracketing

Standard-sample bracketing corrects instrumental biases, assuming standards and samples behave identically during ablation/volatilisation/ionisation. Standards with independently constrained isotopic composition are used to calculate a normalisation factor which is applied to samples as a function of time (McLean et al., 2016). Standards must be run frequently to characterise instrumental drift. A good standard is isotopically, and ideally chemically homogenous, and chemically and physically similar to samples.

Using standard bracketing, precision of ±50ppm is routinely achieved, compared to ±40ppm when processed using a mass bias correction (i.e. precision is 10-20% lower when bracketing). This demonstrates that the mass bias correction eliminates noise related to short timescale variations in mass fractionation (sometimes termed mass-bias flicker). We also found mass bias behaviour varied between sample matrices; e.g. barites, NIST glass and carbonates, but also between compositionally different carbonates showing that matrixes control plasma loading effects and thus mass-fractionation. For example, NCC, which has 1wt% Fe, causes drift of ≈100ppm on $^{87}Sr/^{86}Sr$ in subsequent samples (see figure 3.8). Using internal normalisation for mass bias these drift effects are removed, so are not related to FeO_2 interferences, but to either ablation behaviour or plasma loading. It takes approximately 10 minutes for mass-bias to return to its pre-NCC state meaning sample-standard bracketing approaches do not capture this transient mass-bias change.

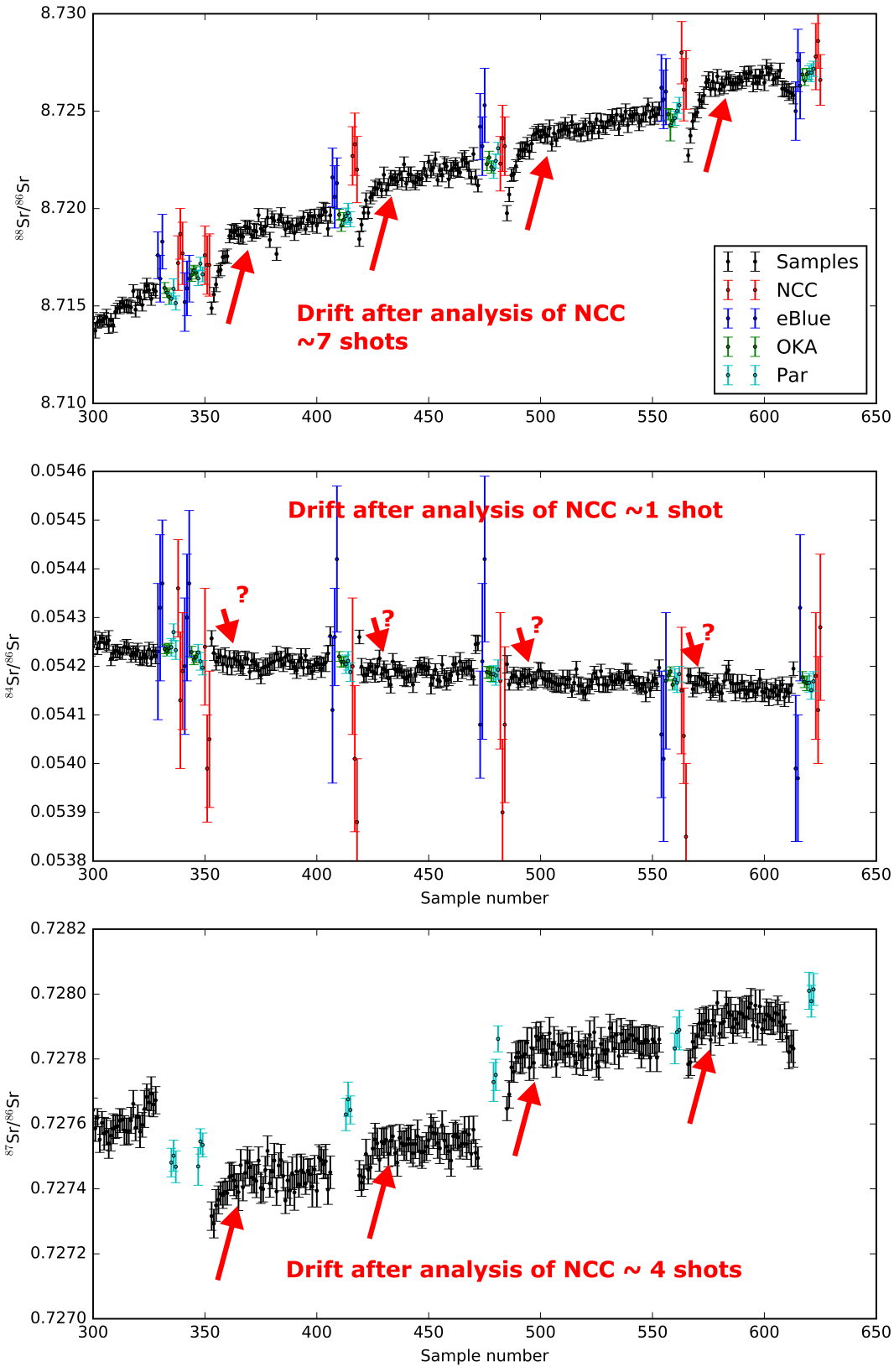

Fig. 3.8 Session drift patterns. Rapid drift is seen in periods after the ablation of NCC which has a concentration of ≈1% Fe by weight. Even within a very similar matrix, matching is important. This drift is cancelled out when applying an internal mass fractionation correction, but will impart a bias during sample standard bracketing. Some studies use standard-bracketing techniques, assessing long term reproducibility using a different matrix standard (i.e. Barites and Carbonates (Jamieson et al., 2016)).

Direct linear response

The direct linear response method proposed by Fietzke et al. (2008) was applied to the same samples used in the optimisation experiment. In this processing method, raw signal intensities are regressed against one another, and the gradient of the resulting line is the isotope ratio of interest. The precision on individual spot analyses is much more variable, and repeat analyses of standards more scattered (see figure 3.9). Increases in precision per analysis are lost in poorer long-term reproducibility and much larger MSWD values for repeats of Oka (2.35×10^7 compared to 1.68). The variation in Sr concentration is small during each ablation and therefore the scatter is insufficient for a robust regression. However, this suggests sample concentration heterogeneity is required for this method to work. The origin of this heterogeneity will dictate whether the assumption of isotopic homogeneity is reasonable, but this assumption is fundamentally no different to the limitations of physical subsampling for TIMS analysis. With regards to δ^{88}Sr determination, partitioning and isotopic fractionation in carbonates are growth rate and temperature dependent, so concentration variations are likely accompanied by isotopic variation (AlKhatib and Eisenhauer, 2016a,b). Concentration heterogeneity is better sampled by line rasters which Fietzke et al. (2008) and Jamieson et al. (2016) have applied to analysis of carbonates and barites.

Conceptually, this approach works well for dealing with unresolvable or uncorrectable matrix interferences at a constant formation rate (as this shifts the intercept of the regression line, but has no effect on the gradient). However, it remains to be seen how the results reflect interferences of varying intensity. An unweighted regression does not propagate the uncertainty on individual integrations. Therefore, the 2 standard error of the gradient is likely to be an underestimate of the uncertainty (Yang et al., 2011). Based upon our analyses, any gains in precision are lost by degradation of accuracy, so this method was not pursued further.

LA-MC-ICPMS measurement of stable strontium isotopes

Variation in stable Strontium isotopes (δ^{88}Sr) imparts biases to ^{87}Sr/^{86}Sr and ^{84}Sr/^{86}Sr when ^{86}Sr/^{88}Sr is used to correct for mass fractionation (where δ^{88}Sr = 0 is assumed for calculation of β_{Sr}). Natural variability has been recorded between -1‰ and +1.4‰, but most values are in the range 0.1‰ to 0.5‰ (Irrgeher et al., 2016). Some of this variability is related to growth rate (Stevenson et al., 2014), and temperature dependent partitioning behaviour is debated (Raddatz et al., 2013). (AlKhatib and Eisenhauer, 2016a,b) show that fractionation between fluid and minerals can cause variation of 0.05 to 0.35‰ in δ^{88}Sr of calcite and 0.15 to 0.25‰ in δ^{88}Sr of aragonite. The impact that these fractionations have on ^{87}Sr/^{86}Sr and ^{84}Sr/^{86}Sr

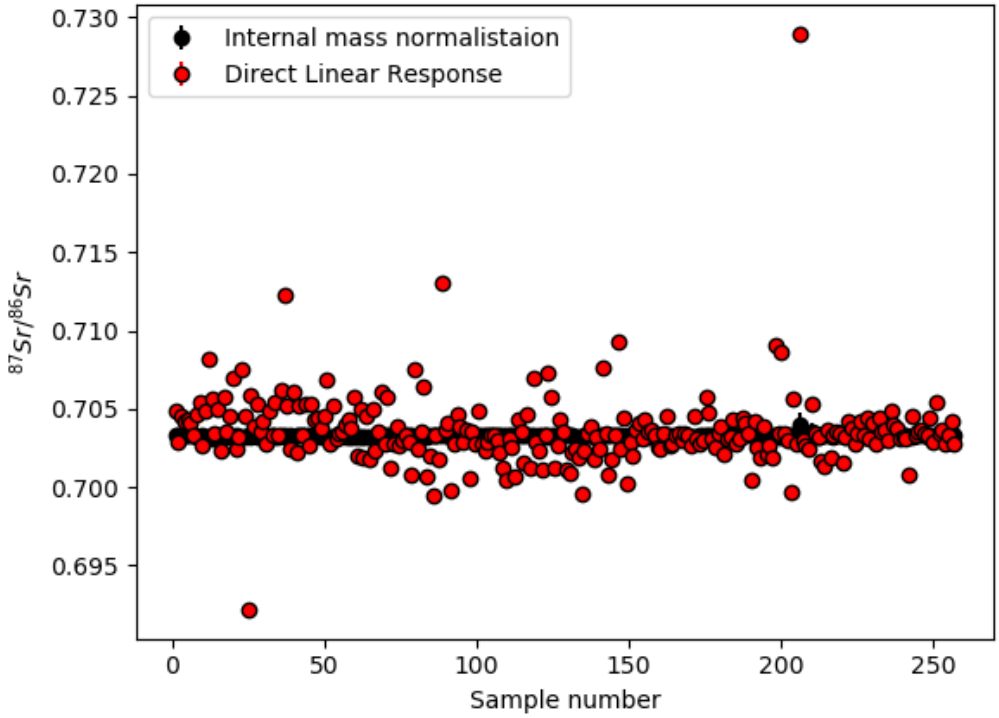

Fig. 3.9 Comparison of data using internal mass normalisation (black) and direct linear response (red). In this case, the direct linear response data reduction method shows much poorer long-term reproducibility. A robust regression is not possible on short collections

ratios depends upon the size of instrumental fractionation, but a value of δ^{88}Sr 0.1‰ larger will offset ^{87}Sr/^{86}Sr by +36ppm and ^{84}Sr/^{86}Sr by -6ppm (assuming 'true' ^{87}Sr/^{86}Sr = 0.713 and $\beta_{Sr}\approx$-1.6). Variations on this scale are of similar magnitude to external precision, and will also impact assessment of β_{Sr}- β_{Rb} relationship.

Standards are not analysed for δ^{88}Sr, but relative values and repeatability are assessed relative to Oka, assuming it has a δ^{88}Sr=0. A block of bracketing standards were analysed every 10 samples. Individual analysis spots are precise to ±0.05‰ (2SE), but repeat analyses show external reproducibility of ±0.18‰ (2σ) for Par, and ±0.45‰ on NCC and eBlue (2σ) (See figure 3.10). These analysis were not intended to determine δ^{88}Sr, and can be improved by more frequent bracketing standards, longer collection times, and more heterogenous standards and without running NCC for matrix matching. If precision is limited by counting statistics, collections would need to be 5-10 times longer to become comparable to the ±0.015‰ precision from TIMS analyses (Stevenson et al., 2014). Alternatively, newly developed $10^{13}\Omega$ amplifiers may help increasing the precision of the ^{86}Sr signal. Without further development screening for extremes of δ^{88}Sr is possible in higher concentration samples, but the limitations of standard heterogeneity and external repeatability remain.

3.2.5 Conclusions

Our results demonstrate that application of medium resolution LA MC-ICP-MS both improves and simplifies analysis of Sr isotopes by laser ablation when REE interferences are present. Data acquisition and reduction is significantly shortened relative to low resolution methods, as only correction for Rb and Kr are necessary. The medium resolution approach also makes it easier to parameterize the relative behaviour of Rb and Sr. The precision and accuracy of the method is insensitive to the range of laser spot sizes and repetition rates tested (25-130µm and 2-10Hz). Low signal to noise arising from electronic noise of the $10^{11}\Omega$ amplifiers limits the precision of analyses at ^{87}Sr < 0.4V, and counting statistics dominates at ^{87}Sr > 0.4V. However, laser parameters can be adjusted to optimize sampling, especially in lower concentration materials. In carbonates, barites and NIST glass no downhole fractionation effect is observed. The long-term reproducibility of the method is ±42ppm for high-Sr carbonates, and is limited by short collection times and analytical noise, but standard heterogeneity may also act as limitation. With an optimised method, 100ppm precision can theoretically be achieved on carbonate with Sr concentration as low as 1000ppm Sr using individual spots.

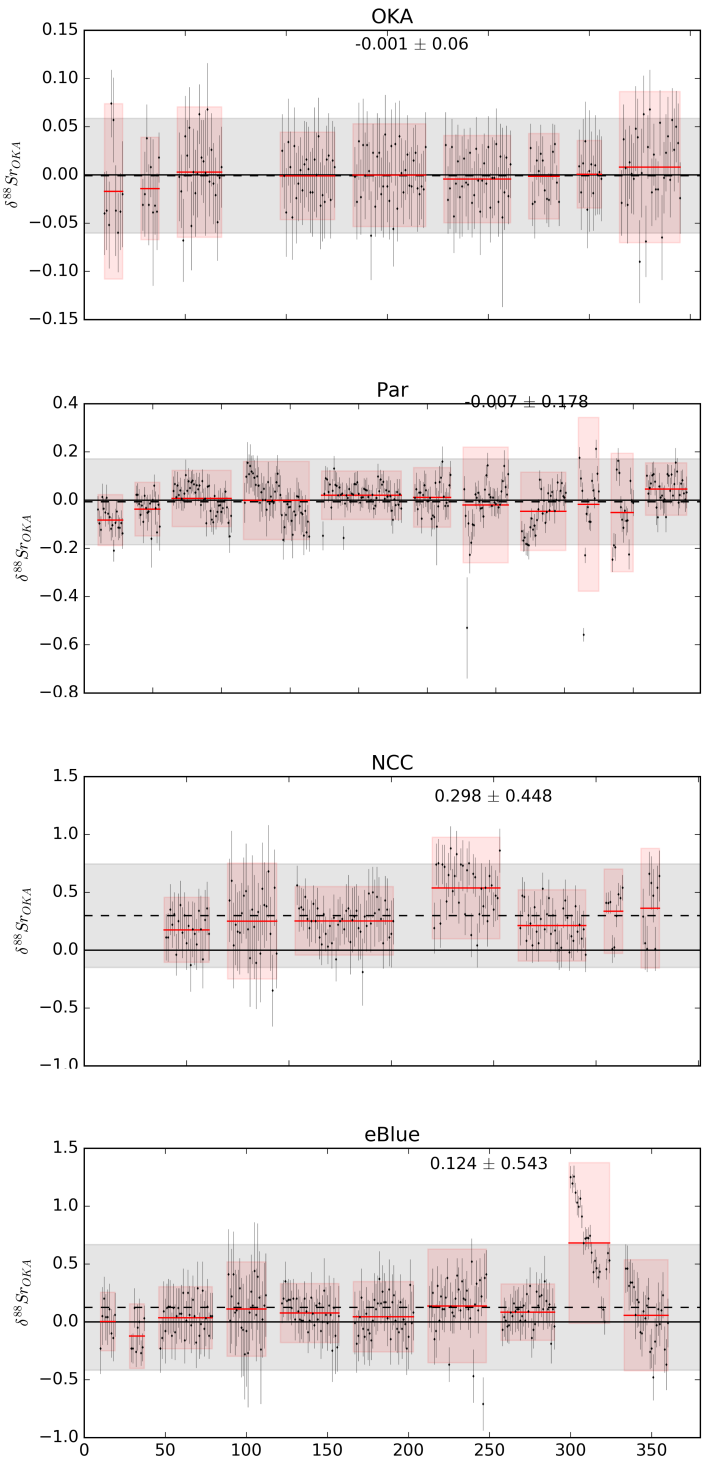

Fig. 3.10 Repeatability of δ^{88}Sr relative to Oka, these short collections do not give suitable stability or counting statistics. The frequency of bracketing standards is low, and therefore can be improved

Comparisons of data reduction approaches show internal mass fractionation corrections give the best precision as short timescale variations in mass fractionation behaviour are corrected. However, for analysis of non-radiogenic isotope ratios (i.e. δ^{88}Sr) bracketing is the only possible approach. Assumption of the δ^{88}Sr ratio during internal mass fractionation correction impart offsets of similar size to external reproducibility in ^{87}Sr/^{86}Sr. This can be recognised in the ^{84}Sr/^{86}Sr ratio, which is offset from 'true' if δ^{88}Sr has value other than 0‰ (as will be shown for an Aragonite vein from Green River, Utah in chapter 4). The size of the offset depends upon the magnitude of instrumental mass fractionation. These offsets can only be recognised through improvements of δ^{88}Sr analysis, but are of much smaller magnitude than the range of ^{87}Sr/^{86}Sr ratios.

During sample bracketing, matrix matching is necessary even within the same mineral, as drift was observed after analysis of carbonate with ≈1wt% Fe. This is particularly important for determination of δ^{88}Sr, where standard bracketing is the only appropriate approach. Our results for δ^{88}Sr are limited by counting statistics, background noise, and standard heterogeneity. Improvements can be made by longer collection times, better bracketing routines, and determination of more appropriate homogenous standards for δ^{88}Sr.

3.3 LA U-series

3.3.1 Introduction

U-Th dating is a powerful geochronological tool, allowing the dating of geological and archaeological materials up to 500kyr in age (Bourdon, 2003; Ivanovich and Harmon, 1992). Authigenic carbonate minerals are frequently dated, for example speleothems for monsoon reconstructions (Cheng et al., 2006; Wang et al., 2005, 2001) permafrost melt (Vaks et al., 2013), speleothems or corals for sealevel variability (Andersen et al., 2010; Thomas et al., 2009; Wainer et al., 2017), archaeological specimens for early human evolution and migration patterns, veins for tectonics and fluid-rock reactions (Kampman et al., 2012), and methane derived carbonates for hydrocarbon seeps and methane clathrate dissociation (Bayon et al., 2015; Crémière et al., 2016). Many other phases, including but not restricted to zircons and feldspars can also be dated, with a wide range of potential applications (Cooper and Kent, 2014; Reid et al., 1997).

Conventionally, samples are physically sampled using milling or drilling to powder the sample. These are dissolved and chemically separated into monoelemental solutions using ion exchange resins, and the resulting solutions have isotope ratios analysed by ICP-MS

or TIMS. Such an approach provides the most precise and accurate results, but is time and labour intensive. Laser ablation offers the advantage of high spatial precision, reduced sample preparation/handling and rapid analysis. The later point, however, is responsible for lower precision which limits application to higher concentration materials. Initial studies focussed on glasses with U concentrations of 100-500ppm (Bernal et al., 2005; Stirling et al., 2000). More recently zoned carbonates or bioapatites such as teeth, bones, speleothems or moluscs with U concentrations down to 1ppm have been sucessfully measured (Eggins et al., 2005; Potter et al., 2005). However, LA-U-Th remains used as a screening method due to lower precision limited by counting statistics on ^{230}Th ($\approx$ 2-5%). Attempts to improve precision rely on longer collections and heavy ablation parameters (Lin et al., 2017). The volume of material consumed in those ablations are comparable to physical sampling and solution methods. If possible, improvements in precision should not come at the expense of sample volume.

The low abundance of several isotopes (^{230}Th, ^{234}U and ideally ^{232}Th) restrict analyses to instruments with ion counters. Simultaneous collection is desirable, for which 3-4 low mass ion counters are required (Hoffmann, 2008; Hoffmann et al., 2009). Analysis can be performed with a single ion counter, but requires a dynamic collection (i.e. a "peak hop" (Lin et al., 2017; Spooner et al., 2016)). This increases the mass of sample analysed and may potentially miss isotopic heterogeneity. Biases with detectors may require careful calibration (Hoffmann et al., 2005). Large spot sizes (100-1000μm), high fluence (>10J/cm^2) and high repetition rates (10-20Hz) have been used to achieve reasonable precision on line rasters. In all studies, standard-sample bracketing is required to correct for interelemental fractionation between Th and U.

Treatment of uncertainties varies between studies. In most cases, only data point uncertainties are propagated (Spooner et al., 2016), or uncertainty from correction factors is propagated (Lin et al., 2017). In keeping with other geochronometers, such as U-Pb, standardised procedures allow for comparison of ages and thorough understanding of uncertainty propagation (i.e. EARTHTIME, Condon et al. (2015)). This is particularly important for future data users, as decay constants can be revised (i.e. (Cheng et al., 2000, 2013), values used for correction updated (Hiess et al., 2012), or reinterpretation of data make recalculation necessary. For U-series data, Dutton et al. (2017) advise necessary data reporting standards for solution work with some mention of how they may be applied to laser ablation data. For LA-U-Pb analyses, Horstwood et al. (2016) and Schaltegger et al. (2015) lay out the current best practices for uncertainty propagation. In particular the calculation of weighted mean statistics, such as the mean squared weighted deviation (Wendt and Carl, 1991) with an

associated excess variance correction is recommended. This approach is used as it accounts for the external reproducibility of the method.

3.3.2 U-Th chronology

U-Th dating uses the natural radioactive decay of ^{238}U, ^{234}U and ^{230}Th, which are members of the U-series decay chain:

$$^{238}_{92}\mathrm{U} \xrightarrow[4.47\,\mathrm{Ba}]{\alpha} {}^{234}_{90}\mathrm{Th} \xrightarrow[24.1\,\mathrm{days}]{\beta} {}^{234}_{91}\mathrm{Pa} \xrightarrow[6.69\,\mathrm{hours}]{\beta} {}^{234}_{92}\mathrm{U} \xrightarrow[245\,\mathrm{ka}]{\alpha} {}^{230}_{90}\mathrm{Th} \xrightarrow[75\,\mathrm{ka}]{\alpha} {}^{226}_{88}\mathrm{Ra} \xrightarrow[1600\,\mathrm{a}]{\alpha} \quad (3.4)$$

As parent and daughter are both unstable, a date can be calculated using the following decay equation:

$$\left(\frac{^{230}Th}{^{238}U}\right)_m = 1 - e^{-\lambda_{230}t} - \left(\left(\frac{^{234}U}{^{238}U}\right)_m - 1\right)\left(\frac{\lambda_{230}}{\lambda_{234}-\lambda_{230}}\right)\left(1 - e^{(\lambda_{234}-\lambda_{230})t}\right) \quad (3.5)$$

Where $\left(\frac{^{230}Th}{^{238}U}\right)_m$ and $\left(\frac{^{234}U}{^{238}U}\right)_m$ are measured isotope ratios and λ_{230} and λ_{234} are decay constants, which are related to half-life through the equation $\lambda = \frac{Ln(2)}{t_{1/2}}$. This decay equation assumes the system has remained closed (i.e. since mineral formation there is no loss or gain of radionuclides) and there is no initial daughter isotope (^{230}Th) present. The α-decay process can lead to open system behaviour which is discussed below. Initial ^{230}Th can be incorporated during crystal growth from the precursor fluid (often termed hydrogenetic) or from included mineral phases (termed detrital; commonly clays, iron-manganese oxyhydroxides or organic material). The decay equation can be modified for initial ^{230}Th and detrital contamination by the following substitution for the left hand term $\left(\frac{^{230}Th}{^{238}U}\right)_m$ of equation 3.5:

$$\left(\frac{^{230}Th}{^{238}U}\right) = \left(\frac{^{230}Th}{^{238}U}\right)_m - \left(\frac{^{230}Th}{^{238}U}\right)_i e^{-\lambda_{230}t} - \left(\frac{^{230}Th}{^{232}Th}\right)\left(\frac{^{232}Th}{^{238}U}\right)_m e^{-\lambda_{230}t} \quad (3.6)$$

where $\left(\frac{^{230}Th}{^{238}U}\right)_i e^{-\lambda_{230}t}$ represents the decay of the initial ^{230}Th, and $\left(\frac{^{230}Th}{^{232}Th}\right)\left(\frac{^{232}Th}{^{238}U}\right)_m e^{-\lambda_{230}t}$ is the decay of a detrital contaminant. Analogously, $\left(\frac{^{234}U}{^{238}U}_m\right)$ of equation 3.5 can also be substituted to include a detrital term. For a single detrital phase an isochron approach with samples with varying degrees of detrital contamination are used to infer clean and detrital end-members. This can also be used to calculate initial ^{230}Th. Otherwise, reasonable assump-

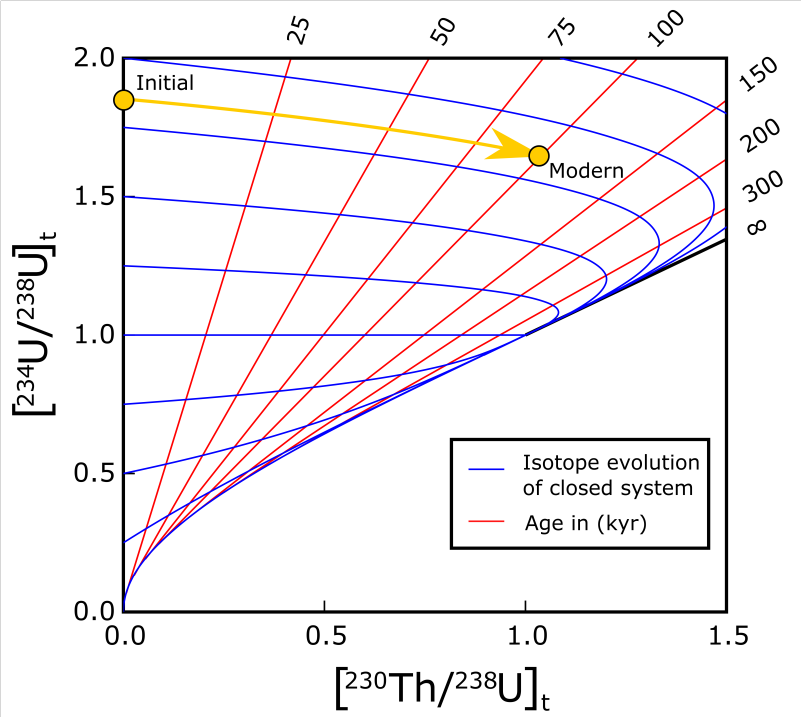

Fig. 3.11 Evolution of isotope ratios within a closed system occurs along blue contours for a given starting isotopic composition. Red contours represent lines of constant age (kyr). Modified from UThXL software

tions can be made based upon literature values. The decay equations are solved iteratively for t (date) using a Newton-Raphson method, and uncertainties propagated using monte-carlo simulations. The typical closed system evolution of a clean sample is shown in figure 3.11.

Once a date is calculated, the initial Uranium isotope composition is calculated by:

$$\left(\frac{^{234}U}{^{238}U}\right)_i = \left(\frac{^{234}U}{^{238}U}\right)_m e^{\lambda_{234} t} \tag{3.7}$$

With a propagation of the uncertainty associated with t (the age). This ratio is frequently expressed in delta notation relative to the secular equilibrium isotope ratio (the isotope ratio when decay rates are equal):

$$\delta^{234}U = 1000\left(\left[\frac{^{234}U}{^{238}U}\right] - 1\right) = 1000\left(\left(\frac{^{234}U}{^{238}U}\right) - 0.0000549687\right) \tag{3.8}$$

where square brackets are used to refer to activity ratios (where $\left[\frac{^{234}U}{^{238}U}\right] = \left(\frac{^{234}U}{^{238}U}\right)\left(\frac{\lambda_{234}}{\lambda_{238}}\right)$). Carbonates are generally good targets for U-Th chronology due to high concentrations of U, low initial Th and (frequently) low detrital contamination.

α-recoil and open system behaviour

Conservation of momentum during α-decay leads to displacement of the daughter nuclide causing damage to the chemical lattice, and results in a fission track 10s of nm long (i.e. 10^{-7} to 10^{-8} m) (Maher et al., 2006b). At the edge of crystals in contact with fluids, direct recoil of daughter nuclei into the fluid (i.e. ^{234}Th and thus ^{234}U) leads to higher activity ratios in the fluid ([^{234}U/^{238}U] » 1) and low activity ratios within the mineral rind (i.e. [^{234}U/^{238}U] < 1). This is summarised in figure 3.12. Fission tracks can act as conduits for fluid infiltration, and depending on fluid saturation can result in etching of the mineral. In some minerals U is coordinated as U^{IV} and during recoil oxidation to U^{VI} may occur, which is more readily soluble (Langmuir, 1978; Langmuir and Herman, 1980). Speciation of U and Th is highly dependant upon solution compositions, and the role of ternary complexes with Ca and Mg appears to be important, particularly in acidic conditions typical of acid mine drainage (Bernhard et al., 1998, 2001; Chen et al., 2017; Dong and Brooks, 2006; Endrizzi and Rao, 2014; Geipel et al., 2008; Lee and Yun, 2013). The physical and chemical change during α-recoil may enhance the mobility of daughter nuclides. Away from crystal boundaries, assuming homogenous concentration distributions, the net effect of recoil is zero, so [^{234}U/^{238}U] approaches a value of 1. If concentration distributions are heterogenous, which is common in carbonates, [^{234}U/^{238}U] will decrease in high concentration zones and increase in low concentration zones. This can contribute to sample heterogeneity. The ^{234}U/^{238}U composition of a fluid is therefore a function of: uranium concentrations, fluid-mineral surface area, dissolution/precipitation reactions and fluid-mineral contact times (i.e. flow rates). In sandstone reservoirs, uranium bearing phases include plagioclase and alkali feldspars, haematite grain coatings and trace phases such as apatites and zircons. This is discussed in more detail in chapter 5.

To account for open system behaviour the decay equations can be modified further using a factor f_{234} and f_{230} which are the fractions of radionuclides remaining in the system or gained through processes like adsorption or diffusion (Henderson and Slowey, 2000; Henderson et al., 2001). If uncorrected, open system behaviour leads to lower ^{234}U/^{238}U and ^{230}Th/^{238}U which gives inaccurate ages. This is described in corals by Thompson et al. (2003). Diffusive loss of ^{230}Th and ^{234}U, has been shown in bones, but may be corrected for through modelling of diffusion (Benson et al., 2013a; Sambridge et al., 2012).

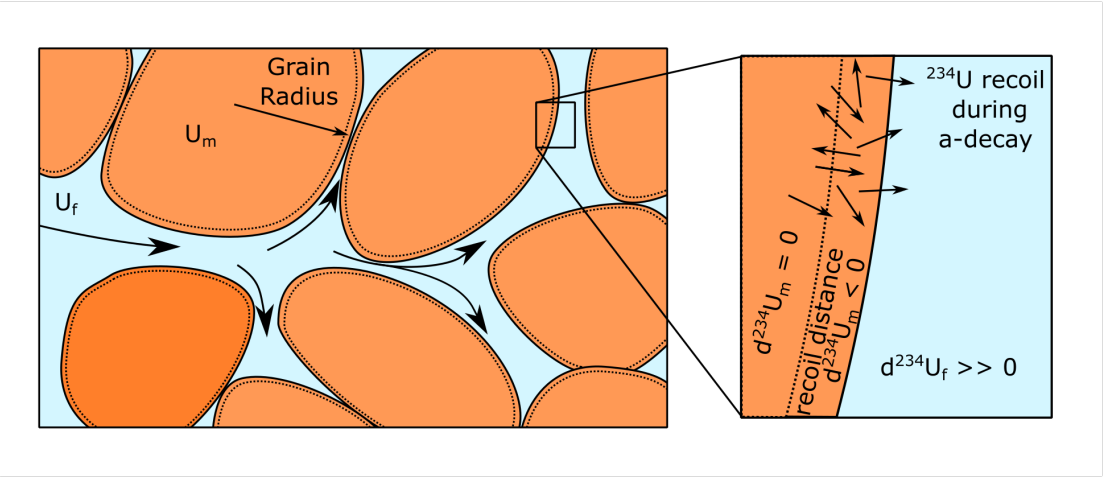

Fig. 3.12 Approximation of α-recoil in from mineral grains. Recoil length is typically 20-30nm, which leads to a depletion of ^{234}U in the mineral surface, and an enrichment of ^{234}U in the fluid.

Uranium isotopes: δ^{234}U and δ^{238}U

Variation in δ^{234}U is much larger than δ^{238}U because of α-recoil, but δ^{238}U variability can impact on U-Th determination through mass fractionation corrections. This is only necessary when double spike methods (^{233}U-^{236}U) cannot be used. An offset of -0.2‰, which is observed in aragonite precipitation experiments (Chen et al., 2016c), will lead to a mass bias undercorrection of -0.26‰ on $\delta^{234}U$, assuming β_U in the range for ICP-MS -0.6 to -2. Natural variability of δ^{234}U is over ≈10000‰; largest variations are in crustal fluids due to α-recoil (Andrews et al., 1982; Andrews and Kay, 1982; Kronfeld, 1974; Maher et al., 2006a,b; Maskell et al., 2015; Priestley et al., 2017), and oceanic variation is much smaller at ≈20-30‰ over glacial-interglacial time periods (Chen et al., 2016b; Esat and Yokoyama, 2006). Imparted bias are therefore small compared to the range of δ^{234}U observed in carbonates.

Variation in δ^{238}U is a mass independant fractionation, caused by differing nuclear volume of each isotope ('nuclear field shift') (Bigeleisen, 1996; Dauphas and Schauble, 2016). During leaching experiments, ^{235}U is preferentially leached relative to ^{238}U, and these processes may be redox sensitive (Andersen et al., 2014, 2016; Brennecka et al., 2010; Stirling et al., 2007; Weyer et al., 2008). Upto 5‰ variation has been observed, with most extreme values associated with ore deposits (Hiess et al., 2012; Murphy et al., 2015, 2014).

3.3.3 LA-ICP-MS analysis

Sample & standard preparation

Aragonite veins from Green River (Utah), were analysed using solution techniques to be used as standard materials. Additional verification speleothem materials were provided by Sebastian Breitenbach, all of which had previous solution U-Th determinations by different laboratories (table 3.10 and 3.11). Of particular use are the speleothems at secular equilibrium (Boti-881 and POLY). These speleothems are calcite, unlike the Green River veins, and POLY is transparent orange-brown presumably from high Mn or Fe concentrations. These reference materials were mounted in epoxy resin and polished using 0.25μm diamond paste to provide a flat surface for ablation. Polishing allows for better visual identification of crystallographic features such as crystal boundaries and twins. The composition of the Green River standard materials varies by ±30% over 10-100μm length-scales for elements such as Sr and U as discussed in chapter 4, and is shown in figures 3.17 and 3.18.

The unknown samples are veins collected from Green River, Utah in 2014. The stratigraphic tops and bottoms of these samples were mounted in resin to measure the oldest and youngest ages respectively. As the primary standard is also from Green River there is a reasonably matrix matching between samples and standard. The age of these deposits indicate periods when fault zone dilation allows CO_2 rich brines to escape to the surface. High $^{234}U/^{238}U$ ratios, U concentrations ≈ 2-8ppm, and low detrital contamination make these ideal materials to be analysed by LA-ICP-MS.

All samples and standards are pre-ablated to remove surface contamination. Highly variable ^{232}Th signal 'spikes' are observed on the first ablation pass but not subsequently. These spikes can cause the detector array to trip for an integration.

Analytical setup

Analysis are performed at NIGL (BGS) on a NEPTUNE+ with a split connection to a NewWave 193nm excimer laser and Aridus 2 desolvator. An off axis, multiple ion collector (MIC) array is used for collection of the smaller isotopes, and a Faraday cup with $10^{11}\Omega$ amplifier is used for the large ^{238}U beam (similar to Hoffmann et al. (2009)). The MIC array is composed of compact discrete diode (CDD) detectors which are a form of secondary electron multipliers (SEM). The dual laser-desolvator input is used for characterizing SEM/CDD gain/yield, hydride formation rates, and mass tailing at the start of each session using a CRM112a solution doped with ^{232}Th. Typical operating parameters are given in table 3.7. Short instrument integration times (0.262s) are used, so that heterogenous signals are

Table 3.7 Operating parameters for laser ablation U-series analyses at NIGL

Laser settings	**NewWave 193**
Raster spot size	100 x 150µm
Raster transect length	0.8mm
Raster transect rate	4-10µm/s
Ablation depth	∼40µm
Fluence	∼10 J/cm^2
Approx. mass CaCO3	∼14µg
Repetition rate	10 Hz
He flow	1 L/min
Mass spec settings	**NEPTUNE+ MC-ICPMS**
Forward RF power	1400W
Interface cones	Jet
Injector	Platinum
Mass resolution	Low (m/Δm ∼300)
Cooling gas	15 L/min
Sweep gas aridus	8-11 L/min
Sample gas	0.7 L/min
N2 flow	8-9 mL/min
Integration time	0.262s
Collection length	∼2.5mins (∼560 integrations)

captured. This is significantly shorter than other studies, which have integration times in excess of 4s.

MIC array: calibration and biases

Ion counters were calibrated for darknoise and operating voltage plateau at the beginning of every set of analytical sessions. Darknoise is <1cps on all detectors used in our analyses. Where there is ambiguity about the plateau voltage location, the lower limit of operating voltage is favoured to avoid double counting.

Gains on the MIC array are calibrated using a solution of CRM112a doped with ^{232}Th and two collector configurations (given in table 3.9). The two cup configurations are offset by 2 atomic mass units. Absolute gains are determined for IC1, IC2, IC3 and IC5 as ^{234}U/^{238}U and ^{235}U/^{238}U are known and the fractionation factor for U (β_U) is determined using ^{235}U/^{238}U on Faradays. A relative gain is measured between IC4 and IC5 using the ^{232}Th/^{238}U ratio. For the other detectors, relative gains are robust compared to absolute

Table 3.8 Laser ablation parameters for each analysis session presented

Session number	Date	Raster rate	Number of integrations	Length of collection
1	19/04/16	10 µm/s	∼200	∼50s
2	20/04/16	8 µm/s	∼280	∼75s
3	21/04/16	4 µm/s	∼560	∼150s
4	22/04/16	4 µm/s	∼560	∼150s

Table 3.9 Collector setup for analysis of U and Th isotopes and for calibration of detector yields

	IC4	IC5	IC3	IC2	IC1B	L4	L3
Collection	^{230}Th	^{232}Th	^{233}U	^{234}U	^{235}U	^{236}U	^{238}U
Relative gain calibration	^{232}Th	^{234}U	^{235}U			^{238}U	

gains. All detectors operate at 85-96% efficiency and are stable to ±0.5% across a week of analyses. However, ^{234}U/^{238}U and ^{235}U/^{238}U drift in opposite directions during some sessions. This cannot be mass discrimination or a nuclear field shift, so implies a drift in detector gains through time. Therefore standard-sample bracketing is the only appropriate method for these detectors. SEM detectors can show strong non-linear effects, such as the Channeltron detectors described by Hoffmann et al. (2005). In this study, the detector was assumed to count perfectly at 100,000cps. At signal intensities <100,000cps this detector undercounted, and at >100,000cps it overcounted. The other detectors tested, which are the same as used at BGS, do not display this effect. To test linearity, we run two bracketing standards at a low and high count rate and show non-linearity is not significant.

The ion beam is deflected (looking like a detector 'trip') when the rate of signal change on any MIC detector is above a threshold. This is to protect the MIC detectors from being damaged by large signals (i.e. >1,000,000 cps). This can happen erroneously on zoned samples, therefore a slow raster rate is used. However, the response time of the faraday detector measuring ^{238}U is longer than the MIC collectors, resulting in a low (^{230}Th – ^{234}U – ^{235}U)/^{238}U ratio. On the following integration the beam centres, and the Faraday responds slowly, giving a high ratio. These outliers are rejected using 2σ outlier rejection scheme (≈25 of 550 integrations). ^{232}Th is responsible for 'trips' during ablation work, and during solution analysis ^{233}U was responsible, originating in the membrane of an Aridus recently used for other U-series work. This is a clear disadvantage of the dual desolvator-laser interface. These 'trips' may act as a limitation to precision in 'dirty' samples.

Peak tailing, hydrides and transmission

The large abundance of ^{238}U imparts an offset on adjacent masses (i.e. ^{236}U, ^{235}U and ^{234}U) through peak tailing. This is assessed using solution analyses at the start of each session. Reverse tailing at 1 amu (m/z=237) is typically ≈2ppm, at 2amu (m/z = 236) is ≈1ppm. At 3amu (m/z = 235) a tail of 0.5ppm and at 4 amu (m/z = 234) a tail of 0.25ppm are assumed following an exponential relationship for the tail shape. Though this small formation rates make <5‰ difference on $\delta^{234}U$. At m/z = 239, signals are ≈3ppm higher, the combined effect of forward mass tailing and hydride formation of $^{238}U^{1}H^{+}$. During ablations $^{236}U^{+}$ is monitored on a Faraday and shows no difference between ablation and background, but at ^{238}U signals around 100mV a 2ppm (≈20cps) signal is indistinguishable from electronic noise. Low Th concentrations make Th tailing corrections unnecessary. Transmission efficiency is ≈1.6-2% for U using analysis of CRM112a, and measurements of nebuliser uptake rate.

Cell effects: variable inter-elemental fractionation

Variable fractionation behaviour is sometimes observed around a laser cell. These effects are thought to be linked with interelement fractionation properties, particularly related to oxidation of the plasma generated by ablation. Variable O_2 concentrations around the laser cell can also be caused by leaks, though O_2 is generated from the ablation of carbonate. Such variations are reduced in two volume cells; we test this by placing multiple copies of our standards around the cell. The resulting ^{230}Th/^{238}U and ^{234}U/^{238}U ratios were stable within $\pm 5.5 \times 10^{-6}$ and $\pm 1.2 \times 10^{-6}$ (2σ) for 3 standard materials; the results are shown as the first analytical session in figure 3.13. Data collected in this session are less precise due to short collection times (table 3.8), but are consistent with external reproducibility of later sessions suggesting minimal impact on analyses. Similarly crystallographic orientation was also tested by mounting approximately parallel, perpendicular and at 45° to vein growth axis. No significant variation was detected.

Interferences and scatterred ion effects

There are not known to be any issues with interferences in carbonate matrices. Theoretically, HgO_2, TlO_2 and PbO_2 can form interfering oxides. Organic molecules interferences were observed during a small oil leak on the instrument, but had strange shark-fin like peak shapes. No significant effect from scattered ions has been found by other studies, which perform a peak hop half a mass unit either side of the main collection during ablation (Hoffmann

et al., 2009; Lin et al., 2017; Spooner et al., 2016). It is assumed these are negligible during analysis, or are accounted for by bracketing.

Data reduction procedures

Data reduction is performed in Iolite v2.5 (Paton et al., 2011). Data is continually collected through the analysis session allowing for determination of baseline measurements. Baselines on ^{234}U and ^{235}U are 0-4cps and on ^{230}Th and ^{232}Th are 0-1cps. Sample ablation intervals were identified using the laser log file output. The following order of corrections are applied:

1. Baseline correction
2. Hydride, tailing and gain correction
3. Standard-sample bracketing of ratios

Standard-sample bracketing corrects for combined instrumental and sample biases, based an independently constrained standard. These biases include mass discrimination, nuclear field shifts, interelement fractionation, detector drift and scattered ion effects. ^{230}Th/^{238}U, ^{234}U/^{238}U and ^{235}U/^{238}U are directly bracketed, and ^{232}Th/^{238}U is corrected using ^{230}Th/^{238}U due to standard heterogeneity. ^{230}Th/^{238}U is offset by 0.5-0.6 when tuned for maximum ^{230}Th sensitivity, i.e. nearly double the amount of U (than Th) is ionised. Drift patterns are smooth and generally linear at most $\approx 4 \times 10^{-6}$ for ^{230}Th/^{238}U, and $\approx 1 \times 10^{-6}$ for ^{234}U/^{238}U across a 6 hour session. Accuracy of the bracketing correction is verified using two secondary standards.

The resulting isotope corrected isotope ratios are exported from Iolite, and if necessary excess variance is propagated for each analytical session. Ages are calculated using algorithms ('U_Th_XL_v1') provided by Noah McLean, which iteratively solve the decay equations using the Newton-Raphson method with Monte-Carlo simulation for uncertainty propagation allowing for uncertainty correlations.

Uncertainties: sources and propagation

Mass spectrometers impart a range of quantifiable systematic biases, which are corrected during data processing. However, precision is limited by factors such as electronic noise or variability in instrumental response at frequencies higher than repeat analyses of bracketing standards. This variability can arise in either the mass spectrometer or the laser. The excess variance correction (discussed in the next section) is used to propagate the uncertainty related to these processes. These measurements uncertainties are then combined with the uncertainty on decay constants and detritus compositions to calculate an absolute age.

Excess variance propagation

The excess variance correction occurs in the following steps, all performed on absolute ratios once bracketing has been applied:

1) MSWD is calculated for the primary standard using the weighted mean of the session as $\bar{x}$. If MSWD > 1 then an excess variance correction is required as the data is overdispersed. If MSWD <= 1 no excess variance correction is necessary as the data is underdispersed, which is observed for $^{235}U/^{238}U$ measurements.

2) Excess variance (ε_1) is calculated as follows:

$$\varepsilon_1 = \sqrt{\sigma^2_{MSWD=1} - \bar{\sigma}^2_{datapoint}} \tag{3.9}$$

Which is a rearrangement of the quadratic sum of errors. $\sigma_{MSWD=1}$ is the uncertainty necessary to give a MSWD = 1 and $\bar{\sigma}_{datapoint}$ is the average uncertainty of individual data points. As the correction is only applied when MSWD > 1, $\sigma_{MSWD=1} > \bar{\sigma}_{datapoint}$. The standard deviation of the population is equal to $\sigma_{MSWD=1}$ for an unweighted MSWD.

3) The calculated excess variance is added quadratically to all measurements:

$$\sigma_{propagated} = \sqrt{\varepsilon_1^2 + \sigma^2_{datapoint}} \tag{3.10}$$

4) MSWD is recalculated. By definition, the primary standard should now have MSWD = 1. The quality of the primary standard is verified against secondary standards. If either standard is heterogeneous then MSWD values will be > 1. In this case, a third standard is required to determine which standard is heterogeneous. By this iterative process, standard selection improves. At least 3 standards are run in case any one standard has an unidentified heterogeneous region.

Steps 1-4 should be performed initially on each analytical session (ε_1) and, if necessary, to all analytical sessions (ε_2). The excess variance correction accounts for the long-term reproducibility of the method; which is the limit of interpretation. Good secondary verification materials should be compositionally different to account for instrumental biases (i.e. a high concentration material and low concentration material should be used to test detector linearity and counting statistics). The interplay of counting statistics and external variance is discussed later. If the primary standard has isotopic heterogeneities, then this uncertainty is also propagated. The result is under-propagation for samples which are more heterogeneous

than the standard, and vice versa, but can only be assessed by multiple analyses. Excess variance determined on a purely homogeneous material reflects instrumental scatter. We report both analytical (s) and propagated (s+ε_1) uncertainties. Such practice is advised for LA-ICP-MS U-Pb or SIMS data (Horstwood et al., 2016; Schaltegger et al., 2015) and is best practice for solution U-Th data (Dutton et al., 2017). As excess variance is calculated using a vein sample from the same locality, it is a good match to samples. It may result in a slight over-propagation on younger samples, which are less precise due to less favourable counting statistics.

Error correlations

Covariance between ^{230}Th/^{238}U and ^{234}U/^{238}U occur because both ratios include ^{238}U in the denominator, and ^{234}U and ^{230}Th are related through decay. The correlation in these terms depends upon age, and also on any detrital corrections. A positive correlation in uncertainties reduces age uncertainties at all ages. This can be visualised on figure 3.11 as the error elipse will cross fewer red contours. Conversely, a negative correlation will increase age uncertainties. Such correlations are calculated within 'U_Th_XL_v1'.

Mass of material analysed

The depth of the ablation trench is $\approx 40\mu m$ and is estimated by focusing on the original sample surface and the base of the trench, and using the difference in stage height. Using a raster 150μm wide and 800μm long then $\approx$14μg of aragonite is ablated. This is a quarter of the mass of carbonate measured in corals by Potter et al. (2005). In VS001/2A, which has a U concentration $\approx$5ppm, $\approx$70pg of U and $\approx$3fg of ^{230}Th are measured. In lower concentration samples, such as POLY ($\approx$0.8ppm U), much smaller masses are analysed; $\approx$12pg of U and $\approx$0.2fg of ^{230}Th.

3.3.4 Results & Discussion

In the following section, VS001/2A is used as the primary standard. POLY and 2/4/005 are used as secondary materials run in all sessions. The raw results are shown in figure 3.13 and results after propagation of excess variance in 3.14. The additional speleothem samples provided by Sebastian Breitenbach (KA, MAW, BLA and Boti) are run in one session to check accuracy. These materials were analysed by ICP-MS in other laboratories, so values may be subject to small systematic offsets dependent upon 1) inter-laboratory calibration of analytical methods, and 2) conversion from activity ratios to atomic ratios,

due to updated decay constants[4]. Propagation of session excess variance (ε_1) onto standards gives MSWD≈1 on all standards and samples, therefore a secondary propagation (ε_2) is not required. Processed isotope ratio results are given in table 3.10, and repeats of the three standard materials are shown in figures 3.13 and 3.14 (before and after propagation of ε_1, respectively). The dates calculated from these isotope ratios are given in table 3.11.

Accuracy and precision: $^{234}U/^{238}U$

Secondary standards 2/4/005 and POLY, both show systematic offsets of $+2.5 \times 10^{-6}$ and $+3.5 \times 10^{-6}$ on mean values of $^{234}U/^{238}U$ relative to solution values (65‰ and 45‰). However, repeats of solution analyses suggest 20‰ variability within these materials. Detector non-linearity can be ruled out as a source of offset as VS001/2A and 2/4/005 show offset at similar count rates and POLY shows a positive offset at lower count rate. POLY behaves in a more consistent manner than 2/4/005, suggesting that the second material has inherent heterogeneity. BLA, KA, MAW and Boti show offsets of 2‰, 75‰, 1‰ and 5‰. However, as noted earlier the data reduction methods on the solution analyses impart biases, and these details are currently not known. Importantly the laser analyses are self-consistent. The uncertainty on individual spots is typically ±20‰, and after propagation of excess variance is ±25‰. Boti, with U concentration of 40ppm, shows improved uncertainties of ±5‰ and ±12‰, whilst KA, with 0.2ppm U, is precise to ±38‰ and ±42‰.

Accuracy and precision: $^{230}Th/^{238}U$

The measurement of $^{230}Th/^{238}U$ is slightly more difficult because of bracketing for interelement fractionation. Similarly to $^{234}U/^{238}U$, POLY shows consistent values with a systematic offset of -8.9×10^{-7} (50‰ relative to secular equilibrium $^{230}Th/^{238}U$ of 1.69157×10^{-5}). 2/4/005 shows much larger variability, particularly in the first two sessions, so is assumed to be heterogenous for $^{230}Th/^{238}U$. Again non-linear detector effects cannot be considered responsible for offsets, as the count rates between VS001/2A and 2/4/005 are similar (100-200cps) and POLY is much lower (5-20cps). Speleothem samples show smaller offsets.

Accuracy and precision: $^{235}U/^{238}U$

It is assumed that VS001/2A has a $^{235}U/^{238}U$ value of 0.00725594 $\left(\frac{1}{137.818}\right)$. Relative to this 2/4/005 shows no offset, and the offset on POLY is +1.8‰ for $\delta^{238}U$, but well within

[4] a resolvable problem, but the constants originally used are currently not known and the results are unpublished

analytical uncertainty of $\pm 2‰$. Such a precision is too small for resolving variation without a large number of repeats, so is not pursued further.

Table 3.10 Isotope data for standards

PIMS analyses: NIGL										
Standard	Lab	U conc	$^{230}Th/^{238}U$	$\pm2\sigma$(int)		$^{234}U/^{238}U$	$\pm2\sigma$(int)		$^{232}Th/^{238}U$	$\pm2\sigma$(int)
VS001/2A	NIGL[1]	3.66	4.22320E-05	9.09E-08		2.10463E-04	2.17E-07		1.665E-05	2.84E-08
2_4_005	NIGL[1]	3.24	4.52404E-05	9.70E-08		2.00541E-04	2.06E-07		2.6082E-05	3.94E-08
VS001/1A[2]	NIGL[1]	4.51	4.34795E-05	9.97E-08		2.08973E-04	2.17E-07		1.40854E-04	1.52E-07
Laser analyses (this study)										
Standard			$^{230}Th/^{238}U$	$\pm2\sigma$(s)	$\pm2\sigma$(s+ε)	$^{234}U/^{238}U$	$\pm2\sigma$(s)	$\pm2\sigma$(s+ε)	$^{232}Th/^{238}U$	$\pm2\sigma$(s)
VS001/2A			4.2232E-05	5.23E-07	6.73E-07	2.10E-04	1.09E-06	1.31E-06	1.41E-06	5.22E-07
2_4_005			4.4456E-05	5.30E-07	6.77E-07	2.04E-04	1.05E-06	1.27E-06	7.24E-06	6.76E-07
Data recalculated from AR: External data										
Standard	Lab	U conc	$^{230}Th/^{238}U$	$\pm2\sigma$(int)		$^{234}U/^{238}U$	$\pm2\sigma$(int)		$^{232}Th/^{238}U$	$\pm2\sigma$(int)
BLA-1	Cheng	0.80	1.53677E-07	2.38484E-09		5.70682E-05	2.23217E-07		4.37E-03	
KA-2	Cheng	0.17	2.75807E-07	9.03603E-09		3.91611E-05	5.96789E-08		2.93E-03	
MAW-1	Cheng	7.80	1.04721E-05	1.94202E-08		4.4926E-05	6.55072E-08		4.0653E-05	
BOTI-881[3]	Adkins	40	1.74969E-05	9.81613E-07		5.57E-05	1.48E-07		1.97E-05	1.31E-05
POLY-1[3]	Adkins	0.70	1.73908E-05	9.25088E-08		5.38E-05	4.10E-06		7.50E-03	1.11E-02
Laser analyses (this study)										
Standard			$^{230}Th/^{238}U$	$\pm2\sigma$(s)	$\pm2\sigma$(s+ε)	$^{234}U/^{238}U$	$\pm2\sigma$(s)	$\pm2\sigma$(s+ε)	$^{232}Th/^{238}U$	$\pm2\sigma$(s)
BLA-1			9.1000E-07	1.90E-07	4.62E-07	5.72E-05	1.40E-06	1.57E-06	3.02E-02	6.50E-04
KA-2			2.9000E-07	2.20E-07	4.75E-07	4.33E-05	2.10E-06	2.22E-06	6.25E-03	5.10E-04
MAW-1			1.0110E-05	1.80E-07	4.58E-07	4.50E-05	3.60E-07	8.03E-07	1.19E-05	5.50E-07
BOTI-881			1.7420E-05	1.70E-07	4.54E-07	5.60E-05	2.70E-07	7.67E-07	2.13E-07	2.90E-08
POLY-1			1.6496E-05	5.99E-07	7.32E-07	5.62E-05	1.08E-06	1.30E-06	6.91E-05	7.32E-06

[1] Repeat analyses of material show same age (n=3, 3 materials), but variable modern [230/238] and [234/238] of 2-3%. Ages on replicates are the same, confirming closed system behaviour. Therefore [234/238]i or open system behaviour is responsible for variability.

[2] Determined in early analysis session to low precision, and not sampled in later sessions due to higher U conc variability and (relatively) dirtier bands. Used as a standard material by Spooner et al. (2016), though is reanalysed for a less precise value of $^{230}Th/^{238}U$

[3] Secular equilibrium materials, thus no calculated age (>500 kyr)

Table 3.11 Calculated dates and $\delta^{234}U_i$ for the standards

PIMS analyses: NIGL							
Standard	Lab	U conc	[^{230}Th/^{232}Th]	Calculated date	±2s	Initial [234/238]	±2s
VS001/2A	NIGLa	3.66	471486	98.48	0.33	4.743	0.005
2_4_005	NIGLa	3.24	322428	117.15	0.44	4.694	0.005
VS001/1Ab	NIGLa	4.51	57380	102.63	0.39	4.779	0.005
Laser analyses (this study)							
Standard			[^{230}Th/^{232}Th]	Calculated date	±2s+ε_1	Initial [234/238]	±2s+ε_1
VS001/2A			5553324	98.686	2.440	4.735	0.032
2_4_005			1140663	116.908	2.877	4.715	0.034
Data recalculated from AR: External data							
Standard	Lab	U conc	[^{230}Th/^{232}Th]	Calculated date	±2s	Initial [234/238]	±2s
BLA-1	Cheng	0.80	7	2.65	0.05	1.039	0.004
KA-2	Cheng	0.17	17	2.35	0.12	0.710	0.001
MAW-1	Cheng	7.80	47883	172.66	1.23	0.703	0.002
BOTI-881c	Adkins	40	165046	-	-	-	-
POLY-1c	Adkins	0.70	431	-	-	-	-
Laser analyses (this study)							
Standard			[^{230}Th/^{232}Th]	Calculated date	±2s+ε_1	Initial [234/238]	±2s+ε_1
BLA-1			6	4.994	3.077	1.041	0.030
KA-2			9	2.222	3.985	0.786	0.041
MAW-1			157924	157.113	19.364	0.717	0.033
BOTI-881			15202415	-	-	-	-
POLY-1			44375	-	-	-	-

[1] Determined in early analysis session to low precision, and not sampled in later sessions due to higher U conc variability and (relatively) dirtier bands

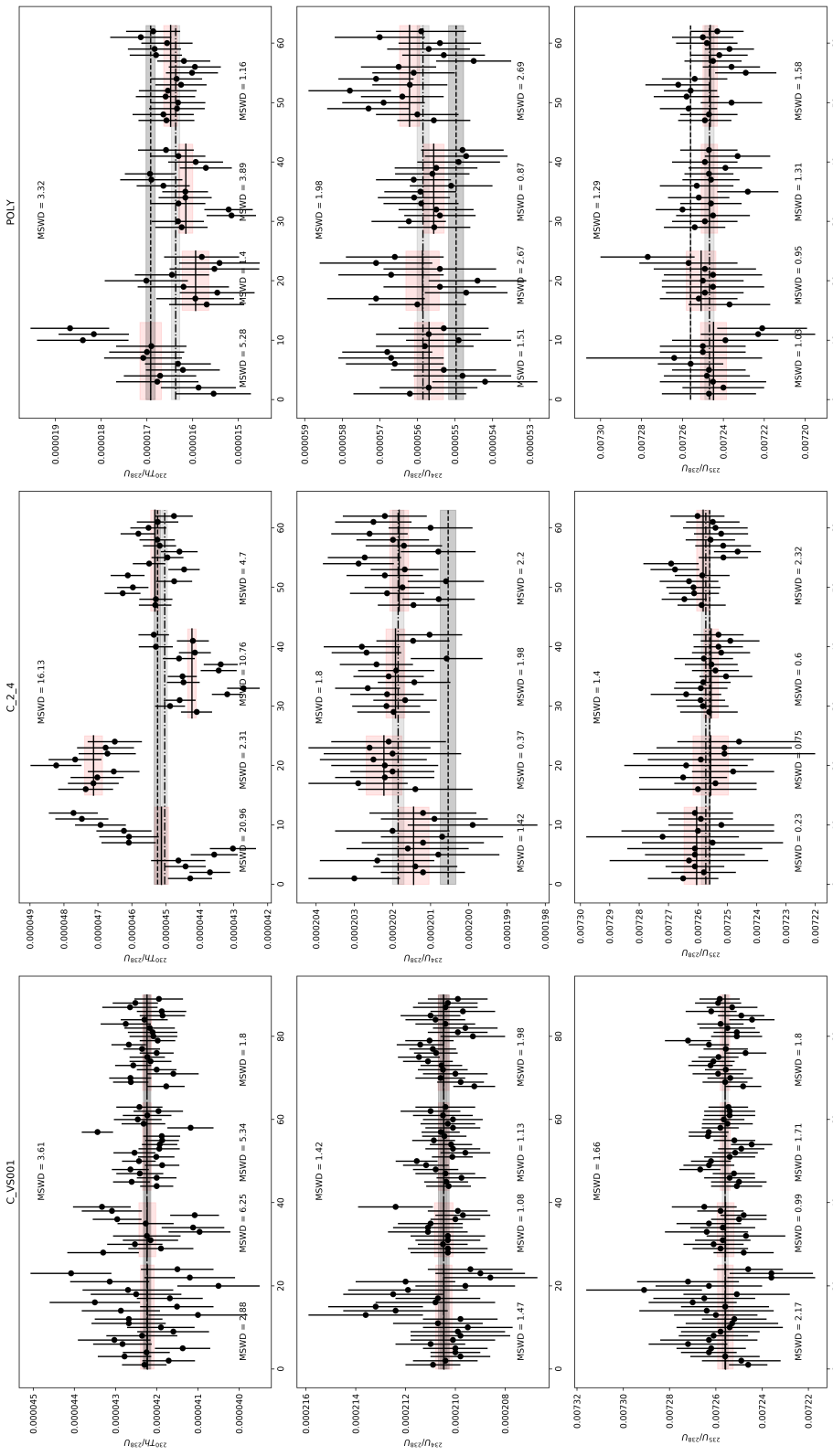

Fig. 3.13 Results for 4 analytical sessions. Data points are shown with 2s analytical errors. Pink shaded regions represent 2σ for each analytical session, and MSWD values for each session are displayed beneath each session. The weighted average for all of the sessions is the light grey shaded box, and the solution analysis equivalent is shown in dark grey.

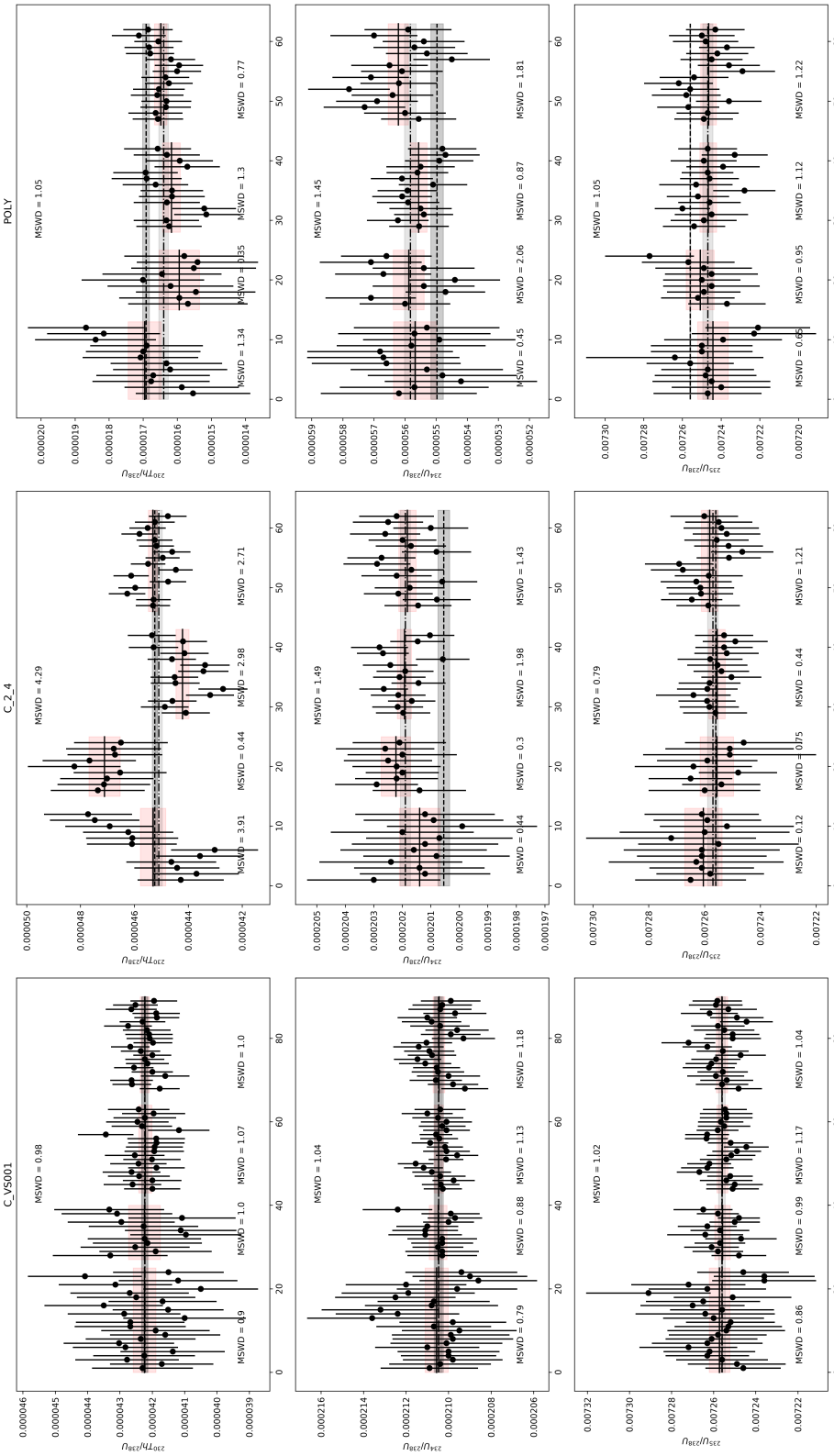

Fig. 3.14 Results for 4 analytical sessions. Data points have 2(s+ε_1) errors. Colours are the same as in the previous figure

Accuracy and precision: calculated dates and $\delta^{234}U_i$

Figure 3.15 shows the calculated ages before and after propagation of ε_1, and figure 3.16 shows the same for initial $^{234}U/^{238}U$ isotope values. On VS001/2A MSWD values on ages are 3.08 prior to propagation and 0.83 afterwards. On 2/4/005 the high values of $^{230}Th/^{238}U$ in the second session lead to age overestimation, which is thought to be due to isotopic heterogeneity. In turn this older age leads to overcalculation of $\delta^{234}U_i$. The systematic offset on U_i is ≈10-15‰ which is well within the uncertainties (≈30-40‰).

Assuming the uncertainties on POLY are most similar to coral matrixes, our fully propagated uncertainties are slightly smaller than those quoted by Spooner et al. (2016), similar to those from Potter et al. (2005). However, we analysed a quarter of the material used in these studies. This approach if applied to corals (or other materials with low $[^{234}U/^{238}U_i]$) remains a screening technique on materials >20ka and potentially unable to date very young materials due to very low count rates of ^{230}Th. This information is still valuable when age screening.

Standard heterogeneity

Figures 3.17 and 3.18 show the raw count distributions of VS001/2A and 2/4/005. Slow raster transect rates were used to minimise the rate of signal change on detectors to minimise the possibility of detector tripping. Chemical zonation occurs on the 10-100μm scale in these veins, which is seen across multiple elements, as presented in chapter 4. Compatible elements such as U, Sr and Ba loosely correlate, due to either mixing, rayleigh fractionation or rate dependant partitioning (AlKhatib and Eisenhauer, 2016a,b; Weremeichik et al., 2017). Such variability may subtly influence plasma loading, and thus be a source of minor plasma instability. A small degree of isotopic zonation may occur during fluid-mineral partitioning. The α-recoil process can distribute ^{234}U between chemical zones over $0.03\mu m$ lengthscales, which are much too small compared to the length of zonation and the laser spot size.

^{232}Th counts are low, and $[^{230}Th/^{232}Th]$ is very high (>40,000; isochrons are necessary when <15), indicating that there is no detrital contamination in most samples. Laser analyses of standards are 3-10 times cleaner than their corresponding solution analyses, see table 3.11. However, the offset samples of 2/4/005 exhibit initial ^{230}Th, such as in figure 3.18. The smooth nature of the ^{232}Th signal makes it unlikely to be detrital contamination. Some of the heterogeneity for $^{230}Th/^{238}U$ on sample 2/4/005 may be due to initial ^{230}Th. Similar observations have been made in coral samples e.g. Spooner et al. (2016).

NIST 612 glass was also run initially in the hope that it would be a good homogeneous standard. Unfortunately U/Th variability of ≈5% was greater than in carbonate standards.

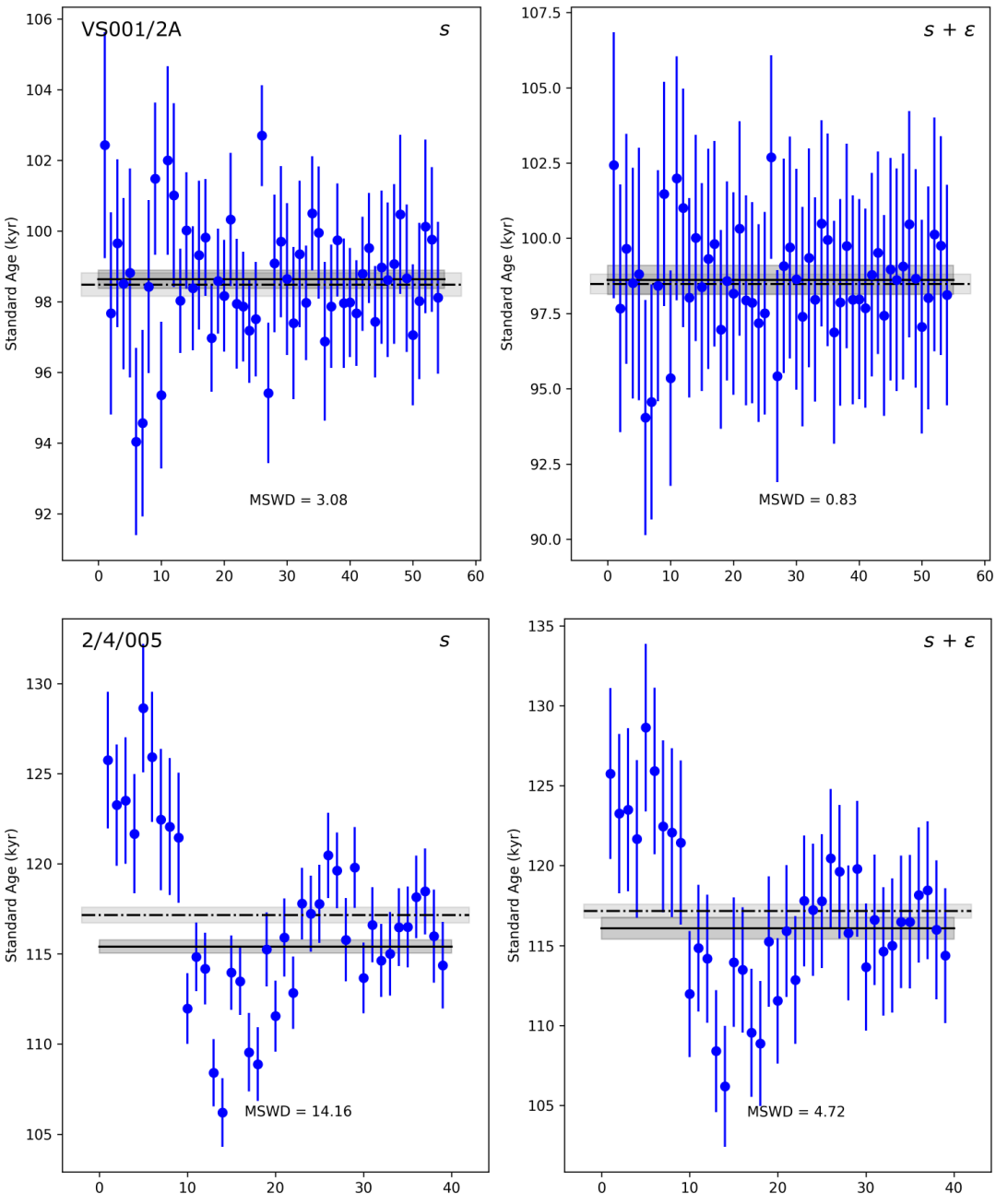

Fig. 3.15 Calculated ages before (left) and after (right) propagation of excess variance for primary (VS001/2A; top) and secondary (2/4/005; bottom) standards. The secondary standard (2/4/005) is interpreted to be isotopically heterogeneous, thus is less reproducible.

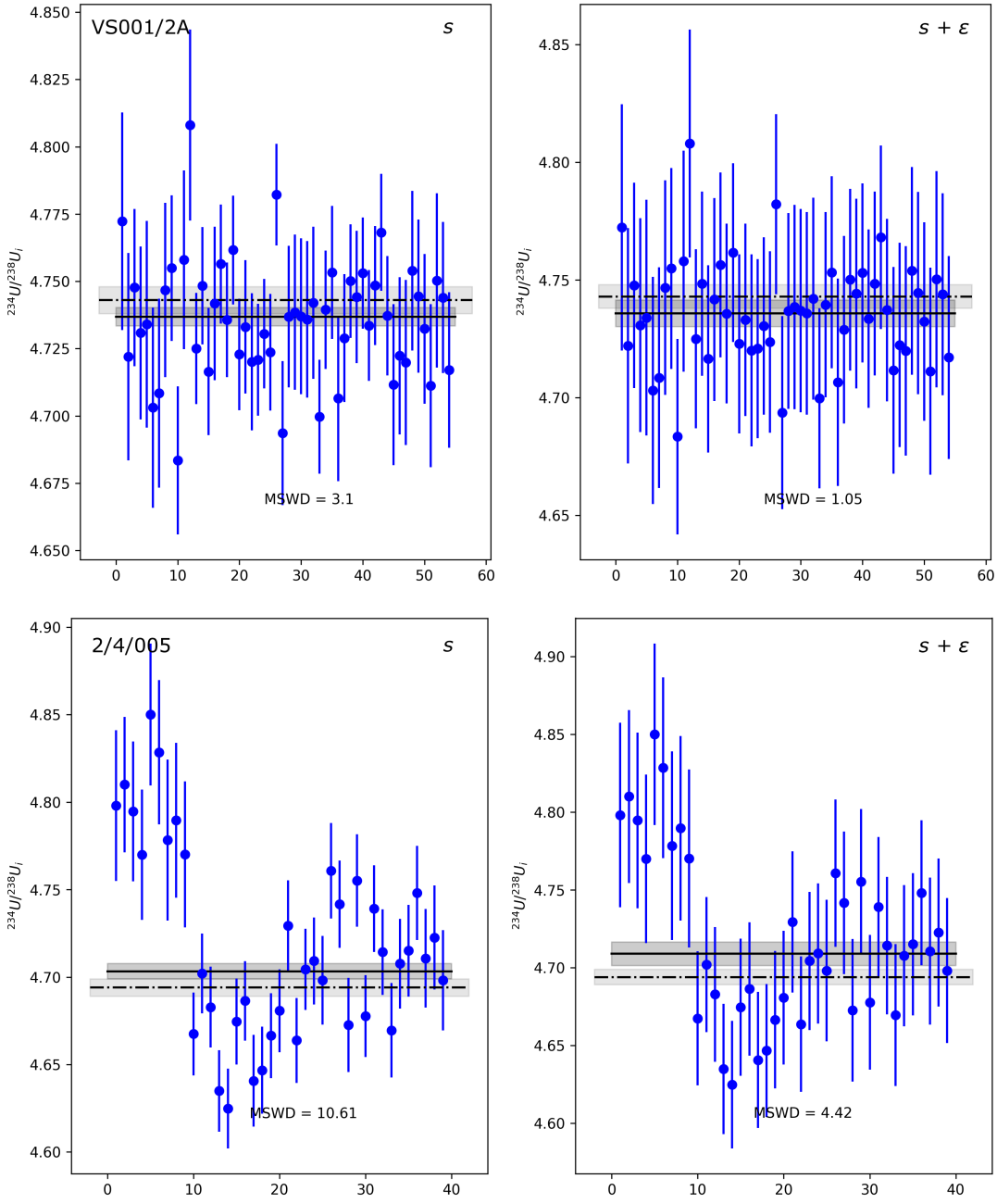

Fig. 3.16 Calculated $\delta^{234}U_i$ before (left) and after (right) propagation of excess variance for primary (VS001/2A; top) and secondary (2/4/005; bottom) standards. $\delta^{234}U_i$ offsets on the secondary standard are inherited from offset ages.

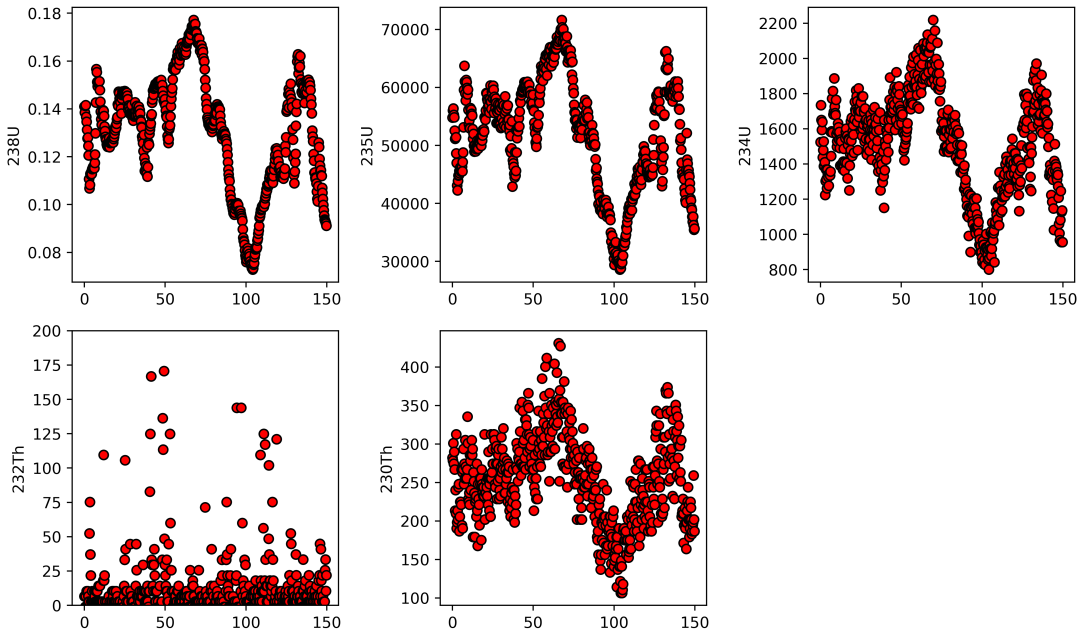

Fig. 3.17 Distribution of U and Th count rates on VS001/2A. A random distribution of ^{232}Th is seen with spikes occurring near grain/twin boundaries indicated by steps in U concentrations. Count rates of U can vary by 100% during the 0.8mm transect

Different interelement fractionation to carbonates makes glass analyses inappropriate for carbonate samples, and mixing sample matrices could cause instrumental instability similar to that shown for Sr isotope analyses.

Precision limits: Counting statistics, excess variance or heterogeneity

To investigate whether counting statistics, excess variance or heterogeneity act as a limitation on precision, analyses from the final analytical session were reprocessed at different lengths of collection. Instrumental drift was assumed to be best characterized on the longest collections, and therefore bracketing routines were not re-calculated. Figures 3.19 and 3.20 show the recalculated precision on ^{230}Th/^{238}U and ^{234}U/^{238}U for the three different standards. Unweighted (blue) and weighted (orange) MSWD values were calculated at each step (the top panels of the figures), but only the unweighted value is used for calculation of session excess variance. If the weighted and unweighted MSWD values diverge, then data point uncertainties show a wider range of values. The lower panels show the uncertainty size: the average data point uncertainty (2SE; green), external variability of the repeats (2σ; blue), and if MSWD > 1 the excess variance correction ($2\ \varepsilon_1$; orange).

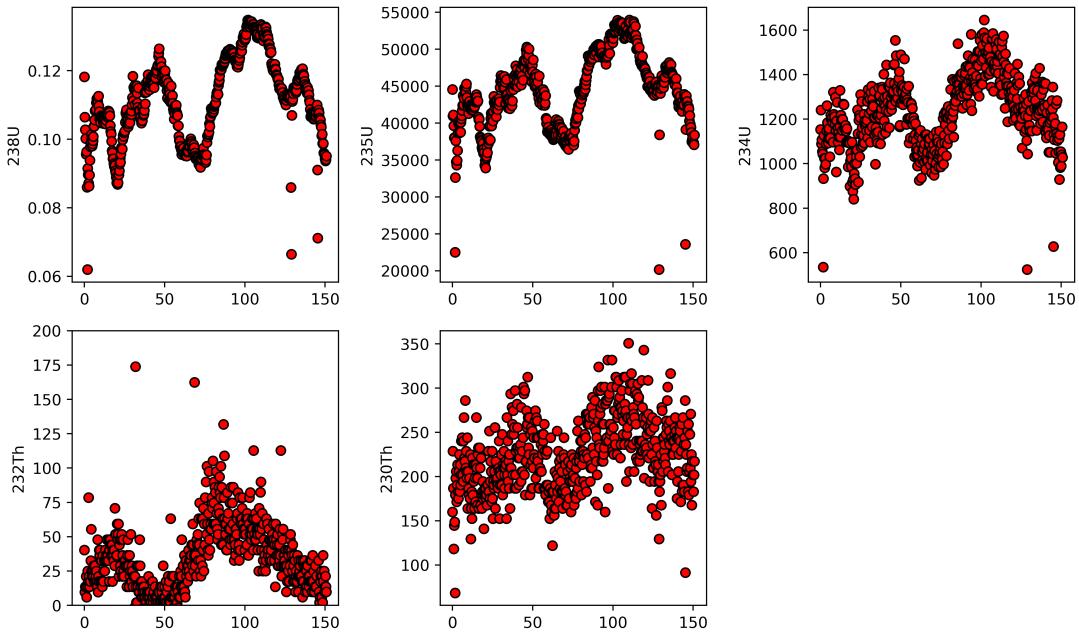

Fig. 3.18 Non random distribution of ^{232}Th suggests there may be initial ^{230}Th in the sample matrix, this is likely responsible for the offsets of the secondary standard during the first session

^{234}U/^{238}U ratios converge smoothly for all standards. The average data point error is approximately the same as external reproducibility, therefore a very small correction for excess variance is required. The external precision of POLY replicates levels off at ≈350 integrations, suggesting a limit on external reproducibility at lower count rates. The use of excess variance from VS001/2A in this case is therefore an underpropagation on this ratio.

However, ^{230}Th/^{238}U measurements on VS001/2A and 2/4/005 show rapid improvements in data point precision, but the external reproducibility converges more slowly. Data point uncertainty and external reproducibility on POLY both improve in step (as was the case for U-isotopes). The poorer convergence of two of the standard materials suggests that heterogeneity rather than instrument instability is responsible. The size of excess correction required for both of these materials is similar and therefore appropriate. However, it is an overpropagation on POLY. The treatment of uncertainties in materials at different count rates is therefore worth further consideration, though can simply be avoided by repeat measurements of a similar sample. This may be improved in future work by using other secular equilibrium isotope standards such as Boti.

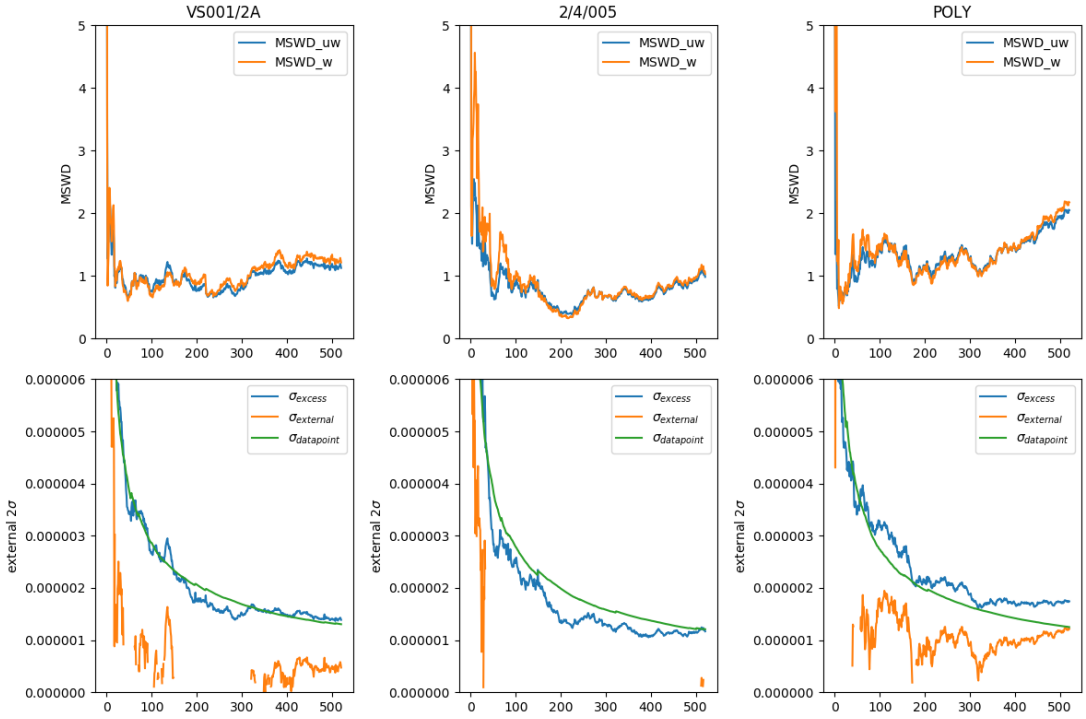

Fig. 3.19 Variation in MSWD (top) and precision (bottom) of $^{234}U/^{238}U$ with collection length (number of integrations) in carbonate standards VS001/2A, left; 2/4/005, middle; and POLY, right. Weighted and unweighted MSWD values are shown by orange and blue in the top panels. The bottom panel shows precision sizes, with analysis uncertainty is in green, external reproducibility in blue, and external excess variability in orange.

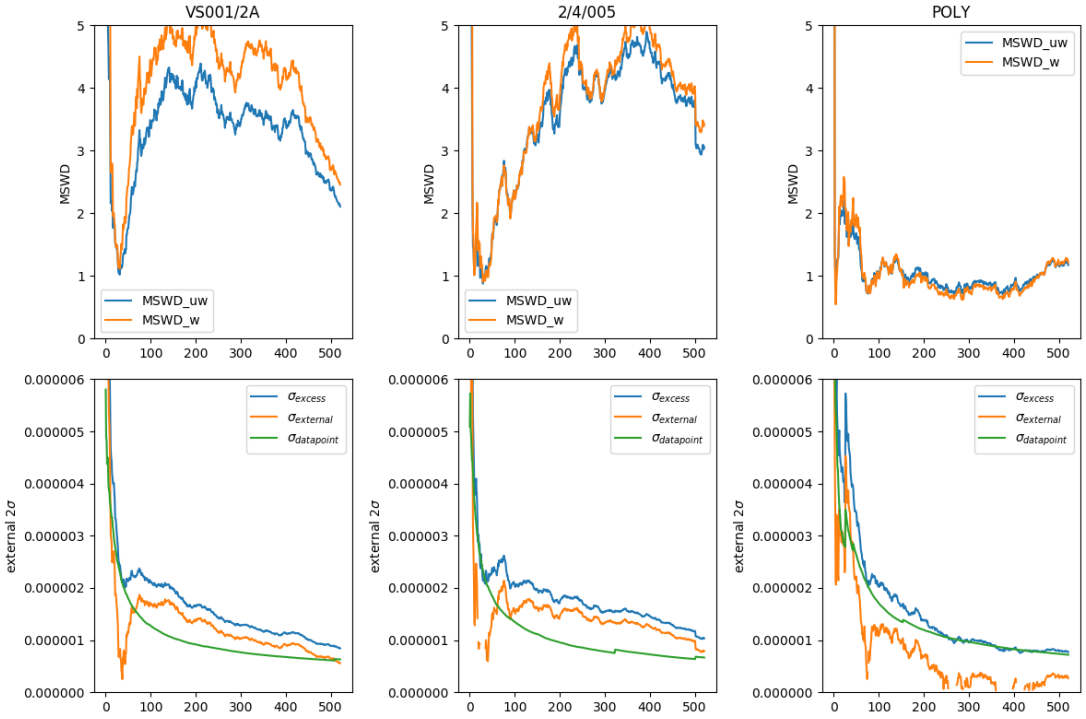

Fig. 3.20 Variation in MSWD and precision of $^{230}Th/^{238}U$ with collection length (number of integrations) in carbonate standards VS001/2A, left; 2/4/005, middle and POLY, right. Weighted and unweighted MSWD values are shown by orange and blue in the top panels. The bottom panel shows precision sizes, with analysis uncertainty is in green, external reproducibility in blue, and external excess variability in orange.

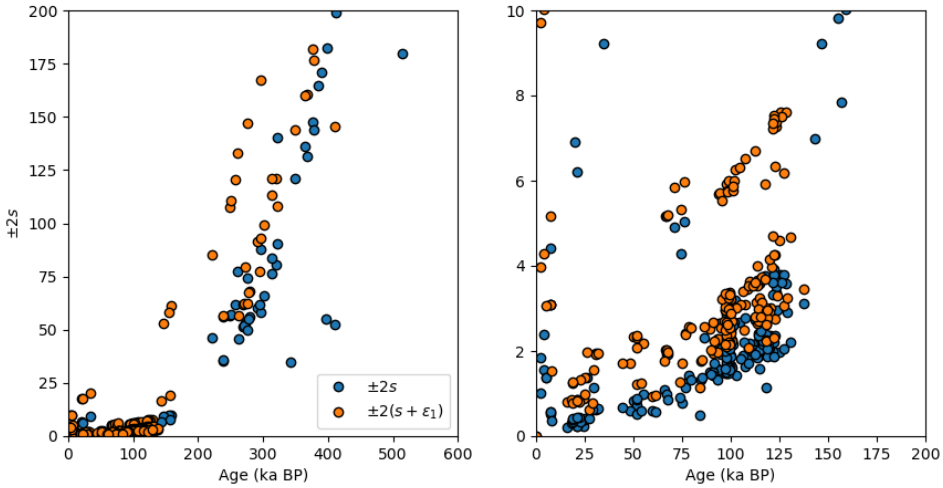

Fig. 3.21 Date precision on unknown samples. Blue points show data point errors only and orange points show propagation uncertainties. At ages younger than 130ka, sample precisions approximately behave in a linear fashion, samples older than this become uncertain very quickly.

High resolution studies: limitations on determining age-depth relationships

The major advantage of LA-ICP-MS sampling is the rapid acquisition of spatially high resolution data. Only Lin et al. (2017) have used LA-U-Th to investigate age-depth relationships. However, laser cell sizes limit the size of a sample which can be measured and the lower precision means that samples must be slow growing in order to have distinguishable ages. The ages on determined veins find linear extension rates in the range of 0.08-0.77mm/yr on Holocene age veins (Frery et al., 2016). Veins measured in this work extend more slowly, at around 0.02mm/yr. Layer counting on fast growing samples suggest preservation annual signals (discussed in chapter 4). Figure 3.21 shows the precision achieved on veins of different ages.

To fit in the laser cell at NIGL a sample must be <120-150mm long, therefore resolvable ages will only be possible on slower growing samples without cutting the sample further. As precision depends upon the age, a sample 120mm long, growing at a typical Green River extension rate ($\approx 24 \mu$m/yr; sample duration 5ka) will have resolvable ages if it is <22ka which may approach counting statistic limits. Older samples must grow more slowly to have resolvable ages. Multiple repeat analyses in different analytical sessions may improve precision, or running mean statistics can be used to reduce uncertainties.

3.3.5 Conclusions

Accurate and precise U-Th dating can be performed on small sample volumes (≈15µg), up to a quarter of the size of previous studies, due to shorter instrumental integration times. These short integration times reveal small scale heterogeneity, particularly related to the inclusion of detrital phases. These heterogeneous distributions cause detector 'trips', but this data can be easily excluded. Propagation of session excess variance gives comparable precision to previous studies, which omit this correction (and thus underestimate total uncertainties). This is necessary to account for instability caused by standard-sample bracketing. The limitation on both isotope ratios is counting statistics, but standard heterogeneity may be an additional limitation on ^{230}Th/^{238}U. This can arise through initial ^{230}Th in the carbonate lattice, as suggested by one of our standard materials. Additionally heterogeneity of up to ≈2% is identified by solution analysis on $\delta^{234}U_i$, whilst ages ±0.1ka suggest closed system behaviour. This may be sample specific, but is a relevant propagation on similar vein samples. Future sampling will determine if these heterogeneities exists in other carbonates, and hopefully allow better choice of standards.

The excess variation correction will propagate these heterogeneities. For ^{234}U/^{238}U the excess variance calculated on one standard is applicable to other materials, but for ^{230}Th/^{238}U the current standards are applicable to other Aragonite veins from Green River, but may be an overpropagation on more homogenous materials (i.e. the speleothem POLY). The calculated ages on Green River veins are more reproducible after excess variance correction. Vein samples of ≈125kyr age can be determined to ±5ka. If the method were to be applied to corals of the same age, the lower ^{230}Th/^{238}U value will limit precision to around ±12ka, similar to previous studies.

Chapter 4

Carbonates as records of palaeo-fluids

This chapter presents trace metal and isotope records from within a number of veins measured at Green River. These records can be used to infer the composition of palaeo-fluids and in turn information about historic fluid-rock interaction. First, carbonate mineral properties such as polymorphism, trace metal partitioning, stable isotope fractionation and the role of fluid mixing are discussed. This is followed by discussion of records at decreasing scales: fault scale, cm to mm scale and mm to μm scale. Increasing resolution reveals larger degrees of variability, arising from a combination of fluid mixing and Rayleigh fractionation. One sample on the anticline hinge at Little Grand preserves annual signals, suggesting a link to climate. Within this sample chemical trends display similarities to mixing during modern cold-water Geyser activity. The flux of fluids from the fault zone may vary due to a seasonal stress response.

4.1 Carbonate properties

This section reviews the relevant aspects concerning carbonate precipitation at Green River: polymorphism (why are the veins composed of aragonite and not calcite?) and trace metal partitioning in aragonite.

4.1.1 Controls on calcium carbonate polymorphism

Calcium carbonate ($CaCO_3$) has several polymorphs, of which aragonite and calcite are stable and amorphous calcium carbonate (ACC), vaterite, ikaiite and mono-hydrocalcite (MHC) are meta-stable. Each of the polymorphs belong to a different crystal class: aragonite is orthorhombic, calcite is trigonal and vaterite is hexagonal. This leads to differing

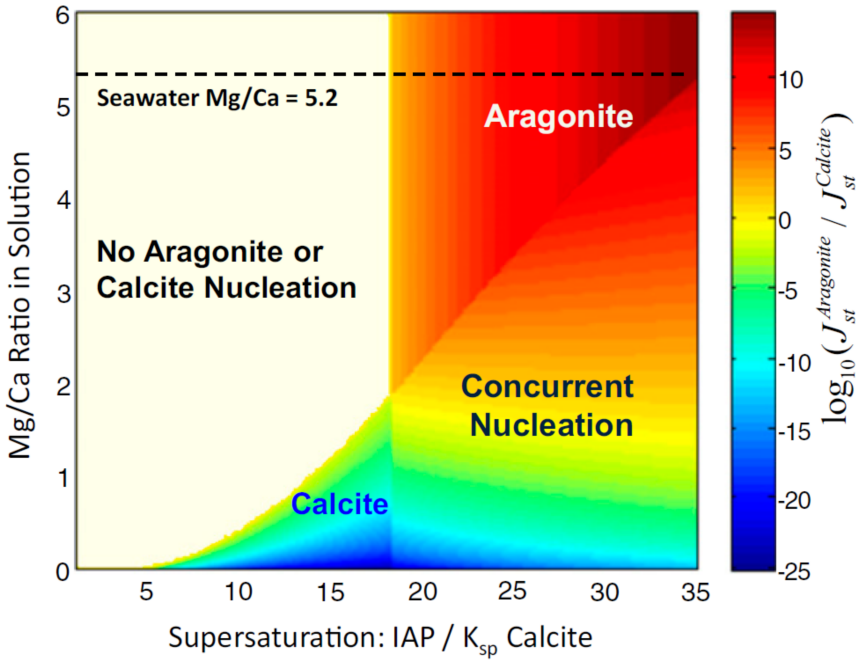

Fig. 4.1 Figure from Sun et al. (2015) showing a kinetic model for calcite and aragonite precipitation. Aragonite precipitation is favoured at higher carbonate oversaturation, and higher concentrations of calcite nucleation inhibitors (in this case Mg). Modern Green River fluids have Mg/Ca $\approx$ 0.5, but have Ca concentrations twice as high as modern seawater. The colourbar is the ratio of J, the surface energy ratio of nucleating aragonite and calcite. Negative values indicate preferential calcite nucleation (cool colours) and positive values indicate preferential aragonite nucleation (warm colours).

elemental partitioning behaviour, as the Ca_2^+ site differs between polymorphs. In general, aragonite is more stable than calcite at higher pressures and temperatures (Li et al., 2015), but at near surface conditions calcite is the thermodynamically stable phase. Nucleation kinetics determine which polymorph precipitates and can be influenced by temperature and concentrations of Mg, SO_4^-, U, Cr and PO_4^- (Blue et al., 2017; Buchardt et al., 1997; Davis et al., 2000; Fernández-Díaz et al., 2010; Hu et al., 2015; Kitano et al., 1975; Nielsen and DePaolo, 2013; Nielsen et al., 2016; Sánchez-Pastor and Gigler, 2011; Sun et al., 2015). For example, Mg impurities in calcite (high-Mg calcite) causes higher solubility than pure calcite, and Mg also disrupts the hydration sphere of nucleating calcite which inhibits further crystal growth (figure 4.1) (Busenberg and Niel Plummer, 1989; Sun et al., 2015). The precipitation pathway may proceed via metastable precursor phases which invert to more stable phases over time (Besselink et al., 2017; Blue et al., 2017; Demény et al., 2016; Jacob et al., 2017; Kawano et al., 2009).

High Mg/Ca and high fluid oversaturation is generally considered a necessity for aragonite precipitation (Sun et al., 2015). However, the Mg/Ca in modern fluids is ≈ 0.5, which is below the threshold of 2 that the model in Sun et al. (2015) suggests is the minimum limit for only aragonite precipitation. This suggests coupled precipitation of calcite and aragonite occurs regardless of nucleation rate, as shown in figure 4.1. However, calcite is very rarely observed at Green River, suggesting the nucleation control in these fluids is not Mg/Ca. Other ratios such as $SO_4{}^-$/Ca and Na/Ca are lower than modern seawater, therefore ionic strength which is about twice modern seawater may be responsible. Other compounds such as amino acids have also been used to promote aragonite precipitation (Xie et al., 2005) but such organic compounds should be irrelevant in these crustal fluids.

4.1.2 Trace metal partitioning

Trace metal partitioning can be described through a partition (or distribution) coefficient K_D, as given in equation 4.1, where M denotes a chemical species or element:

$$K_{\frac{M}{Ca}} = \frac{\left(\frac{M}{Ca}\right)_{solid}}{\left(\frac{M}{Ca}\right)_{fluid}} \tag{4.1}$$

These coefficients have been shown to depend upon temperature, growth rate, and concentration. If fluid concentrations are independently constrained, these governing variables can be solved for. The mechanism of incorporation can vary, as elements can either be incorporated directly into the Ca^{II} or $CO_3{}^{II-}$ site of the $CaCO_3$ lattice or at defects. Most results are therefore based upon observations from either organic cultures or inorganic precipitation experiments. The chemistry of each element, the carbonate polymorph, and the crystallisation pathway are important in determining K_D. Alkali group metals, such as Sr^{2+} and Ba^{2+} can substitute directly into Ca^{2+} sites, whilst others may be incorporated at defects in the chemical lattice. The density of defect sites may (but not necessarily) correlate with growth rate or solution chemistry. The speciation of each element in solution may dictate its availability at the growing crystal surface, which is limited by growth rate and diffusion (De Yoreo et al., 2015; Nielsen et al., 2013, 2012; Smeets et al., 2017). Coupled substitution with Na may be required to satisfy charge balance for elements such as REE, which are trivalent (Voigt et al., 2017). This mechanism is important, but not predominant as REE can be incorporated without the presence Na (Gabitov et al., 2017). Competition between the group I metals Na, K, Rb and Li has been observed (Okumura and Kitano, 1986), where K, Rb and Li are less compatible in the presence of Na. It is therefore difficult to generalise

element behaviour across a wide range of fluid compositions. U distributions in calcite have been shown to depend upon crystal growth faces due to adsorption properties (Reeder et al., 2001, 2000). No study has shown this for aragonite, but it may be hinted at by the U-distributions across twin faces presented along laminations in chapter 3. Presumably, such a process also influences isotopic fractionation. In organic carbonates (foraminifera), the carbonate ion concentration has been shown to impact stable isotope fractionation (Spero et al., 1997; Ziveri et al., 2012), and incorporation of trace metals (Rathmann and Kuhnert, 2008) but this is ultimately a function of alkalinity and pH. This is a function of vital effects and hasn't been shown in inorganic experiments. Finally, physical or fluid inclusions may inform about physical growth mechanisms or the parent fluid chemistry; they also represent a potential cause of bias during sampling.

Table 4.1 gives values of K_D measured during inorganic aragonite precipitation experiments, and where such data is not available inferred values from biomineralised aragonite (though 'vital effects' from internal cellular mechanisms limit comparability). Most of these precipitation experiments occur at intermediate pH values (7-9) and due to chemical speciation may not remain true at lower pH typical of CO_2-rich fluids (5-6.5). The large range of K_D values for some elements suggest incorporation mechanisms are a complex combination of processes. These partition coefficients are a general indicator of chemical behaviour but are limited in their application to these samples because of differing fluid chemistry, notably lower pH and higher/variable ionic strength.

Temperature and growth rate dependent partitioning

Experimental determinations of partition coefficients reveal temperature, growth rate and concentration dependence. However, in some cases it is not possible to deconvolve these differing effects. Growth rate and temperature probably show coupling through variation in saturation index; at higher temperatures carbonate is more oversaturated and thus faster growth is likely. Similarly fluid concentrations also influence growth rate, where higher M/Ca ratios reduce growth rate, through nucleation controls or chemical adsorption.

Rayleigh fractionation

In order to interpret trace elements concentrations it is necessary to model fluid evolution in an evolving vein system. This can be approximated by Rayleigh fractionation (or fractional distillation/crystallisation), where continuous growth of aragonite modifies M/Ca ratios. Fractional crystallisation can be described by equation 4.2:

Table 4.1 Partition coefficients (K_d) between solution and inorganic aragonite

Element	K_d range	Notes
Sr	0.85-1.25	Growth rate and temperature dependence AlKhatib and Eisenhauer (2016a); Dietzel et al. (2004); Gaetani and Cohen (2006); Gagnon et al. (2007); Kinsman and Holland (1969)
Ba	0.6-3	Temperature dependence Dietzel et al. (2004); Gaetani and Cohen (2006)
Mg	0.0005 - 0.015	Positive Temperature and growth rate dependence Gabitov et al. (2008); Gaetani and Cohen (2006); Gagnon et al. (2007)
U	0.15 - 9.8	Gabitov et al. (2008); Meece and Benninger (1993)
REE(Y)	$10^{1.4}$ - $10^{2.8}$	Inverse growth rate or concentration dependence. Approximately MREE>LREE>HREE according to lattice strain model Blundy and Wood (1994); Terakado and Masuda (1988); Voigt et al. (2017)[a]
Na	>350?[b]	Aragonitic corals suggest > 350 assuming average seawater Itsuguchi et al. (2010); inorganic precipitation by White (1977). Required for charge balance of other elements Voigt et al. (2017) Growth rate dependent Busenberg and Niel Plummer (1985) Incorporated at defect sites in calcite Ishikawa and Ichikuni (1984, 1986) but substitute for Ca in aragonite, increasing Na decreases K, Rb, Li Okumura and Kitano (1986)
K	>150?[b]	Aragonitic corals suggest > 150 assuming average seawater Mitsuguchi and Kawakami (2012); inorganic precipitation by White (1977)
Fe	?	
Mn	0.86	Raiswell and Brimblecombe (1977)
Zn	?	
Al	?	
V	?	
Zr	?	
Li	0.001-0.003	Marriott et al. (2004) Similar to Mg Gabitov et al. (2011) Inverse temperature dependence in corals Hathorne et al. (2013)
B	0.0016 - 0.981	Allison and Finch (2010); Hemming et al. (1995)

[a] Calcite and aragonite are 2.5-10 and 2.5-5 respectively (Terakado and Masuda, 1988). Whilst Voigt et al. (2017) measure calcite, it is reasonable to assume similar behaviour

[b] Inferred from biogenic aragonite, cannot account for vital effects

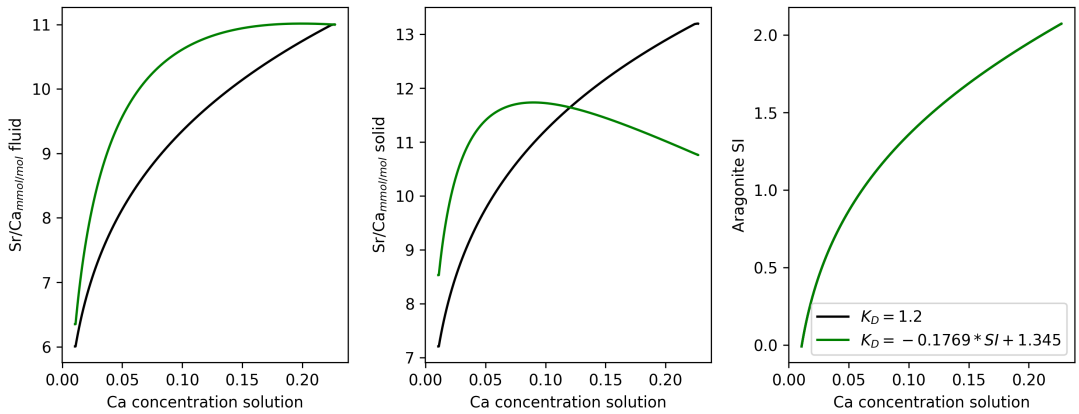

Fig. 4.2 Rayleigh fractionation curve in black using a constant partition coefficient of 1.2, and in green using a saturation index dependent partition coefficient calculated from AlKhatib and Eisenhauer (2016a). This relationship is assumed to approximate the growth rate relationship which they observe. Figure panels from left to right show: fluid composition, solid composition and Aragonite saturation index. Fluid compositions are calculated using an iterative coupling of PHREEQC calculations, where target Aragonite saturation is decreased by 0.01 unit per step.

$$C_L = C_0 F^{(K_D - 1)} \tag{4.2}$$

where C_0 is the initial ratio of the fluid, C_L is the ratio of fluid at a given fraction of the reservoir remaining, F and K_D is the partition coefficient. During the formation of a single lamination of a vein, a volume of fluid will undergo Rayleigh fractionation as carbonate is formed. This signal is often termed prior carbonate precipitation (PCP). Compatible elements, those with $K_D > 1$, will show a depletion in C_L as F decreases; incompatible elements, those with $K_D < 1$, will show increasing fluid concentrations.

These equations can also be solved numerically using a program such as PHREEQC, allowing incremental volumes of carbonate to precipitate. Assuming that growth rate can be approximated by saturation index ($K_D = f(SI)$), it is then possible to approximate observed growth rate dependent fractionation effects during fractional crystallisation. In such a model F from equation 4.2 represents the range from initial concentration to equilibrium concentration (SI=0). A comparison of these for Sr/Ca ratios is shown in figure 4.2.

This comparison shows that growth rate dependent effects observed in aragonite by AlKhatib and Eisenhauer (2016a) can become significant when magnified by fractional crystallisation processes. This is because at lower saturation index Sr is more compatible, than at higher saturation indexes. The calibrated data extends from a saturation index of

0.65 to 2.1, so the final stages of Rayleigh fractionation lie outside of the calibration. An R^2 of 0.61 suggests that the relationship reasonably explains the variance within the data. Unfortunately, other than Sr and Mg no other elements have had growth rate dependent partition coefficients determined in aragonite.

4.1.3 Stable isotope fractionation

Stable isotope fractionation can also be described by a fractional distillation equation by substituting (α) for the partition coefficient (K_D) in equation 4.2, and where C_0 and C_L are the respective isotope ratios. This style of modelling was performed by Kampman et al. (2012), and shows that isotopic variability is accounted for by CO_2 degassing with aragonite precipitation. The much heavier values for $\delta^{18}O$ and $\delta^{18}O$ in the veins compared to fluid samples can be explained by equilibrium fractionation (Kim et al., 2007). A small number of high outliers in the Kampman et al. (2012) study were used to suggest CO_2 degassing without carbonate precipitation, and most samples lie between these two processes, shown by the gradients in figure 4.3. Isotopic fractionation effects are known to depend upon speciation kinetics; particularly $\delta^{18}O$ which can show more sluggish equilibration between H_2O and C-species. Equilibration times for $\delta^{13}C$ depend upon pH, but at low pH should be <1 minute (Uchikawa and Zeebe, 2012; Watkins et al., 2013). Faster growth rates were found to decrease the size of $\delta^{18}O$ fractionation, with aragonite values more similar to $CO_3{}^{2-}$ values (Gabitov, 2013). These results fit a general entrapment model, where a depleted/enriched layer is inorporated into the growing crystal at very fast growth rates (0.001-10nm/s; 86μm/day) (DePaolo, 2011; Dietzel et al., 2009; Gabitov, 2013; Gabitov et al., 2012; Watson, 1996, 2004). These rates are much faster than any average growth rates observed at Green River which are up to 200μm/year.

4.1.4 Vein formation

Fluids in the Navajo at Little Grand are CO_2 saturated (Kampman et al., 2013b), and as they decompress solubility decreases (Dubacq et al., 2013). CO_2 degassing therefore drives precipitation, through the reaction $Ca_2{}^{+} + 2\,HCO_3{}^{-} \longrightarrow CO_2(g) + H_2O + CaCO_3$ as $CO_2(g)$ is removed. This reaction is coupled to pH and alkalinity through carbonate speciation in the solution. It has been suggested by Gratier et al. (2012) that due to a overstep in gas nucleation, degassing is sudden and violent enough to induce fractures in which the veins form. Rapid change in fluid chemistry would favour fast precipitation rates, favouring aragonite precipitation. These are then held open by carbonate crystalisation. No robust

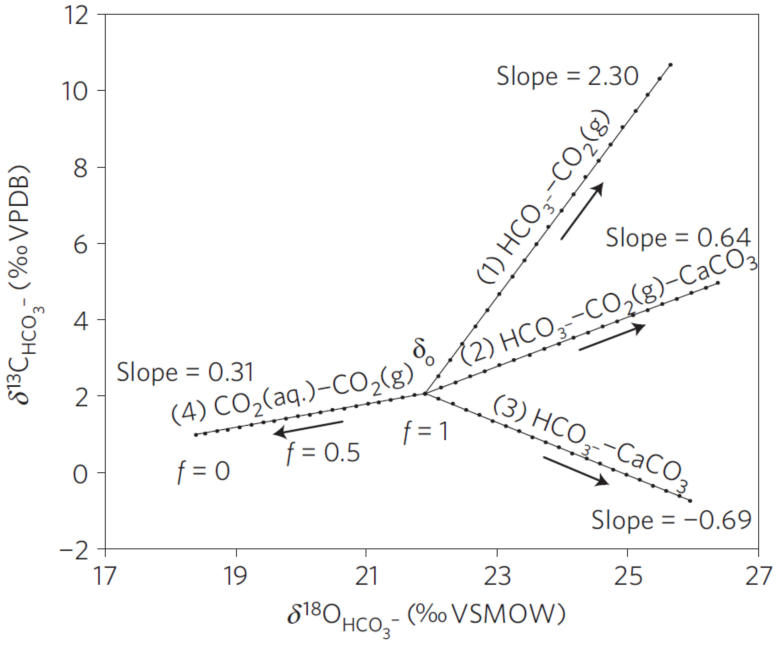

Fig. 4.3 Rayleigh fractionation trends predicted for different CO_2 degassing mechanisms from (Kampman et al., 2012)

geomechanical evidence has been provided for this, but the veins can be observed exploiting fractures parrallel to the fault trace or bedding planes. A schematic of a vein can be seen in figure 4.4.

4.1.5 Fluid end-members and mixing

Fluid mixing has been inferred from spring fluids and from downhole fluids sampled during drilling in 2012 (Kampman et al., 2009, 2014b). Prior to collection of downhole fluids, mixing has been interpreted to occur between reservoir fluids and brines which originate from deeper formations (>1.5km). Mixing at this scale has been inferred from hydrological measurements of δ^{18}O and δD. Spangler et al. (1996) analysed fluid samples from the Navajo in South East Utah which have δ^{18}O values between ≈ -18‰ and -13‰. All samples lie on the local meteoric water line (LMWL) and the most negative values reflect local snow melt. At Green River, the spring samples in Kampman et al. (2009) are slightly offset from the LMWL, showing a mixing trend towards Ismay brine compositions. This end-member is an oil field brine sampled from the Paradox formation, with a δ^{18}O value ≈ 2‰. The mixing fraction of this brine in spring samples is between 0-10% with most samples around 4-6% (calculated using either $^{87}Sr/^{86}Sr$, δ^{18}O, δD or Na, Cl, I, Br concentrations (Kampman et al., 2009) and see appendix B). Mixing trends in time series at Crystal Geyser show variation

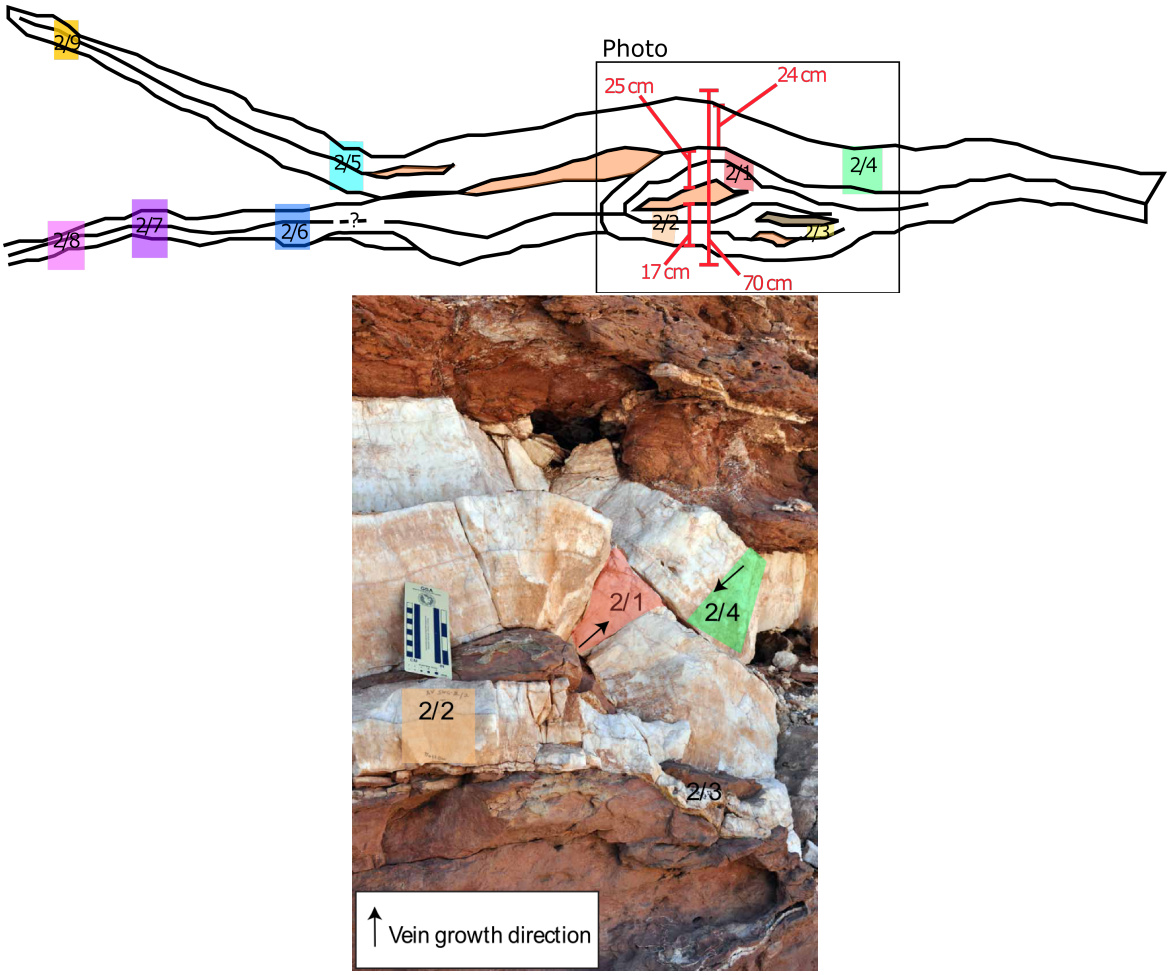

Fig. 4.4 Vein geometry on the anticline hinge at Salt Wash. Sampled by Niko Kampman and Lily Horne, a masters student at Utah State University. Presented at GSA 2013 (Horne et al., 2013). Samples 2/1, 2/2 and 2/4 were analysed in Cambridge. Coarse crystaline textures towards the centre of the veins suggest growth into open space.

between a fault zone brine and a 'meteoric' fluid from the Entrada formation (Heath et al., 2009; Kampman et al., 2014b). This is also observable in $^{87}Sr/^{86}Sr$ and in trace metals.

This simple binary approach to fluid mixing was re-interpreted when downhole fluids were sampled during drilling (Kampman et al., 2014b). Local end-members were then defined: a fault zone brine, which can be explained as a binary mix of meteoric fluid and Ismay brine; meteoric water in the Entrada which appears to have reacted with haematite; and fluids from the Carmel formation. Downcore fluids in the Navajo lie on a mixing line between the Carmel formation and fault zone brines, whilst Geyser fluids continue to lie between fault zone brines and Entrada fluids. During Geyser eruptions, when the fraction of fluids from the Entrada increases ratios such as Fe/Ca, Mn/Ca, Sr/Ca and Mg/Ca increase. The figures from Kampman et al. (2014b) showing these mixing trends are included in appendix B.

Secondary mineral phases recovered from the drillcore; carbonate cements and sulphates in fractures show a similar range of $\delta^{18}O$ as meteoric samples, but are offset from the LMWL by equilibrium fractionation factors and by prior precipitation (Chen et al., 2016a; Kim et al., 2007; Maskell et al., 2015).

4.2 Fault scale records

Low resolution records along Salt Wash through the last 140ka are shown in figure 4.5 (Kampman et al., 2012). Each data point is a single point on a vein sample, and therefore represents both the variation between sample locations and the variation in time. A range of proxies were used to argue that the flux of CO_2-rich brines varies across glacial interglacial cycles, recording variation in weathering of silicate minerals. The next chapter goes onto show that most variability in $^{87}Sr/^{86}Sr$ and $\delta^{234}U$ can be explained by evolution along a single fluid flow path. Not discussed in the paper are high Al/Ca and Mg/Ca on the largest Ba/Ca peaks, which may indicate impure carbonate rather than silicate dissolution.

Given the wide range of stable isotope values for recharging aquifer fluids, the narrow range of values observed in carbonates is surprising (Dockrill, 2006; Frery et al., 2016; Kampman et al., 2012). Additionally the variability in stable isotope ratios ($\delta^{18}O$ and $\delta^{13}C$) along the fault is only slightly larger than the variability within individual samples as will be discussed in the next section. The volumetric estimates of carbonate volume appear to remain robust, and high Holocene fluxes are confirmed by Frery et al. (2015), though vein growth rate is not a particularly robust proxy given the 3d geometry of vein systems. Burnside et al. (2013) use volumetric estimates of carbonate volume to show that fluid fluxes are larger at Little Grand than Salt Wash, and that fault-hosted flow is 13 times larger than

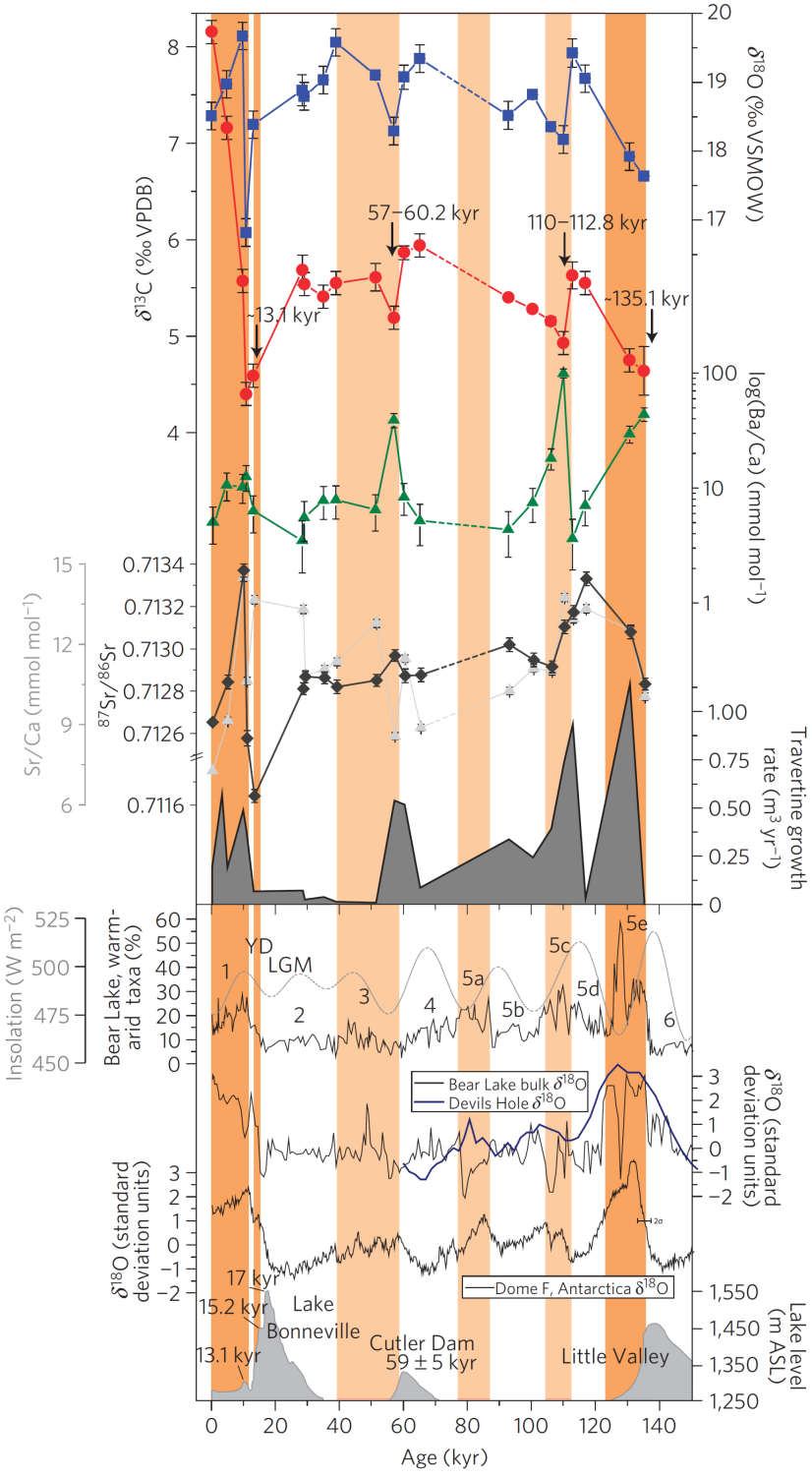

Fig. 4.5 Low resolution multi-vein record from (Kampman et al., 2012). Decreases in $\delta^{13}C$ and $\delta^{18}O$, combined with higher Ba/Ca and lower $^{87}Sr/^{86}Sr$ infer leaks of CO_2 saturated brine occur due to changes in crustal stresses. In this case, these stresses are caused by the unloading of glacial lakes, indicated at the bottom of the figure.

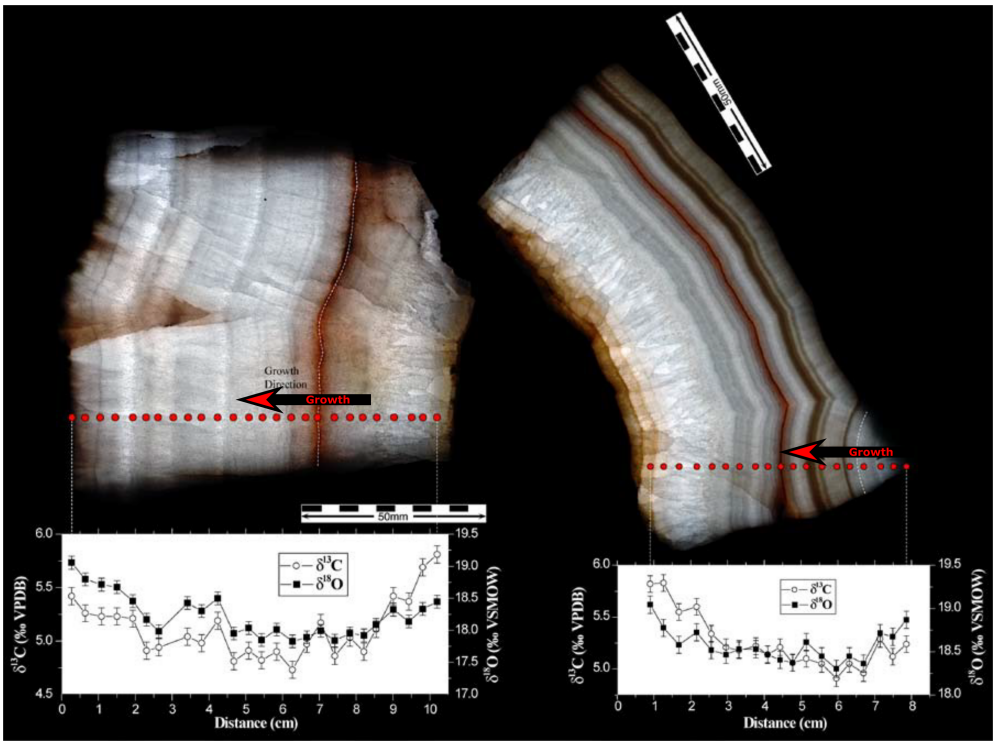

Fig. 4.6 Samples VS001/1A and VS001/2A modified from supplementary material of (Kampman et al., 2012). The variability of stable isotopes within veins is only marginally smaller than the variability between veins. The increase in isotope values is due to prior carbonate precipitation (PCP), but decreasing values at the beginning suggest either greater PCP or fluid mixing

modern flow from the unconfined borehole at Crystal Geyser. Similar estimates were used in Kampman et al. (2012) to calculate travertine growth rates; larger growth rates following glacial terminations form the basis of their climatic forcing argument.

4.3 cm to mm scale records

This section describes records preserved within the veins, starting with presenting other published records and moving onto new data.

4.3.1 Previously published records: stable isotopes

The stable isotope records in Kampman et al. (2012) were shown to follow a Rayleigh fractionation trend for carbonate precipitation with CO_2 degassing (figures 4.3 and 4.6). Since then, other records of $\delta^{18}O$ and $\delta^{13}C$ have been produced (Frery et al., 2016, 2015).

These show the same coupling of δ^{18}O and δ^{13}C (with a gradient $\approx$0.7), but with time isotope ratios decrease rather than increase. This can be observed in figure 4.6 at the beginning of sample VS001/1A and VS001/2A. There are two possibilities for this: less carbonate precipitation occurs along the flow path before this part of the vein (larger F in equation 4.2), or fluid mixing occurs. Both processes should be detectable using trace metal trends.

4.3.2 New records: Trace metals, stable and radiogenic isotopes

To distinguish Rayleigh or mixing trends, this section presents new trace metal and stable isotope results.

Analysis methods

Veins were physically subsampled by hand drill, using a tungsten-carbide end-mill bit. Slow speeds were used to ensure that no contamination from drill bits occurred (a problem using cheap diamond coated cutting tools), and to avoid thermal resetting of samples (a potential issue for clumped isotope analyses, which were considered for temperature reconstruction). Three holes of 1mm were made to allow sufficient sample for U-Th dating, Sr isotopes, stable isotopes and major/trace metals (100-150mg of carbonate), but much smaller volumes could be used. The powder was stored in pre-cleaned 1.5ml centrifuge tubes, and was physically homogenised during drilling.

Major metals were measured by ICP-AES (Varian Vista) using ratio bracketing for Sr/Ca, Mg/Ca and Na/Ca (Villiers et al., 2002). Other trace metals (Al, Fe, Mn) were measured using concentration bracketing. Trace metals (Mg, Li, B and Cd) were measured on the Element XR. All solutions were measured at 100ppm Ca on the Vista and 20ppm Ca on the Element. External reproducibility on all elements was assessed using repeat measurements of an internal standard created from vein VS001/1A, and are shown as 2σ uncertainty ranges in all figures.

U-Th dates on samples were determined at NIGL, and were presented in chapter 3. Measurements were performed by addition of a mixed single spike ^{229}Th and ^{233}U, ion chromatography to separate U and Th fractions, and analysis on a NEPTUNE+ at NIGL. There are hints that δ^{238}U may be non-zero for these samples. Sr isotopes were measured by similar solution methods in Cambridge, and analysed by TIMS (VG-sector 54). Laser ablation methods were discussed in Chapter 3.

Stable isotopes (δ^{13}C and δ^{18}O) were measured by reacting 250μg of carbonate with orthophosphoric acid and analysed using a Thermo Gasbench and Thermo MAT 253. Car-

bonates are measured relative to VPDB, and δ^{18}O converted to SMOW using the equation $SMOW = 1.03092 * VPDB + 30.92$. Precision is better than $\pm 0.08‰$ and $\pm 0.10‰$ respectively.

The veins 2/1, 2/2 and 2/4, shown in figures 4.4 and 4.9, were sampled in this manner. Analyses were presented by Horne et al. (2013) but trace metal trends were erratic ('spikes' on Al/Ca, Ba/Ca and Mg/Ca) so are presumed contaminated during subsampling and are not discussed further.

Vein spatial trends

Figure 4.7 shows the trends in metals and isotopes in the three veins against distance from the vein centre; figures 4.4 and 4.9 shows the veins themselves. The trends in 2/1 and 2/4 are identical to one another, and 2/2 is identical to the trends in the earlier parts of 2/1 and 2/4. Vein 2/2 is composed of two veins growing in from the top and bottom sides of the fracture. The coarse crystal structures of all the samples suggest that growth occurs within a fluid filled cavity. Vein 2/1 shows evidence of a dissolution surface 3-4cm from the centre of the vein, suggesting either transient flow of carbonate undersaturated fluids during the growth period, or pressure dissolution caused by contact with the upper vein. However, this event appears brief as it is not observed in trace metal trends. Structures on the laminations suggest pulsed growth increments, with crysals often truncating forming smooth flat surfaces.

Towards the centre of the veins (i.e. more recently) stable isotope ratios increase, in keeping with Rayleigh trends. However, all trace metals show lower concentrations, whereas incompatible elements such as Li, B, and Mg (table 4.1) would increase in a fractional crystallisation trend. This suggests that fluid mixing is responsible for the variability. There is, however, an offset of δ^{18}O between veins 2/1 and 2/4, with the upper vein showing $0.5‰$ higher values, hinting at kinetic control. Ba/Ca are much lower than anything in Kampman et al. (2012). Decreases in all metal/Ca ratios mean that this fluid is not constrained by mixing of Entrada, Carmel fluids with fault brines from Kampman et al. (2014b), nor mixing with meteoric waters. Either a process must add only Ca to the fluids without other elements, or a process removes everything else. Additionally this source must have heavier δ^{13}C and δ^{18}O. Sr isotopes (figure 4.8) show no significant variability across this sample, but there is a discernible variability in U isotopes that suggest variable fluid residence times or reaction with U-bearing phases.

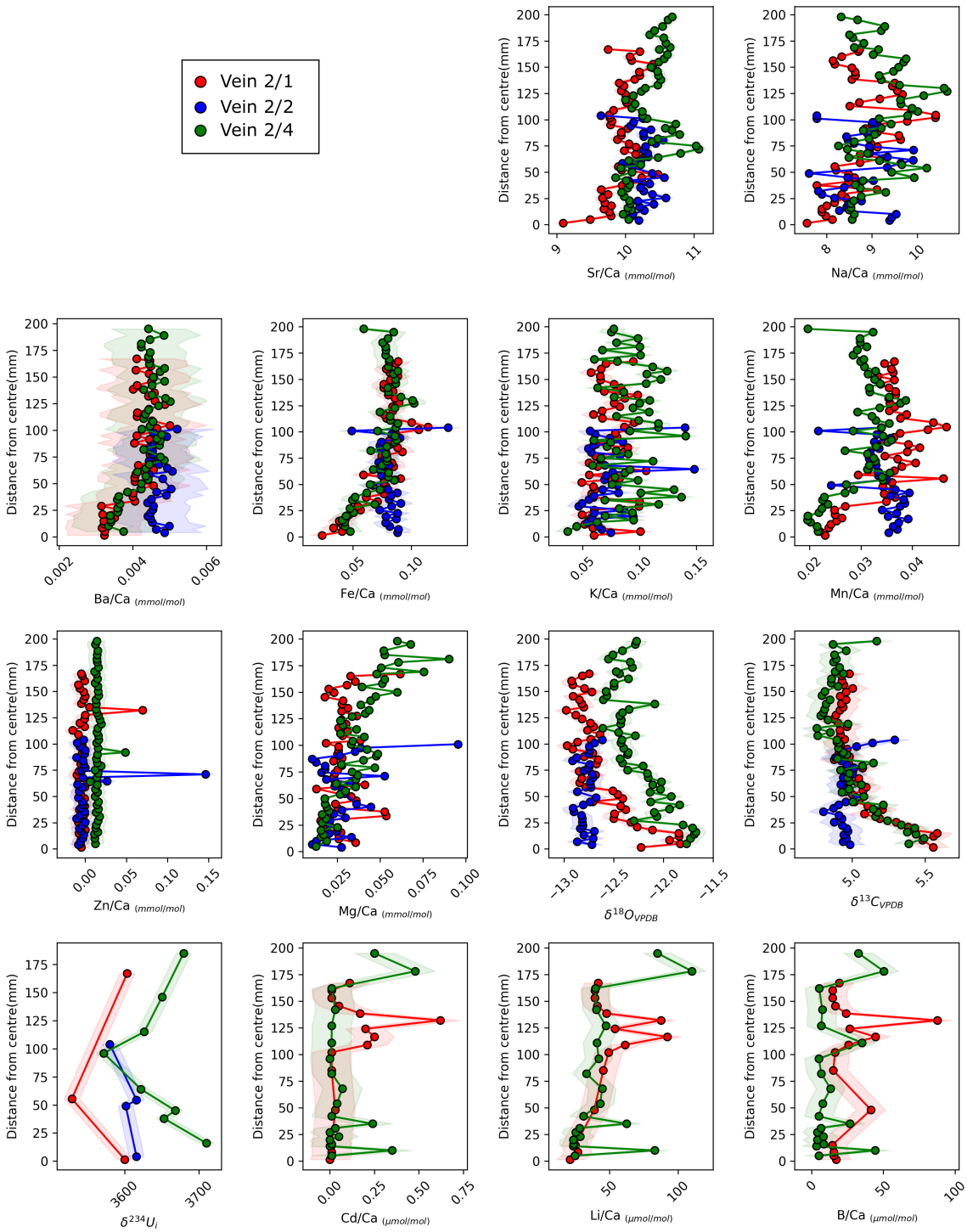

Fig. 4.7 Trace metal data on veins, distance from centre of vein (2/1 and 2/4) and across from the base of the vein (2/2). Units for trace metals are mmol/mol, with the exception of Li and B which are μmol/mol.

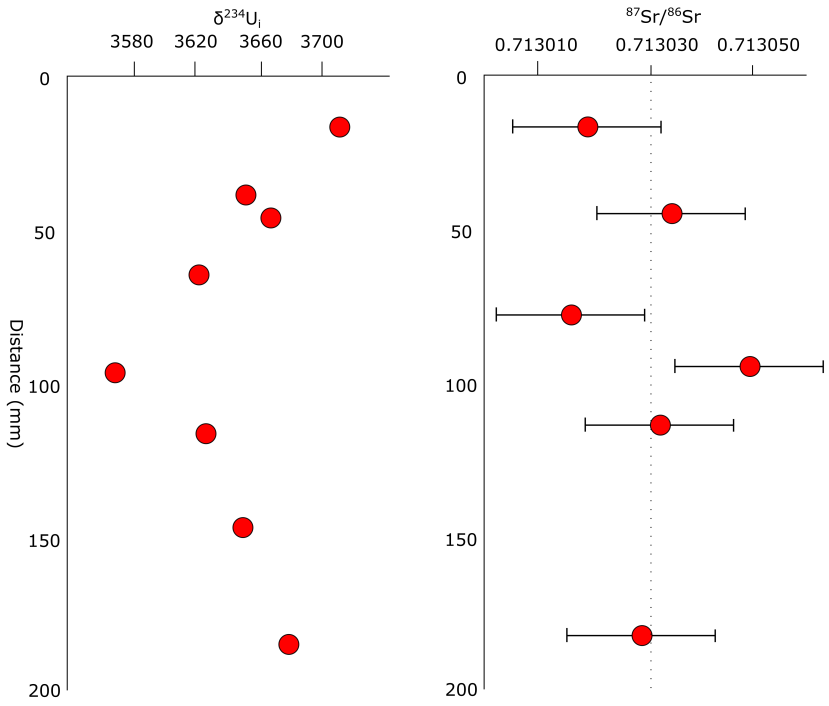

Fig. 4.8 Isotope composition of vein 2/4. Uncertainties are 2σ, and U isotope uncertainty is often smaller than data points.

Vein temporal trends

Ages on the veins allow for the trends to expressed as a function of time and allow estimates of crystal growth rates. U-Th dates for the veins are shown in figure 4.9 with approximate matching of growth layers inferred from age-depth models. Given the symmetry of trace metal and stable isotope records within 2/1 and 2/4 it is odd that their ages are offset by ≈2kyr. However, each sample represents 5kyr of growth at ≈115-120kyr with no age inversions. Sample 2/2 which comprises an upper and lower vein pair shows a similar offset between upper and lower veins. Repeat analyses on the younger section of 2/4(/005) were mentioned in chapter 3, when it was trialled as a standard. These repeats confirm a constant age, but show isotope heterogeneity. Laser transects suggest that initial ^{230}Th could be present in some regions. Initial Th gives an older age, in turn increasing $\delta^{234}U_i$ on these samples as observed. This is not open system behaviour, but can account for a systematic offset.

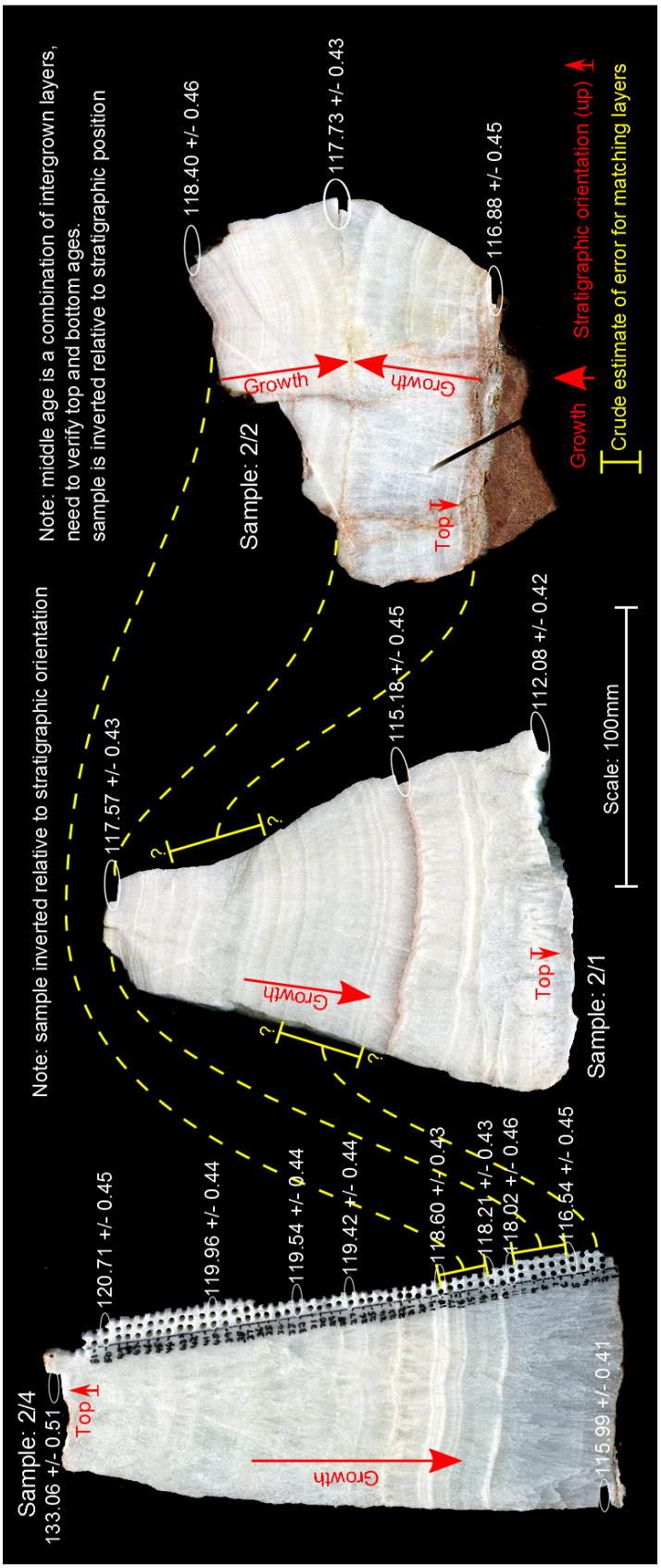

Fig. 4.9 Apparent stratigraphy of vein system on Salt Wash anticline based upon ages. The top of 2/1 can be seen to have some slightly disrupted laminations which may result from either dissolution of the solid, or contact with the upper part of the vein. Assuming accurate ages, the yellow lines match approximate stratigraphic layers, however dates may be offset due to initial Th or open system behaviour, as trace metal and field observations suggest that these are 'partners'.

Assuming robust relative ages, age depth profiles can constructed using software such as OxCal, Stalage or COPRA (Breitenbach et al., 2012; Scholz and Hoffmann, 2011). COPRA is used, which runs a Monte-Carlo simulation fitting smoothed curves through the ages, rejecting simulations which show age inversions. Sample 2/4 gives the age-depth relationship shown in figure 4.10. A decrease in growth rate occurs across the last 40mm of the sample: the region where proxies show variability. This suggests a differing fluid composition to the earlier parts of the vein, with lower $CaCO_3$ oversaturation, possibly through lower Ca concentrations, lower pH or a change in temperature. This region corresponds to the region on 2/1 which shows dissolution. Growth rates could vary partitioning behaviour, accounting for the lower M/Ca ratios; but average extension rates are small compared to experiments displaying such behaviour. Visually this region is more transparent, suggesting fewer growth defects or inclusions.

Using these age models, would indicate gradients in chemistry between the veins as in figure 4.11. However, it requires assymetrical vein formation, which is not supported by field observations or the symmetry of vein trace metal trends. It suggests an unresolved bias in the accuracy of the geochronology, which is related to the samples. An isochron approach on future samples might be beneficial, though the existing repeats do not give a very large scatter. This presents a unique problem for 'clean' materials: it is difficult to assess initial ^{230}Th without ^{232}Th.

4.3.3 Sr isotopes: LA-MC-ICPMS isotopes on veins

The laser ablation Sr isotope method (chapter 3) was applied to scan veins for internal variability, that may point to significant changes in fluid sources. This approach is significantly faster and at higher spatial resolution than physical subsampling for TIMS analysis, though at the expense of some precision. Triplicate spots were placed every 2mm along samples SW/02/36J and SW/06/14E from Salt Wash, giving measurements 252 measurements at 84 unique sample locations in a 6 hour session. Both of these samples were measured in (Kampman et al., 2012), with ages of ≈112ka and ≈30ka and were chosen as they were the largest continuous samples measured in that study. Subsequent dates, shown in figures 4.12 and 4.13 show that these samples represent ≈5kyr and ≈3kyr of growth. Both samples agree with the ^{87}Sr/^{86}Sr measurements of Kampman et al. (2012). However, the variability in each sample is relatively limited; SW/02/36J shows a ≈200ppm increase in ^{87}Sr/^{86}Sr and a 400‰ decrease in $\delta^{234}U_i$ (figure 4.12) and SW/06/14E shows a ≈100ppm decrease in ^{87}Sr/^{86}Sr and a 500‰ increase in $\delta^{234}U_i$ (figure 4.13). These internal variabilities are much smaller

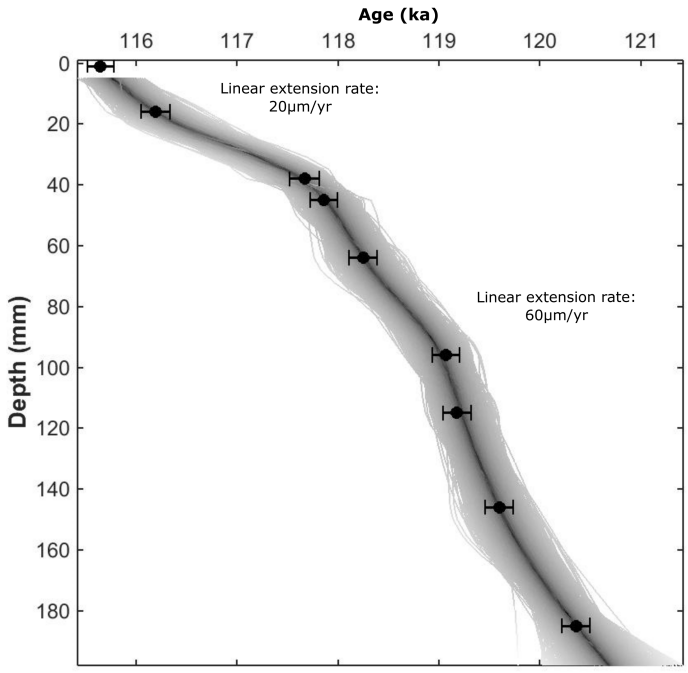

Fig. 4.10 Example age-depth model calculated by Monte-Carlo simulation within COPRA for sample 2/4.

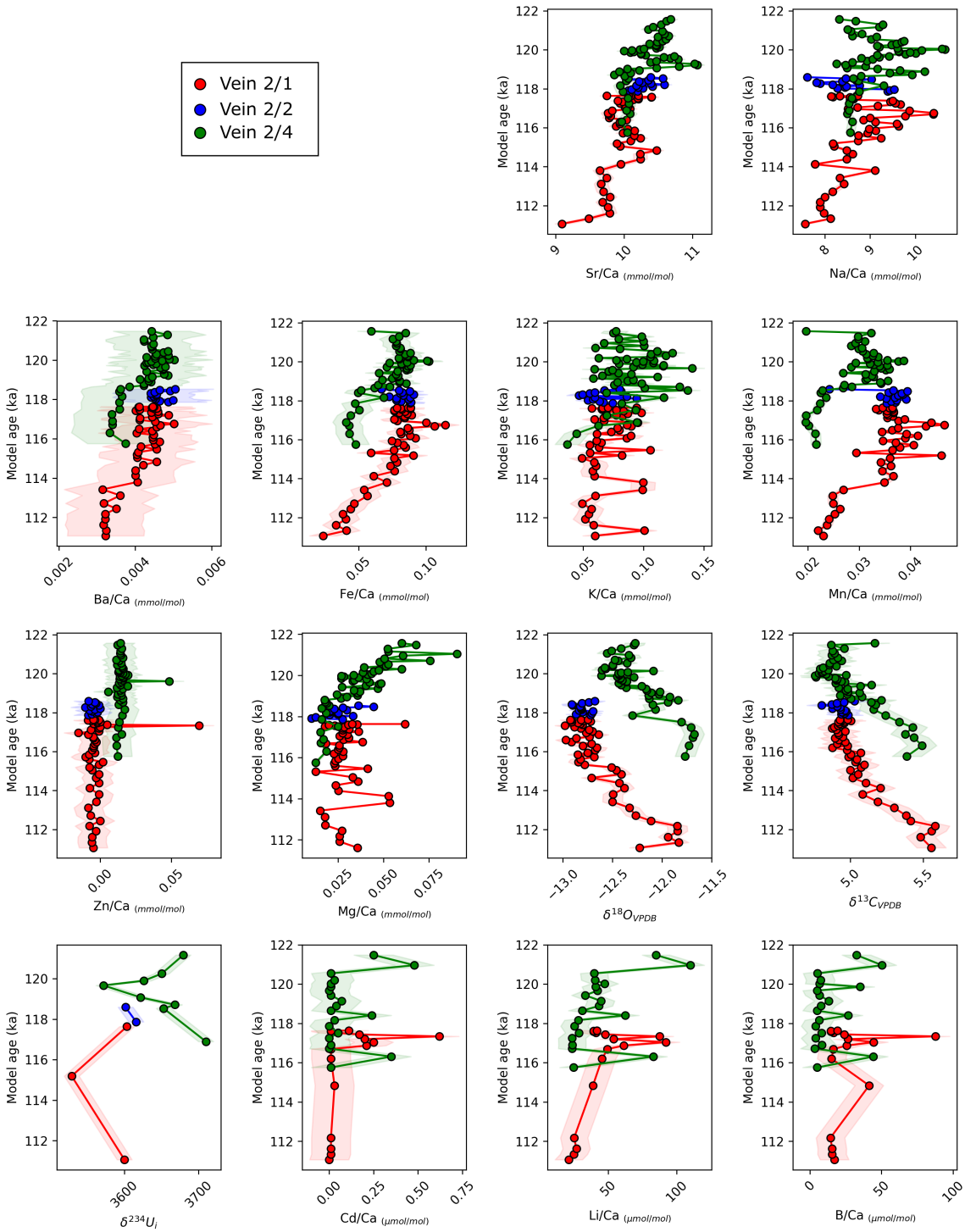

Fig. 4.11 Trace metal data on vein age models; the offset implied by the age models would infer unreasonable chemical gradients over 30cm. Units for trace metals are mmol/mol, with the exception of Li and B which are μmol/mol.

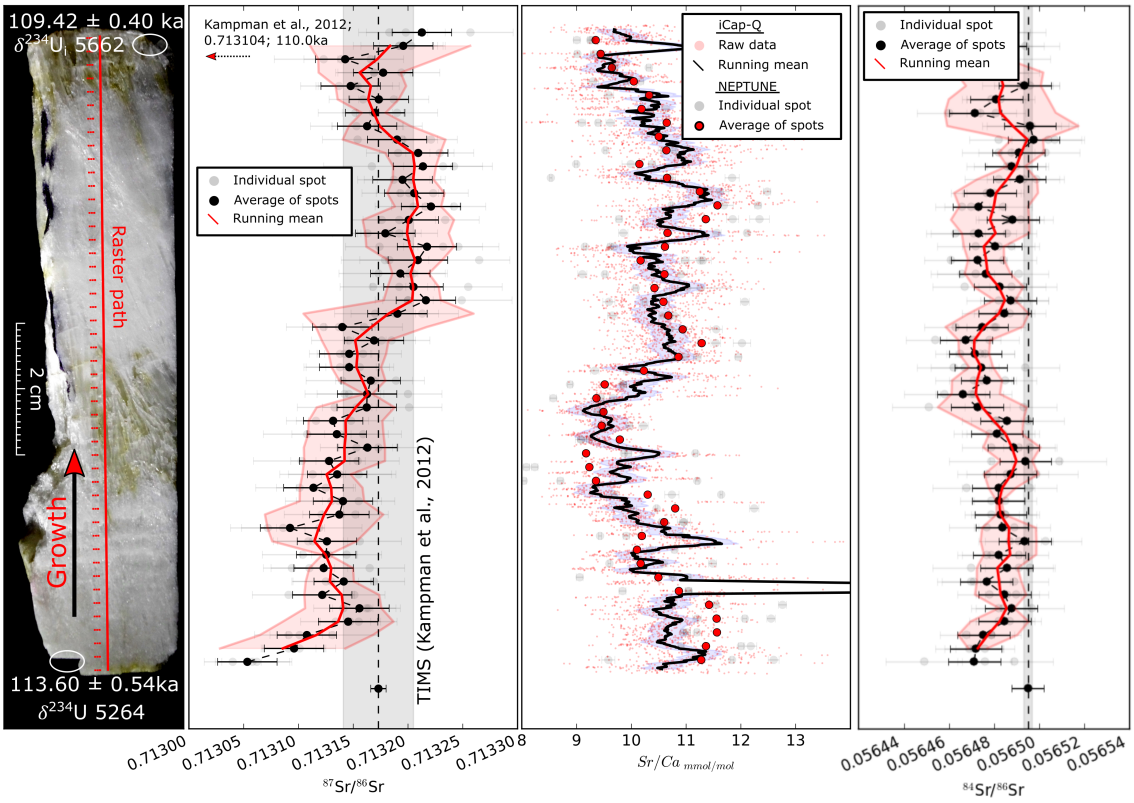

Fig. 4.12 Laser ablation Sr isotope and Sr concentration profiles across vein SW/02/36J. This sample was measured in Kampman et al. (2012), with an age of 112.8ka. Based on that record, from 112.8ka to 110ka proxies such as Ba/Ca and Sr/Ca increase, and $^{87}Sr/^{86}Sr$ and $\delta^{13}C$ decrease. New ages on this sample show that it crosses this transition and there is no change in radiogenic Sr composition across this sample across that time period. The large peak in Sr/Ca is not celestine, (as observed elsewhere) as S concentrations decrease across this band

than the variability between localities discussed in chapter 5, but suggest a minor role for fluid mixing.

Both samples have $^{84}Sr/^{86}Sr$ values ≈14ppm lower than expected values, which suggests the true value of $\delta^{88}Sr$ is ≈0.18‰ higher than assumed (β≈-1.71 during analysis). This inferred offset is similar in size to the 0.15-0.25‰ fractionation observed during aragonite precipitation (AlKhatib and Eisenhauer, 2016a,b). Neither sample shows a clear correlation of $^{87}Sr/^{86}Sr$ with concentrations, though higher $^{87}Sr/^{86}Sr$ and lower Sr/Ca in SW/02/36J might suggest a higher sensitivity to silicate dissolution inputs (but not SW/06/14E). Both samples suggest there is no major change in Sr isotope sources between the samples, although it is relatively insensitive to changes due to high fluid concentrations and other metal isotopic

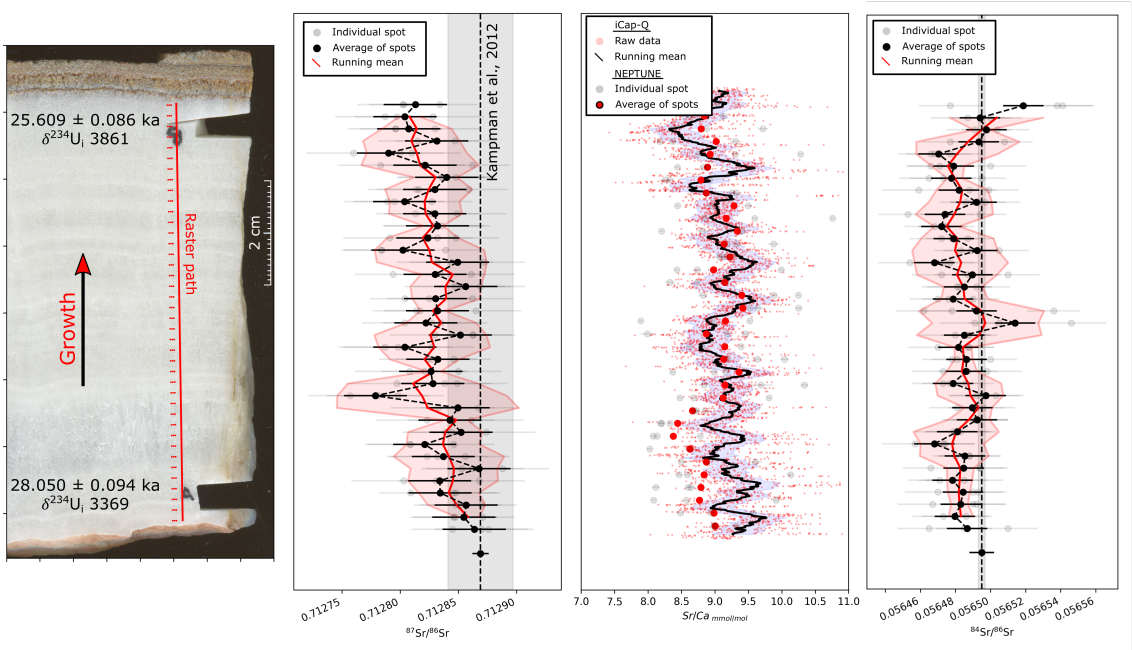

Fig. 4.13 Laser ablation isotope and trends on sample SW/06/14E. Vein measured due to existing U-series dates, but reveals a small systematic decrease in ratio from 28.0 to 25.6 kyr

tracers may be more sensitive to fluid sources or reaction processes. Additional trace metal data for SW/02/36J can be both samples can be found in appendix B.

4.4 mm to μm records

This final section presents laser ablation trace metal results from sample LG/03/50B because of prominent growth banding and a rapid linear extension rate. This sample grows at a linear extension rate of 200-300μm/yr whereas samples such as 2/4 or SW/02/36J extend at 20-40μm/yr. LG/03/50B is a sample from the travertine mound nearest to Crystal Geyser, and obtained from a collection of Neil Burnside's samples. Time series samples of Geysering activity were presented in Kampman et al. (2014b), showing variability between two fluid sources: fault brines and Entrada fluids (a third fluid source; the Carmel is observed in downhole fluids but not in Geyser samples). Time series sampling of Crystal Geyser is shown in appendix B. The sample is located on the anticline hinge, and therefore is a focussing point of fluid flow. Stable isotopes for aragonite samples from the same locality were presented in Frery et al. (2015), and the linear extension rates of these samples were used to infer mass fluxes of CO_2 (Frery et al., 2016).

4.4.1 Analysis methods

Trace metals were analysed using an iCap-Q (quadrupole mass spectrometer, Thermo-Fischer) with an excimer laser, as used previously for isotope work. Laser operating parameters were: 25um spot; raster rate 5μm/s; repetition rate 6Hz; fluence 2.4mJ/cm^2; 1l/min He (split 0.7l/min cup, 0.3l/min cell), 10ml/min N_2. The iCap-Q is equipped with a collision cell, which improves accuracy and precision of elements susceptible to molecular interferences. This improves signal backgrounds at the expense of sensitivity and the ability to measure some lighter elements. The isotopes monitored for each element can be found in appendix B. Data are bracketed by analyses of both NIST glasses and carbonates, and processing is performed in Iolite v2.5. As some elements are not present or independently constrained in carbonate standards, NIST glasses are used as primary standards despite known inaccuracy through matrix mismatching; relative trends are robust. Parallel neighbouring transects on the sample were performed as an additional verification check, and can be found in appendix B.

Not all elements could be included during analysis. Mg, for example, could not be measured due to low concentrations and to measure Mg would require long dwell times and spot sizes approaching the thickness of laminations. In the data presented Sr dwell times were too short, resulting from efforts to minimise total cycle times ($\approx$0.9s) to maintain high spatial resolution. Individual integrations are imprecise, but long-term averages are robust. Elements such as Zr and V were included as they are interesting for U sourcing: detrital zircons, or V-U-ore deposits. Other elements such as Al, Fe, Mn, P, Cl & S were intended for monitoring of physical or fluid inclusions, but show interesting trends in clean sections of the carbonate.

4.4.2 High resolution laser ablation trace metal data

Annual laminations and potential origins

U-series dates show the sample represents 509$\pm$20 years of growth, and there are $\approx$530 layers which are counted manually or by automatic peak matching software on the RGB values (figures 4.14 and 4.15). An intermediate age in the middle of the sample confirms these counts. It is reasonable to say that these laminations represent annual banding. Banding represents a physical difference in the aragonite crystals caused by differing growth rate or density of fluid inclusions (i.e. through saturation state caused by Rayleigh fractionation or mixing). Thin section photographs in Frery et al. (2015) show coarse aragonite fibres which truncate every 60-200μm which is the same scale as this layering. In some samples

luminescent in CL can be observed (Frery et al., 2016). In hand specimen each layer is visible due to slightly variable opacity, which represents the difference between coarse and fine crystal growth. Each annual layer observed has a peak in Y concentration (figure 4.15). This raises the question: how do veins forming from fluids passing up a fault zone preserve an apparent response to climate? Seasonal stress and seismic trends have been observed related to groundwater recharge and usage (Johnson et al., 2017, 2016), and it is possible that fractures around Little Grand fault behave in a similar fashion, especially if the fractures are near to critical stress. This does not require seismicity to drive flow (i.e. seismic pumping Byerlee (1993); Sibson et al. (1975)). However, small scale seismicity has been observed near Crystal Geyser in 2006 and 2010 and it is suggested that these modify geyser eruption style (magnitudes 1.17 and 2.63 with hypocentres within 3km of Crystal Geyser Han et al. (2013)). Alternatively, the banding can also be caused by seasonal mixing with meteoric fluids; as with the cm to mm records this should be detectable in trace metal trends.

Chemical trends across laminations

Figure 4.16 shows the chemical trends across 8 laminations. This region was chosen due to the absence of any included phases, an example of which is included in appendix B. All elements are interpreted to be within the carbonate lattice rather than accessory phases. Figure 4.17 shows the correlation of these elements with Y, which is highly compatible in carbonates especially in the presence of Na. Increasing Y therefore suggests input of fluid that has not previously precipitated carbonate. It shows the most clearly pronounced chemical banding. Other elements show similar zoning, for example U, V and Al show largest similarity with slightly asymmetric bands on the left of figure 4.16. Mn and Fe show also show pronounced variability, but are in anti-phase. Unfortunately, the partitioning behaviour of these elements is not well constrained, with Mn having a single experimental determination suggesting it is slightly incompatible and V, Fe and Al have not been investigated. To be explained by a Rayleigh trend, it requires V and Al being compatible and Fe and Mn incompatible. Alternatively, mixing of fault brines and meteoric fluids could explain the data. Geyser eruptions at Crystal Geyser show quiescent periods with small eruptions (‘type A’) followed by larger eruptions (‘type B’) (Han et al., 2017; Kampman et al., 2014b). After the type B eruptions start larger fractions of fluids from the Entrada are observed, leading to higher Fe/Ca, Mn/Ca and Mg/Ca ratios. Prior to the creation of Crystal Geyser, fluid pressures in the reservoir builds until stresses allow for fracture apertures to increase and allow flow through fracture networks. If the reservoir is close to this threshold then seasonal crustal stresses are sufficient to cause annual migration of fluids from the Navajo. Modern gas

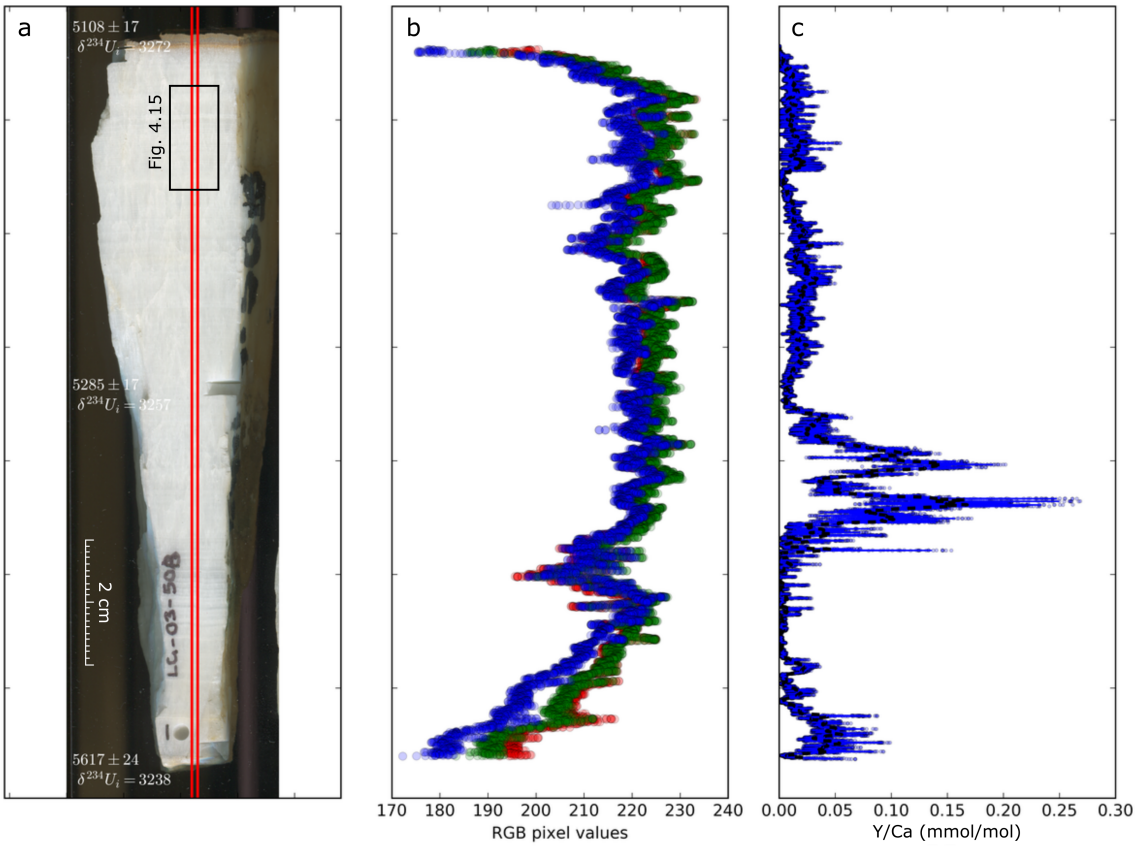

Fig. 4.14 a) Image of sample LG/03/50B b) RGB values averaged between the red lines approximating and c) trace metal zoning of $^{89}Y/^{43}Ca$. Red lines indicate the approximate path of the laser ablation raster, and the region of averaging for RGB values. The black box at the top of the figure denotes the zoomed in area displayed in the following figure.

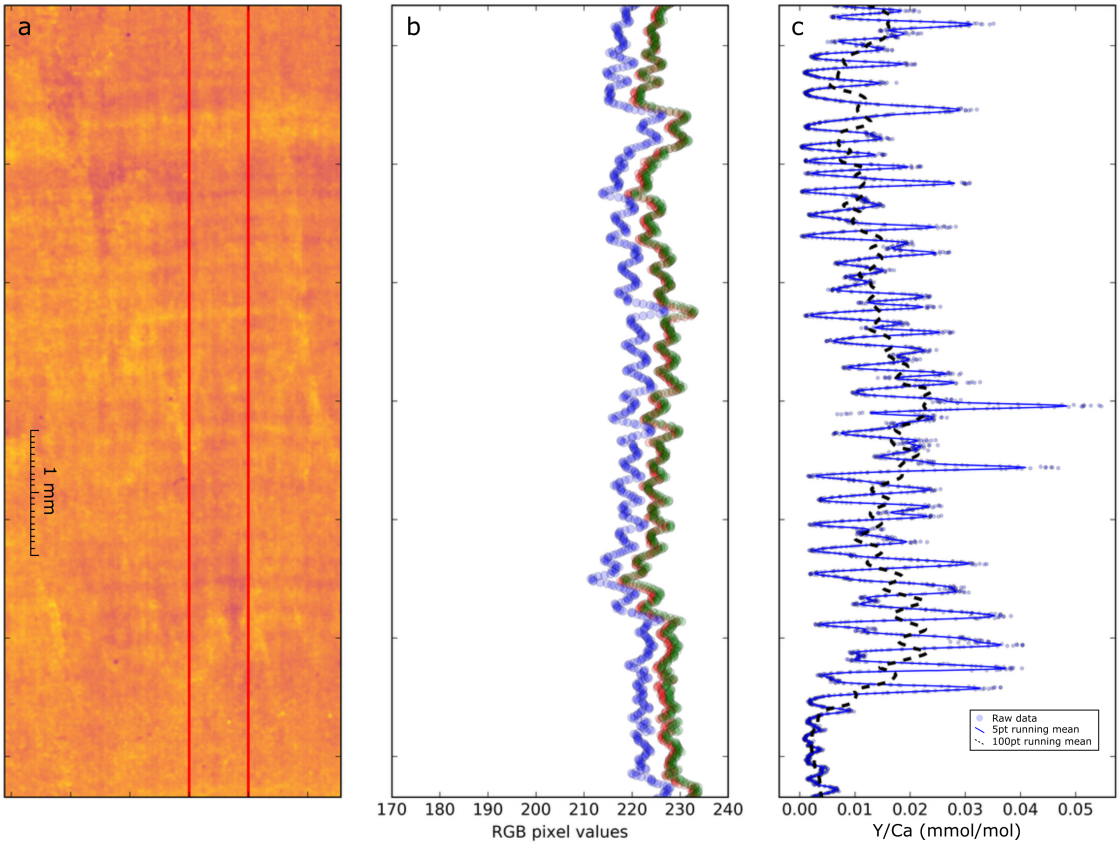

Fig. 4.15 a) False colour image of the top of sample LG/03/50B, used to make growth banding appear more prominent. b) RGB values averaged between the red lines in the image and c) $^{89}Y/^{43}Ca$ showing the most prominent trace metal banding associated with the laminations. Blue points are raw measurements, the blue line is the 15pt running mean, and the dashed black line is the 100pt running mean.

fluxes in the fault zone suggest that fractures are currently slightly transmissive in the upper units (Jung et al., 2015). Decompression of the reservoir through Crystal Geyser since the 1930's will have reduced reservoir pressure relative to historic behaviour. The limiting factor is behaviour of fractures within the Carmel formation, which are the barrier to flow from the Navajo. The release of fluid from the Navajo will decrease fluid over-pressures, reduce fracture transmissivity and potentially lead to temporary sealing of those fractures, during this time the fraction of Entrada derived fluids will increase until precipitation stops. This mixing mechanism can be tested by measuring $^{87}Sr/^{86}Sr$, as the Entrada and fault brines show up to 600ppm difference from one another (Kampman et al., 2014b). Small scale variability of $^{87}Sr/^{86}Sr$ is hinted at by lower reproducibility of replicates on laminated vein sample 2/4/005 relative to unlaminated standards of similar concentration, and also the 100ppm scatter of replicates across laminations of SW/06/14E and SW/02/36J (figures 4.12 and 4.13).

4.5 Conclusions

Records within the veins show interesting variability at a range of scales. With decreasing scale, higher variability is revealed. Fault scale records show lower, or similar, variability to high resolution records for proxies such as $\delta^{18}O$, $\delta^{13}C$ and trace metal/Ca ratios. However the combined records would suggest that Rayleigh fractionation driven by carbonate precipitation is not responsible for variation (Kampman et al., 2012). Instead, either fluid mixing or growth rate dependent partitioning during Rayleigh fractionation can be used to explain the data trends. However, for many elements there is little data available for partition coefficients, let alone their dependence upon mineral saturation state/growth rate. Some kinetic processes such as growth entrapment seem unlikely to be responsible due to much smaller growth rates.

Isotope ratios such as $^{87}Sr/^{86}Sr$ and $\delta^{234}U_i$ show a small range of variation within individual samples ($\approx$100-200ppm and 500‰ respectively). However, this is much smaller than the total variation observed in the low resolution study by Kampman et al. (2012). One sample, SW/02/36J does not show a jump in isotope ratio across one of the 'drops' in isotope ratio seen in the fault scale record. This suggests that the variation may be due to sample locations. This idea will be expanded in the following chapter. The two samples SW/02/36J and SW/06/14E show mixing trends in either direction, but the total variation within them is small relative to the spatial trends which will be presented.

One measured sample next to Crystal Geyser extends much faster than other samples elsewhere. Pronounced laminations on it can be counted, and U-series ages suggest that this sample has annual laminations, around 200-300μm width. Each of these laminations

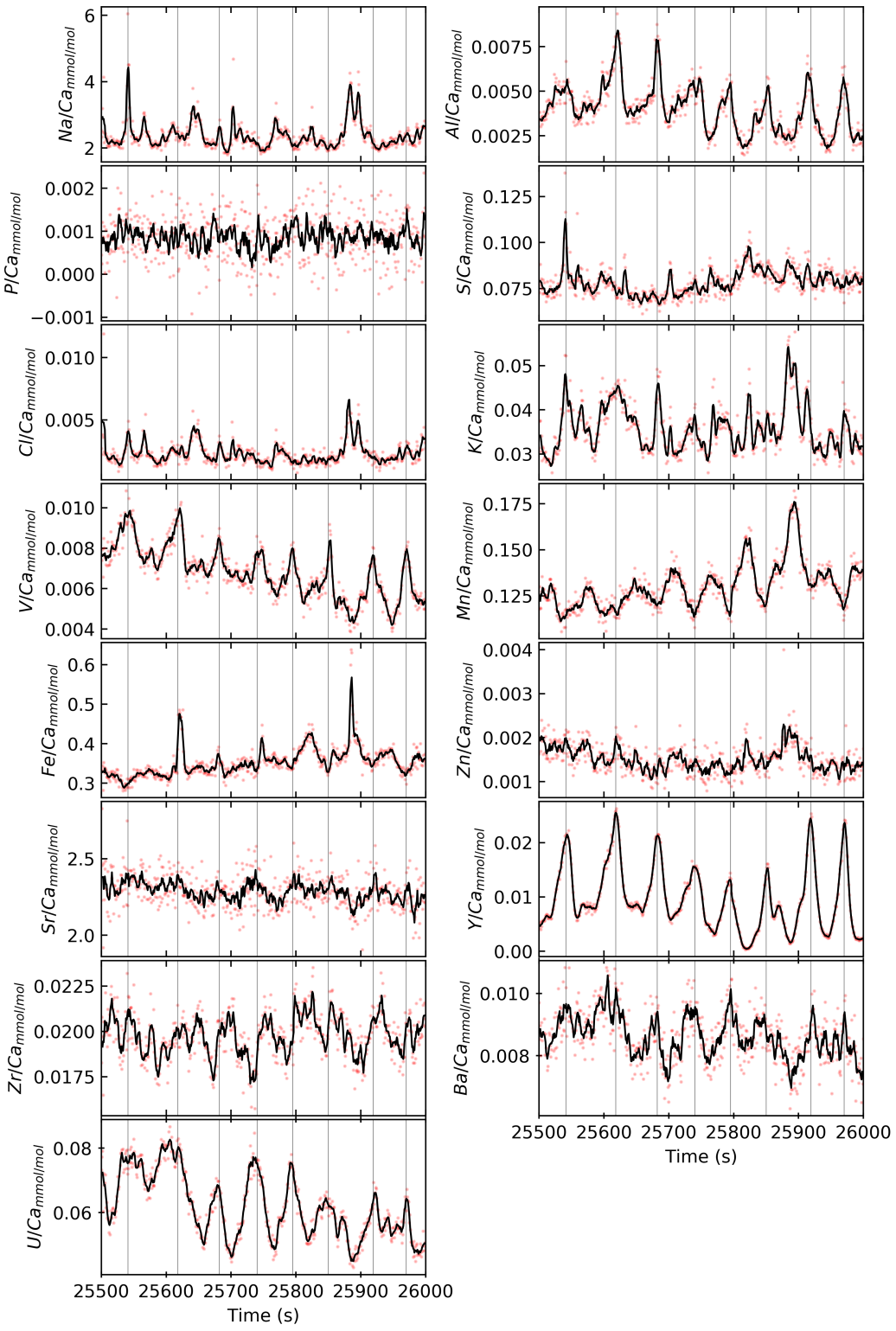

Fig. 4.16 Zonation at the top of the vein, clearly visible in most elements. Fe and Mn are in anti-phase to Y and other highly compatible elements. Field of view presented is 2.5mm, and vertical lines show the location of Y peaks.

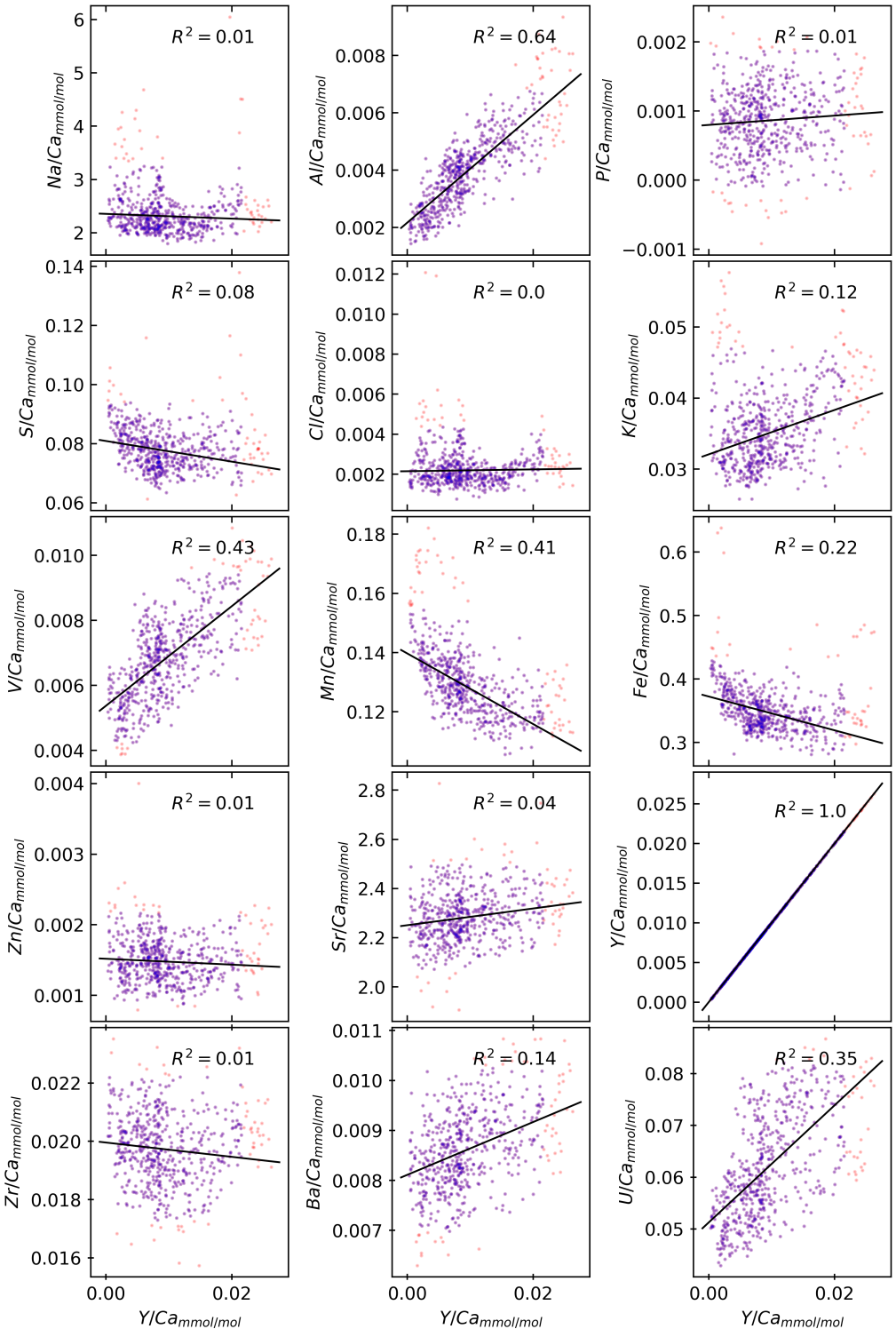

Fig. 4.17 Cross plot of previous figure against Y, all data are pink data points, and those within 2σ of the mean are highlighted in blue and used for linear regression. Negative correlation with Mn and Fe suggests fluid mixing of brines with Entrada fluids, in a manner similar to eruptions at Crystal Geyser

preserves annual chemical records, and is most pronounced for Y/Ca. Fe and Mn are in anti-phase to the other elements. The partition coefficients on these elements into aragonite is not constrained, but if they are incompatible then trends can be explained by rayleigh fractionation alone. Otherwise, fluid mixing is required. Assuming that they are mixing trends, then there is a suggestion that it is due to changes in the ratio of Navajo to Entrada fluids. This is similar to what is observed during cold water, man-made geysering at Crystal Geyser which is $\approx$10m away. An increase in the flux of fluid from the Navajo sandstone could be driven by annual changes in crustal stresses increasing the aperture of fractures, and thus increasing effective vertical permeability. The crustal stresses for such behaviour would have to be in quite a narrow window for this to occur, but with an over-pressured reservoir (one which has not been drained by Geysering activity) this does not seem unreasonable, and is a method to relieve fluid over-pressures prior to Geysering activity.

Chapter 5

Reactive transport modelling of U and Sr isotopes

This chapter presents a simple analytical reactive transport model for the evolution of Sr and U isotopes along a one dimensional flow path. As the variability of isotope ratios across vein samples is small, this suggests the role of fluid mixing is minor. This chapter explores the isotopic variability caused by fluid-rock interaction between sample localities. The parameters within the model are calibrated using modern fluid samples, and this calibration is applied to the fossil travertine samples ('feeder' veins), measured by laser ablation methods presented in chapter 3. These samples are spatially and temporally distributed, therefore fluid end-members are not constant. A reactive transport approach can therefore be used to show how these end-members vary with flow through the Navajo formation.

5.1 Reactive transport

Reactive transport can be used to explain the concentration of elements within pore fluids as a function of chemical and physical processes. The governing equations include transport terms (dispersion and advection), reaction terms (dissolution, precipitation and adsorption), and radiogenic decay terms (decay ingrowth, outgrowth and α-recoil). The general equation for the change in element concentration per unit time is summarised below (Bethke, 2008):

$$\phi \frac{\partial C_f}{\partial t} = \underbrace{\frac{\partial}{\partial z}\left(\phi D_e \frac{\partial C_f}{\partial z}\right)}_{\text{Dispersion}} - \underbrace{\phi v \frac{\partial C_f}{\partial z}}_{\text{Advection}} + \underbrace{\phi R_d}_{\text{Dissolution}} - \underbrace{\phi R_p}_{\text{Precipitation}} \pm \underbrace{\phi R_\lambda}_{\text{Radiogenic decay}} + \underbrace{\phi R_\alpha}_{\alpha\text{-recoil}} \tag{5.1}$$

where ϕ is the porosity, C_f is the concentration of an element (or isotope) in the fluid, D_e is the dispersion coefficient (which accounts for molecular diffusion and hydrodynamic dispersion) and v is the velocity of fluid advection. R_d, R_p, R_λ, and R_α are rate constants for input of an element, and each term can be described by other functions. The following sections discuss the formation of these equations for analysis of U and Sr isotopes, in a similar manner to models presented by Johnson and DePaolo (1997, 1994); Lichtner (1985, 1988); Maher et al. (2006a, 2003, 2006b). All the equations presented are continuum models and assume that physical flow can be averaged across a representative elementary volume (REV). Physical flow in these equations is modelled by simple flow relationships such as Darcy's law, but not more complex relationships such as Navier-Stokes (Steefel et al., 2005). Numerical models are often used to solve equation 5.1 in up to 3 spatial dimensions, and can then include more complex flow physics (Steefel et al., 2015). The approach presented here derives simple analytical solution to equation 5.1. This allows a better understanding of the main controlling parameters in the system, which frequently are insufficiently well constrained to justify more complex treatments (Lichtner, 1988).

5.1.1 Fluid mixing

It is assumed that fluid mixing is not significant, as the variability observed at any locality is small (as presented in chapter 4) compared to the variation between localities. The model presented therefore shows the evolution of a single fluid source. An offset from this model shows either miscalbration of model parameters, or mixing. However, as end-members come from different aquifers, their composition is anticipated to vary in a similar fashion. The fluid samples used for calibration have calculated Ismay brine fractions of around 2-6% (Kampman et al., 2009), a relatively small total contribution.

5.1.2 Modelling of U isotopes

The U series decay chain was discussed with application to U-Th dating in chapter 3. The radiogenic isotopes ^{234}U and ^{238}U are considered in this chapter, but similar models could be constructed for ^{235}U to understand stable isotope variation (δ^{238}U). Each isotope can be expressed separately and the two equation combined can be used to model the evolution of the U-isotope ratio with time and/or distance. This approach is derived from models presented by Maher et al. (2006a).

For example, the change in concentration of ^{238}U with time can be written as follows:

$$K_{r,238}\frac{\partial C_{f,238}}{\partial t} = \underbrace{\frac{\partial}{\partial z}\left(D_e\frac{\partial C_{f,238}}{\partial z}\right)}_{\text{Dispersion}} - \underbrace{v\frac{\partial C_{f,238}}{\partial z}}_{\text{Advection}} + \\ + \underbrace{\sum_i M_{s,i}k_{d,i}S_iC_{s,i}}_{\textit{Dissolution}} - \underbrace{M_sk_pK_sC_f}_{\text{Precipitation}} - \underbrace{\lambda_{238}C_{f,238}K_{r,238}}_{\text{Decay outgrowth}} \tag{5.2}$$

where $K_{r,238}$ is the retardation factor (a combination of all processes removing U from solution), D_e is the dispersion coefficient and v is the velocity of fluid flow. The dissolution term is the sum of i U-bearing phases, where k_d is the surface area normalised dissolution rate constant and S_i is the surface area of a given mineral phase. Therefore, k_dS_i is the bulk dissolution rate of phase i. C_s and C_f are the concentration of U in the solid and fluid. M_s is the solid to fluid mass ratio, calculated in equation 5.3, which is required to convert dissolution and precipitation terms from per-unit-mass to per-unit-volume. For a water saturated sandstone with well interconnected porosity, it is assumed that volumetric water (θ) is equal to the porosity ($\phi \approx \theta$). For the Navajo sandstone θ is ≈ 0.2 (Hood and Patterson, 1984; Kampman et al., 2012), fluid density (ρ_f) is $1.05\,\mathrm{g/cm^3}$ and bulk density (ρ_b) is $2.65\,\mathrm{g/cm^3}$:

$$M_s = \frac{\rho_b(1-\phi))}{\rho_f\theta} \tag{5.3}$$

therefore the value for the solid to fluid mass ratio, M_s, in the Navajo sandstone is ≈ 10. The precipitation term in equation 5.2 consists of M_s, k_p the bulk precipitation time constant and K_s the partition coefficient between the solid and fluid. For simplicity, precipitation is treated as negligible. Finally, the decay outgrowth term accounts for the loss of ^{238}U through radiogenic decay by the decay constant λ_{238}, and adsorption $K_{r,238}$. For simplicity it is assumed that U is not impacted by sorption processes, i.e. that $K_{r,238} \approx 1$.

The corresponding equation for ^{234}U can be written including a term for decay ingrowth and for α-recoil as shown in equation 5.4:

$$K_{r,234}\frac{\partial C_{f,234}}{\partial t} = \underbrace{\frac{\partial}{\partial z}\left(D_e\frac{\partial C_{f,234}}{\partial z}\right)}_{\text{Dispersion}} - \underbrace{v\frac{\partial C_{f,234}}{\partial z}}_{\text{Advection}} + \underbrace{\sum_i M_{s,i}f_{\alpha,i}\lambda_{238}C_{s,i,238}}_{\alpha\text{-recoil}} + \underbrace{\sum_i M_{s,i}k_{d,i}S_iC_{s,i}}_{Dissolution} - \underbrace{\sum_j M_{s,j}k_{p,j}K_{s,j}C_f}_{\text{Precipitation}} + \underbrace{\lambda_{238}C_{f,238}K_{r,238}}_{\text{Decay ingrowth}} - \underbrace{\lambda_{234}C_{f,234}K_{r,234}}_{\text{Decay outgrowth}} \tag{5.4}$$

The additional term alpha recoil, accounts for transfer of ^{234}U from solid phases during α-decay of ^{238}U at the rate λ_{238}. The orientation of decay is random, and the likelihood of ^{234}Th recoil intersecting the mineral surface and being ejected from the crystal is given by f_α. This term is a function of surface area, and can be approximated by grain size. Additionally, decay outgrowth of ^{234}U in the solution is accounted for by λ_{234}.

The two U isotope equations can then be combined to express the change in isotope ratio with time by assuming:

- $D_{e,234} = D_{e,238}$; both isotopes disperse at the same rate
- $K_{r,234} = K_{r,238}$; during retardation there is no isotopic fractionation
- ^{234}U behaves chemically the same as ^{238}U
- There is no isotopic fractionation during precipitation
- $\lambda_{238} - \lambda_{234} \approx -\lambda_{234}$
- The concentration of ^{238}U is total U

Which results in the following equation, where A is used to represent the activity ratio $\left[^{234}U/^{238}U\right]$ and precipitation is assumed not to occur:

$$K_r\frac{\partial A_f}{\partial t} = \underbrace{D_e\frac{\partial^2 A_f}{\partial z^2}}_{\text{Dispersion}} - \underbrace{v\frac{\partial A_f}{\partial z}}_{\text{Advection}} + \underbrace{\sum_i \frac{M_sC_sk_fS_i}{C_f}(A_s - A_f)}_{\text{Dissolution}} + \underbrace{\frac{M_sf_\alpha\lambda_{234}C_s}{C_f}}_{\alpha\text{-recoil}} + \underbrace{K_r\lambda_{234}(1-A_f)}_{\text{Solution Decay}} \tag{5.5}$$

It can be assumed that the change in concentration per unit time is trivial compared to the other terms (i.e. $\frac{\partial C_f}{\partial t} \approx 0$ and therefore $\frac{\partial A_f}{\partial t} \approx 0$), which allows for the above equations to be solved as a function of distance; i.e. it is in quasi-steady state (Lichtner, 1988). Additionally, based upon transport processes either the dispersive or advective term can be treated as insignificant. The Peclet number, *Pe*, is the ratio of advective to dispersive transport. A dispersion rate is not constrained in the Navajo sandstone, but as an initial estimate a rate of $0.031 m^2/yr$ can be used as determined for Hanford sands (Kincaid et al., 1998; Maher et al., 2006a), these are much shallower units so this is likely an overestimate. As will be shown, flow rates in the Navajo are ≈0.4m/yr, therefore $Pe > 1$ so it is reasonable to omit the dispersion term. The equation can therefore be written as:

$$\frac{\partial A_f}{\partial z} = \underbrace{\frac{M_s C_s k_d S_i}{v C_f}(A_s - A_f)}_{\text{Dissolution}} + \underbrace{\frac{M_s f_\alpha \lambda_{234} C_s}{v C_f}}_{\alpha\text{-recoil}} + \underbrace{\frac{K_r \lambda_{234}}{v}(1 - A_f)}_{\text{Solution decay}} \tag{5.6}$$

The arrangement of certain terms are Damköhler numbers; the ratio of a reaction rate to a transport rate. The above equation contains two such ratios: bulk dissolution rate to flow rate $\left(\frac{Sk_d}{v}\right)$ and decay to flow rate $\left(\frac{\lambda_{234}}{v}\right)$. The lower the concentration in the fluid to solid $\left(\frac{M_s C_f}{C_s}\right)$, the larger the impact of dissolution and α-recoil on isotopic compositions. As will be discussed later, $A_s < 1$ for old reservoir minerals, therefore α-recoil is the only process increasing A_f when $A_f > 1$. When $A_f < 1$ both α-recoil and decay of ^{238}U in the solution can increase the ratio. Equation 5.6 can be integrated to solve for A_f, the U-isotope ratio of the fluid. Solutions for this equation are shown in appendix C. For consistency with the methods presented in chapter 3, $A_{f,s}$ (the activity ratio of fluid and solid phases) are converted to $\delta^{234}U$ notation, where $\delta^{234}U = 1000(A - 1)$.

5.1.3 Modelling of Sr isotopes

Similarly to the U-isotope model, an equation for Sr isotopes can be constructed. These models are presented in Maher et al. (2003) based and derived by Johnson and DePaolo (1997, 1994). The combination of these equations is displayed in equation 5.7, where r_f is used to represent the ^{87}Sr/^{86}Sr ratio in the fluid and r_s the ratio of solid phases:

$$K_r \frac{\partial r_f}{\partial t} = \underbrace{D_e \frac{\partial^2 r_f}{\partial z^2}}_{\text{Dispersion}} - \underbrace{v \frac{\partial r_f}{\partial z}}_{\text{Advection}} + \underbrace{\frac{M_s S k_d W_d C_s}{C_f}(r_s - r_f)}_{\text{Dissolution}} \tag{5.7}$$

Table 5.1 Definition of symbols and unit ranges for use in reactive transport models.

Symbol	Description	Range/units
A_f	$^{234}U/^{238}U$ activity ratio in fluid	measured
A_s	$^{234}U/^{238}U$ activity ratio in solid phase	0.53-1
C_f	Concentration of an element in fluid	10-12 ppm Sr 3-20 ppb U
C_s	Concentration of element in solid phase	0-4000 ppm Sr[a] 0-400 ppb U[a]
D_e	Dispersion coefficient, including hydrodynamic dispersivity and molecular diffusion	0.031 m^2/yr[b]
f_α	α-recoil loss factor	???
F_α	Weighted geometric α-recoil loss factor	0.001-0.05
K_r	Retardation factor	Assumed 1[b]
k_d	Surface–area normalized dissolution rate constant	10^{-16}-10^{-10} $mol/m^2/s$
k_p	Time constant for precipitation	Assumed 0 yr^{-1}[c]
$\lambda_{234,238}$	Decay constant for ^{234}U or ^{238}U	yr^{-1}
M_s	Solid mass to fluid volume ratio	g/cm^3 fluid
θ	Volumetric water content	cm^3/cm^3
ϕ	Porosity	$\approx 0.2 cm^3/cm^3$
ρ_b, ρ_m	Bulk density/mineral density	1.9/2.7 g/cm^3
ρ_f	Fluid density	≈1-1.1 g/cm^3
r_f	$^{87}Sr/^{86}Sr$ atomic ratio for fluid phase	measured
r_s	$^{87}Sr/^{86}Sr$ atomic ratio for solid phase	0.717-0.733[d]
R_d	Weathering rate	$atoms/cm^3/yr$
R_p	Precipitation rate of secondary minerals	Assumed 0[c]
R_a	a-Recoil loss rate	$atoms/cm^3/yr$
S	Specific surface area	$\approx 0.7 m^2/g$
v	Fluid velocity	0.04-0.4 m/yr
z	Distance coordinate along flowpath	m

[a] conservative value of 300ppm assumed for Sr (depends upon anorthite content, weathering history) and 200 ppb for U

[b] Kincaid et al. (1998); Maher et al. (2006a) U in Hanford sediments

[c] other values requires a modification of f_α terms as the concentration of U on solids varies

[d] 0.720 assumed during modelling

Again, assuming that dispersion is negligible, and that concentrations are in quasi-steady state, equation 5.7 can be reorganised as:

$$\frac{\partial r_f}{\partial z} = \frac{M_s S k_d C_s}{v C_f}(r_s - r_f) \tag{5.8}$$

As with the U-equations, the ratio of bulk dissolution rate to flow rate $\left(\frac{Sk_d}{v}\right)$ is a Damköhler number. Similarly to U, lower values of the ratio $\left(\frac{M_s C_f}{C_s}\right)$ (concentration in the fluid vs. the solid), the larger the impact of dissolution on fluid isotopic composition. Equation 5.8 can be integrated to solve for r_f, the Sr-isotope ratio, solutions for this are shown in appendix C.

5.1.4 Coupling Sr and U isotopes

The evolution of Sr isotopes in equation 5.8 and U isotopes in equation 5.6 are coupled when U and Sr occur in the same mineral phases. In sandstones the major phases containing both elements are plagioclase and alkali feldspars. Therefore there is a relationship between C_s for each isotope system and their dissolution rates. Due to the differing concentrations in fluids and solids $\left(\frac{C_s}{C_f}\right)$ each isotope system shows different sensitivity. Calibration of these ratios and other parameters at Green River is discussed in the following section.

5.2 Model parameters and calibration to Green River fluid samples

Springs along different flow paths at Green River allow for calibration of different model parameters. Sr concentrations and isotopes are published in Kampman et al. (2009), and U isotope data was measured at NIGL (for Niko Kampman) by solution methods mentioned in chapter 4. These data are unpublished, and can be seen in table 5.2. Corresponding major ion chemistry and isotope data was presented in Kampman et al. (2009, 2014b) and can be found in appendix B. The fluid flow path adjacent to the Salt Wash fault is thought to be from west to east, following the potentiometric surface of the aquifer (Hood and Patterson, 1984). The samples along the Salt Wash fault (from west to east) with measurements of both isotope ratios are: Small Bubbling Spring, Big Bubbling Spring and Pseudo-Tenmile Geyser (lower panel of figure 2.2). These samples show an increase in both isotope ratios with distance along the flow path, which is consistent with increasing dissolution of feldspars calculated from the major element composition by Kampman et al. (2009). This section

Table 5.2 Isotope ratios in fluid samples around Green River, Utah

Location Name	Sr $\mu mol/l$	Sr ppm	$\frac{Sr}{Ca}$ $mmol/mol$	$^{87}Sr/^{86}Sr$[a]	U $\mu mol/l$	U ppb	$\frac{U}{Ca}$ $\mu mol/mol$	$\delta^{234}U$[b]
Crystal Geyser	147.1	12.87	5.6	0.712660	33	7.9	1.3	4390
Torreys Spring	132.6	11.60	5.2	0.712588	13	3.1	0.5	1940
Tenmile Geyser	221.3	19.36	9.2	0.711755	85	20.2	3.5	-
Pseudo-Tenmile Geyser	150.7	13.19	7.3	0.712798	21	5.1	1.0	4250
Chaffin Ranch Geyser	147.1	12.87	5.3	0.713053	78	18.5	2.8	3950
Green River Airport Well	104.2	9.12	4.7	0.713327	21	5.1	0.9	-
Big Bubbling Spring	148.6	13.00	6.4	0.712720	21	5.1	0.9	3310
Small Bubbling Spring	128.5	11.24	6.5	0.712554	75	17.8	3.8	1030
Side Seep, BBS	127.5	11.16	6.1	0.712663	-	-	-	-
Tumble Weed Geyser	154.4	13.51	5.5	0.712581	23	5.5	0.8	3040

[a] Uncertainty is $\pm 10\times10^{-6}$ 2SE
[b] Uncertainty is $\pm$ 10‰ 2SE

discusses each parameter required as model inputs. The flow path between Big Bubbling spring and Pseudo-Tenmile spring is used to constrain an isotopic gradient over ≈1100m, figure 5.1. Theses samples are ideal for characterisation of this gradient as they have similar concentrations of U and Sr suggesting minimal fluid mixing. Small Bubbling, which also lies on the same flow path, has U concentrations 3.5 times greater so is not used initially. Flow is assumed to be through the Navajo sandstone. The advantage of using fluid samples is that they average reservoir heterogeneities. In the following discussion, parameters are grouped together as their representative Damköhler numbers.

5.2.1 Concentrations and mineral isotope ratios: $\left(\frac{C_s}{C_f}\right)$, r_s

Mineral abundances

The Navajo sandstone is composed mainly of quartz but estimates of modal mineral abundances vary. Parry et al. (2007) find it composed mainly of quartz (≈ 71% by volume), K-felspar (≈ 3.8%), illite (≈ 3%), kaolinite (≈ 1.5%) and calcite (≈ 0.6%) and a porosity of 20%. Abundances were recalculated by Kampman et al. (2009), presented in (Kampman

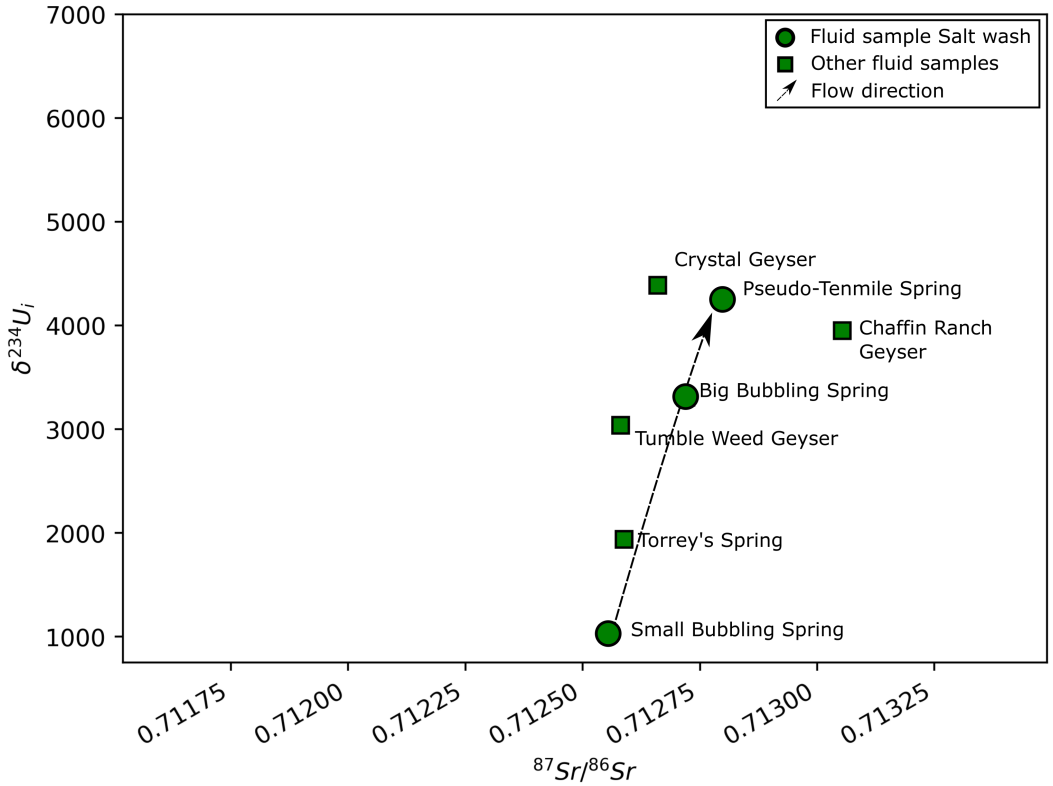

Fig. 5.1 Fluid samples from around Green River, with samples along Salt Wash displayed as circles, and other samples around the area shown as squares. The evolution of fluids along the flow path from West to East at Salt Wash is shown by the dashed arrow. This gradient is used to constrain model parameters.

2010, PhD Thesis). In order of decreasing modal volumetric mineral abundances are: Quartz ($\approx$ 81%), K-feldspar ($\approx$ 9.6%), Plagioclase feldspar (Albite, $\approx$ 4.4%), Smectite ($\approx$ 2.5%), Calcite ($\approx$ 1.3%), and Haematite ($\approx$ 0.8%). Samples from the drill core at Little Grand fault were measured by XRD showing 2.5-9% K-feldspar, <0.4% Albite, 1.5-8.5% Illite, <0.4% calcite, 0.3-4.8% Dolomite and <0.1% Haematite (Kampman et al., 2014b). It is worth noting the large variation in Albite content as samples directly next to the fault zone may not be representative of the entire reservoir due to historical fluid flow and associated alteration (Kampman et al., 2016). For consistency the modal abundances of Kampman et al. (2009) are used to allow direct comparison of Damköhler numbers. For simplicity, it is assumed that feldspars are the main Sr and U bearing phases, and weighted average compositions are used so they can be modelled as a single mineral phase.

Mineral concentrations: C_s

The concentrations of Sr and U have not been determined on feldspars from the Navajo sandstone. U concentrations of 0-200ppb in K-feldspars and 200-400ppb in plagioclase feldspars are expected based upon compiled partition coefficients and bulk granite U concentrations (Smedley and Pearce, 2016).

Sr concentrations in feldspars can be much larger, and depend strongly upon composition and temperature. The full range of compositions is 0-4000ppm (Heier, 1962). For example, concentrations $\approx$ 1,100-1,700ppm correlate with anorthite content, though diffusion of Sr prior to closure can reduce these concentrations (Cooper and Kent, 2014). Older albites can have lower concentrations of 0-250ppm (Neiva, 1995). As a conservative estimate, a concentration of 300ppm is assumed.

Fluid concentrations: C_f

The concentrations of Sr and U (expressed in ppm, $\mu mol/mol$, and as a ratio to Ca) are given in table 5.2. Sr has concentrations $\approx$ 10-12ppm, and U has much lower concentrations $\approx$ 3-20ppb.

Mineral isotopic compositions: r_s

Feldspars within the Navajo show a range of $^{87}Sr/^{86}Sr$ isotopic compositions, between 0.717-0.733 (Kampman et al., 2014b, 2012). A mid-value of 0.720 is used for initial modelling. U-isotope compositions is discussed later, as it is modified by α-decay.

Relating fluid and mineral concentrations: $\mathbf{M_s}$ and $\left(\frac{\mathbf{C_s}}{\mathbf{C_f}}\right)$

Estimates of $\left(\frac{C_s}{C_f}\right)_{Sr}$ are around 5-10, whilst $\left(\frac{C_s}{C_f}\right)_{U}$ are slightly larger at around 40-80. This suggests that during dissolution, U is more sensitive to reaction than Sr. M_s is used to relate the size of solid and fluid elemental reservoirs. For example a larger porosity will increase M_s (assuming the same mineralogical composition). Porosity (ϕ) of the Navajo sandstone varies between 0.1 and 0.35, with a mean of 0.2±0.04 (Kampman et al. (2009), using values from Hood and Patterson (1984)). Values for M_s are around 10 (for ϕ=0.2), giving $\left(\frac{M_s C_s}{C_f}\right)_{U}$ $\approx$ 400-800. This is much lower than the measured for Hanford sediments at $\approx$ 6000 (Maher et al., 2006a).

5.2.2 Dissolution: Surface area, dissolution rate and flow rate $\left(\frac{\mathbf{Sk_d}}{\mathbf{v}}\right)$

Surface area: S

Surface area for the Navajo sandstone was determined using Brunauer–Emmett–Teller gas adsorption (BET) by Zhu (2005) at $0.7 m^2/g$ ($1.484 \times 10^6 m^2/m^3$ when scaled for bulk density and porosity). This surface area is scaled for modal mineral abundance giving surface areas of 51×10^3 m^2/m^3 $\pm$ 6×10^3 m^2/m^3 for plagioclase and 112×10^3 m^2/m^3 $\pm$ 10×10^3 m^2/m^3 for alkali feldspars (Kampman et al., 2009). It is worth noting that BET gas adsorption is known to overestimate surface area due to molecular scale surface roughness. In comparison to geometric measurements or CT-scanner (X-ray) methods, BET area overestimates by around an order of magnitude (Lai et al., 2015). Additionally, surface area will not necessarily scale linearly with volumetric mineral abundances because of grain contacts. As a final caveat, the available surface of an 'aged' mineral may be lower from incongruent weathering depositing secondary minerals (clays) on mineral surfaces (Kampman et al., 2009; Zhu, 2005). Smectite/illite coatings on feldspar surfaces up to 3 μm deep are seen in larger pores at Green River (Kampman et al., 2009).

Dissolution rate: $\mathbf{k_d}$

The rates of dissolution in the Navajo sandstone were calculated to be much higher when in contact with CO_2, than similar aquifers without CO_2 (Kampman et al., 2009; Zhu, 2005). Compiled experimental and analogue experiment results in Kampman et al. (2009) show decreasing dissolution rates with increasing pH, and their own results suggest decreasing dissolution rate with proximity to equilibrium. The range of feldspar dissolution rates at Green River is inferred to be 1-4$\times 10^{-16}$ $mol/m^2/s$ for K-feldspar and 0.2-2$\times 10^{-14}$ $mol/m^2/s$ for

plagioclase (Kampman et al., 2009). These rates are an order of magnitude slower than observed in experimental studies, which can have rates as high as $10^{-10}\ mol/m^2/s$ (Brantley et al., 2008).

Assuming bulk dissolution rates and modal mineral abundance calculated by Kampman et al. (2009), it takes $\approx$ 0.7-2.7 Myr to consume all the K-felspar in a m^3 of the Navajo sandstone, and 13-130 kyr to consume all of the plagioclase feldspar. These are minimum age bounds, as the dissolution rates may decrease as mineral surfaces become shielded by products of incongruent weathering (clays), and as fluids approach equilibrium with the rock. Further, the presence of CO_2 in the reservoir may be transient, and during these periods of lower CO_2 concentration dissolution rate could to decrease by up to two orders of magnitude to the values observed in Zhu (2005) for the Navajo sandstone at Black Mesa in Arizona. The concentrations of CO_2 in historic fluids must generally be lower than the present day in order to preserve any feldspars within the sandstones since their deposition during the Jurassic.

Fluid velocity: v

In Kampman et al. (2009), the fluid velocity in the Navajo sandstone was calculated using the following equation:

$$v = K\frac{\mathrm{d}h}{\mathrm{d}x} \tag{5.9}$$

where v is the fluid velocity, K is hydraulic conductivity (0.47m/day from a compilation of Hood and Patterson (1984)) and $\frac{\mathrm{d}h}{\mathrm{d}x}$ is the hydraulic head. A flow rate is not quoted in Kampman et al. (2009). Assuming the change in potentiometric surface between Airport well and Chaffin ranch is $\approx$ 60m over 25km (shown in Kampman 2010, PhD thesis) from Hood and Patterson (1984)). This suggests the fluid velocity is $\approx 1.3\times10^{-8} m/s$ (0.4m/yr). At this flow rate, fluids have a residence time of $\approx$ 62,500 years along the most direct flow path (25km). Samples along Salt Wash fault are separated by $\approx$ 1600m, therefore at this flow rate fluids have a residence time $\approx$ 4,000 years. However, flow does not necessarily occur along the fault. Additionally, in the damage zone of the fault fluid flow may be accommodated by fracture networks. Flow will be more rapid in these heterogeneities, slowing the flow in the porous matrix.

Similar calculations performed on the Navajo sampled during drilling next to the Little Grand fault zone giving flow estimates an order of magnitude lower (Maskell 2016, PhD thesis). However, for the reasons stated above, flow may be accommodated in fracture networks, or is locally disrupted by fault properties: next to the drill site the Navajo is likely

sealed by clay smearing and development of low permeability cataclastites (Dockrill and Shipton, 2010). Flow rates at short distances away from the faults may not be representative of larger scale flow rates. As will be discussed, U-isotope evidence suggests slower flow rates.

Dissolution Damköhler number: $\left(\frac{\mathbf{Sk_d}}{\mathbf{v}}\right)$

Given the above estimations, the Damköhler number $\left(\frac{Sk_d}{v}\right)$ has a value of $\approx 6.37 \times 10^{-10} mol.g^{-1}$ for K-feldspar, and $\approx 1.45 \times 10^{-8} mol.g^{-1}$ for plagioclase feldspar. These small numbers show that transport dominates over dissolution reactions. As a bulk dissolution rate was calculated and then scaled for surface area and modal abundance, we are not imparting any systematic offsets whilst results are comparable to Kampman et al. (2009). This is discussed further later with regard to fluid samples.

5.2.3 Radiogenic: α-recoil $(\mathbf{f}_\alpha)$

This final section on equation terms discusses radiogenic decay processes. The impact of these terms is sensitive to the relative concentrations of U in the fluid and solid.

Alpha recoil: $\mathbf{f}_\alpha$

α-recoil during decay of ^{238}U to ^{234}Th (and then rapidly to ^{234}U), causes displacement of the daughter nucleus. This distance depends upon mineral density, but is typically ≈20-50nm (Maher et al., 2006a). The random nature of decay means only a fraction of decays within this distance lead to ejection from the mineral structure, this fraction is given the symbol f_α. This is dependant upon the surface area of U-bearing minerals, which for example can be approximated by a sphere (Kigoshi, 1971):

$$\begin{aligned} f_\alpha &= \frac{3\lambda_r}{2}\left(\frac{L}{d_p}\right) - \frac{1}{2}\left(\frac{L}{d_p}\right)^3 \\ &\approx \frac{3\lambda_r L}{2d_p} \text{ for } L << d_p \end{aligned} \tag{5.10}$$

where L is the length of recoil, λ_r is a correction for surface roughness and d_p is the grain diameter. Smaller grain diameters lead to larger surface area to volume ratios, and therefore larger f_α. These geometric assumptions overestimate surface area, as they do not

account for grain-grain contacts. ^{234}U can also be lost from the mineral to the solution by etching of α-recoil tracks in the mineral. This can be enhanced by dissolution exposing previously sealed recoil tracks as the mineral surface retreats. Estimates of f_α, can also be calculated through mineral leaches such as done in Maher et al. (2006a). If the grain size distribution of U bearing phases in a sediment is known, a geometric scaling for f_α can be used (Maher et al., 2006a) (see figure 5.2). Median grain sizes in the Navajo are $60-200\mu m$ with coarser grains sizes nearer the top of the unit. However, in the middle of the unit up to 20% clay can be found ($<4\mu m$), which gives a bimodal sediment size distribution. The sands can be considered poorly to moderately sorted (sorting coefficient $\sqrt{\frac{Q_3}{Q_1}} = 1.2-2.6$, where Q is a quartile range) (Hood and Patterson, 1984). This inherent heterogeneity makes geometric estimates of f_α difficult. For example in figure 5.2, Navajo samples can have F_α (the weighted sum of f_α's in different grain sizes) in the range 0.0001-0.1 depending upon sorting. Recoil is dominated by the fine grained fraction of sediments due to their high surface area (>5% fine grained sediment (<45μm) can account for 90%+ of α-recoil). For small grains, it is possible to estimate f_α by measuring bulk solid of these fine grained sediment phases and approximating the loss of ^{234}U (Maher et al., 2006a). Sandstones at the Hanford site show values of f_α around 0.002-0.01 based upon HNO_3 leaches, and 0.01-0.02 based upon geometric approximations, or measurements of f_α on the <45μm fraction (Maher et al., 2006a). Navajo sands may show up to 20% clays and silts (Hood and Patterson, 1984), suggesting in some regions that f_α could be as high as 0.05 (assuming a geometric similarity to silty layers at the Hanford site).

There are two advantages to using fluid samples to characterise the bulk reservoir response, as chemical and physical heterogeneities are averaged, and uncertainty from geometric assumptions is avoided.

Isotope ratio of solids through time: A_s

As discussed above, α-recoil leads to a very thin layer at mineral surfaces which becomes depleted in the daughter isotope ^{234}U. It is reasonable to assume that the cores of reservoir minerals are in secular equilbrium because their depositional age is >1.5Ma. A mechanically produced fresh surface will have the same isotope composition as the bulk mineral, which will develop a progressively heavier isotope signature as ^{234}U is lost by α-recoil with time. This can be seen in figure 5.3. Surface coatings (clays) on felspar grains may act as a barrier, preventing ^{234}U from reaching the pore space, as these coatings are much thicker than recoil length-scales.

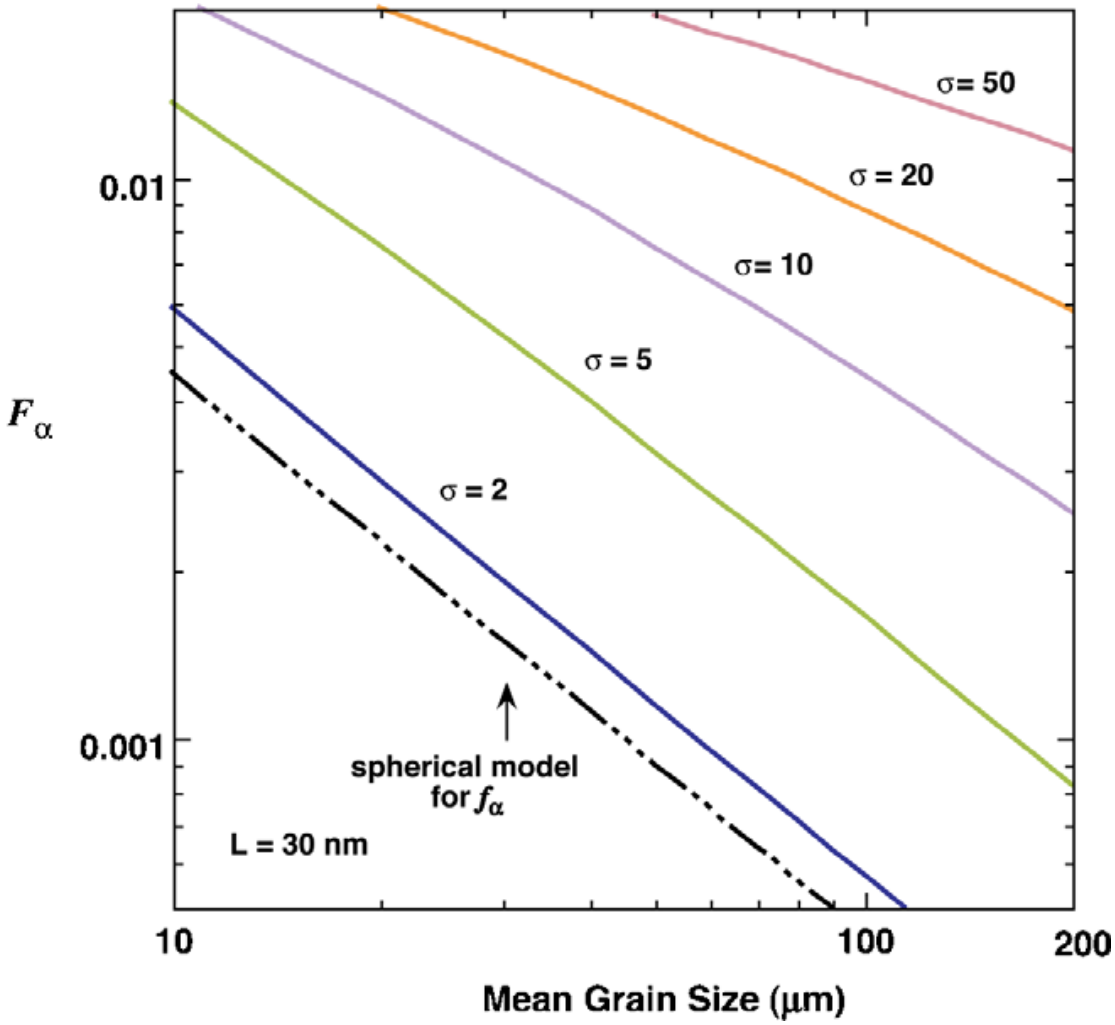

Fig. 5.2 Unmodified from figure 7 in Maher et al. (2006a). Weighted a-recoil loss factor (F_α) for lognormal grain size distribution with standard deviation (σ). When σ is larger, there is more fine grained sediment, which leads to larger F_α. The model is purely geometrical, and does not account for grain contacts and other processes which may reduce available surface area. It is worth noting that σ in this figure is the width of the log-normal grain size distribution, an approximation of sorting coefficient.

Dissolution of a fresh mineral will release U with an isotopic composition of 0‰ (i.e. at secular equilibrium), whereas dissolution of a steady-state recoil surface could have a value as low as -470‰ in figure 5.3. The exact value will depend upon the rate of mineral face retreat, as the mineral surface may not exist long enough to reach steady state. Rescaling k_d from Kampman et al. (2009) suggests a maximum surface retreat rate $\approx 1.26 \times 10^{-7} \mu m/yr$ for K-feldspar and $6.3 \times 10^{-6} \mu m/yr$ for plagioclase feldspars. After 100,000 years the K-feldspar mineral surface will have retreated by $\approx 0.012 \mu m$ ($0.63 \mu m$ for plagioclase) therefore the mineral never reaches radiogenic steady state. Instead K-feldspars will reach values of $A_s \approx 0.9$ (-100‰), whilst the faster retreat of plagioclase leaves ratios near to ≈ 1 (0‰). This is only the case if weathering of solid phases is uniform, which is unlikely due to the large range of particle sizes. Therefore mineral values will lie somewhere between the extremes shown in figure 5.3.

Radiogenic Damköhler number: $\left(\frac{\mathbf{f_\alpha \lambda_{234}}}{\mathbf{v}}\right)$

The radiogenic Damköhler number $\left(\frac{f_\alpha \lambda_{234}}{v}\right)$ depends mostly upon the size of f_α, which is the most uncertain parameter. $\frac{\lambda_{234}}{v}$ is a measure of fluid residence time where λ_{234} is the decay constant ($2.82206 \times 10^{-6} yr^{-1}$, corresponding to $t_{1/2} = 245,250$ years (Cheng et al., 2013)). The value for $\left(\frac{\lambda_{234}}{v}\right)$ is $\approx 7.07 \times 10^{-3} m^{-1}$, and is essentially a measure of fluid residence time. The 'older' the fluids, the larger the cumulative input from α-recoil. This eventually becomes balanced out by radiogenic decay in the solution, and is discussed in following sections.

5.3 Using isotope gradients and U-isotope steady state constraints at Green River

Isotope gradients

As shown in figure 5.1, the gradient of $^{87}Sr/^{86}Sr$ (r_f) and $\delta^{234}U_i$ (A_f) in the fluids are constrained along a flow path at Salt Wash. Fluid flow can be assumed to be parallel along the fault based upon high shale-smear and shale gouge ratios (Dockrill and Shipton, 2010). The distance between Pseudo Tenmile spring and Big bubbling spring is used as they show most similar Sr and U fluid concentrations (the sample at the beginning of this flow path, Small bubbling, has U concentrations 4 times larger and lower U activity ratios suggesting dissolution of a U-bearing phase). The flow path between these two samples is

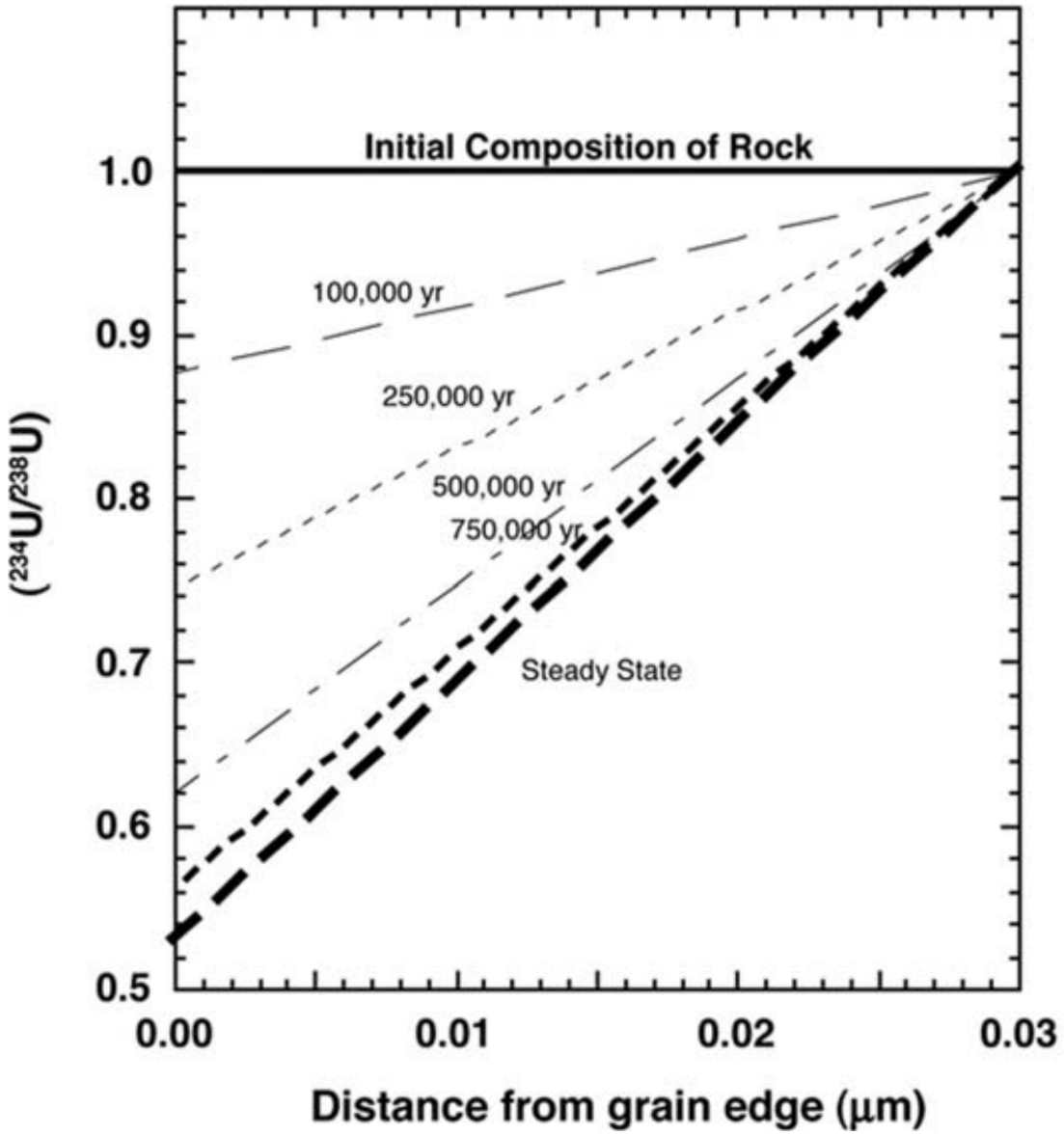

Fig. 5.3 Modified from figure 8 of Maher et al. (2006a). Evolution of the surface layer activity ratio. Predicted α-recoil loss along the cross-section of the surface of a spherical grain as a function of time. Activity ratios can be converted to delta notation using $\delta^{234}U = 1000(A-1)$, with the scale on the left ranging from -500‰ to 0‰.

1100m by a direct (non-tortuous) flow path. Therefore $\frac{\partial r_f}{\partial z}$ is $\approx 7 \times 10^{-8} m^{-1}$ and $\frac{\partial A_f}{\partial z}$ is $\approx 8.43 \times 10^{-4} m^{-1}$.

Substituting this value for $\frac{\partial r_f}{\partial z}$ into equation 5.8 (with $r_f = 0.712720$ at Big bubbling and $r_s = 0.720$) gives a value of 9.6×10^{-6} for $\frac{M_s S k_d C_s}{v C_f}$ and therefore a value of $9.6 \times 10^{-8} mol.g^{-1}.yr^{-1}$ for the Damköhler number $\frac{S k_d}{v}$. This is an order of magnitude larger than calculated above using estimates from Kampman et al. (2009). Assuming the bulk dissolution rate in Kampman et al. (2009) is accurate, then the fluid velocity (v) must be an order of magnitude smaller which is similar to the values calculated next to the fault zone (≈0.04m/yr, similar to estimates in Maskell, 2016). A slower flow rate helps explain variation in δ^{234}U.

Similarly, substituting values for $\frac{\partial A_f}{\partial z}$, $\frac{S k_d}{v}$ and v into equation 5.6 (with $A_f = 4.31$ at Big bubbling and $A_s = 1$), allows f_α to be estimated. The resulting value is 0.0235, which is well within the range expected geometrically for the Navajo. As v occurs in the final term (solution decay) of equation 5.6, there is a linear dependance between f_α and v. This reflects fluid residence time: when flow is faster, a larger input from α-recoil is required to explain the data.

U-isotope decay steady state

At large residence times, the $\delta^{234}U$ composition will be at steady state, where α-recoil is balanced by decay and dissolution; i.e. $v\frac{\partial A_f}{\partial z} = 0$ in equation 5.6 giving equation 5.11:

$$\frac{M_s f_\alpha \lambda_{234} C_s}{C_f} = \frac{M_s S k_d C_s}{C_f}(A_s - A_f) - \lambda_{234}(1 - A_f) \tag{5.11}$$

Therefore the maximum isotope composition is the balance of α-recoil, and loss from decay and dissolution. This allows for calibration of unknown parameters, such as f_α. This can be achieved by sampling fluids which have resided in a reservoir for >1.5Ma ($\approx$ 6 half lives of ^{234}U). This secular equilibrium will be reached sooner if either recoil or dissolution is very large. Fluid residence times around Green River are not long-enough for samples to have reached this state and therefore this constraint cannot be used. Similar aquifers in Texas appear to achieve maximum δ^{234}U values around 9000-12000‰ (Kronfeld, 1974; Kronfeld et al., 1975) and values as high as 20000‰ have been observed in the Great Artesian basin in Australia (Priestley et al., 2017). A model outputting much higher values would be unrealistic.

5.3.1 General model behaviour

This section briefly describes the general behaviour of each model, using the parameters discussed above. Flow paths are modelled at flow rates of 0.04m/yr for 1.5Myr (6 half lives of ^{234}U). The flow rate is closer to those determined next to the fault, otherwise the residence time of fluids in the reservoir is too small for significant input of ^{234}U through α-recoil. At this transport velocity, the flow path is $\approx$ 60km long, approximately the distance from the San Raphael Swell to Salt Wash (see chapter 2).

Sr-isotopes

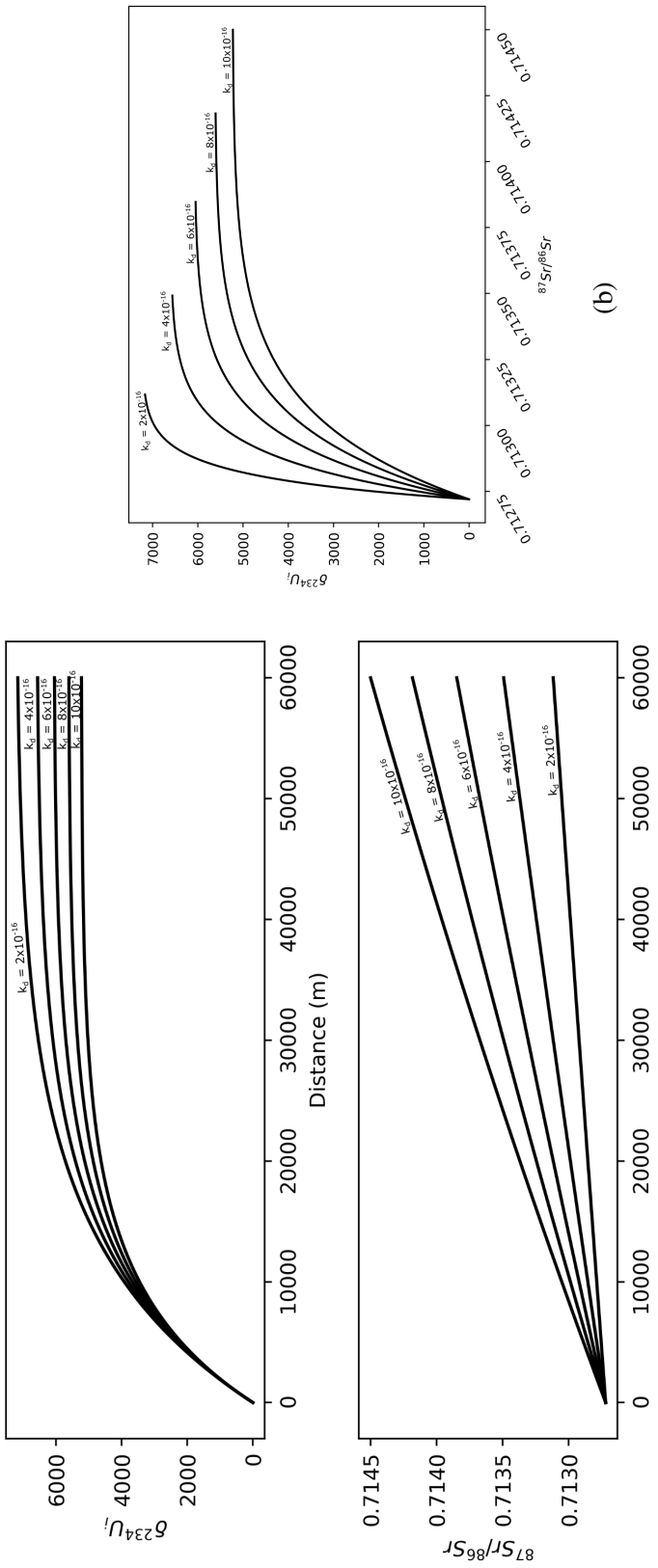

Fig. 5.4 Variable dissolution rate, from $2 \times 10^{-16} mol/m^2/s$ to $10 \times 10^{-16} mol/m^2/s$ at intervals of $2 \times 10^{-16} mol/m^2/s$ for $f_\alpha = 0.01$. Increased dissolution rate suppresses the maximum δ^{234}U value that can be achieved (top left), whilst increasing ^{87}Sr/^{86}Sr (bottom left). The interaction of the two isotope ratios is shown in the right panel

The starting $^{87}Sr/^{86}Sr$ fluid composition (r_f) is only modified by dissolution processes, as can be seen in figure 5.4. Therefore, with increasing distance (z) the composition of the fluid tends towards the composition of the solid (r_s) at the rate controlled by the Damköhler number $\left(\frac{Sk_d}{v}\right)$, and the fluid/solid concentration ratio $\left(\frac{M_s C_f}{C_s}\right)$. Larger values for both of these terms decrease the time/distance for complete equilibration with the solid phase (i.e. when $r_f = r_s$). This follows an exponential relationship, as can be seen in equation solutions in figure 5.4 and appendix C.

U-isotopes

The U isotope equation behaves similarly to that of Sr, but has a rate term for α-recoil and radiogenic decay in solution in addition to dissolution (see figure 5.5). As was the case for Sr isotopes, dissolution will cause A_f to trend towards A_s. Radiogenic decay in the solution will cause fluids to tend towards secular equilibrium (i.e. $A_f = 1$). The α-recoil term causes A_f to increase, and the magnitude of this effect depends upon $\left(\frac{M_s C_f}{C_s}\right)$. The balance of these processes dictates the 'steady-state' isotope composition which can be achieved along a flow path. If dissolution is dominant, the composition will be A_s. If, however, α-recoil is dominant then A_f depends upon $\frac{f_\alpha C_s}{C_f}$. Again, the solutions can be seen in appendix C, where α-recoil is a constant input and dissolution and solution decay set the size of the exponent. If it can be shown that isotopic 'steady-state' has been reached, or an isotopic gradient observed along a flow path, this can be used to calibrate α-recoil terms.

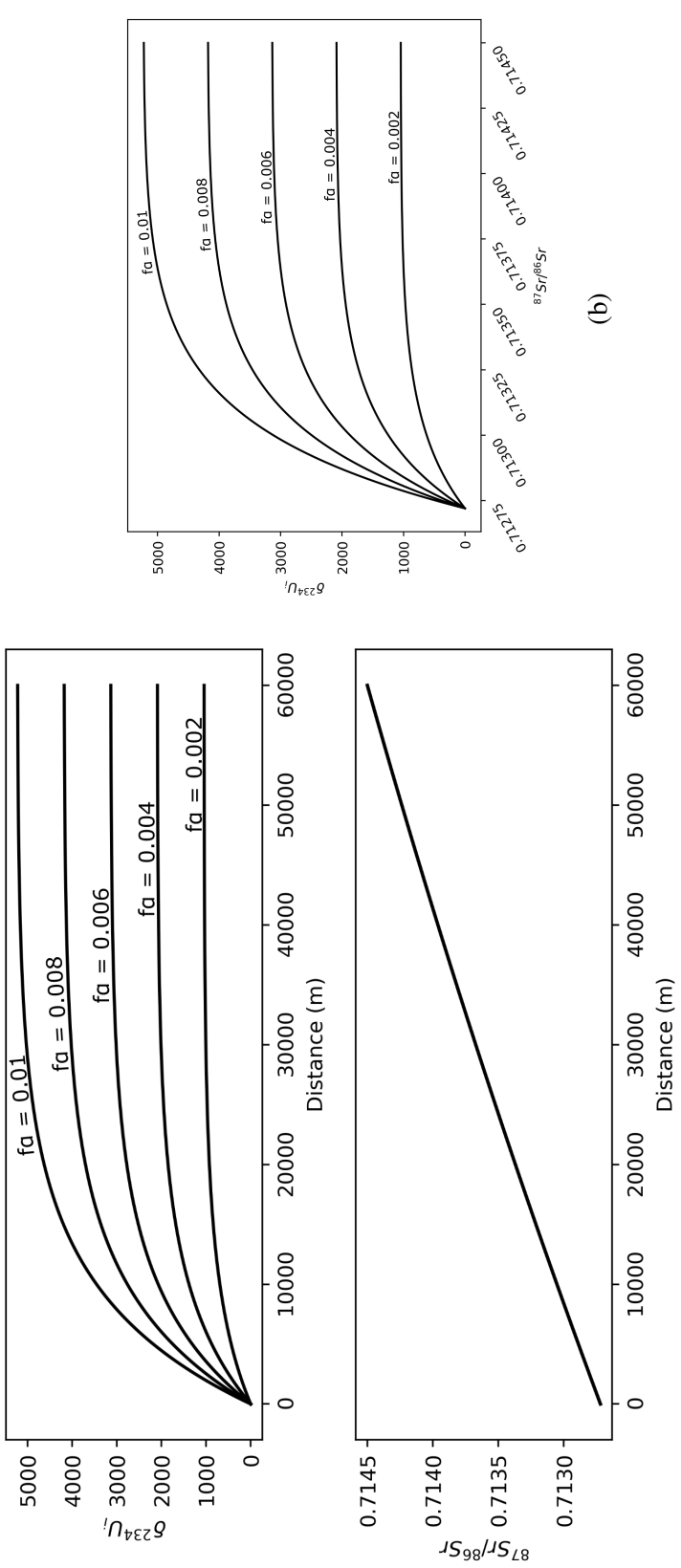

Fig. 5.5 Variable alpha recoil fraction, from 0.002-0.01 at intervals of 0.002, at $k_d = 10 \times 10^{-16} mol/m^2/s$. At higher recoil fractions a larger δ^{234}U can be achieved (top left). ^{87}Sr/^{86}Sr (bottom left) continues to rise because of dissolution. The interaction of the two isotope ratios is shown in the right panel

5.4 Travertine samples

This next section introduces and discusses the travertine data, firstly showing the spatial and temporal trends at the two fault systems.

5.4.1 Spatial records

The distribution of travertine and fluid samples along both the faults are shown in figures 5.6 and 5.7.

Salt Wash

The samples along Salt Wash generally show increasing δ^{234}U and ^{87}Sr/^{86}Sr with distance. Some of the data from Kampman et al. (2012) could be considered outliers with the addition of this new data. The scatter at any location shows the full extent of temporal variation, which is slightly smaller than the variation of both isotope systems between localities. Samples are oldest around the anticline hinge, but otherwise the distribution of samples is largely random.

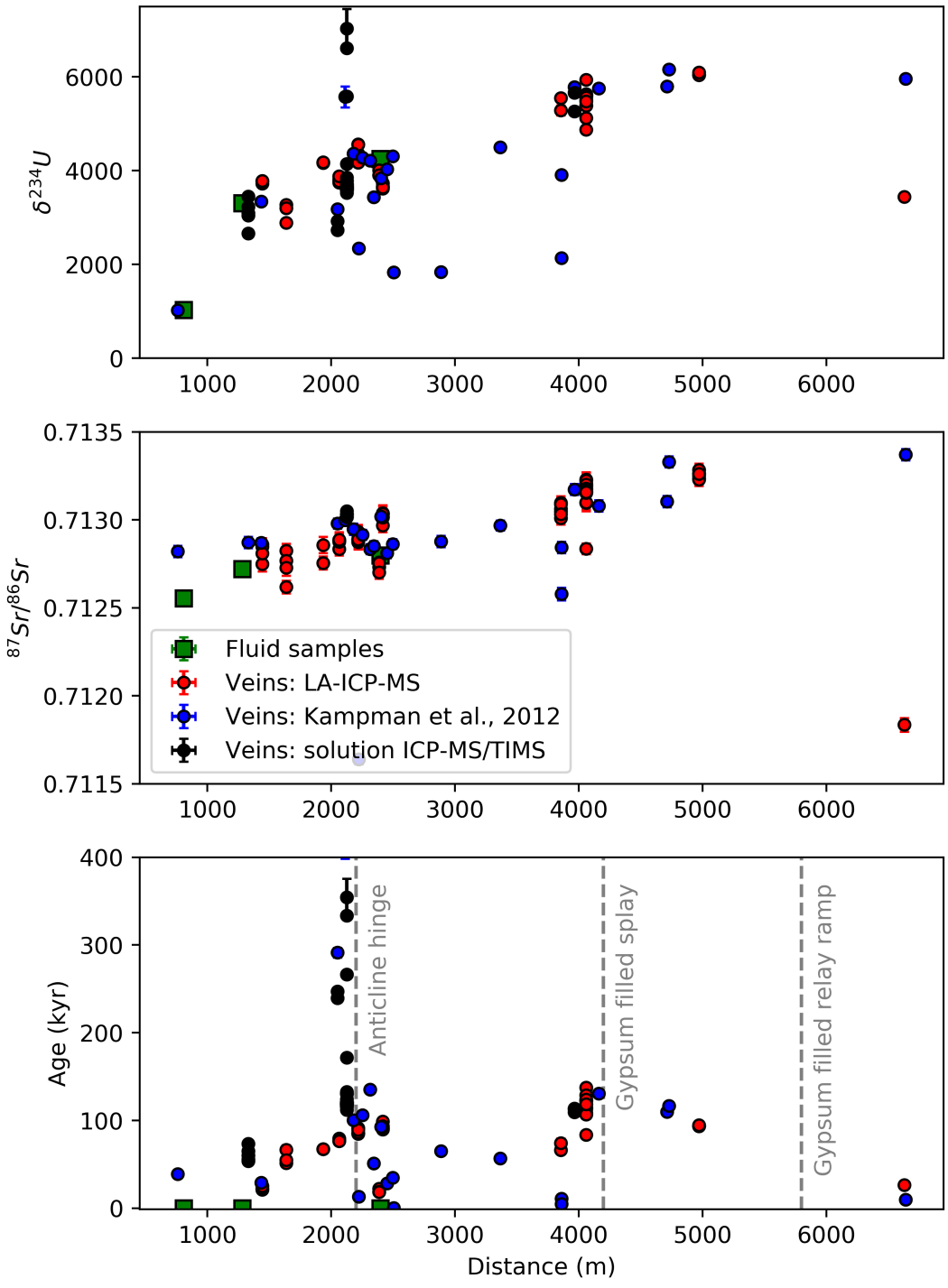

Fig. 5.6 Spatial trends in isotopic composition and age of travertine 'mounds' along Salt Wash from West to East. Zero distance is arbitrarily defined just outside the range of observed travertine (38.8750°N,-110.1370°E). Fluid samples are displayed as green squares and travertine analyses are shown as circles. The data from Kampman et al. (2012) is shown in blue, and black shows new solution analyses. 2σ uncertainties are often smaller than the data points. In red are the travertine samples analysed by laser ablation methods and U data includes excess variance propagation.

Little Grand

Samples along Little grand show increasing δ^{234}U but unlike Salt Wash show decreasing ^{87}Sr/^{86}Sr with distance along the fault. Sample ages are again quite random, but older samples are generally not observed towards the east.

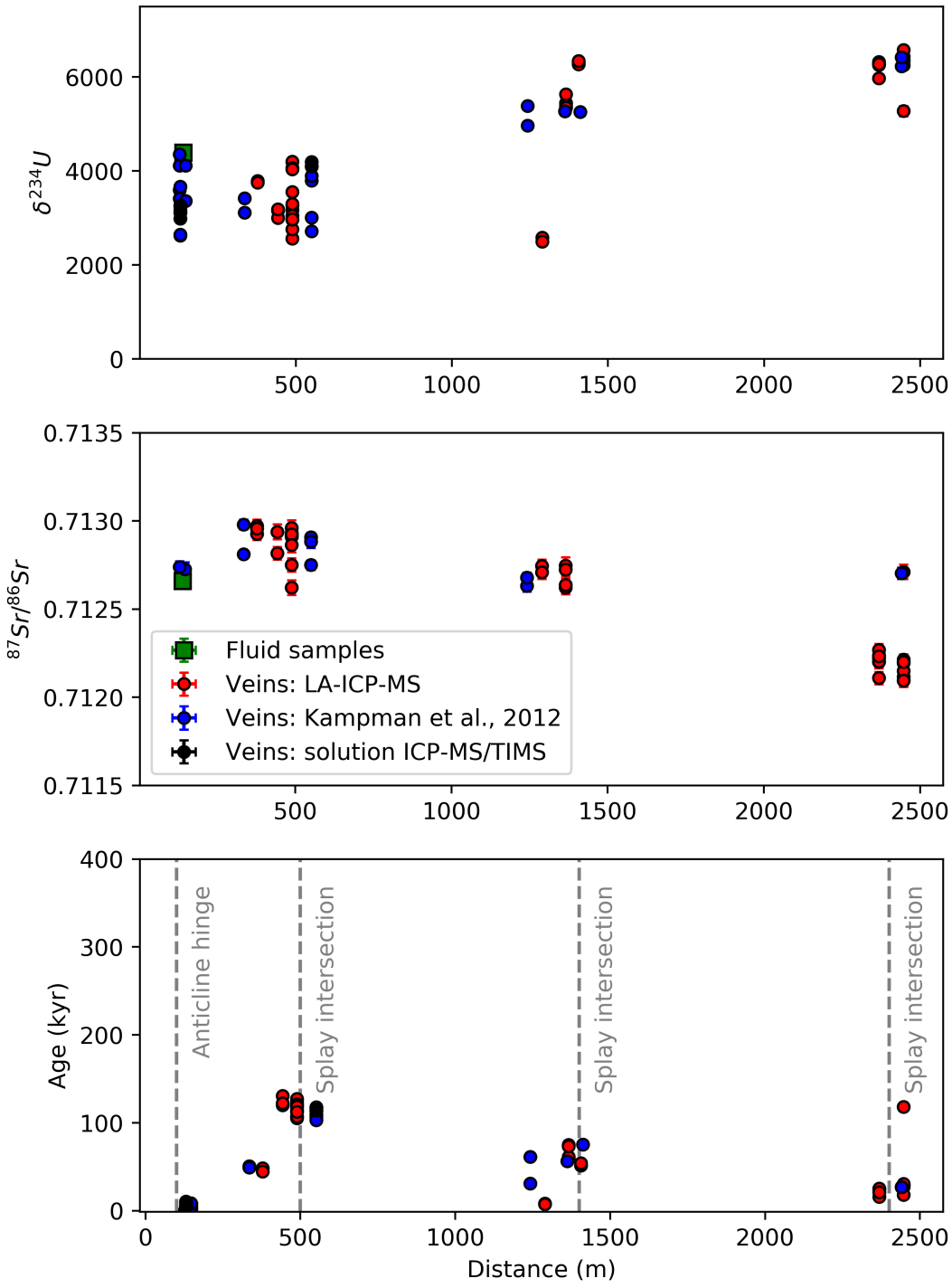

Fig. 5.7 Spatial trends in isotopic composition and age along Little Grand from West to East. Zero distance is defined at the Green River, which is also the position of the anticline hinge. Fluid samples are displayed as green squares and travertine analyses are shown as circles. The data from Kampman et al. (2012) is shown in blue, and black shows new solution analyses. 2σ uncertainties are often smaller than the data points. In red are the travertine samples analysed by laser ablation methods and U data includes excess variance propagation.

5.4.2 Temporal records

The temporal records at each fault and combined are shown in figures 5.8, 5.9 and 5.10.

Salt Wash

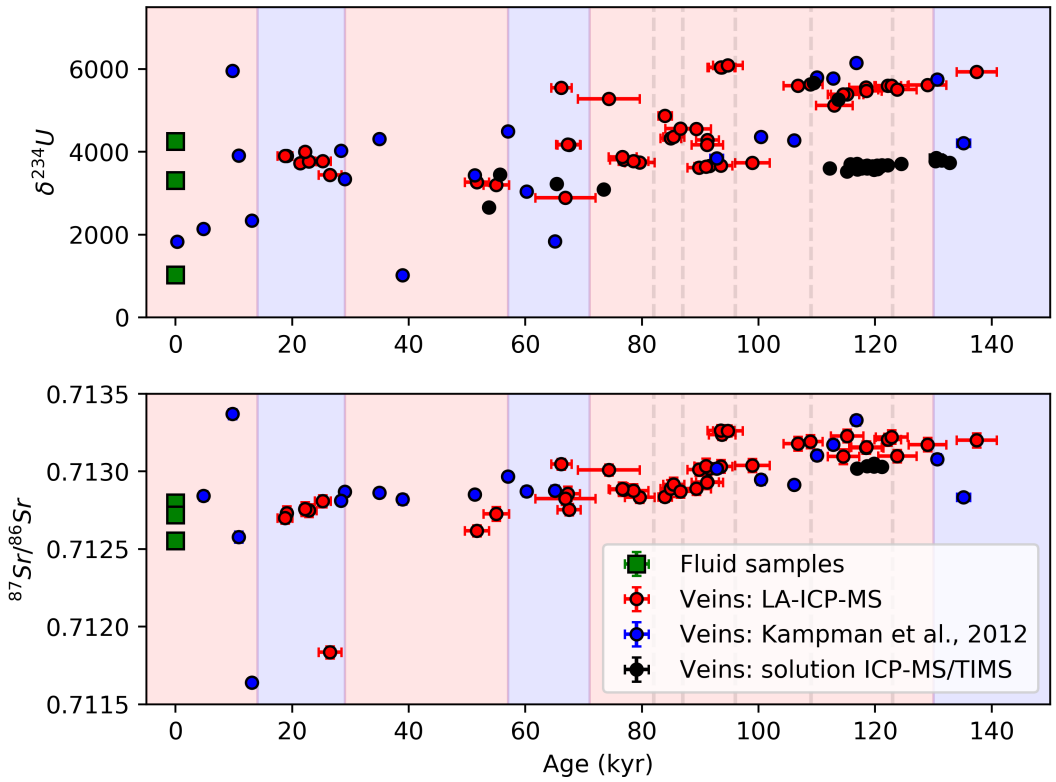

Fig. 5.8 Time series samples along Salt wash fault. Blue/red represent glacial/interglacial periods based upon benthic climate records (Lisiecki and Raymo, 2005). Pink is used to represent interglacials (odd isotope stages), and blue glacials (even isotope stages). Stage 5, 130kyr-71kyr has multiple warming events the peaks of which are indicated by dashed grey lines. Terrestrial records, such as palaeo-lake level, taxonomic records and stable isotopes indicate the impact of these events in the continental interior (Kampman et al., 2012). Data points are coloured as previously, and all data points have 2σ uncertainties.

At Salt Wash, $^{87}Sr/^{86}Sr$ appear to decrease towards the modern day. There is no discernible trend in $\delta^{234}U$. However, these samples are dispersed along the length of the fault zone, with many of the samples with ages $\approx$ 100-150kyr further to the east. The blue data points, which represent the data presented in Kampman et al. (2012) however appear to be outliers, particularly the samples from the LGM into the Holocene ($\approx$ 15-17kyr). Surprisingly, neither of the isotope ratios appear sensitive to larger scale climatic shifts.

Little Grand

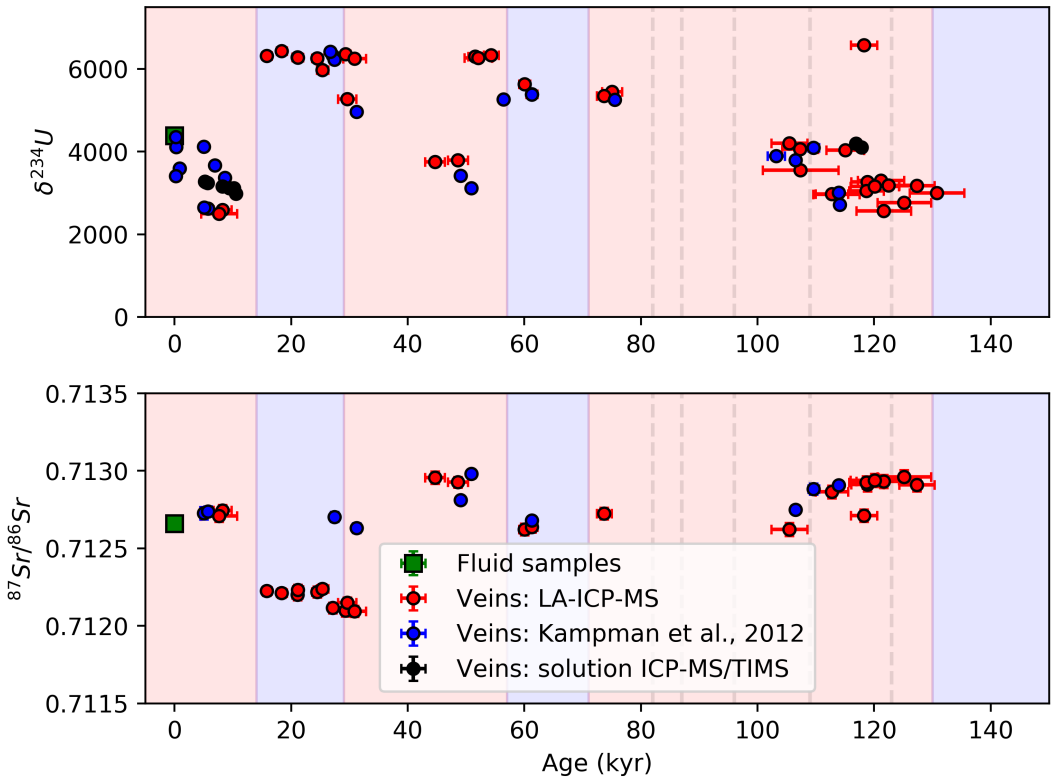

Fig. 5.9 Time series samples along Little Grand fault, colours as in figure 5.8

All samples

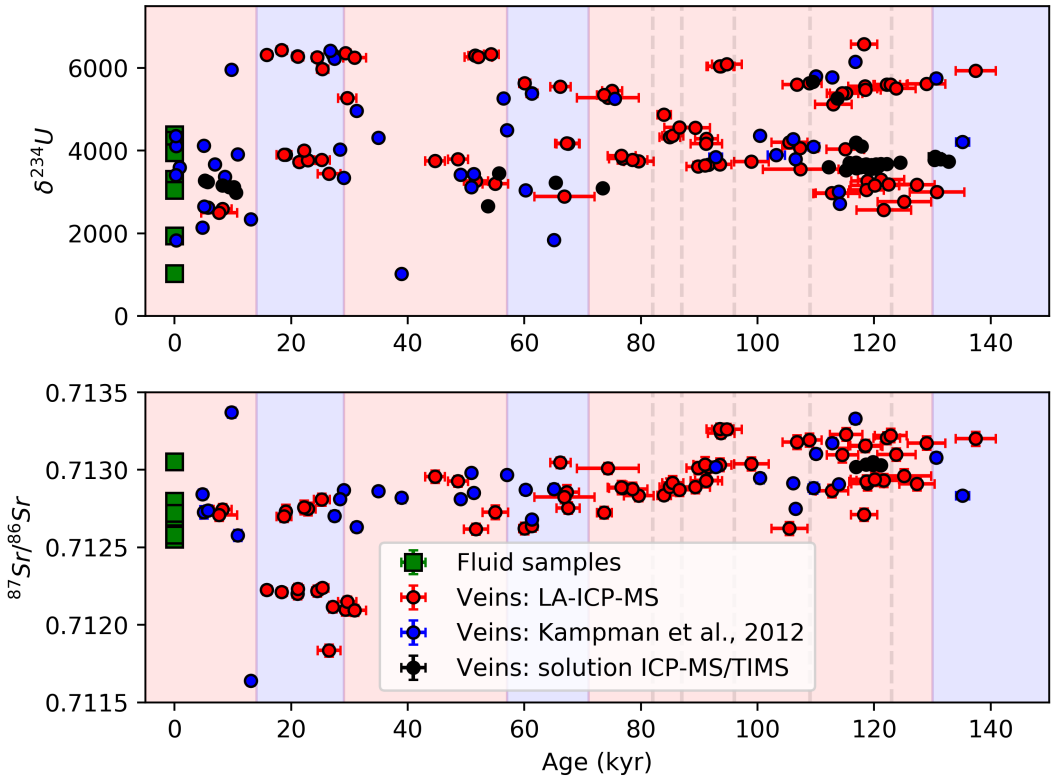

Fig. 5.10 Time series samples along both faults, colours as in figure 5.8

5.4.3 Isotope co-variation

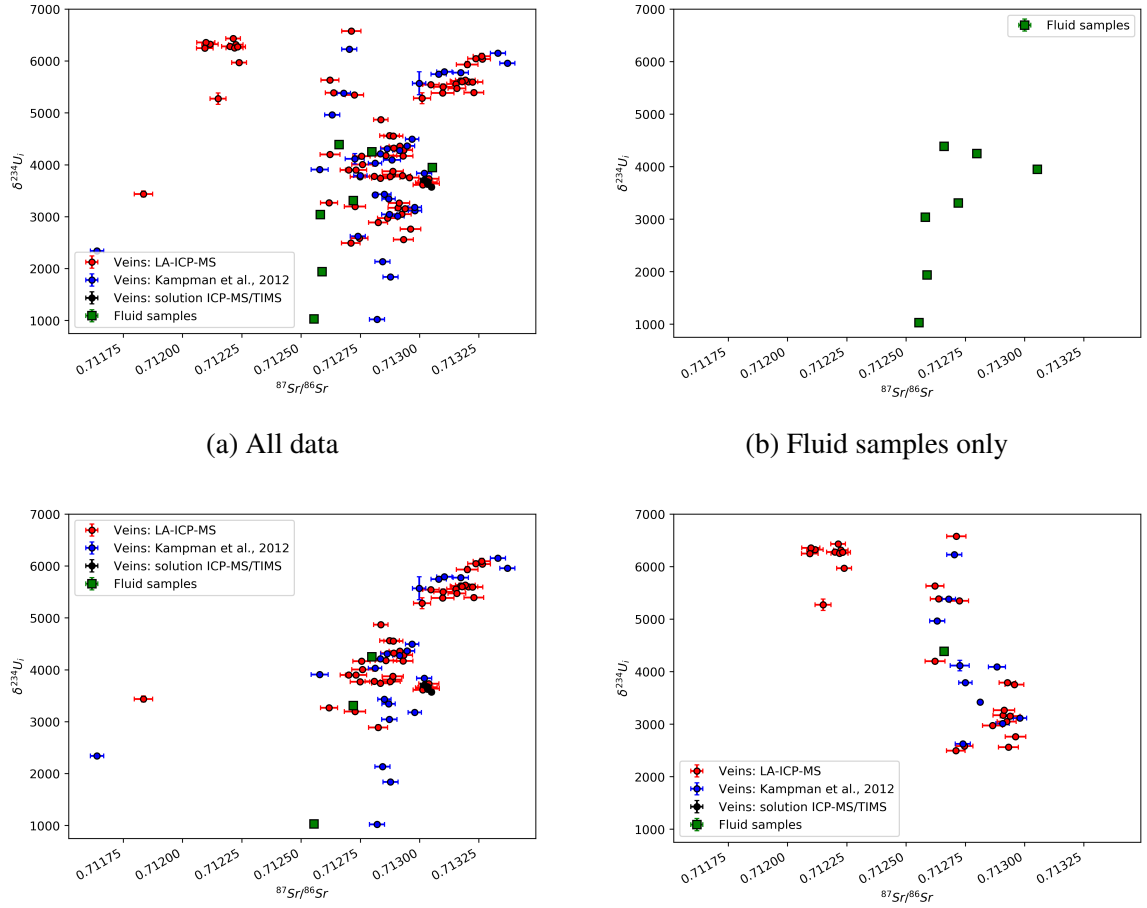

(a) All data

(b) Fluid samples only

(c) Salt wash only

(d) Little Grand only

Fig. 5.11 Covariation in $^{87}Sr/^{86}Sr$ and $\delta^{234}U_i$ in a) All samples, b) Fluid samples, c) Salt Wash samples and d) Little Grand samples.

As previously discussed, at Salt Wash there is visually a positive correlation of $^{87}Sr/^{86}Sr$ and $\delta^{234}U$, which is modelled in the following section. Little Grand, however, remains puzzling as low $^{87}Sr/^{86}Sr$, high $\delta^{234}U$ fall outside of all other data. Potentially, this could be a location of brine input from deeper reservoirs, but would suggest 1) a significant amount of reaction has occurred within these reservoirs to raise the Ismay brine from $^{87}Sr/^{86}Sr$ ≈0.708 to 0.712, and 2) that this reaction has happened slowly to allow α-recoil from U-minerals to occur. Little Grand has a wider fault core than Salt Wash, and vertical migration of CO_2 brines is more likely, and thus the role of mixing more important.

5.4.4 Application of fluid calibrated model to Salt wash travertine veins

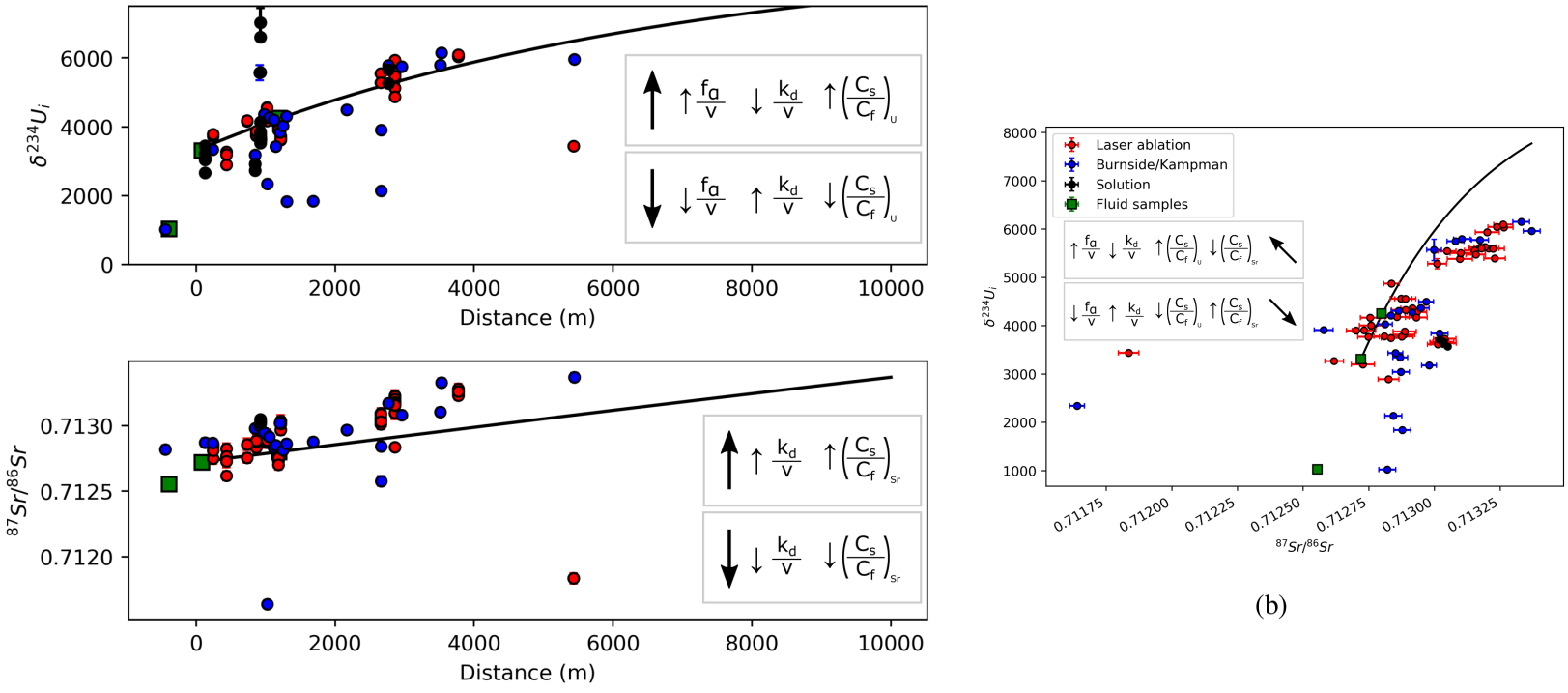

(a) (b)

Fig. 5.12 Samples from along Salt Wash, as previously presented. The black line denotes the evolution of a fluid along a flow path where model parameters are calibrated using fluid samples. Panel a) shows these trends against distance, and b) shows the co-evolution of the two isotope ratios. Inset boxes show the effect of increasing/decreasing parameters within the model. These are only appropriate for the region modelled and are not applicable when the U-isotope system reaches secular equilibrium (as presented in earlier figures). Travertine samples are slightly offset from the modelled flow path as Sr isotope spatial gradient is slightly underestimated by fluid samples. A better fit to the data can be achieved through increasing dissolution rate, the solid/fluid ratio or by decreasing fluid velocities. This may suggest that historic fluid flow is slower relative to the modern day.

Figure 5.12 shows the evolution of fluids along Salt Wash, calibration using the gradient between fluid samples, as discussed earlier. Most of the travertine samples scatter around this trend. A better fit to the travertine data can be achieved by increasing the sensitivity to Sr or decreasing the sensitivity to U. Higher dissolution rates (k_d) achieves this change in both systems. This would provide a mechanism to explain lower Sr isotope compositions with time: rather than invoking fluid mixing (i.e. brine inputs), slower reaction rates in the modern day prevent $^{87}Sr/^{86}Sr$ reaching values as high.

5.5 Model complications/caveats

5.5.1 Particle sizes, weathering history and reservoir heterogeneity

α-recoil is more important in finer grained sediments due to higher surface areas, and therefore contribute a disproportionate fraction of the ^{234}U input. Additionally, these layers likely have lower permeability and therefore slower fluid transport speeds. These reservoir heterogeneities are stratigraphically controlled. However, smaller grain sizes will weather more quickly, and therefore the reacting minerals will be consumed over geoglogical time. The degree to which weathering is incongruent (i.e. secondary minerals deposited) determines the future impact of these beds. Any U left in the secondary phase will continue to provide U through α-recoil, and the U and Sr isotope systems will become decoupled. U adsorption onto clays and other fine grained materials is well observed, and α-recoil from these phases is potentially important. Adsorption will therefore lower the concentration of U in the fluid phase, but the corresponding increase in solid concentration will increase α-recoil. In the model this can be accounted for by increased f_α.

On large feldspar grains, smectite/illite clay layers are observed up to $3\mu m$ thick (Kampman et al., 2009). This is much thicker than the α-recoil distance, and therefore the behaviour of this layer is important, but not understood. These coatings may act to protect the 'pristine' mineral from reacting, and alongside approach to equilibrium can be used as a mechanism to explain lower weathering rates in these reservoirs (Zhu, 2005).

5.5.2 Trace mineral phases, and hints at historic fluid concentrations

Other mineral phases present in the reservoir have been treated as negligible due to their trace nature (despite potentially high concentrations up to 1wt%). For example, Zircon and Apatite are often present <0.1%. In other sediments inputs from these phases have been shown to influence α-recoil by <1%, and can generally be considered negligible (Maher et al., 2006a).

The concentration of historic fluids is inferred to differ from modern fluids, due to the presence of other secondary phases such as celestine $SrSO_4$. Modern fluids require Sr concentrations twice as high to reach celestine saturation, and presumably higher for it to precipitate. Aragonite Sr/Ca ratios back this up: most veins are $\approx 10 mmol/mol$ compared to $\approx 5 mmol/mol$ in modern fluids (the Sr partition coefficient is ≈ 1, see chapter 4 for more thorough discussion). The Sr isotope ratio of historic fluids is therefore likely less sensitive to Sr inputs from dissolution, as $\left(\frac{C_s}{C_f}\right)_{Sr}$ would be smaller and in the wrong direction to improve the model fit to the data.

5.5.3 Effects of migration to the surface

It is assumed that fluid samples have not been altered by precipitation or dissolution reactions during their transport from the reservoir to the surface. This transport most likely occurs through fracture networks, when pressures allow flow. During vertical migration of CO_2-rich brines CO_2 becomes less soluble, and the loss of CO_2 raises solution pH and can cause carbonate over-saturation. This is reflected by precipitation of carbonates and sulphates (dolomite, calcite, aragonite, gypsum and celestine) in fractures. The fluids in aragonite veins represent a minimum concentration bound, assuming no dissolution reactions. However, as is seen in the Entrada formation some fractures show evidence of bleaching and have similar sluggish reaction rates to the reservoir (Kampman et al., 2009; Wigley et al., 2013). Residence times in fracture networks are likely much shorter than the residence time in the reservoir, so such overprinting is small.

5.5.4 Non-steady state: reaction rates and flow paths

Reaction rates

A kinetic relationship between dissolution rates and equilibrium state/saturation index (k_d and ΔG) has been shown (Kampman et al., 2009; Maskell et al., 2015), inferred due to variable saturation state of feldspars along the flow path at Green River. This is driven by higher CO_2 saturations which lower saturation indexes. It is not known if the CO_2 source is entirely dissolved at the original source, or if there is a free phase (gas or supercritical depending upon pressure) within any of the reservoirs at Green River. CO_2 saturated fluids recoverred in the Navajo during drilling imply free CO_2 must be produced during vertical migration (Kampman et al., 2014b). Input of free phase CO_2 which subsequently dissolves will result in higher reaction rates. Along the flow path, dissolution will bring fluids closer to

equilibrium which should lower dissolution rates. Therefore, with increasing distance (as equilibrium is approached) dissolution rates decrease, but α-recoil continues at the same rate. This slows the rate of change on $^{87}Sr/^{86}Sr$ and increases the maximum value for $\delta^{234}U$. If steady state between recoil and dissolution has not yet been met, the rate of change of $\delta^{234}U$ will increase. Such a relationship can be implemented numerically.

Flow paths

The flow paths inferred represent the minimum distance which could be travelled by a volume of fluid. At Salt Wash, it is reasonable that flow occurs along the fault due to high shale-gouge ratios (Dockrill and Shipton, 2010). Alternatively flow occurs from Little Grand to Salt Wash, in keeping with regional pressure gradients. Most vertical leakage occurs around the anticline hinge, suggesting some degree of fluid channelling. The NNW-SSE trending graben along the hinge of the anticline between Little Grand and Salt Wash is not transmissive to fluids and therefore may promote channelling of fluids along the hinge. Once beyond these two faults, the dominant groundwater flow sweeps fluids parallel to the fault. However, it is possible that the most easterly samples take slower fluid pathways from the north.

The fluids at Little Grand probably come from more diverse flow paths, as fluids from the north could take very slow flow paths. Additionally the wider fault core may increase the likelihood of fluids from underlying reservoirs leaking vertically into the Navajo.

5.5.5 Multiphase effects

A free gas phase (CO_2(g)) in the reservoir will significantly reduce the volume of interacting fluid and rock. The residual fluid (water/brine) trapped by surface tension between reservoir grains will continue reacting, potentially at higher rates due to CO_2 saturation driving pH down. Interactions will depend upon which phase (CO_2 or H_2O) wets mineral surfaces due to surface tension (contact angles). If a mineral is water wet, the fluid will continue to evolve similarly as before, possibly faster from lower pH increasing dissolution rates. However, the smaller volume of fluid will lead to larger values of M_s which also increase the impact of α-recoil terms. If a mineral is CO_2 wet, dissolution is less likely to occur (hydrolysis reactions cannot occur), but α-recoil continues and the daughter nuclide settles on mineral surfaces at the base of the pore. If water flushes through (imbibition) this pore again, then the ^{234}U will likely dissolve, leading to a much higher $\delta^{234}U$ than would be anticipated. These effects could be responsible for some of the high $\delta^{234}U$ signatures observed at Little Grand fault.

5.6 Conclusions

This chapter derived and calibrated a simple advective reactive transport model. The model provides a framework to interpret chemical observations along the fault (modern spring samples and historic travertine) and allows us to estimate dissolution rates and α-recoil fraction (a function of mineral surface areas). Fluid samples along Salt Wash are used to calibrate these parameters within this model, and has the advantage that reservoir heterogeneities such as mineralogical composition, grain sizes and bulk element concentrations are averaged. Flow is assumed to be within the Navajo sandstone, but the deeper aquifers will respond in a similar manner. This calibrated model shows a reasonable fit to travertine vein samples along Salt Wash, showing that mineral dissolution and α-recoil along the flow path are responsible for the increase of both δ^{234}U and ^{87}Sr/^{86}Sr along the flow path. This contradicts previous interpretations of ^{87}Sr/^{86}Sr, which did not account for this spatial variability (i.e. Kampman et al. (2012)). Samples at Little Grand fault cannot be interpreted as easily with these models. This is probably related mixing; either accommodated by the structures of the fault zone, allowing for vertical fluid migration or the flow paths leading towards Little Grand are more diverse. During some time periods, for example $\approx$100-120kyr, the gradient between the two fault zones can fit with the reactive transport model but this is inconsistent for δ^{234}U at $\approx$18-24kyr.

The temporal trends for δ^{234}U at each fault show no systematic structure, which suggests the spatial trends are more robust. However, for ^{87}Sr/^{86}Sr there is a suggestion of a general decrease in ratio. The large variability in ^{87}Sr/^{86}Sr, and some of the larger jumps in composition observed by Kampman et al. (2012), do not appear robust and do not record clear climatic trends. As δ^{234}U and ^{87}Sr/^{86}Sr can decouple, it is possible that the decreasing temporal trend is real. In this case, it would infer decreasing rates of silicate dissolution or fluid with larger Sr concentrations. However, further work is necessary to deconvolve temporal and spatial variability.

Chapter 6

Discussion and conclusions

Geological carbon storage is a necessary tool for reducing anthropogenic CO_2 emissions, which currently are not falling fast enough to avoid severe climatic change. The fate of injected CO_2 within reservoirs must be quantified, in order to quantify risk. A range of geochemical and geomechanical fluid-rock interactions can act to increase or decrease the potential risk of leakage. Fractures, fault seals, well-holes and caprocks are the main areas where these interactions may pose risk. Processes which decrease the integrity of these features or increase fluid fluxes are undesirable to site storage security. CO_2 accumulations in the Colorado plateau show that long-term storage is possible in the correct settings. The field site at Green River (Utah), used in this study, is unique as CO_2 seeps to the surface along two fault systems. Modern fluids, a cold-water geyser, elevated CO_2 soil gas fluxes and historic carbonate deposits attest to a history of leakage over at least 150-400kyr. This thesis has investigated the records preserved in aragonite feeder veins, furthering an initial low resolution studies conducted by Kampman et al. (2012) and Burnside et al. (2013). The main finding are summarised below, with short comments on potential further work.

6.1 Laser Ablation methods

To measure these records, laser ablation methods for $^{87}Sr/^{86}Sr$ and $^{234}U/^{238}U$-$^{230}Th/^{238}U$ have been developed. These methods allow for rapid screening of carbonate samples for both isotopic compositions and age. However, issues with isobaric interferences must be solved, and the short collection times must be optimised to maximise precision.

Sr isotopes have potential issues with a range of isobaric interferences, and it is shown that many of these can be avoided by using medium instrument resolution. This improves the accuracy of measurements in difficult matrices, such as NIST glasses, and provides

certainty of accuracy in terrestrial carbonates which precipitate from a diverse range of parent fluid compositions. The long-term reproducibility of this technique is $\pm 42 \times 10^{-6} (2\sigma)$ for $^{87}Sr/^{86}Sr$. The use of medium resolution also avoids interferences on the minor Sr isotope ratio $^{84}Sr/^{86}Sr$, which can then be used as an indirect method for monitoring stable Sr isotope compositions (which are used for mass bias correction). This is not possible using previous methods because of Ca-dimer and REE^{++} interferences. The stable isotope composition $^{88}Sr/^{86}Sr$ (or $\delta^{88}Sr$) can only be determined using standard-sample bracketing techniques. $\delta^{88}Sr$ determined relative to a standard does not show sufficient accuracy or precision to be useful on these short collections. During standard-sample bracketing, significant matrix related drift is observed between carbonate matrices with compositions differing by $\approx 1-2\%$. This is particularly important, as some users continue to mix matrices which compromises results. Additionally 'novel' means of data reduction; i.e. direct linear response give inaccurate results on short collections of relatively homogeneous materials.

U-Th isotopes do not have significant isobaric interferences, but the low abundance of ^{230}Th limits achievable precision. Additionally, the inter-element fractionation between U and Th makes standard-sample bracketing the only appropriate method of data collection. Studies to date have used intense ablation parameters for collections up to 15 minutes long to achieve dates of sufficient precision. Often uncertainties are not propagated. We show that accurate and precise results can be achieved at very low count rates (<30cps). Less intensive laser ablation parameters are used and collection times are relatively short at 2.5 minutes. In total this allows smaller masses of material to be analysed, at around a quarter of the size of Spooner et al. (2016) and smaller still compared to Lin et al. (2017). Excess variance propagation is included, and total propagated uncertainties are the same size as other methods. We show that the excess variance propagation is reasonable on samples from the same field area, and that on a secular equilibrium speleothem this represents an over-propagation. The precision on stable U isotopes ($\delta^{238}U$) is sufficient to screen the extremes in variation, but not small enough to capture most variation.

Both methods may be improved by using new $10^{13}\Omega$ resistors, though detectors need to be carefully calibrated to avoid biases from slower response times. This may even allow determination of the stable isotope ratios.

6.2 Vein records

The records preserved within travertine veins vary at a range of scales. Prior to this thesis records at fault scale for $\delta^{18}O$, $\delta^{13}C$, $^{87}Sr/^{86}Sr$ and trace metals (Kampman et al., 2012),

and at cm to mm scale for $\delta^{18}O$, $\delta^{13}C$ (Frery et al., 2016; Horne et al., 2013; Kampman et al., 2012). These are interpreted either to represent fluid mixing at fault-scale, or Rayleigh fractionation trends caused by decompression induced exsolution of CO_2. Records for $\delta^{234}U_i$ have existed, but only qualitatively explained (Burnside et al., 2013).

At cm to mm scale, I have presented new results for $\delta^{13}C$, $\delta^{18}O$ and trace metals. The stable isotopes appear to show the same Rayleigh fractionation trend as modelled by Kampman et al. (2012). However, trace metals do not support this evidence, though partition coefficients in aragonite formed at low pH are not particularly well constrained. Overall, this suggests that the trends at this scale are largely induced by fluid mixing but potentially with a small component of growth rate dependant partitioning. However, laser ablation measurements of $^{87}Sr/^{86}Sr$ and $\delta^{234}U_i$ show limited variation within a given sample compared to the variability between sample localities. The veins represent relatively short periods of time; typically 5kyr, and there may be some small, currently unresolvable biases in the geochronology due to initial ^{230}Th.

At high resolution (200-300μm), annual laminations are visible on a fast growing sample from next to Crystal Geyser. The chemical trends across these laminations show similarities to mixing trends seen during man-made geysering activity. The laminations preserve either a mixing signal or rayleigh signal, as elements such as Mn and Fe are in anti-phase to U-Y-V. Each lamination has a corresponding peak in Y, which is highly compatible. This peak therefore suggests that fluids which have not precipitated carbonate are input into the system. Whilst the partition coefficients for Fe and Mn are not constrained it cannot be confirmed that this does not represent a rayleigh fractionation process. If it is explained by fractional crystallisation, then a single fluid is required rather than mixing of two fluids. Therefore in both scenarios a fresh fluid input is required. This suggests a variable annual flux of fluid from the Navajo. Seasonal trends in stress (and seismicity) can arise from to groundwater storage and use (Johnson et al., 2017). Stresses are known to influence the size of fracture apertures and therefore vertical permeabilities, which could be used to explain such cyclicity. This is essentially the same argument as Kampman et al. (2012), but rather than the crust responding to glacial-interglacial climatic forcing, it is responding to annual stresses. This is probably only possible when fractures are under (not quite near critical) tensile stress, so respond to small local changes in pore fluid pressures. The anticline hinge is the most likely place that such behaviour occurs, and fluid pressures will be higher prior to the reservoir being drained by man-made Geysering activity.

This work can be furthered by analysis of the geyser timeseries samples and downhole fluid samples to confirm/deny these elemental trends in the modern day. Also estimates of

currently unknown partition coefficients (Al, Zr, Fe, Mn) may be achievable, if those end-members are determined. Finally, analysis of $^{87}Sr/^{86}Sr$ and $\delta^{234}U_i$ across these laminations may also be used to indicate mixing trends, but may be close to the achievable limits of precision.

6.3 Reactive transport modelling

The limited variation of $^{87}Sr/^{86}Sr$ and $\delta^{234}U_i$ preserved within veins forms the basis for implementing a reactive transport approach. A simple one dimensional analytical solution is derived for advective transport, incorporating dissolution and α-recoil terms. These parameters are tuned to modern fluid samples. Flow is assumed to occur through the Navajo sandstone, parallel to the fault, and the range of flow rates is constrained from hydraulic heads (defining a potentiometric surface) and conductivity measurements. Using fluid samples to calibrate the model is advantageous, as they averages out reservoir heterogeneities and eliminates some uncertainties. Using this model, it can be shown that most variation is readily explained by evolution of a single fluid with distance along the fault. The deeper, un-sampled aquifers will behave in similar fashion. Using such a calibration infers slower flow rates than used in Kampman et al. (2009), as otherwise fluid residence times are too short to describe $\delta^{234}U_i$ variation.

Samples along Salt Wash show increasing $^{87}Sr/^{86}Sr$ and $\delta^{234}U_i$ along the distance of the fault, and show reasonable fit to the fluid-calibrated model. This contradicts previous interpretation of samples by their depositional age (Kampman et al., 2012), as the sample location along the flow path appear more important in determining the isotopic composition. Samples at Little Grand do not conform to this model and requires either more diverse flow paths towards the fault or more vertical flow of fluids between reservoirs.

There are caveats to this model; dissolution rates are assumed constant, but are known to vary with solution composition (Kampman et al., 2009). More complex numerical models could include such a relationship, but require estimates of starting compositions. Potential biases' in thermodynamic datasets would require quantification. Alternatively, the simple model could be run in reverse: each sample is treated as the end of a flow path and the flow path leading to that point is modelled. A third isotope system that is sensitive to silicate dissolution could aid in identifying where mixing is a significant cause of variation. Direct measurements of $\delta^{234}U$ on Navajo core samples could improve estimates of f_α, and test the method of tuning to fluid samples. Alternatively, the next isotope in the U-series decay chain ^{226}Ra could be measured on fluid samples, as it is influenced by similar α-recoil processes.

6.4 Changing interpretations of Green River

The travertine veins preserved at Green River, and the chemical trends within them, inform that:

- The largest travertine volumes correlate with glacial-interglacial transitions, in keeping with the main argument of Kampman et al. (2012).
- The variability of isotopic tracers within carbonate veins at individual localities (i.e. $^{87}Sr/^{86}Sr$ and $\delta^{234}U_i$) is limited compared to the total range observed by Kampman et al. (2012). Veins spanning time intervals where isotopic change is anticipated show no such variability, and was a slightly surprising result.
- Variation in isotope ratios along the Salt Wash Fault show strong spatial correlations whilst records at individual localities show limited temporal variability. This suggests that large swings in chemical composition observed by Kampman et al. (2012) are artefacts of the spatial distribution of travertine deposits, and more similar to the interpretation of modern spring samples (Kampman et al., 2009).
- Variation in isotope ratios along the Little Grand Wash Fault show poorer correlation, and much higher U isotope ratios and lower Sr isotope ratios suggest more sluggish flow rates with a low degree of chemical reaction or more varied fluid mixing. These fluids are potentially sourced from the north and north-east of the fault, where CO_2 inputs are less significant.
- Spatial variations in both U and Sr isotope ratios can be used to parameterise reactive transport models. These models may be inverted to solve for unknowns such as flow rate, alpha-recoil factor and surface area. No significant variation in flow rate is detectable during glacial-interglacials periods due to large uncertainties on model parameters, but may be reduced in future work.
- One sample location preserves annual laminations. Seasonal dilution can be discarded using trace metal concentrations. Fluid mixing appears dominant and can be explained by mixing of Navajo and Entrada derived fluids. Presently, Crystal Geyser erupts at the same location and eruptions show similar mixing trends. During a CO_2 leak, vertical fluxes respond to small scale climatic forcing. As the two formations are separated by the faulted Carmel formation (a fractured caprock) a seasonal response of fracture aperture within the fault zone to crustal stresses could be responsible. However, Rayleigh fractionation as an explanation of chemical trends cannot be eliminated without further

determination of partition coefficients.

This work presented in this thesis shows that lateral flow within the Navajo sandstone along the Salt Wash fault can be used to explain the major isotopic trends. At Little Grand Wash fault more diverse fluid flow paths and fluid mixing make interpretation using these models less simple. The travertine deposits reflect unique periods of intense vertical fluid migration through a fractured fault zone. During these leak events, larger scale pressure conditions driven by climate can influence fluid fluxes suggesting variable response of fracture apertures. The mixing trends observed resemble those during cold-watering geysering at Crystal Geyser.

6.5 Summary and future work

The CO_2 seeps at Green River in Utah, are an excellent analogue for understanding the long-term storage of CO_2 in crustal reservoirs. However, there are limits to using proxies preserved within vein records at this site. Fluid-end members, and particularly historic fluid end-members, have shifting compositions due to fluid-rock interactions along a flow path. Untangling the processes occurring in reservoirs, especially once they have been overprinted by carbonate precipitation processes when using vein records, can prove tricky. Further constraint is required on partition coefficients during aragonite precipitation at low pH if palaeo-fluids compositions are to be accurately quantified. However, in the absence of this knowledge it is still possible to infer differences between mixing and Rayleigh fractionation processes (or mixtures of the two). Given the composition of fluids from the major reservoirs (the Navajo and the Entrada), it is likely that fluid mixing is dominant in these veins. To explain this mixing trend requires vertical fluid migration across the fractured Carmel caprock which must vary annually in response to climatic drivers.

Reactive transport modelling of these travertine deposits confirms previous observations of low silicate dissolution rates, which is commonly observed in fluids near to equilibrium. However, the reactive surface area remains uncertain and ultimately limits reaction rates. At Green River, there are also hints of microbial processes occurring at the surface and in the shallow subsurface. It is reasonable to assume that such activity also occurs in the reservoirs. The impact of these on mineral weathering, and on permeability-porosity changes in reservoirs could be very interesting.

Ultimately though, with regards to carbon capture and storage most parameters are well enough understood for larger scale injection to occur. The barriers to this are not scientific;

they are economic and politic. The integrity of caprocks are well constrained, fault zone and fracture networks are well characterised at potential injection sites and well cement integrity is proven. Reactions in silicate reservoirs appear sluggish with pure CO_2, but dissolution rates are less well constrained, and consequences of reactions in silicate reservoirs have not been shown to negatively impact either reservoir permeability or integrity. In stacked aquifer systems, such as Green River, it is shown that the leakage of CO_2 to the surface is inhibited by stacked aquifer systems in shallow reservoirs. The Green River faults are of similar throw to reservoir bounding faults within the North Sea; however these faults are not continuous to the surface, and most sites have $\approx$1500m of overburden to pass through. The risks of leakage at such sites is therefore quite low.

References

Albarède, F., Albalat, E., and Télouk, P. (2015). Instrumental isotope fractionation in multiple-collector icp-ms. *Journal of Analytical Atomic Spectrometry*, 30:1736–1742.

AlKhatib, M. and Eisenhauer, A. (2016a). Calcium and Strontium Isotope Fractionation during precipitation from aqeous solutions as a function of temperature and reaction Rate; II. Aragonite. *Geochimica et Cosmochimica Acta*, 209:320–342.

AlKhatib, M. and Eisenhauer, A. (2016b). Calcium and Strontium Isotope Fractionation in Aqueous Solutions as a Function of Temperature and Reaction Rate; I. Calcite. *Geochimica et Cosmochimica Acta*, 209:296–319.

Allis, R., Chidsey, T., Gwynn, W., and Allis T. Chidsey, W. Gwynn, C. Morgan, S. White, Michael Adams, and Joseph Moore., R. (2001). Natural CO2 reservoirs on the Colorado Plateau and southern Rocky Mountains: Candidates for CO2 sequestration. ... *Carbon Sequestration*, page 3.

Allison, N. and Finch, A. A. (2010). δ11B, Sr, Mg and B in a modern Porites coral: the relationship between calcification site pH and skeletal chemistry. *Geochimica et Cosmochimica Acta*, 74(6):1790–1800.

Andersen, M. B., Elliott, T., Freymuth, H., Sims, K. W. W., Niu, Y., and Kelley, K. a. (2014). The terrestrial uranium isotope cycle. *Nature*, 517(7534):356–359.

Andersen, M. B., Stirling, C. H., Potter, E.-K., Halliday, A. N., Blake, S. G., McCulloch, M. T., Ayling, B. F., and O'Leary, M. J. (2010). The timing of sea-level high-stands during Marine Isotope Stages 7.5 and 9: Constraints from the uranium-series dating of fossil corals from Henderson Island. *Geochimica et Cosmochimica Acta*, 74(12):3598–3620.

Andersen, M. B., Vance, D., Morford, J. L., Bura-Nakić, E., Breitenbach, S. F. M., and Och, L. (2016). Closing in on the marine 238U/235U budget. *Chemical Geology*, 420:11–22.

Andreasen, R. and Sharma, M. (2007). Mixing and Homogenization in the Early Solar System: Clues from Sr, Ba, Nd, and Sm Isotopes in Meteorites. *The Astrophysical Journal*, 665(1):874–883.

Andrews, J. N., Giles, I. S., Kay, R. L. F., Lee, D. J., Osmond, J. K., Cowart, J. B., Fritz, P., Barker, J. F., and Gale, J. (1982). Radioelements, radiogenic helium and age relationships for groundwaters from the granites at Stripa, Sweden. *Geochimica et Cosmochimica Acta*, 46(9):1533–1543.

Andrews, J. N. and Kay, R. L. F. (1982). 234U/238U activity ratios of dissolved uranium in groundwaters from a jurassic limestone aquifer in England. *Earth and Planetary Science Letters*, 57:139–151.

Assayag, N., Bickle, M., Kampman, N., and Becker, J. (2009). Carbon isotopic constraints on CO2 degassing in cold-water Geysers, Green River, Utah. *Energy Procedia*, 1(1):2361–2366.

Bachu, S. (2015). Review of CO2 storage efficiency in deep saline aquifers. *International Journal of Greenhouse Gas Control*, pages 1–15.

Balcaen, L., Bolea-Fernandez, E., Resano, M., and Vanhaecke, F. (2015). Inductively coupled plasma - Tandem mass spectrometry (ICP-MS/MS): A powerful and universal tool for the interference-free determination of (ultra)trace elements - A tutorial review. *Analytica Chimica Acta*, 894:7–19.

Barth, J. A. and Chafetz, H. S. (2015). Cool water geyser travertine: Crystal Geyser, Utah, USA. *Sedimentology*, 62(3):607–620.

Bayon, G., Henderson, G. M., Etoubleau, J., Caprais, J.-C., Ruffine, L., Marsset, T., Dennielou, B., Cauquil, E., Voisset, M., and Sultan, N. (2015). U-Th isotope constraints on gas hydrate and pockmark dynamics at the Niger delta margin. *Marine Geology*, 370:87–98.

References

Bense, V. F., Gleeson, T., Loveless, S. E., Bour, O., and Scibek, J. (2013). Fault zone hydrogeology. *Earth-Science Reviews*, 127:171–192.

Benson, A., Kinsley, L., Willmes, M., Defleur, A., Kokkonen, H., Mussi, M., and Grün, R. (2013a). Laser ablation depth profiling of U-series and Sr isotopes in human fossils. *Journal of Archaeological Science*, 40(7):2991–3000.

Benson, S., Pini, R., Reynolds, C., and Krevor, S. (2013b). *Relative permeability analyses to describe multi-phase flow in CO2 storage reservoirs*. Number 2.

Bernal, J.-p., Eggins, S. M., and Mcculloch, M. T. (2005). Accurate in situ 238U-234U–232Th–230Th analysis of silicate glasses and iron oxides by laser-ablation MC-ICP-MS. *Journal of Analytical Atomic Spectrometry*, 20:1240–1249.

Bernhard, G., Geipel, G., Brendler, V., and Nitsche, H. (1998). Uranium speciation in waters of different uranium mining areas. *Journal of Alloys and Compounds*, 271-273:201–205.

Bernhard, G., Geipel, G., Reich, T., Brendler, V., Amayri, S., Nitsche, H., and Nitsche, H. (2001). Uranyl(VI) carbonate complex formation: Validation of the Ca2UO2(CO3)3(aq.) species. *Radiochimica Acta*, 89(37104):511.

Besselink, R., Rodriguez-Blanco, J. D., Stawski, T. M., Benning, L. G., and Tobler, D. J. (2017). How short-lived ikaite affects calcite crystallisation. *Crystal Growth & Design*, page acs.cgd.7b00743.

Bickle, M. (2009). Geological carbon storage. *Nature Geoscience*, 2(December).

Bickle, M. J., Bunbury, J., Chapman, H. J., Harris, N. B. W., Fairchild, I. J., and Ahmad, T. (2003). Fluxes of Sr into the headwaters of the Ganges. *Geochimica et Cosmochimica Acta*, 67(14):2567–2584.

Bickle, M. J., Chapman, H. J., Bunbury, J., Harris, N. B. W., Fairchild, I. J., Ahmad, T., and Pomiès, C. (2005). Relative contributions of silicate and carbonate rocks to riverine Sr fluxes in the headwaters of the Ganges. *Geochimica et Cosmochimica Acta*, 69(9):2221–2240.

Bigeleisen, J. (1996). Temperature dependence of the isotope chemistry of the heavy elements. *Proceedings of the National Academy of Sciences*, 93(September):9393–9396.

Blue, C. R., Giuffre, A., Mergelsberg, S., Han, N., De Yoreo, J. J., and Dove, P. M. (2017). Chemical and physical controls on the transformation of amorphous calcium carbonate into crystalline CaCO3 polymorphs. *Geochimica et Cosmochimica Acta*, 196:179–196.

Blundy, J. and Wood, B. (1994). Prediction of crystal-melt partition coefficients from elastic moduli. *Nature*, 372(6505):452–454.

Bolea-Fernandez, E., Balcaen, L., Resano, M., and Vanhaecke, F. (2016a). Tandem ICP-mass spectrometry for Sr isotopic analysis without prior Rb/Sr separation. *Journal of Analytical Atomic Spectrometry*, 31(1):303–310.

Bolea-Fernandez, E., Van Malderen, S. J. M., Balcaen, L., Resano, M., and Vanhaecke, F. (2016b). Laser ablation-tandem ICP-mass spectrometry (LA-ICP-MS/MS) for direct Sr isotopic analysis of solid samples with high Rb/Sr ratios. *Journal of Analytical Atomic Spectrometry*, 31(2):464–472.

Bourdon, B. (2003). *Uranium-series Geochemistry*. Mineralogical Society of America,, vol 52; re edition.

Brantley, S. L., White, A. F., and Kubicki, J. D. (2008). *Kinetics of water-rock interaction*.

Breitenbach, S. F. M., Rehfeld, K., Goswami, B., Baldini, J. U. L., Ridley, H. E., Kennett, D. J., Prufer, K. M., Aquino, V. V., Asmerom, Y., Polyak, V. J., Cheng, H., Kurths, J., and Marwan, N. (2012). Constructing proxy records from age models (COPRA). *Climate of the Past*, 8(2007):1765–1779.

Brennecka, G. a., Borg, L. E., Hutcheon, I. D., Sharp, M. a., and Anbar, A. D. (2010). Natural variations in uranium isotope ratios of uranium ore concentrates: Understanding the 238U/235U fractionation mechanism. *Earth and Planetary Science Letters*, 291(1-4):228–233.

Buchardt, B., Seaman, P., Stockmann, G., Vous, M., Wilken, U., Düwel, L., Kristiansen, A., Jenner, C., Whiticar, M. J., Kristensen, R. M., Petersen, G. H., and Thorbjørn, L. (1997). Submarine columns of ikaite tufa. *Nature*, 390(6656):129–130.

Burnside, N. (2010). U-Th dating of travertines on the Colorado Plateau: implications for the leakage of geologically stored CO2.

Burnside, N. M. and Naylor, M. (2014). Review and implications of relative permeability of CO2/brine systems and residual trapping of CO2. *International Journal of Greenhouse Gas Control*, 23:1–11.

Burnside, N. M., Shipton, Z. K., Dockrill, B., and Ellam, R. M. (2013). Man-made versus natural CO2 leakage: A 400 k.y. history of an analogue for engineered geological storage of CO2. *Geology*, 41(4):471–474.

Busenberg, E. and Niel Plummer, L. (1985). Kinetic and thermodynamic factors controlling the distribution of SO3 2- and Na+ in calcites and selected aragonites. *Geochimica et Cosmochimica Acta*, 49(3):713–725.

Busenberg, E. and Niel Plummer, L. (1989). Thermodynamics of magnesian calcite solid-solutions at 25°C and 1 atm total pressure. *Geochimica et Cosmochimica Acta*, 53(1984):1189–1208.

Byerlee, J. (1993). Model for episodic flow of high-pressure water in fault zones before earthquakes.

Caine, J. S., Evans, J. P., and Forster, C. B. (1996). Fault zone architechture and permeability structure. *Geology*, 24(11):1025–1028.

Capo, R. C., Stewart, B. W., and Chadwick, O. A. (1998). Strontium isotopes as tracers of ecosystem processes: Theory and methods. *Geoderma*, 82(1-3):197–225.

Chen, F., Turchyn, A. V., Kampman, N., Hodell, D., Gázquez, F., Maskell, A., and Bickle, M. (2016a). Isotopic Analysis of Sulfur Cycling and Gypsum Vein Formation in a Natural CO2 Reservoir. *Chemical Geology*, 436:1–51.

Chen, T., Robinson, L. F., Beasley, M. P., Claxton, L. M., Andersen, M. B., Gregoire, L. J., Wadham, J., Fornari, D. J., and Harpp, K. S. (2016b). Ocean mixing and ice-sheet control of seawater 234U/238U during the last deglaciation. *Science*, 354(6312):626–629.

Chen, W., Lu, J., Jiang, S.-Y., Zhao, K., and Duan, D.-F. (2017). In situ carbon stable isotope analysis by laser ablation MC-ICP-MS. *Analytical Chemistry*, page acs.analchem.7b03678.

Chen, W. and Simonetti, A. (2013). In-situ determination of major and trace elements in calcite and apatite, and U-Pb ages of apatite from the Oka carbonatite complex: Insights into a complex crystallization history. *Chemical Geology*, 353:151–172.

Chen, X., Romaniello, S. J., Herrmann, A. D., Wasylenki, L. E., and Anbar, A. D. (2016c). Uranium isotope fractionation during coprecipitation with aragonite and calcite. *Geochimica et Cosmochimica Acta*, 188(June):189–207.

Cheng, H., Edwards, R., Hoff, J., Gallup, C., Richards, D., and Asmerom, Y. (2000). The half-lives of uranium-234 and thorium-230. *Chemical Geology*, 169(1-2):17–33.

Cheng, H., Edwards, R. L., Wang, Y., Kong, X., Ming, Y., Kelly, M. J., Wang, X., Gallup, C. D., and Liu, W. (2006). A penultimate glacial monsoon record from Hulu Cave and two-phase glacial terminations. *Geology*, 34(3):217.

Cheng, H., Lawrence Edwards, R., Shen, C.-C., Polyak, V. J., Asmerom, Y., Woodhead, J., Hellstrom, J., Wang, Y., Kong, X., Spötl, C., Wang, X., and Calvin Alexander, E. (2013). Improvements in 230Th dating, 230Th and 234U half-life values, and U–Th isotopic measurements by multi-collector inductively coupled plasma mass spectrometry. *Earth and Planetary Science Letters*, 371-372:82–91.

Christensen, J. N., Halliday, A. N., Lee, D.-C., and Hall, C. M. (1995). In situ Sr isotopic analysis by laser ablation. *Earth and Planetary Science Letters*, 136(1-2):79–85.

Condon, D., Schoene, B., McLean, N., Bowring, S., and Parrish, R. (2015). Metrology and Traceability of U-Pb Isotope Dilution Geochronology (EARTH-TIME Tracer Calibration Part I). *Geochimica et Cosmochimica Acta*.

Cooper, K. M. and Kent, A. J. R. (2014). Rapid remobilization of magmatic crystals kept in cold storage. *Nature*, 506(7489):480–483.

Crémière, A., Lepland, A., Chand, S., Sahy, D., Condon, D. J., Noble, S. R., Martma, T., Thorsnes, T., Sauer, S., and Brunstad, H. (2016). Timescales of methane seepage on the Norwegian margin following collapse of the Scandinavian Ice Sheet. *Nature Communications*, 7(May):1–10.

Dauphas, N. and Schauble, E. A. (2016). Mass Fractionation Laws, Mass-Independent Effects, and Isotopic Anomalies. *Annu. Rev. Earth Planet. Sci*, 44(May):709–83.

Davis, K. J., Dove, P. M., and De Yoreo, J. J. (2000). The Role of Mg2+ as an Impurity in Calcite Growth. *Science*, 290(5494):1134–1137.

De Yoreo, J. J., Gilbert, P. U. P. A., Sommerdijk, N. A. J. M., Penn, R. L., Whitelam, S., Joester, D., Zhang, H., Rimer, J. D., Navrotsky, A., Banfield, J. F., Wallace, A. F., Michel, F. M., Meldrum, F. C., Colfen, H., and Dove, P. M. (2015). Crystallization by particle attachment in synthetic, biogenic, and geologic environments. *Science*, 349(aaa6760):1–9.

References

Demény, A., Németh, P., Czuppon, G., Leél-Őssy, S., Szabó, M., Judik, K., Németh, T., and Stieber, J. (2016). Formation of amorphous calcium carbonate in caves and its implications for speleothem research. *Scientific Reports*, 6:39602:1–10.

DePaolo, D. J. (2011). Surface kinetic model for isotopic and trace element fractionation during precipitation of calcite from aqueous solutions. *Geochimica et Cosmochimica Acta*, 75(4):1039–1056.

Diener, A., Ebneth, S., Veizer, J., and Buhl, D. (1996). Strontium isotope stratigraphy of the Middle Devonian: Brachiopods and conodonts. *Geochimica et Cosmochimica Acta*, 60(4):639–652.

Dietzel, M., Gussone, N., and Eisenhauer, A. (2004). Co-precipitation of Sr2+ and Ba2+ with aragonite by membrane diffusion of CO2 between 10 and 50°C. *Chemical Geology*, 203(1-2):139–151.

Dietzel, M., Tang, J., Leis, A., and Köhler, S. J. (2009). Oxygen isotopic fractionation during inorganic calcite precipitation — Effects of temperature, precipitation rate and pH. *Chemical Geology*, 268(1-2):107–115.

Dockrill, B. (2006). *Understanding leakage from a fault-sealed CO2 reservoir in east-central Utah: A natural analogue applicable to CO2 storage*. PhD thesis.

Dockrill, B. and Shipton, Z. K. (2010). Structural controls on leakage from a natural CO2 geologic storage site: Central Utah, U.S.A. *Journal of Structural Geology*, 32(11):1768–1782.

Doe, B. R., Leeman, W. P., Christiansen, R. L., and Hedge, C. E. (1982). Lead and strontium isotopes and related trace elements as genetic tracers in the Upper Cenozoic rhyolite-basalt association of the Yellowstone Plateau Volcanic Field. *Journal of Geophysical Research*, 87(B6):4785–4806.

Doelling, H. H. (2002). Geologic map of the Moab and eastern part of the San Rafael desert 30' x 60' quadrangles, Grand and Emery counties, Utah, and Mesa county, Colorado. *UTAH GEOLOGICAL SURVEY*.

Doelling, H. H., Kuehne, P. A., Willis, G. C., and Ehler, J. B. (2015). Geologic map of the San Rafael desert 30 ' x 60 ' quadrangle, Emery and Grand counties, Utah. *UTAH GEOLOGICAL SURVEY*, MAP 267DM.

Dong, W. and Brooks, S. C. (2006). Determination of the formation constants of ternary complexes of uranyl and carbonate with alkaline earth metals (Mg2+, Ca2+, Sr 2+, and Ba2+) using anion exchange method. *Environmental Science and Technology*, 40(15):4689–4695.

Duan, Z., Sun, R., Zhu, C., and Chou, I.-M. M. (2006). An improved model for the calculation of CO2 solubility in aqueous solutions containing Na+, K+, Ca2+, Mg2+, Cl-, and SO42-. *Marine Chemistry*, 98(2-4):131–139.

Dubacq, B., Bickle, M. J., and Evans, K. a. (2013). An activity model for phase equilibria in the H2O–CO2–NaCl system. *Geochimica et Cosmochimica Acta*, 110:229–252.

Dutton, A., Rubin, K., McLean, N., Bowring, J., Bard, E., Edwards, R. L., Henderson, G. M., Reid, M. R., Richards, D. A., Sims, K. W. W., Walker, J. D., and Yokoyama, Y. (2017). Data reporting standards for publication of U-series data for geochronology and timescale assessment in the earth sciences. *Quaternary Geochronology*, 39:142–149.

Edmond, J. M. (1992). Himalayan tectonics, weathering processes, and the strontium isotope record in marine limestones. *Science (New York, N.Y.)*, 258(5088):1594–1597.

Eggins, S., Kinsley, L., and Shelley, J. (1998). Deposition and element fractionation processes during atmospheric pressure laser sampling for analysis by ICP-MS. *Applied Surface Science*, 127-129:278–286.

Eggins, S. M., Grün, R., McCulloch, M. T., Pike, A. W., Chappell, J., Kinsley, L., Mortimer, G., Shelley, M., Murray-Wallace, C. V., Spötl, C., and Taylor, L. (2005). In situ U-series dating by laser-ablation multi-collector ICPMS: new prospects for Quaternary geochronology. *Quaternary Science Reviews*, 24(23-24):2523–2538.

Elderfield, H. (1986). Strontium isotope stratigraphy. *Palaeogeography, Palaeoclimatology, Palaeoecology*, 57(1):71–90.

Endrizzi, F. and Rao, L. (2014). Chemical speciation of uranium(VI) in marine environments: Complexation of calcium and magnesium ions with [(UO2)(CO3)3]4-and the effect on the extraction of uranium from seawater. *Chemistry - A European Journal*, 20(44):14499–14506.

Esat, T. M. and Yokoyama, Y. (2006). Variability in the uranium isotopic composition of the oceans over glacial-interglacial timescales. *Geochimica et Cosmochimica Acta*, 70(16):4140–4150.

Fehrenbacher, J. S., Spero, H. J., Russell, A. D., Vetter, L., and Eggins, S. (2015). Optimizing LA-ICP-MS analytical procedures for elemental depth profiling of foraminifera shells. *Chemical Geology*, 407-408:2–9.

Fernández-Díaz, L., Fernández-González, Á., and Prieto, M. (2010). The role of sulfate groups in controlling CaCO3 polymorphism. *Geochimica et Cosmochimica Acta*, 74(21):6064–6076.

Fietzke, J. and Frische, M. (2016). Experimental evaluation of elemental behavior during LA-ICP-MS: influences of plasma conditions and limits of plasma robustness. *J. Anal. At. Spectrom.*, 00:1–11.

Fietzke, J., Liebetrau, V., Günther, D., Gürs, K., Hametner, K., Zumholz, K., Hansteen, T. H., and Eisenhauer, a. (2008). An alternative data acquisition and evaluation strategy for improved isotope ratio precision using LA-MC-ICP-MS applied to stable and radiogenic strontium isotopes in carbonates. *Journal of Analytical Atomic Spectrometry*, 23(7):955.

Font, L., Nowell, G. M., Graham Pearson, D., Ottley, C. J., and Willis, S. G. (2007). Sr isotope analysis of bird feathers by TIMS: a tool to trace bird migration paths and breeding sites. *Journal of Analytical Atomic Spectrometry*, 22(5):513.

Frery, E., Gratier, J.-P., Ellouz-Zimmerman, N., Deschamps, P., Blamart, D., Hamelin, B., and Swennen, R. (2016). Geochemical transect through a travertine mount: A detailed record of CO2-enriched fluid leakage from Late Pleistocene to present-day – Little Grand Wash fault (Utah, USA). *Quaternary International*, pages 1–9.

Frery, E., Gratier, J.-P., Ellouz-Zimmerman, N., Loiselet, C., Braun, J., Deschamps, P., Blamart, D., Hamelin, B., and Swennen, R. (2015). Evolution of fault permeability during episodic fluid circulation: Evidence for the effects of fluid–rock interactions from travertine studies (Utah–USA). *Tectonophysics*.

Gabitov, R., Gaetani, G., Watson, E., a.L. Cohen, and Ehrlich, H. (2008). Experimental determination of growth rate effect on U6+ and Mg2+ partitioning between aragonite and fluid at elevated U6+ concentration. *Geochimica et Cosmochimica Acta*, 72(16):4058–4068.

Gabitov, R., Sadekov, A., and Migdisov, A. (2017). REE Incorporation into Calcite Individual Crystals as One Time Spike Addition. *Minerals*, 7(11):204.

Gabitov, R. I. (2013). Growth-rate induced disequilibrium of oxygen isotopes in aragonite: An in situ study. *Chemical Geology*, 351:268–275.

Gabitov, R. I., Schmitt, a. K., Rosner, M., McKeegan, K. D., Gaetani, G. a., Cohen, a. L., Watson, E. B., and Harrison, T. M. (2011). In situ δ7Li, Li/Ca, and Mg/Ca analyses of synthetic aragonites. *Geochemistry, Geophysics, Geosystems*, 12(3):n/a–n/a.

Gabitov, R. I., Watson, E. B., and Sadekov, A. (2012). Oxygen isotope fractionation between calcite and fluid as a function of growth rate and temperature: An in situ study. *Chemical Geology*, 306-307:92–102.

Gaetani, G. A. and Cohen, A. L. (2006). Element partitioning during precipitation of aragonite from seawater: A framework for understanding paleoproxies. *Geochimica et Cosmochimica Acta*, 70(18):4617–4634.

Gagnon, A. C., Adkins, J. F., Fernandez, D. P., and Robinson, L. F. (2007). Sr/Ca and Mg/Ca vital effects correlated with skeletal architecture in a scleractinian deep-sea coral and the role of Rayleigh fractionation. *Earth and Planetary Science Letters*, 261(1-2):280–295.

Geipel, G., Amayri, S., and Bernhard, G. (2008). Mixed complexes of alkaline earth uranyl carbonates: A laser-induced time-resolved fluorescence spectroscopic study. *Spectrochimica Acta - Part A: Molecular and Biomolecular Spectroscopy*, 71(1):53–58.

Gilfillan, S. M., Ballentine, C. J., Holland, G., Blagburn, D., Lollar, B. S., Stevens, S., Schoell, M., and Cassidy, M. (2008). The noble gas geochemistry of natural CO2 gas reservoirs from the Colorado Plateau and Rocky Mountain provinces, USA. *Geochimica et Cosmochimica Acta*, 72(4):1174–1198.

Gratier, J.-P., Frery, E., Deschamps, P., Royne, a., Renard, F., Dysthe, D., Ellouz-Zimmerman, N., and Hamelin, B. (2012). How travertine veins grow from top to bottom and lift the rocks above them: The effect of crystallization force. *Geology*, 40(11):1015–1018.

Grünenfelder, M. H., Tilton, G. R., Bell, K., and Blenkinsop, J. (1986). Lead and strontium isotope relationships in the Oka carbonatite complex, Quebec. *Geochimica et Cosmochimica Acta*, 50(3):461–468.

References

Guillong, M. and Gunther, D. (2002). Effect of particle size distribution on ICP-induced elemental fractionation in laser ablation-inductively coupled plasma-mass spectrometry. *Journal of Analytical Atomic Spectrometry*, 17(8):831–837.

Halland, E., Gjeldvik, I. T., Johansen, W. T., Magnus, C., Meling, I. M., Mujezinović, J., Pham, V. T. H., Riis, F., Rød, R. S., and M.Tappel, I. (2014). *CO2 Storage Atlas Norwegian Sea*.

Han, W. S., Lu, M., McPherson, B. J., Keating, E. H., Moore, J., Park, E., Watson, Z. T., and Jung, N.-H. (2013). Characteristics of CO 2 -driven cold-water geyser, Crystal Geyser in Utah: experimental observation and mechanism analyses. *Geofluids*, 13(3):283–297.

Han, W. S., Watson, Z., Kampman, N., Grundl, T., Graham, J. P., and Keating, E. H. (2017). Periodic changes in effluent chemistry at cold-water geyser: Crystal geyser in Utah. *Journal of Hydrology*, 550:54–64.

Hathorne, E. C., Felis, T., Suzuki, A., Kawahata, H., and Cabioch, G. (2013). Lithium in the aragonite skeletons of massive Porites corals: A new tool to reconstruct tropical sea surface temperatures. *Paleoceanography*, 28:143–152.

Heath, J. E., Lachmar, T. E., Evans, J. P., Kolesar, P. T., and Williams, A. P. (2009). Hydrogeochemical characterization of leaking, carbon dioxide-charged fault zones in east-central utah, with implications for geologic carbon storage. *Geophysical Monograph Series*, 183:147–158.

Heier, K. S. (1962). Trace elements in feldspars - A review. *Norks Geologisk Tidsskrift*, 42:415–454.

Hemming, N. N. G., Reeder, R. R. J., and Hanson, G. G. N. (1995). Mineral-fluid partitioning and isotopic fractionation of boron in synthetic calcium carbonate. *Geochimica et Cosmochimica Acta*, 59(2):371–379.

Hemming, S. R., Broecker, W. S., Sharp, W. D., Bond, G. C., Gwiazda, R. H., McManus, J. F., Klas, M., and Hajdas, I. (1998). Provenance of Heinrich layers in core V28-82, northeastern Atlantic: 40Ar/39Ar ages of ice-rafted hornblende, Pb isotopes in feldspar grains, and Nd-Sr-Pb isotopes in the fine sediment fraction. *Earth and Planetary Science Letters*, 164(1-2):317–333.

Henderson, G. and Slowey, N. (2000). Evidence from U–Th dating against Northern Hemisphere forcing of the penultimate deglaciation. *Nature*, 404(March):61–66.

Henderson, G. M. G., Slowey, N. N. C., and Fleisher, M. Q. M. M. Q. (2001). U-Th dating of carbonate platform and slope sediments. *Geochimica et Cosmochimica Acta*, 65(16):2757–2770.

Hiess, J., Condon, D. J., McLean, N., Stephen R. Noble1, and Noble, S. R. (2012). 238U/235U Systematics in Terrestrial Uranium-Bearing Minerals. *Science*, 2(March):1610–1615.

Hobson, K. A. (1999). Tracing origins and migration of wildlife using stable isotopes: A review. *Oecologia*, 120(3):314–326.

Hodell, D. A., Mueller, P. A., McKenzie, J. A., and Mead, G. A. (1989). Strontium isotope stratigraphy and geochemistry of the late Neogene ocean. *Earth and Planetary Science Letters*, 92(2):165–178.

Hodell, D. A., Quinn, R. L., Brenner, M., and Kamenov, G. (2004). Spatial variation of strontium isotopes (87Sr/86Sr) in the Maya region: A tool for tracking ancient human migration. *Journal of Archaeological Science*, 31(8):585–601.

Hoffmann, D., Richards, D., Elliott, T., Smart, P., Coath, C., and Hawkesworth, C. (2005). Characterisation of secondary electron multiplier nonlinearity using MC-ICPMS. *International Journal of Mass Spectrometry*, 244(2-3):97–108.

Hoffmann, D. L. (2008). 230Th isotope measurements of femtogram quantities for U-series dating using multi ion counting (MIC) MC-ICPMS. *International Journal of Mass Spectrometry*, 275(1-3):75–79.

Hoffmann, D. L. D., Spötl, C., and Mangini, A. (2009). Micromill and in situ laser ablation sampling techniques for high spatial resolution MC-ICPMS U-Th dating of carbonates. *Chemical Geology*, 259(3-4):253–261.

Hogmalm, K. J., Zack, T., Karlsson, A. K.-O., Sjöqvist, A. S. L., and Garbe-Schönberg, D. (2017). In situ Rb–Sr and K–Ca dating by LA-ICP-MS/MS: an evaluation of N2O and SF6 as reaction gases. *J. Anal. At. Spectrom.*, 32(2):305–313.

Hood, J. and Patterson, D. (1984). Bedrock Aquifers in the Northern San Rafael Swell Area , Utah , with Special Emphasis on the Navajo Sandstone. *All U.S. Government Documents (Utah Regional Repository). Paper 274*, (78):103.

Horne, E. A., Evans, J. P., Newell, D., Kampman, N., Nelson, S., Petrie, E. S., Elizabeth, A., James, P., and Elizabeth, S. (2013). Field Observations and Geochemical Analysis of Laterally Continuous Aragonite Veins : Insight into Ancient Field Observations and Geochemical Analysis of Laterally Continuous Aragonite Veins : Insight into Ancient Fluid Travel Stable Oxygen and Carbon Iso. In *GSA*, volume 50887, pages 1–2.

Horsky, M., Irrgeher, J., and Prohaska, T. (2016). Evaluation strategies and uncertainty calculation of isotope amount ratios measured by MC ICP-MS on the example of Sr. *Analytical and Bioanalytical Chemistry*, 408(2):351–367.

Horstwood, M., Evans, J., and Montgomery, J. (2008). Determination of Sr isotopes in calcium phosphates using laser ablation inductively coupled plasma mass spectrometry and their application to archaeological tooth enamel. *Geochimica et Cosmochimica Acta*, 72(23):5659–5674.

Horstwood, M. S., Košler, J., Gehrels, G., Jackson, S. E., McLean, N. M., Paton, C., Pearson, N. J., Sircombe, K., Sylvester, P., Vermeesch, P., Bowring, J. F., Condon, D. J., and Schoene, B. (2016). Community-Derived Standards for LA-ICP-MS U-(Th-)Pb Geochronology – Uncertainty Propagation, Age Interpretation and Data Reporting. *Geostandards and Geoanalytical Research*, 40(3):311–332.

Hu, Y. B., Wolthers, M., Wolf-Gladrow, D. A., and Nehrke, G. (2015). Effect of pH and phosphate on calcium carbonate polymorphs precipitated at near-freezing temperature. *Crystal Growth and Design*, 15(4):1596–1601.

IPCC (2005). *Carbon Dioxide Capture and Storage*.

IPCC, W. T., Pachauri, R. K., and Meyer, L. (2014). Climate change 2014. *Synthesis Report*, page 133.

Irrgeher, J., Galler, P., and Prohaska, T. (2016). 87 Sr / 86 Sr isotope ratio measurements by laser ablation multicollector inductively coupled plasma mass spectrometry : Reconsidering matrix interferences in bioapatites and biogenic carbonates. *Spectrochimica Acta Part B: Atomic Spectroscopy*, 125:31–42.

Ishikawa, M. and Ichikuni, M. (1984). Uptake of sodium and potassium by calcite. *Chemical Geology*, 42(1-4):137–146.

Ishikawa, M. and Ichikuni, M. (1986). A Model of Crystal Defects in Calcite by Sodium and Potassium Uptake.

Itsuguchi, T. A. M., Chida, T. E. U., Atsumoto, E. I. J. I. M., Mitsuguchi, T., Uchida, T., and Matsumoto, E. (2010). Na/Ca variability in coral skeletons. *Geochemical Journal*, 44:261–273.

Ivanovich, M. and Harmon, R. S. (1992). *Uranium-series Disequilibrium: Applications to Earth, Marine, and Environmental Sciences*. Clarendon Press, 2nd edition.

Jacob, D. E., Wirth, R., Agbaje, O. B. A., Branson, O., and Eggins, S. M. (2017). Planktic foraminifera form their shells via metastable carbonate phases. *Nature Communications*, 8(1):1265.

Jamieson, J. W., Hannington, M. D., Tivey, M. K., Hansteen, T., Williamson, N. M. B., Stewart, M., Fietzke, J., Butterfield, D., Frische, M., Allen, L., Cousens, B., and Langer, J. (2016). Precipitation and growth of barite within hydrothermal vent deposits from the Endeavour Segment, Juan de Fuca Ridge. *Geochimica et Cosmochimica Acta*, 173:64–85.

Jochum, K. P., Weis, U., Stoll, B., Kuzmin, D., Yang, Q., Raczek, I., Jacob, D. E., Stracke, A., Birbaum, K., Frick, D. A., Günther, D., and Enzweiler, J. (2011). Determination of reference values for NIST SRM 610-617 glasses following ISO guidelines. *Geostandards and Geoanalytical Research*, 35(4):397–429.

Johnson, C. W., Fu, Y., and Bürgmann, R. (2017). Seasonal water storage, stress modulation, and California seismicity. *Science*, 356(6343):1161–1164.

Johnson, C. W., Totten, E. J., and Bürgmann, R. (2016). Depth migration of seasonally induced seismicity at The Geysers geothermal field. *Geophysical Research Letters*, 43(12):6196–6204.

Johnson, M. and DePaolo, D. J. (1997). Rapide exchange effects on isotope ratios in groundwater systems 1. Development of a transport-dissolution-exchange model. *Water Resources Research*, 33(1):187–195.

Johnson, T. M. and DePaolo, D. J. (1994). Interpretation of isotopic data in groundwater-rock systems: Model development and application to Sr isotope data from Yucca Mountain. *Water Resources Research*, 30(5):1571–1587.

Jung, N.-H. H., Han, W. S., Han, K., and Park, E. (2015). Regional-Scale Advective, Diffusive and Eruptive Dynamics of CO2 and Brine Leakage through Faults and Wellbores. *Journal of Geophysical Research: Solid Earth*, 120(5):n/a–n/a.

References

Kampman, N. (2011). Fluid-rock interactions in a carbon storage site analogue, Green River, Utah. (January).

Kampman, N., Bickle, M., Becker, J., Assayag, N., and Chapman, H. (2009). Feldspar dissolution kinetics and Gibbs free energy dependence in a CO2-enriched groundwater system, Green River, Utah. *Earth and Planetary Science Letters*, 284(3-4):473–488.

Kampman, N., Bickle, M., Wigley, M., and Dubacq, B. (2013a). Fluid flow and CO2–fluid–mineral interactions during CO2-storage in sedimentary basins. *Chemical Geology*.

Kampman, N., Bickle, M., Wigley, M., and Dubacq, B. (2014a). Fluid flow and CO2-fluid-mineral interactions during CO2-storage in sedimentary basins. *Chemical Geology*, 369:22–50.

Kampman, N., Bickle, M. J., Maskell, A., Chapman, H. J., Evans, J. P., Purser, G., Zhou, Z., Schaller, M. F., Gattacceca, J. C., Bertier, P., Chen, F., Turchyn, A. V., Assayag, N., Rochelle, C., Ballentine, C. J., and Busch, A. (2014b). Drilling and sampling a natural CO2 reservoir: Implications for fluid flow and CO2-fluid-rock reactions during CO2 migration through the overburden. *Chemical Geology*, 369:51–82.

Kampman, N., Burnside, N. M., Shipton, Z. K., Chapman, H. J., Nicholl, J. a., Ellam, R. M., and Bickle, M. J. (2012). Pulses of carbon dioxide emissions from intracrustal faults following climatic warming. *Nature Geoscience*, 5(5):352–358.

Kampman, N., Busch, A., Bertier, P., Snippe, J., Hangx, S., Pipich, V., Di, Z., Rother, G., Harrington, J. F., Evans, J. P., Maskell, A., Chapman, H. J., and Bickle, M. J. (2016). Observational evidence confirms modelling of the long-term integrity of CO2-reservoir caprocks. *Nature Communications*, 7:12268.

Kampman, N., Maskell, a., Bickle, M. J., Evans, J. P., Schaller, M., Purser, G., Zhou, Z., Gattacceca, J., Peitre, E. S., Rochelle, C. a., Ballentine, C. J., Busch, a., Utley, B., Vyas, D., Garcia, L., Giles, N., Hooton, C., Jean, M., Strange, M., and Young, B. (2013b). Scientific drilling and downhole fluid sampling of a natural CO2 reservoir, Green River, Utah. *Scientific Drilling*, 16(16):33–43.

Kawano, J., Shimobayashi, N., Miyake, A., and Kitamura, M. (2009). Precipitation diagram of calcium carbonate polymorphs: its construction and significance. *Journal of Physics: Condensed Matter*, 21(42):425102.

Kelemen, P. B. and Matter, J. (2008). In situ carbonation of peridotite for CO2 storage. *Proceedings of the National Academy of Sciences*, 105(45):17295–17300.

Kennedy, B. P., Klaue, A., Blum, J. D., Folt, C. L., and Nislow, K. H. (2002). Reconstructing the lives of fish using Sr isotopes in otoliths. *Canadian Journal of Fisheries and Aquatic Sciences*, 59(6):925–929.

Kigoshi, K. (1971). Alpha-Recoil Thorium-234: Dissolution into Water and the Uranium-234/Uranium-238 Disequilibrium in Nature. *Science*, 173(3991):47–48.

Kim, S.-T. T., O'Neil, J. R., Hillaire-Marcel, C., Mucci, A., O'Neil, J. R., Hillaire-Marcel, C., and Mucci, A. (2007). Oxygen isotope fractionation between synthetic aragonite and water: Influence of temperature and Mg2+ concentration. *Geochimica et Cosmochimica Acta*, 71(19):4704–4715.

Kincaid, C. T., Bergeron, M. P., Cole, C. R., Freshley, M. D., Kaplan, D. I., Serne, R. J., Streile, G. P., Strenge, D. L., Thorne, P. D., Vail, L. W., Whyatt, G. A., and Wurstner, S. (1998). Composite Analysis for Low-Level Waste Disposal in the 200 Area Plateau of the Hanf ord Site. (March 1998).

Kinsman, D. J. J. and Holland, H. H. D. (1969). The co-precipitation of cations with CaCO3-IV . The co-precipitation of Sr2+ with aragonite between 16 and 96C. *Geochimica et Cosmochimica Acta*, 33(October 1964):1–17.

Kitano, Y., Okumura, M., and Idogaki, M. (1975). Incorporation of sodium, chloride and sulfate with calcium carbonate. *Geochemical Journal*, 9(2):75–84.

Kosler, J., Longerich, H. P., and Tubrett, M. N. (2002). Effect of oxygen on laser-induced elemental fractionation in LA-ICP-MS analysis. *Analytical and Bioanalytical Chemistry*, 374(2):251–254.

Krabbenhöft, A., Eisenhauer, A., Böhm, F., Vollstaedt, H., Fietzke, J., Liebetrau, V., Augustin, N., Peucker-Ehrenbrink, B., Müller, M. N., Horn, C., Hansen, B. T., Nolte, N., and Wallmann, K. (2010). Constraining the marine strontium budget with natural strontium isotope fractionations (87Sr/86Sr*, δ88/86Sr) of carbonates, hydrothermal solutions and river waters. *Geochimica et Cosmochimica Acta*, 74(14):4097–4109.

Kronfeld, J. (1974). Uranium deposition and Th-234 alpha-recoil: An explanation for extreme U-234/U-238 fractionation within the trinity aquifer. *Earth and Planetary Science Letters*, 21(3):327–330.

Kronfeld, J., Gradsztajn, E., Müller, H. W., Radin, J., Yaniv, A., and Zach, R. (1975). Excess 234U: An aging effect in confined waters. *Earth and Planetary Science Letters*, 27(2):342–345.

Kroslakova, I. and Günther, D. (2007). Elemental fractionation in laser ablation-inductively coupled plasma-mass spectrometry: evidence for mass load induced matrix effects in the ICP during ablation of a silicate glass. *J. Anal. At. Spectrom.*, 22(1):51–62.

Kuhn, H.-R. and Günther, D. (2003). Elemental fractionation Studies in Laser Ablation Inductively Coupled Plasma Mass Spectrometry on Laser-Induced Brass Aerosols. *Analytical Chemistry*, 75:747–753.

Laabs, B. J. C., Refsnider, K. A., Munroe, J. S., Mickelson, D. M., Applegate, P. J., Singer, B. S., and Caffee, M. W. (2009). Latest Pleistocene glacial chronology of the Uinta Mountains: support for moisture-driven asynchrony of the last deglaciation. *Quaternary Science Reviews*, 28(13-14):1171–1187.

Lai, P., Moulton, K., and Krevor, S. (2015). Pore-scale heterogeneity in the mineral distribution and reactive surface area of porous rocks. *Chemical Geology*, 411:260–273.

Langmuir, D. (1978). Uranium solution-mineral equilibria at low temperatures with applications to sedimentary ore deposits. *Geochimica et Cosmochimica Acta*, 42(6):547–569.

Langmuir, D. and Herman, J. S. (1980). The mobility of thorium in natural waters at low temperatures. *Geochimica et Cosmochimica Acta*, 44(11):1753–1766.

Lee, J.-Y. and Yun, J.-I. (2013). Formation of ternary CaUO2(CO3)3^2- and Ca2UO2(CO3)3(aq) complexes under neutral to weakly alkaline conditions. *Dalton Transactions*, 42(27):9862.

Lewis, J., Coath, C. D., and Pike, A. W. G. (2014). An improved protocol for 87Sr/86Sr by laser ablation multi-collector inductively coupled plasma mass spectrometry using oxide reduction and a customised plasma interface. *Chemical Geology*, 390:173–181.

Li, Y., Zou, Y., Chen, T., Wang, X., Qi, X., Chen, H., Du, J., and Li, B. (2015). P-V-T equation of state and high-pressure behavior of CaCO3 aragonite. *American Mineralogist*, 100(10):2323–2329.

Lichtner, P. C. (1985). Continuum model for simultaneous chemical reactions and mass transport in hydrothermal systems. *Geochimica et Cosmochimica Acta*, 49(3):779–800.

Lichtner, P. C. (1988). The quasi-stationary state approximation to coupled mass transport and fluid-rock interaction in a porous medium. *Geochimica et Cosmochimica Acta*, 52(1):143–165.

Lin, Y., Jochum, K. P., Scholz, D., Hoffmann, D. L., Stoll, B., Weis, U., and Andreae, M. O. (2017). In-situ high spatial resolution LA-MC-ICPMS 230 Th/U dating enables detection of small-scale age inversions in speleothems. *Solid Earth Sciences*, 2(1):1–9.

Lisiecki, L. E. and Raymo, M. E. (2005). A Pliocene-Pleistocene stack of 57 globally distributed benthic δ 18 O records. *Paleoceanography*, 20(PA1003):1–17.

Luo, T., Wang, Y., Hu, Z., Günther, D., Liu, Y., Gao, S., Li, M., and Hu, S. (2015). Further investigation into ICP-induced elemental fractionation in LA-ICP-MS using a local aerosol extraction strategy. *J. Anal. At. Spectrom.*, 30(4):941–949.

Maher, K., DePaolo, D. J., and Christensen, J. N. (2006a). U-Sr isotopic speedometer: Fluid flow and chemical weathering rates in aquifers. *Geochimica et Cosmochimica Acta*, 70(17):4417–4435.

Maher, K., DePaolo, D. J., Conrad, M. E., and Serne, R. J. (2003). Vadose zone infiltration rate at Hanford, Washington, inferred from Sr isotope measurements. *Water Resources Research*, 39(8):n/a—-n/a.

Maher, K., Steefel, C. I., DePaolo, D. J., and Viani, B. E. (2006b). The mineral dissolution rate conundrum: Insights from reactive transport modeling of U isotopes and pore fluid chemistry in marine sediments. *Geochimica et Cosmochimica Acta*, 70(2):337–363.

Malde, H. E. (1968). The Catastrophic Late Pleistocene Bonneville Flood in the Snake River Plain. *Geological Survey Proffesional Paper*.

Marriott, C. S., Henderson, G. M., Belshaw, N. S., and Tudhope, A. W. (2004). Temperature dependence of δ7Li, δ44Ca and Li/Ca during growth of calcium carbonate. *Earth and Planetary Science Letters*, 222(2):615–624.

Maskell, A., Kampman, N., Chapman, H., Condon, D. J., and Bickle, M. (2015). Kinetics of CO2–fluid–rock reactions in a basalt aquifer, Soda Springs, Idaho. *Applied Geochemistry*, 61:272–283.

Maskell, A., Scott, P. M., Buisman, I., and Bickle, M. (2017). A siltstone reaction front related to CO2 and sulfur bearing fluids : Integrating quantitative elemental mapping with reactive transport modeling. *American Mineralogist*, in press.

References

Matter, J. M., Stute, M., Snaebjornsdottir, S. O., Oelkers, E. H., Gislason, S. R., Aradottir, E. S., Sigfusson, B., Gunnarsson, I., Sigurdardottir, H., Gunnlaugsson, E., Axelsson, G., Alfredsson, H. A., Wolff-Boenisch, D., Mesfin, K., Taya, D. F. d. l. R., Hall, J., Dideriksen, K., and Broecker, W. S. (2016). Rapid carbon mineralization for permanent disposal of anthropogenic carbon dioxide emissions. *Science*, 352(6291):1312–1314.

McArthur, J. M., Howarth, R. J., and Bailey, T. R. (2001). Strontium Isotope Stratigraphy: LOWESS Version 3: Best Fit to the Marine Sr-Isotope Curve for 0–509 Ma and Accompanying Look-up Table for Deriving Numerical Age. *The Journal of Geology*, 109(2):155–170.

McLean, N. M., Bowring, J. F., and Gehrels, G. (2016). Algorithms and software for U-Pb geochronology by LA-ICPMS. *Geochemistry, Geophysics, Geosystems*, 17(7):2480–2496.

Meece, D. and Benninger, L. (1993). The coprecipitation of Pu and other radionuclides with CaCO3. *Geochimica et Cosmochimica Acta*, 57(7):1447–1458.

Mitsuguchi, T. and Kawakami, T. (2012). Potassium and other minor elements in Porites corals: Implications for skeletal geochemistry and paleoenvironmental reconstruction. *Coral Reefs*, 31:671–681.

Müller, W. and Anczkiewicz, R. (2016). Accuracy of Laser-Ablation (LA)-MC-ICPMS Sr Isotope Analysis of (Bio)Apatite – a Problem Reassessed. *J. Anal. At. Spectrom.*, pages 259–269.

Murphy, M. J., Froehlich, M. B., Fifield, L. K., Turner, S. P., and Schaefer, B. F. (2015). In-situ production of natural 236U in groundwaters and ores in high-grade uranium deposits. *Chemical Geology*, 410:213–222.

Murphy, M. J., Stirling, C. H., Kaltenbach, A., Turner, S. P., and Schaefer, B. F. (2014). Fractionation of 238U/235U by reduction during low temperature uranium mineralisation processes. *Earth and Planetary Science Letters*, 388:306–317.

Neiva, A. M. R. (1995). Distribution of trace elements in feldspars of granitic aplites and pegmatites from Alijó-Sanfins, northern Portugal. *Mineralogical Magazine*, 59(March):35–45.

Nielsen, L. C., De Yoreo, J. J., and DePaolo, D. J. (2013). General model for calcite growth kinetics in the presence of impurity ions. *Geochimica et Cosmochimica Acta*, 115:100–114.

Nielsen, L. C. and DePaolo, D. J. (2013). Ca isotope fractionation in a high-alkalinity lake system: Mono Lake, California. *Geochimica et Cosmochimica Acta*, 118:276–294.

Nielsen, L. C., DePaolo, D. J., and De Yoreo, J. J. (2012). Self-consistent ion-by-ion growth model for kinetic isotopic fractionation during calcite precipitation. *Geochimica et Cosmochimica Acta*, 86:166–181.

Nielsen, M. R., Sand, K. K., Rodriguez-Blanco, J. D., Bovet, N., Generosi, J., Dalby, K. N., and Stipp, S. L. (2016). Inhibition of Calcite Growth: Combined Effects of Mg2+ and SO42-. *Crystal Growth and Design*, 16(11):6199–6207.

Okumura, M. and Kitano, Y. (1986). Coprecipitation of alkali metal ions with calcium carbonate. *Geochimica et Cosmochimica Acta*, 50(1):49–58.

Palmer, M. R. and Elderfield, H. (1985). Sr isotope composition of sea water over the past 75 Myr. *Nature*, 314(6011):526–528.

Parry, W. T., Forster, C. B., Evans, J. P., Bowen, B. B., and Chan, M. A. (2007). Geochemistry of CO2 sequestration in the Jurassic Navajo Sandstone, Colorado Plateau, Utah. *Environmental Geosciences*, 14(2):91–109.

Patil, V. V., McPherson, B. J., Priewisch, A., Moore, J., and Moodie, N. (2017). Factors affecting self-sealing of geological faults due to CO2-leakage. *Greenhouse Gases: Science and Technology*, 7(2):273–294.

Paton, C., Hellstrom, J., Paul, B., Woodhead, J., and Hergt, J. (2011). Iolite: Freeware for the visualisation and processing of mass spectrometric data. *Journal of Analytical Atomic Spectrometry*, 26(12):2508.

Paton, C., Woodhead, J. D., Hellstrom, J. C., Hergt, J. M., Greig, A., and Maas, R. (2010). Improved laser ablation U-Pb zircon geochronology through robust downhole fractionation correction. *Geochemistry, Geophysics, Geosystems*, 11(3).

Paton, C., Woodhead, J. D., Hergt, J. M., Phillips, D., and Shee, S. (2007). Strontium isotope analysis of kimberlitic groundmass perovskite via LA-MC-ICP-MS. *Geostandards and Geoanalytical Research*, 31(4):321–330.

Potter, E.-K., Stirling, C. H., Wiechert, U. H., Halliday, A. N., and Spötl, C. (2005). Uranium-series dating of corals in situ using laser-ablation MC-ICPMS. *International Journal of Mass Spectrometry*, 240(1):27–35.

Priestley, S. C., Karlstrom, K. E., Love, A. J., Crossey, L. J., Polyak, V. J., Asmerom, Y., Meredith, K. T., Crow, R., Keppel, M. N., and Habermehl, M. A. (2017). Uranium series dating of Great Artesian Basin travertine deposits: Implications for palaeohydrogeology and palaeoclimate. *Palaeogeography, Palaeoclimatology, Palaeoecology*.

Pruess, K. (2005). Numerical studies of fluid leakage from a geologic disposal reservoir for CO2 show self-limiting feedback between fluid flow and heat transfer. *Geophysical Research Letters*, 32(14):1–4.

Raddatz, J., Liebetrau, V., Rüggeberg, A., Hathorne, E., Krabbenhöft, A., Eisenhauer, A., Böhm, F., Vollstaedt, H., Fietzke, J., López Correa, M., Freiwald, A., and Dullo, W. C. (2013). Stable Sr-isotope, Sr/Ca, Mg/Ca, Li/Ca and Mg/Li ratios in the scleractinian cold-water coral Lophelia pertusa. *Chemical Geology*, 352:143–152.

Raftery, A. E., Zimmer, A., Frierson, D. M., Startz, R., and Liu, P. (2017). Less than 2 °c warming by 2100 unlikely. *Nature Climate Change*, 7(9):637–641.

Raiswell, R. and Brimblecombe, P. (1977). The partition of manganese into aragonite between 30 and 60°C. *Chemical Geology*, 19(1-4):145–151.

Ramos, F. C., Wolff, J. A., and Tollstrup, D. L. (2004). Measuring 87Sr/86Sr variations in minerals and groundmass from basalts using LA-MC-ICPMS. *Chemical Geology*, 211(1-2):135–158.

Rathmann, S. and Kuhnert, H. (2008). Carbonate ion effect on Mg/Ca, Sr/Ca and stable isotopes on the benthic foraminifera Oridorsalis umbonatus off Namibia. *Marine Micropaleontology*, 66(2):120–133.

Reeder, R. J., Nugent, M., Tait, C. D., Morris, D. E., Heald, S. M., Beck, K. M., Hess, W. P., and Lanzirotti, A. (2001). Coprecipitation of uranium(VI) with calcite: XAFS, micro-XAS, and luminescence characterization. *Geochimica et Cosmochimica Acta*, 65(20):3491–3503.

Reeder, R. J. R., Nugent, M., Lamble, G. M., Tait, C. D., and Morris, D. E. (2000). Uranyl Incorporation into Calcite and Aragonite: XAFS and Luminescence Studies. ... *science & technology*, 34(4):638–644.

Reid, M. R., Coath, C. D., Mark Harrison, T., and McKeegan, K. D. (1997). Prolonged residence times for the youngest rhyolites associated with Long Valley Caldera:230Th—238U ion microprobe dating of young zircons. *Earth and Planetary Science Letters*, 150:27–39.

Revel, M., Sinko, J. A., and Grousset, F. E. (1996). Sr and Nd isotopes as tracers of North Atlantic lithic particles' Paleoclimatic implications. *Paleoceanography*, 11(1):95–113.

Sambridge, M., Grün, R., and Eggins, S. (2012). U-series dating of bone in an open system: The diffusion-adsorption-decay model. *Quaternary Geochronology*, 9:42–53.

Sánchez-Pastor, N. and Gigler, A. (2011). Growth of calcium carbonate in the presence of Cr (VI). *Crystal Growth & Design*, 98(Vi):3081–3089.

Schaltegger, U., Schmitt, a. K., and Horstwood, M. S. A. (2015). U-Th-Pb zircon geochronology by ID-TIMS, SIMS, and laser ablation ICP-MS: Recipes, interpretations, and opportunities. *Chemical Geology*, 402:89–110.

Schmidberger, S. S., Simonetti, A., and Francis, D. (2003). Small-scale Sr isotope investigation of clinopyroxenes from peridotite xenoliths by laser ablation MC-ICP-MS - Implications for mantle metasomatism. *Chemical Geology*, 199(3-4):317–329.

Scholz, D. and Hoffmann, D. L. (2011). StalAge - An algorithm designed for construction of speleothem age models. *Quaternary Geochronology*, 6(3-4):369–382.

Shipton, Z., Evans, J., Kirchner, D., Kolesar, P., Williams, A., and Heath, J. (2004). Analysis of CO2 leakage through "low-permeability" faults from natural reservoirs in the Colorado Plateau, southern Utah. In: Baines, S. J. & Worden, R. H. (eds.). *Geological Storage of Carbon Dioxide. Geological Society, London, Special Publications 233*, pages 43–58.

Sibson, R. H., Moore, J. M. M., and Rankin, A. H. (1975). Seismic pumping - a hydrothermal fluid transport mechanism. *Journal of the Geological Society*, 131(6):653–659.

Smedley, R. K. and Pearce, N. J. (2016). Internal U, Th and Rb concentrations of alkali-feldspar grains: Implications for luminescence dating. *Quaternary Geochronology*, 35:16–25.

Smeets, P. J. M., Finney, A. R., Habraken, W. J. E. M., Nudelman, F., Friedrich, H., Laven, J., De Yoreo, J. J., Rodger, P. M., and Sommerdijk, N. A. J. M. (2017). A classical view on nonclassical nucleation. *Proceedings of the National Academy of Sciences*, page 201700342.

References

Snippe, J., Gdanski, R., and Ott, H. (2017). Multiphase Modelling of Wormhole Formation in Carbonates by the Injection of CO2. *Energy Procedia*, 114(November 2016):2972–2984.

Spangler, L. E., Naftz, D. L., Peterman, Z. E., Agency, U. S. E. P., and (U.S.), G. S. (1996). Hydrology, chemical quality, and characterization of salinity in the Navajo aquifer in and near the Greater Aneth Oil Field, San Juan County, Utah. Technical report.

Spencer, C. J., Kirkland, C. L., and Taylor, R. J. (2016). Strategies towards statistically robust interpretations of in situ U-Pb zircon geochronology. *Geoscience Frontiers*, 7(4):581–589.

Spero, H. J., Bijma, J., Lea, D. W., and Bemis, B. E. (1997). Effect of seawater carbonate concentrations on foraminiferal carbon and oxygen isotopes. *Nature*, 390:497—-500—-.

Spooner, P. T., Chen, T., Robinson, L. F., and Coath, C. D. (2016). Rapid uranium-series age screening of carbonates by laser ablation mass spectrometry. *Quaternary Geochronology*, 31:28–39.

Steefel, C. I., Appelo, C. a. J., Arora, B., Jacques, D., Kalbacher, T., Kolditz, O., Lagneau, V., Lichtner, P. C., Mayer, K. U., Meeussen, J. C. L., Molins, S., Moulton, D., Shao, H., Šimůnek, J., Spycher, N., Yabusaki, S. B., and Yeh, G. T. (2015). Reactive transport codes for subsurface environmental simulation. *Computational Geosciences*, 19(3):445–478.

Steefel, C. I., DePaolo, D. J., and Lichtner, P. C. (2005). Reactive transport modeling: An essential tool and a new research approach for the Earth sciences. *Earth and Planetary Science Letters*, 240(3-4):539–558.

Stevenson, E. I., Hermoso, M., Rickaby, R. E. M., Tyler, J. J., Minoletti, F., Parkinson, I. J., Mokadem, F., and Burton, K. W. (2014). Controls on stable strontium isotope fractionation in coccolithophores with implications for the marine Sr cycle. *Geochimica et Cosmochimica Acta*, 128(October):225–235.

Stirling, C. H., Andersen, M. B., Potter, E.-K., and Halliday, A. N. (2007). Low-temperature isotopic fractionation of uranium. *Earth and Planetary Science Letters*, 264(1-2):208–225.

Stirling, C. H., Lee, D.-C. C., Christensen, J. N., and Halliday, A. N. (2000). High-precision in situ 238U–234U–230Th isotopic analysis using laser ablation multiple-collector ICPMS. *Geochimica et Cosmochimica Acta*, 64(21):3737–3750.

Sun, W., Jayaraman, S., Chen, W., Persson, K. a., and Ceder, G. (2015). Nucleation of metastable aragonite CaCO3 in seawater. *Proceedings of the National Academy of Sciences*, 112(11):3199–3204.

Tanner, S. D., Baranov, V. I., and Bandura, D. R. (2002). Reaction cells and collision cells for ICP-MS: a tutorial review. *Spectrochimica Acta Part B: Atomic Spectroscopy*, 57(9):1361–1452.

Teng, F.-Z., Dauphas, N., and Watkins, J. M. (2017). Non-Traditional Stable Isotopes: Retrospective and Prospective. In *Non-Traditional Stable Isotopes; Reviews in Mineralogy and Geochemistry*, volume 82, pages 1–26.

Terakado, Y. and Masuda, A. (1988). The coprecipitation of rare-earth elements with calcite and aragonite. *Chemical Geology*, 69(1-2):103–110.

Thomas, A. L., Henderson, G. M., Deschamps, P., Yokoyama, Y., Mason, A. J., Bard, E., Hamelin, B., Durand, N., and Camoin, G. (2009). Penultimate deglacial sea-level timing from uranium/thorium dating of Tahitian corals. *Science (New York, N.Y.)*, 324(5931):1186–1189.

Thompson, W. G., Spiegelman, M. W., Goldstein, S. L., and Speed, R. C. (2003). An open-system model for U-series age determinations of fossil corals. *Earth and Planetary Science Letters*, 210(1-2):365–381.

Tipper, E. T., Bickle, M. J., Galy, A., West, A. J., Pomiès, C., and Chapman, H. J. (2006). The short term climatic sensitivity of carbonate and silicate weathering fluxes: Insight from seasonal variations in river chemistry. *Geochimica et Cosmochimica Acta*, 70(11):2737–2754.

Uchikawa, J. and Zeebe, R. E. (2012). The effect of carbonic anhydrase on the kinetics and equilibrium of the oxygen isotope exchange in the CO2–H2O system: Implications for δ18O vital effects in biogenic carbonates. *Geochimica et Cosmochimica Acta*, 95:15–34.

Vadillo, J. M., Fernández Romero, J. M., Rodríguez, C., and Laserna, J. J. (1999). Effect of plasma shielding on laser ablation rate of pure metals at reduced pressure. *Surface and Interface Analysis*, 27(11):1009–1015.

Vaks, a., Gutareva, O. S., Breitenbach, S. F. M., Avirmed, E., Mason, a. J., Thomas, a. L., Osinzev, a. V., Kononov, a. M., and Henderson, G. M. (2013). Speleothems reveal 500,000-year history of Siberian permafrost. *Science (New York, N.Y.)*, 340(6129):183–6.

Verkerke, J. L., Williams, D. J., and Thoma, E. (2014). Remote sensing of CO2 leakage from geologic sequestration projects. *International Journal of Applied Earth Observation and Geoinformation*, 31:67–77.

Villiers, S. D., Greaves, M., Elderfield, H., de Villiers, S., Greaves, M., Elderfield, H., Villiers, S. D., Greaves, M., Elderfield, H., de Villiers, S., Greaves, M., and Elderfield, H. (2002). An intensity ratio calibration method for the accurate determination of Mg/Ca and Sr/Ca of marine carbonates by ICP-AES. *Geochemistry, Geophysics, Geosystems*, 3(1):Paper number 2001GC000169.

Voigt, M., Mavromatis, V., and Oelkers, E. H. (2017). The experimental determination of REE partition coefficients in the water-calcite system. *Chemical Geology*.

Vroon, P. Z., van der Wagt, B., Koornneef, J. M., and Davies, G. R. (2008). Problems in obtaining precise and accurate Sr isotope analysis from geological materials using laser ablation MC-ICPMS. *Analytical and Bioanalytical Chemistry*, 390:465–476.

Wainer, K. A. I., Rowe, M. P., Thomas, A. L., Mason, A. J., Williams, B., Tamisiea, M. E., Williams, F. H., Düsterhus, A., and Henderson, G. M. (2017). Speleothem evidence for MIS 5c and 5a sea level above modern level at Bermuda. *Earth and Planetary Science Letters*, 457:325–334.

Wang, Y., Cheng, H., Edwards, R. L., He, Y., Kong, X., An, Z., Wu, J., Kelly, M. J., Dykoski, C. a., and Li, X. (2005). The Holocene Asian monsoon: links to solar changes and North Atlantic climate. *Science (New York, N.Y.)*, 308(5723):854–7.

Wang, Y. J., Cheng, H., Edwards, R. L., An, Z. S., Wu, J. Y., Shen, C. C., and Dorale, J. a. (2001). A high-resolution absolute-dated late Pleistocene Monsoon record from Hulu Cave, China. *Science (New York, N.Y.)*, 294(5550):2345–2348.

Wang, Z., Hattendorf, B., and Günther, D. (2006). Analyte Response in Laser Ablation Inductively Coupled Plasma Mass Spectrometry. *Journal of the American Society for Mass Spectrometry*, 17(5):641–651.

Watkins, J. M., Nielsen, L. C., Ryerson, F. J., and DePaolo, D. J. (2013). The influence of kinetics on the oxygen isotope composition of calcium carbonate. *Earth and Planetary Science Letters*, 375:349–360.

Watson, E. B. (1996). Surface enrichment and trace-element uptake during crystal growth. *Geochimica et Cosmochimica Acta*, 60(24):5013–5020.

Watson, E. B. (2004). A conceptual model for near-surface kinetic controls on the trace- element and stable isotope composition of abiogenic calcite crystals. *Geochimica et Cosmochimica Acta*, 68(7):1473–1488.

Wendt, I. and Carl, C. (1991). The statistical distribution of the mean squared weighted deviation. *Chemical Geology: Isotope Geoscience Section*, 86(4):275–285.

Weremeichik, J. M., Gabitov, R. I., Thien, B. M., and Sadekov, A. (2017). The effect of growth rate on uranium partitioning between individual calcite crystals and fluid. *Chemical Geology*, 450:145–153.

Weyer, S., Anbar, a. D., Gerdes, A., Gordon, G. W., Algeo, T. J., and Boyle, E. A. (2008). Natural fractionation of 238U/235U. *Geochimica et Cosmochimica Acta*, 72(2):345–359.

White, A. F. (1977). Sodium and potassium coprecipitation in aragonite. *Geochimica et Cosmochimica Acta*, 41(5):613–625.

Widanagamage, I. H., Schauble, E. a., Scher, H. D., and Griffith, E. M. (2014). Stable strontium isotope fractionation in synthetic barite. *Geochimica et Cosmochimica Acta*, 147:58–75.

Wigley, M. (2012). *Fluid-Mineral Reactions in an Exhumed CO2 Charged Aquifer, Green River , Utah , USA*. PhD thesis.

Wigley, M., Dubacq, B., Kampman, N., and Bickle, M. (2013). Controls of sluggish, CO2-promoted, hematite and K-feldspar dissolution kinetics in sandstones. *Earth and Planetary Science Letters*, 362:76–87.

Woodhead, J. and Hergt, J. M. (2001). Strontium, Neodymium and Lead Isotope Analyses of NIST Glass Certified Reference Materials: SRM 610, 612, 614. *Geostandards Newsletter*, 25(2-3):261–266.

Woodhead, J., Swearer, S., Hergt, J., and Maas, R. (2005). In situ Sr-isotope analysis of carbonates by LA-MC-ICP-MS: interference corrections, high spatial resolution and an example from otolith studies. *Journal of Analytical Atomic Spectrometry*, 20(1):22.

Wu, H., Wu, C., Zhang, N., Zhu, X., Ma, X., and Zhigilei, L. V. (2017). Experimental and computational study of the effect of 1 atm background gas on nanoparticle generation in femtosecond laser ablation of metals. *Applied Surface Science*, (2010).

References

Xie, A. J., Shen, Y. H., Zhang, C. Y., Yuan, Z. W., Zhu, X. M., and Yang, Y. M. (2005). Crystal growth of calcium carbonate with various morphologies in different amino acid systems. *Journal of Crystal Growth*, 285(3):436–443.

Yang, Z., Fryer, B. J., Longerich, H. P., Gagnon, J. E., and Samson, I. M. (2011). 785 nm femtosecond laser ablation for improved precision and reduction of interferences in Sr isotope analyses using MC-ICP-MS. *J. Anal. At. Spectrom.*, 26:341–351.

Yobregat, E., Fitoussi, C., and Bourdon, B. (2017). A new method for TIMS high precision analysis of Ba and Sr isotopes for cosmochemical studies. *J. Anal. At. Spectrom.*, 00:1–12.

York, D. (1969). Least squares fitting of a straight line with correlated errors. *Earth and Planetary Science Letters*, 5(Xi):320–324.

Zack, T. and Hogmalm, K. J. (2016). Laser ablation Rb/Sr dating by online chemical separation of Rb and Sr in an oxygen-filled reaction cell. *Chemical Geology*, 437:120–133.

Zhang, L., Ren, Z. Y., Wu, Y. D., and Li, N. (2018). Strontium isotope measurement of basaltic glasses by laser ablation multiple collector inductively coupled plasma mass spectrometry based on a linear relationship between analytical bias and Rb/Sr ratios. *Rapid Communications in Mass Spectrometry*, 32(2):105–112.

Zheng, X.-Y., Beard, B., and Johnson, C. M. (2017). Assessment of matrix effects associated with Fe isotope analysis using 266 nm femtosecond and 193 nm nanosecond laser ablation multi-collector inductively coupled plasma mass spectrometry. *Journal of Analytical Atomic Spectrometry*.

Zhu, C. (2005). In situ feldspar dissolution rates in an aquifer. *Geochimica et Cosmochimica Acta*, 69(6):1435–1449.

Zindler, A., Hart, S. R., and Brooks, C. (1981). The Shabogamo Intrusive Suite, Labrador: Sr and Nd isotopic evidence for contaminated mafic magmas in the Proterozoic. *Earth and Planetary Science Letters*, 54(2):217–235.

Zindler, A., Hart, S. R., Frey, F. A., and Jakobsson, S. P. (1979). Nd and Sr isotope ratios and rare earth element abundances in Reykjanes Peninsula basalts evidence for mantle heterogeneity beneath Iceland. *Earth and Planetary Science Letters*, 45(2):249–262.

Ziveri, P., Thoms, S., Probert, I., Geisen, M., and Langer, G. (2012). A universal carbonate ion effect on stable oxygen isotope ratios in unicellular planktonic calcifying organisms. *Biogeosciences*, 9(3):1025–1032.

Appendix A

Fracture network characterisation by UAV mapping

Photographic aerial mapping by drone allows accurate 3D mapping of the ground surface, using structure from motion with control points constrained by differential GPS (DGPS). A drone survey of selected areas adjacent at Green River was undertaken at the end of September 2016, using a DJI phantom II drone with a Canon camera with built in GPS. During a survey, control points (orange 1m squares) were laid out at the furthest extents and in the middle of the field area. These locations are recorded using a DGPS. DGPS gives a position precise to $\pm 2 - 3cm$ in all dimensions; the uncertainty in positioning the unit is larger. The images from the drone are processed using AgiSoft software and was performed by Christophe Grutzner. This software calculates the structure by identifying similar points within the images, using the changing perspective to calculate 3d structure. Whilst not necessary, GPS location stamps on image files (i.e. recording the approximate drone position) give additional constraint and reduces computation time. By matching identical points between images, a 'point' cloud is created which gives relative structures, and can be used to stitch together images. The DGPS control points 'anchor' the model to a known datum. In this way, the 3d structure (essentially a digital elevation model) can be constructed. An orthographic image can also be assembled from the stitched photos. 3 main sample areas were targeted: 1) around the 'chimney' structure at the anticline hinge at Salt Wash graben, 2) an area to the east of salt wash anticline hinge and to the north of the fault, where bleached fracture networks are observed and 3) across the eastern end of little grand fault. The area of most interest, due to extensive outcropping is a fracture swarm to the east of the anticline hinge at Salt Wash.

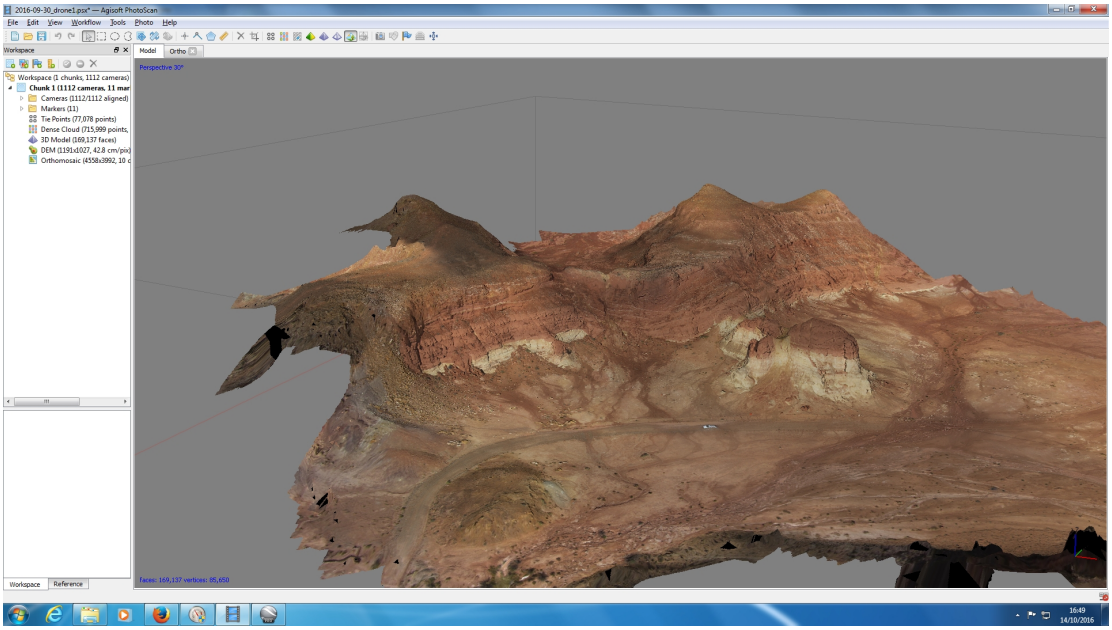

Fig. A.1 3D reconstruction around the chimney area: view 1

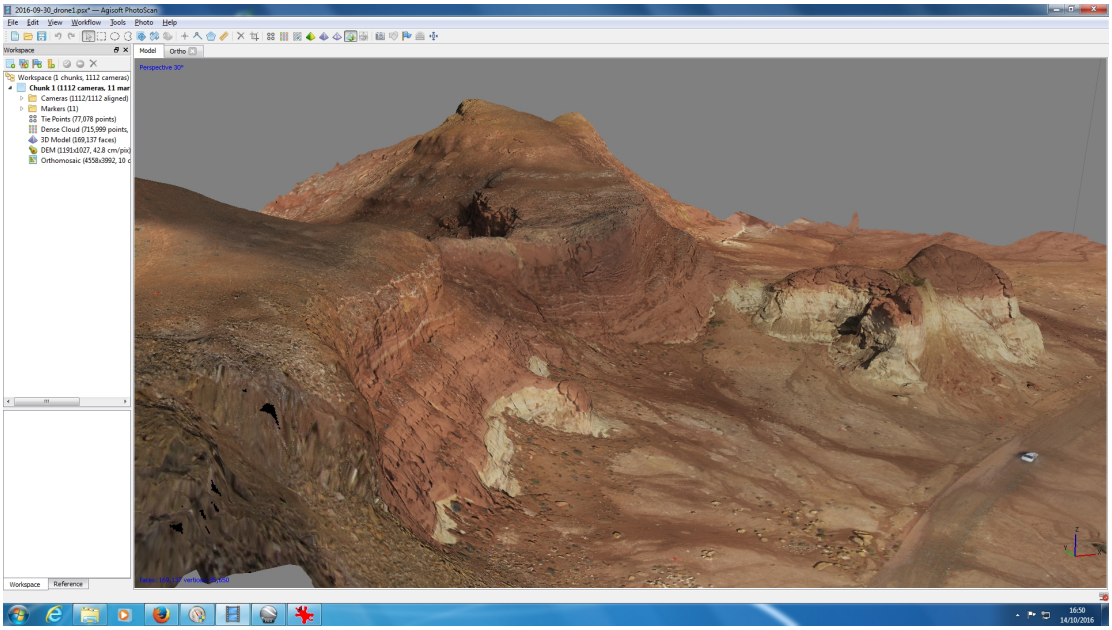

Fig. A.2 3D reconstruction around the chimney area: view 2

Appendix B

Data tables

B.1 Travertine vein locations and labels

B.2 Thin section photo for EBSD and BSE imaging

B.3 Isotopic data

Table B.1 Sample locality locations

Locality	Date	Fault	Longitude (°E)	Latitude (°N)	Altitude (m)	SW dist[a] (km)	LG dist[b] (km)
Gypsum A	06/05/2014	SW	-110.0586	38.8523		6.317	11.749
(A)	06/05/2014	SW	-110.0831	38.8593	1293	4.059	9.969
(B)	06/05/2014	SW	-110.0856	38.8596	1283	3.856	9.845
(C)	06/05/2014	SW	-110.0736	38.8558	1293	4.971	10.712
Gypsum B	06/05/2014	SW	-110.0752	38.8562		4.828	10.603
(D)	06/05/2014	SW	-110.0550	38.8516	1307	6.631	11.993
(F)	07/05/2014	LG	-110.1088	38.9369	1283	6.995	2.447
(F2)	07/05/2014	LG	-110.1091	38.9365	1283	6.981	2.422
(G)	07/05/2014	LG	-110.1097	38.9367	1280	6.995	2.369
(H)	07/05/2014	LG	-110.1215	38.9364	1281	6.837	1.365
(I)	07/05/2014	LG	-110.1328	38.9375	1270	6.985	0.378
(J)	07/05/2014	LG	-110.1316	38.9373	1282	6.946	0.489
(K)	07/05/2014	LG	-110.1320	38.9376	nan	6.986	0.442
(L)	08/05/2014	SW	-110.1006	38.8703	1275	2.217	8.216
(M)	08/05/2014	SW	-110.1024	38.8702	1272	2.064	8.169
(N)	08/05/2014	SW	-110.1040	38.8701	1272	1.935	8.126
(O)	08/05/2014	SW	-110.1081	38.8691	1266	1.637	8.115
(P)	08/05/2014	SW	-110.1100	38.8700	1253	1.443	7.966
(Q)	08/05/2014	SW	-110.1013	38.8647	1272	2.386	8.779
(Q)	08/05/2014	SW	-110.1009	38.8648	1281	2.416	8.782
(R)	09/05/2014	LG	-110.1210	38.9363	1272	6.828	1.407
(S)	09/05/2014	LG	-110.1224	38.9361	1258	6.802	1.289
Unsampled vein	09/05/2014	LG	-110.1267	38.9368	1275	6.873	0.913

[a] Distance relative to arbitrary point on fault Northwest of anticline hinge (38.874989, -110.125467)

[b] Distance relative to the Green River (38.938552, -110.13701)

Table B.2 Locality descriptions, for field work in May 2014. Equivalent name is an approximate conversion to the sample naming structure adopted by Dockrill (2006) and Burnside (2010). This format is Fault/Field year/Sample identifier. I have used alphabetic and numeric characters in the opposite sense to these other studies (i.e. letters represent sample localities).

Locality	Description	Equivalent name
Gypsum A	Gypsum in fault ramp	SW/14/G1
A	vein samples A1-A9	SW/14/A#
B	Vein samples B1-B10; Holocene mound?	SW/14/B#
C	Vein samples C1-C3	SW/14/C#
Gypsum B	Cross-cutting gypsum veining in fault	SW/14/G2
D	Vein sample D	SW/14/D
F	Vein samples F1a-F4	LG/14/F#
F	Vein samples F5a, F5b	LG/14/F#
G	Vein samples G1-G15	LG/14/G#
H	Vein samples H0-H5 and FB (fault breccia)	LG/14/H#
I	Vein samples I1-I4	LG/14/I#
J	Veins from 'Universal mound'; J0-J17	LG/14/J#
K	Fallen boulder, presumed from 'Universal mound'; K1-K4	LG/14/K#
L	Vein samples L1-L4	SW/14/L#
M	Vein samples M1-M5	SW/14/M#
N	Vein samples N1-N5	SW/14/N#
O	Vein samples O1-O4	SW/14/O#
P	Vein samples P1-P19	SW/14/P#
Q	Veins samples Q1,Q2	SW/14/Q#
Q	Vein samples Q3-Q9t	SW/14/Q#
R	Vein samples R1-R5	LG/14/R#
S	Vein samples S0-S2	LG/14/S#
Unsampled vein	Thin vein (<5cm), not on fault tip	-

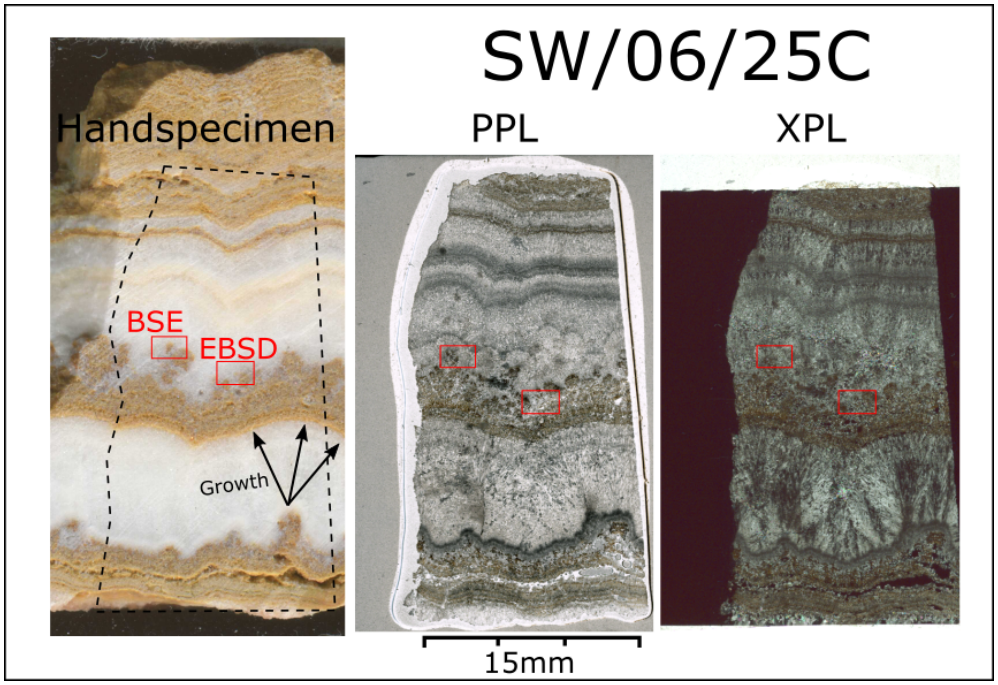

Fig. B.1 Handspecimen, Plane polarised and Cross polarised image of sample SW/06/25C. Areas used for EBSD and SEM (BSE) imaging are shown in red boxes. The dendritic iron rich lamination was of interest, to investigate potential biogenic origins. The growth of aragonite is spherulitic, and in thin section these spherules can be cut at different orientations (visible in XPL), and may interfere with each other. Some of these spherules appear to nucleate on iron oxide surfaces. EBSD confirms that aragonite and celestine are intergrown.

Table B.3 Laser ablation Sr isotope data

Sample Name	$^{84}Sr/^{86}Sr$	±2SE	$^{87}Sr/^{86}Sr$	±2SE	$^{87}Sr/^{86}Sr_b$	±2SE	β_{Sr}	±2SE
A_b	0.056494	0.000016	0.713229	4.13E-05	0.713233	4.13E-05	-1.7696	0.002
A2b	0.056491	1.87E-05	0.713206	0.000039	0.713209	0.000039	-1.77047	0.0021
A2t	0.056476	1.87E-05	0.713192	4.17E-05	0.713196	4.17E-05	-1.77423	0.001933
A3b	0.05649	1.67E-05	0.713097	0.000048	0.713102	0.000048	-1.7688	0.002167
A3t	0.056489	0.000016	0.713223	4.37E-05	0.713229	4.37E-05	-1.76917	0.0018
A4t								
A5b	0.056487	0.000015	0.713188	3.87E-05	0.713193	3.87E-05	-1.77113	0.001733
A5t	0.056491	0.000021	0.713201	4.57E-05	0.713206	4.57E-05	-1.77093	0.0021
A6b	0.056467	1.73E-05	0.713173	0.000044	0.713177	0.000044	-1.77183	0.001967
A6t	0.056472	1.87E-05	0.713179	4.43E-05	0.713182	4.43E-05	-1.77177	0.001933
A7b	0.05648	0.000019	0.71316	4.23E-05	0.713163	4.23E-05	-1.77593	0.0019
A7t	0.056477	1.73E-05	0.713099	3.93E-05	0.713102	3.93E-05	-1.7722	0.001733
A8b	0.05649	1.77E-05	0.713167	0.000037	0.713171	0.000037	-1.77363	0.002
A8t	0.056484	0.000018	0.713153	0.000039	0.713158	0.000039	-1.77457	0.001967
A9b	0.056472	1.67E-05	0.713157	3.73E-05	0.71316	3.73E-05	-1.7773	0.001733
A9t	0.056487	1.23E-05	0.712836	0.00003	0.712838	0.00003	-1.77677	0.0016
B10b	0.056484	1.75E-05	0.713097	3.65E-05	0.71312	3.65E-05	-1.7101	0.0017
B10t	0.056472	0.000016	0.713047	3.43E-05	0.713069	3.43E-05	-1.71063	0.001767
B1b	0.056472	1.73E-05	0.713062	0.00004	0.713084	0.00004	-1.7091	0.0021
B1t	0.056464	0.000018	0.71301	0.000036	0.713033	0.000036	-1.7117	0.001767
B9b	0.056479	1.63E-05	0.713088	0.000037	0.713112	0.000037	-1.7158	0.0017
B9t	0.056493	1.67E-05	0.713032	3.53E-05	0.713055	3.53E-05	-1.71257	0.002
C1b	0.05648	1.37E-05	0.713252	3.77E-05	0.713281	3.77E-05	-1.69473	0.001767
C1t	0.056476	1.33E-05	0.713237	0.000034	0.713266	0.000034	-1.7001	0.001733
C2b	0.056473	0.000015	0.713229	3.57E-05	0.713258	3.57E-05	-1.69143	0.0018
C2t	0.056476	1.37E-05	0.713264	3.43E-05	0.713293	3.43E-05	-1.6938	0.001733
C3b	0.056484	1.53E-05	0.713283	0.000037	0.713311	0.000037	-1.6894	0.001633
C3t	0.056496	1.53E-05	0.713262	0.000036	0.71329	0.000036	-1.68983	0.0016
D1	0.05649	1.47E-05	0.711835	0.000039	0.711864	0.000039	-1.70047	0.001633

Sample Name	$^{84}Sr/^{86}Sr$	±2SE	$^{87}Sr/^{86}Sr$	±2SE	$^{87}Sr/^{86}Sr_b$	±2SE	β_{Sr}	±2SE
F4b	0.05648	1.17E-05	0.712116	3.47E-05	0.712149	3.47E-05	-1.68397	0.0015
F4m	0.056481	1.53E-05	0.712194	3.43E-05	0.712228	3.43E-05	-1.69117	0.0016
F4t	0.056482	1.47E-05	0.712098	0.000038	0.712131	0.000038	-1.69043	0.001933
F5bb	0.056492	1.47E-05	0.71215	3.37E-05	0.712157	3.37E-05	-1.7292	0.0019
F5bt	0.056478	1.63E-05	0.712213	0.000031	0.71222	0.000031	-1.76087	0.001667
F5tb	0.056499	1.33E-05	0.7122	3.57E-05	0.712208	3.57E-05	-1.76137	0.001667
F5tt	0.056478	1.33E-05	0.712094	0.000035	0.712101	0.000035	-1.76383	0.001433
FB	0.056494	0.000017	0.712712	4.03E-05	0.712724	4.03E-05	-1.74663	0.0018
G15b	0.056492	1.37E-05	0.712225	3.03E-05	0.712235	3.03E-05	-1.74967	0.0017
G15t	0.056477	0.000014	0.712109	3.47E-05	0.712121	3.47E-05	-1.74677	0.001467
G1b	0.056469	0.000014	0.7122	3.53E-05	0.712212	3.53E-05	-1.7483	0.001633
G1t	0.056471	1.63E-05	0.712219	0.000036	0.71223	0.000036	-1.74747	0.0018
G6b	0.056474	1.23E-05	0.712202	0.000034	0.712212	0.000034	-1.74643	0.001567
G6t	0.056482	1.37E-05	0.712238	3.17E-05	0.712249	3.17E-05	-1.74673	0.0016
G7b	0.056474	0.000013	0.712268	0.000035	0.712279	0.000035	-1.7488	0.001767
G7t	0.056488	1.37E-05	0.712232	3.33E-05	0.712243	3.33E-05	-1.74833	0.0015
H0t								
H1b	0.056475	1.83E-05	0.712746	4.77E-05	0.712781	4.77E-05	-1.70883	0.001833
H1t	0.056477	1.53E-05	0.712621	0.000038	0.712656	0.000038	-1.69917	0.001633
H3b	0.056473	1.43E-05	0.712637	3.53E-05	0.712671	3.53E-05	-1.6953	0.002
H3t	0.05648	1.63E-05	0.712725	3.83E-05	0.712759	3.83E-05	-1.69463	0.001767
I2b	0.056477	1.37E-05	0.712957	3.57E-05	0.712971	3.57E-05	-1.7302	0.001833
I2t	0.056475	0.000014	0.712927	3.47E-05	0.712941	3.47E-05	-1.72947	0.0016
I4b	0.056477	1.63E-05	0.712973	3.47E-05	0.712987	3.47E-05	-1.73393	0.001567
I4t	0.056465	2.03E-05	0.712957	3.93E-05	0.712971	3.93E-05	-1.733	0.001867
J10b	0.056472	2.27E-05	0.712918	0.000041	0.712927	0.000041	-1.7575	0.002333
J10t	0.056473	1.47E-05	0.712932	0.000042	0.712941	0.000042	-1.75727	0.002133

Sample Name	$^{84}Sr/^{86}Sr$	±2SE	$^{87}Sr/^{86}Sr$	±2SE	$^{87}Sr/^{86}Sr_b$	±2SE	β_{Sr}	±2SE
J17b	0.056489	1.67E-05	0.712923	3.63E-05	0.712932	3.63E-05	-1.75933	0.001867
J17t	0.05648	1.77E-05	0.712961	4.33E-05	0.712969	4.33E-05	-1.75797	0.001767
J1b	0.056478	0.000018	0.712751	0.000037	0.712759	0.000037	-1.75687	0.0019
J1t	0.05648	0.000014	0.712622	0.000042	0.712631	0.000042	-1.76017	0.0019
J2t								
J3b								
J3t								
J5b	0.056464	0.000018	0.712909	4.23E-05	0.712927	4.23E-05	-1.71987	0.002067
J5t	0.056477	2.03E-05	0.712913	0.000045	0.712931	0.000045	-1.72167	0.002
J6ab								
J6at								
J6b	0.05647	1.67E-05	0.712924	0.00004	0.712942	0.00004	-1.72163	0.0019
J6t	0.056488	1.67E-05	0.712864	0.000042	0.712882	0.000042	-1.71593	0.002
K3b	0.056473	1.57E-05	0.712817	3.53E-05	0.712818	3.53E-05	-1.77733	0.001767
K3t	0.056472	1.83E-05	0.712939	4.17E-05	0.71294	4.17E-05	-1.78067	0.001933
K4b								
K4t								
L1b	0.056477	2.17E-05	0.71289	5.47E-05	0.71291	5.47E-05	-1.72617	0.002133
L1t	0.056456	0.000018	0.712933	3.73E-05	0.712952	3.73E-05	-1.72573	0.002133
L2b	0.056472	1.87E-05	0.712926	3.77E-05	0.712946	3.77E-05	-1.72483	0.001633
L2t	0.056488	0.000017	0.712916	4.47E-05	0.712935	4.47E-05	-1.72543	0.002
L3b	0.056481	0.000021	0.712873	4.13E-05	0.712891	4.13E-05	-1.72553	0.002067
L3t	0.056483	1.77E-05	0.71293	4.13E-05	0.712962	4.13E-05	-1.7023	0.002033
L4b	0.05648	0.000018	0.712883	4.23E-05	0.712915	4.23E-05	-1.69297	0.001733
L4t	0.056468	1.83E-05	0.712889	0.00004	0.712921	0.00004	-1.6941	0.001933
M1b	0.056482	0.000019	0.712881	4.07E-05	0.712906	4.07E-05	-1.69343	0.001867
M1t	0.056476	1.77E-05	0.712884	4.07E-05	0.712909	4.07E-05	-1.69693	0.001967

Sample Name	$^{84}Sr/^{86}Sr$	±2SE	$^{87}Sr/^{86}Sr$	±2SE	$^{87}Sr/^{86}Sr_b$	±2SE	β_{Sr}	±2SE
M3b	0.056476	0.00002	0.712834	3.67E-05	0.71286	3.67E-05	-1.69787	0.0018
M3t	0.056466	0.000016	0.712876	4.27E-05	0.712901	4.27E-05	-1.69617	0.0018
M5t	0.056463	0.000018	0.712886	4.43E-05	0.712911	4.43E-05	-1.69683	0.0019
N_b	0.056464	0.000017	0.712755	3.67E-05	0.712779	3.67E-05	-1.6955	0.001667
N_t	0.056472	0.000017	0.712857	4.57E-05	0.712882	4.57E-05	-1.69187	0.001967
O3b	0.056477	0.000016	0.712618	3.57E-05	0.712639	3.57E-05	-1.70817	0.0018
O3t	0.056486	1.97E-05	0.712825	0.00004	0.712846	0.00004	-1.70857	0.002033
O4b	0.056468	1.63E-05	0.712767	0.000034	0.712788	0.000034	-1.708	0.0017
O4t	0.056481	1.97E-05	0.712727	4.43E-05	0.712749	4.43E-05	-1.7056	0.0018
P14b								
P17b	0.056477	1.53E-05	0.71286	3.73E-05	0.712886	3.73E-05	-1.69763	0.001633
P17t	0.056479	0.000018	0.712748	0.000041	0.712775	0.000041	-1.70003	0.002233
P2b	0.056459	1.67E-05	0.712847	0.000045	0.712873	0.000045	-1.70373	0.002
P2t	0.056493	1.77E-05	0.712809	3.93E-05	0.712836	3.93E-05	-1.70637	0.0021
Q1b	0.056481	0.000018	0.712759	4.47E-05	0.712774	4.47E-05	-1.73497	0.002033
Q1t	0.056486	1.87E-05	0.712731	4.47E-05	0.712746	4.47E-05	-1.7329	0.001833
Q2b	0.056459	0.000016	0.712754	0.00004	0.712785	0.00004	-1.68987	0.0021
Q2t	0.056479	0.000019	0.712701	3.63E-05	0.712732	3.63E-05	-1.68933	0.001733
Q3b	0.056478	1.63E-05	0.712969	3.77E-05	0.712999	3.77E-05	-1.68483	0.001967
Q3t	0.056465	1.87E-05	0.713039	4.27E-05	0.713069	4.27E-05	-1.6912	0.0021
Q7b	0.056479	1.73E-05	0.713019	3.63E-05	0.713033	3.63E-05	-1.73673	0.001833
Q7t	0.056486	0.00002	0.713033	4.03E-05	0.713048	4.03E-05	-1.7333	0.002167
Q9b	0.056475	1.93E-05	0.713013	0.00004	0.713029	0.00004	-1.7367	0.0021
Q9t	0.056473	0.000019	0.713034	0.000049	0.71305	0.000049	-1.73595	0.002
R1b								
R1t								
R4b								
S1b	0.056483	1.67E-05	0.712746	3.57E-05	0.712758	3.57E-05	-1.74893	0.0021
S2b	0.056485	1.67E-05	0.71271	3.93E-05	0.712729	3.93E-05	-1.7185	0.001933

Table B.4 LA-U-series isotope ratios

Sample	$^{230}Th/^{238}U$	$\pm 2s$	$\pm 2s+\varepsilon$	$^{234}U/^{238}U$	$\pm 2s$	$\pm 2s+\varepsilon$	$^{235}U/^{238}U$	$\pm 2s$	$\pm 2s+\varepsilon$	$^{232}Th/^{238}U$	$\pm 2s$
A_b	6.04E-05	7.7E-07	1.24E-06	0.000269	1.6E-06	1.81E-06	0.007251	0.00001	1.4E-05	0.000112	0.000014
A2b	6.37E-05	5.5E-07	1.12E-06	0.000273	1.2E-06	1.47E-06	0.007255	0.000013	1.63E-05	7.44E-05	6.2E-06
A2t	6.12E-05	5.8E-07	1.13E-06	0.000283	1.3E-06	1.56E-06	0.007255	0.000009	1.33E-05	7.1E-06	3.3E-06
A3b	6.02E-05	7.5E-07	1.23E-06	0.000269	1.4E-06	1.64E-06	0.007255	0.00001	1.4E-05	3.7E-06	1.4E-06
A3t	6.38E-05	7E-07	1.2E-06	0.000273	1.5E-06	1.73E-06	0.007253	0.00001	1.4E-05	0.000087	5.4E-06
A4t	6.16E-05	1.2E-06	2.15E-06	0.000271	0.000002	2.16E-06	0.00725	0.000025	2.57E-05	0.000134	0.00002
A4t	6.48E-05	1.1E-06	2.09E-06	0.000271	2.1E-06	2.25E-06	0.007255	0.00002	2.08E-05	0.00012	0.000021
A4t	6.33E-05	1.3E-06	2.2E-06	0.000271	2.2E-06	2.34E-06	0.007246	0.000018	1.89E-05	0.00007	0.000013
A4t	5.75E-05	6.7E-07	1.35E-06	0.00026	1.3E-06	1.38E-06	0.00726	0.000012	1.46E-05	0.000373	0.000014
A5t	6.94E-05	8.4E-07	1.29E-06	0.000276	1.7E-06	1.9E-06	0.007262	0.000013	1.63E-05	1.69E-05	5.1E-06
A6b	6.51E-05	8.1E-07	1.27E-06	0.00027	1.7E-06	1.9E-06	0.007253	0.000014	1.71E-05	0.000775	0.000043
A6t	6.04E-05	7.7E-07	1.24E-06	0.000283	1.6E-06	1.81E-06	0.007268	0.000011	1.47E-05	8.8E-06	2.7E-06
A7t	6.31E-05	8.6E-07	1.3E-06	0.000268	1.8E-06	1.99E-06	0.007251	0.000012	1.55E-05	0.000342	0.000027
A8t	6.26E-05	8.1E-07	1.27E-06	0.000274	1.7E-06	1.9E-06	0.007262	0.000012	1.55E-05	0.000268	0.000026
A9b	6.18E-05	6.9E-07	1.19E-06	0.00027	1.4E-06	1.64E-06	0.007258	0.000011	1.47E-05	0.000465	0.000072
A9t	4.79E-05	1.9E-07	9.93E-07	0.000266	4.6E-07	9.72E-07	0.007244	8.5E-06	1.29E-05	8.3E-07	2.8E-07
B10t	4.62E-05	5.6E-07	1.3E-06	0.000308	1.4E-06	1.48E-06	0.007252	0.000013	1.54E-05	0.00009	0.000011
B1t	4.49E-05	2.3E-06	2.91E-06	0.000283	4.6E-06	4.67E-06	0.007269	0.000036	3.65E-05	0.000455	0.000077
B1t	4.77E-05	0.000002	2.68E-06	0.000291	4.1E-06	4.18E-06	0.007249	0.000027	2.76E-05	0.00017	0.000019
B1t	4.83E-05	2.3E-06	2.91E-06	0.000289	4.8E-06	4.87E-06	0.007255	0.000031	3.15E-05	0.000152	0.000024
C1t	6.06E-05	6.5E-07	1.34E-06	0.00031	1.6E-06	1.67E-06	0.007263	0.000016	1.8E-05	0.000096	0.000012
C2t	6.05E-05	6.6E-07	1.34E-06	0.00031	1.6E-06	1.67E-06	0.007258	0.00002	2.16E-05	0.000138	0.000013
C3t	6.13E-05	8E-07	1.42E-06	0.000311	1.9E-06	1.96E-06	0.007256	0.000016	1.8E-05	0.00082	0.0001
D	1.57E-05	7.1E-07	1.37E-06	0.00023	2.9E-06	2.94E-06	0.007267	0.00002	2.16E-05	0.000687	0.000067

Sample	$^{230}Th/^{238}U$	$\pm 2s$	$\pm 2s+\varepsilon$	$^{234}U/^{238}U$	$\pm 2s$	$\pm 2s+\varepsilon$	$^{235}U/^{238}U$	$\pm 2s$	$\pm 2s+\varepsilon$	$^{232}Th/^{238}U$	$\pm 2s$
F4b	2.64E-05	3.5E-07	1.04E-06	0.000377	1.3E-06	1.56E-06	0.007256	0.00001	1.4E-05	0.00022	0.000015
F4t	2.83E-05	5.3E-07	1.11E-06	0.000377	1.7E-06	1.9E-06	0.007262	0.000013	1.63E-05	0.000059	0.00001
F5bb	2.42E-05	7.2E-07	1.37E-06	0.00032	5.7E-06	5.72E-06	0.00644	0.0001	0.0001	0.0317	0.00066
F5bt	1.9E-05	3.1E-07	1.21E-06	0.000391	1.2E-06	1.29E-06	0.007253	8.8E-06	1.21E-05	0.000858	0.000058
F5tt	2.9E-05	5.3E-07	1.86E-06	0.00037	1.9E-06	2.06E-06	0.007253	0.00002	2.08E-05	6.01E-05	8.6E-06
F5tt	2.87E-05	5E-07	1.85E-06	0.000369	2.1E-06	2.25E-06	0.007253	0.000029	2.96E-05	0.000093	0.000012
F5tt	2.99E-05	5.2E-07	1.85E-06	0.00037	2.1E-06	2.25E-06	0.007254	0.000036	3.65E-05	0.000097	0.000014
FB	7.2E-05	4.1E-07	1.24E-06	0.000314	8.3E-07	9.52E-07	0.00726	0.000015	1.71E-05	6.1E-06	1.3E-06
G15t	1.64E-05	1.9E-07	1.18E-06	0.000387	1.1E-06	1.19E-06	0.007262	7.7E-06	1.13E-05	2.4E-06	1.1E-06
G1b	2.1E-05	2.2E-07	1.19E-06	0.00038	9.6E-07	1.07E-06	0.007255	9.8E-06	1.28E-05	4.9E-06	1.3E-06
G1t	2.39E-05	2E-07	1.19E-06	0.000376	9.4E-07	1.05E-06	0.007255	0.000011	1.38E-05	9.78E-05	8.8E-06
G6t	2.37E-05	3.2E-07	1.21E-06	0.000361	1.3E-06	1.38E-06	0.007261	0.000012	1.46E-05	1.75E-05	3.8E-06
G7t	2.11E-05	2E-07	1.19E-06	0.00038	1.1E-06	1.19E-06	0.007266	0.000011	1.38E-05	9.41E-05	8.8E-06
H0t	4.92E-05	3.6E-07	1.22E-06	0.000297	9.8E-07	1.09E-06	0.007249	0.000014	1.63E-05	5.7E-06	1.5E-06
H1t	4.4E-05	3.3E-07	1.03E-06	0.000316	9.4E-07	1.27E-06	0.00726	0.000011	1.47E-05	0.000026	2.6E-06
H3b	4.3E-05	3E-07	1.02E-06	0.000304	8.8E-07	1.23E-06	0.007256	0.000012	1.55E-05	0.000086	0.000003
H3t	4.8E-05	4.3E-07	1.07E-06	0.000294	9.9E-07	1.31E-06	0.007253	9.7E-06	1.38E-05	0.000004	9.8E-07
I2t	2.75E-05	2.7E-07	1.2E-06	0.000237	8.4E-07	9.61E-07	0.007259	0.000016	1.8E-05	0.000045	4.1E-06
I4t	2.56E-05	3.1E-07	1.21E-06	0.000237	0.000001	1.1E-06	0.007258	0.000014	1.63E-05	6.33E-05	0.000007
J10t	3.53E-05	3.3E-07	1.21E-06	0.000155	6.3E-07	7.84E-07	0.007253	8.6E-06	1.19E-05	0.000491	0.000024
J17t	3.76E-05	3.3E-07	1.21E-06	0.000162	6.6E-07	8.08E-07	0.007256	0.000008	1.15E-05	0.000174	0.000015
J1t	4.77E-05	5.1E-07	1.27E-06	0.000227	0.000001	1.1E-06	0.007249	0.000011	1.38E-05	0.000019	2.9E-06
J2t	4.68E-05	4.4E-07	1.25E-06	0.00022	8.5E-07	9.7E-07	0.007252	0.000011	1.38E-05	9.6E-06	1.8E-06
J3b	4.19E-05	6.7E-07	1.9E-06	0.000201	1.3E-06	1.53E-06	0.007262	0.000013	1.42E-05	5.4E-06	1.8E-06
J3b	4.23E-05	6.9E-07	1.91E-06	0.000199	1.1E-06	1.36E-06	0.007252	0.000014	1.52E-05	6.5E-07	2.4E-07
J3b	4.36E-05	6.5E-07	1.89E-06	0.000199	1.1E-06	1.36E-06	0.007251	0.000015	1.61E-05	3.6E-06	0.000002

Sample	$^{230}Th/^{238}U$	$\pm 2s$	$\pm 2s+\varepsilon$	$^{234}U/^{238}U$	$\pm 2s$	$\pm 2s+\varepsilon$	$^{235}U/^{238}U$	$\pm 2s$	$\pm 2s+\varepsilon$	$^{232}Th/^{238}U$	$\pm 2s$
J3t	4.8E-05	4E-07	1.24E-06	0.000215	7.2E-07	8.58E-07	0.007261	7.5E-06	1.12E-05	3.5E-06	1.1E-06
J5b	4.17E-05	3.7E-07	1.04E-06	0.000177	7.4E-07	1.13E-06	0.007261	0.00001	1.4E-05	0.000195	0.000028
J5t	4.15E-05	3.8E-07	1.05E-06	0.000183	7.5E-07	1.14E-06	0.00726	0.000012	1.55E-05	3.21E-05	3.6E-06
J6ab	4.21E-05	3.7E-07	1.23E-06	0.000184	7.9E-07	9.17E-07	0.007254	0.000011	1.38E-05	0.000066	0.000011
J6at	3.8E-05	3.6E-07	1.22E-06	0.000173	7.8E-07	9.09E-07	0.007257	7.7E-06	1.13E-05	8.56E-05	0.000008
J6b	3.94E-05	3.9E-07	1.05E-06	0.000175	8.1E-07	1.18E-06	0.00726	0.000014	1.71E-05	7.9E-06	1.9E-06
J6t	3.79E-05	3.8E-07	1.05E-06	0.000174	7.8E-07	1.16E-06	0.007265	0.000012	1.55E-05	0.000168	0.000019
K3t	4.06E-05	4E-07	1.24E-06	0.000179	8.3E-07	9.52E-07	0.007259	0.000014	1.63E-05	0.001055	0.00004
K4b	4.04E-05	3.7E-07	1.23E-06	0.000169	7.4E-07	8.75E-07	0.007243	9.8E-06	1.28E-05	0.000711	0.000013
K4t	4.12E-05	4.1E-07	1.24E-06	0.000179	9.1E-07	1.02E-06	0.007255	0.000016	1.8E-05	0.001229	0.000027
L1b	4.38E-05	4.7E-07	1.08E-06	0.000242	9.5E-07	1.28E-06	0.007256	8.5E-06	1.29E-05	4.73E-06	5.4E-07
L1t	4.52E-05	4.9E-07	1.09E-06	0.000237	1.1E-06	1.39E-06	0.007268	0.000011	1.47E-05	0.000221	0.000011
L2t	4.42E-05	4.8E-07	1.09E-06	0.000243	1.1E-06	1.39E-06	0.007258	0.000011	1.47E-05	0.00002	4.7E-06
L3b	4.62E-05	8.3E-07	1.28E-06	0.000252	1.9E-06	2.08E-06	0.007252	0.000011	1.47E-05	9.8E-06	1.5E-06
L3t	4.42E-05	4.8E-07	1.26E-06	0.000232	1.1E-06	1.19E-06	0.007253	0.000012	1.46E-05	0.000215	0.000014
L4t	4.69E-05	5.3E-07	1.28E-06	0.00025	1.1E-06	1.19E-06	0.00726	0.00001	1.3E-05	0.000108	0.000013
M1t	3.75E-05	3.9E-07	1.23E-06	0.000224	9.9E-07	1.09E-06	0.007254	0.000012	1.46E-05	1.15E-05	3.1E-06
M3b	3.77E-05	4.4E-07	1.25E-06	0.000219	9.6E-07	1.07E-06	0.00725	8.1E-06	1.16E-05	0.000779	0.000065
M3t	3.77E-05	4.6E-07	1.26E-06	0.000221	1.3E-06	1.38E-06	0.007257	0.000011	1.38E-05	0.000168	0.000017
M5t	3.79E-05	4.3E-07	1.25E-06	0.000227	1.1E-06	1.19E-06	0.007263	0.000012	1.46E-05	5.73E-05	0.000009
N-b	3.71E-05	3.4E-07	1.22E-06	0.000244	9.5E-07	1.06E-06	0.007258	0.000012	1.46E-05	4.8E-06	1.3E-06
N-t	3.71E-05	4E-07	1.24E-06	0.000245	0.000001	1.1E-06	0.007259	0.000012	1.46E-05	4.3E-06	1.6E-06
O3b	2.57E-05	3.5E-07	1.22E-06	0.00021	8.6E-07	9.78E-07	0.00726	0.000008	1.15E-05	6.2E-06	7.4E-07
O3t	2.8E-05	6.3E-07	1.89E-06	0.000187	1.4E-06	1.62E-06	0.007246	0.000016	1.7E-05	0.000108	0.000013
O3t	2.77E-05	5.7E-07	1.87E-06	0.000184	1.5E-06	1.7E-06	0.007243	0.000019	1.99E-05	0.000103	0.000012
O3t	2.8E-05	5.8E-07	1.87E-06	0.000185	1.3E-06	1.53E-06	0.007247	0.000017	1.8E-05	0.000138	0.000016

Sample	$^{230}Th/^{238}U$	$\pm 2s$	$\pm 2s+\varepsilon$	$^{234}U/^{238}U$	$\pm 2s$	$\pm 2s+\varepsilon$	$^{235}U/^{238}U$	$\pm 2s$	$\pm 2s+\varepsilon$	$^{232}Th/^{238}U$	$\pm 2s$
O4t	2.64E-05	3.7E-07	1.23E-06	0.000206	0.000001	1.1E-06	0.007261	8.9E-06	1.22E-05	4.32E-05	4.6E-06
P14b	1.39E-05	2.6E-07	1.01E-06	0.000248	1.1E-06	1.39E-06	0.007243	0.000008	1.26E-05	4.4E-07	1.9E-07
P17t	1.48E-05	1.9E-07	1.18E-06	0.000249	7.9E-07	9.17E-07	0.007258	8.6E-06	1.19E-05	9.5E-06	1.3E-06
P2t	1.62E-05	2.4E-07	1.19E-06	0.000249	0.000001	1.1E-06	0.007265	0.000012	1.46E-05	2.14E-05	4.4E-06
Q1b	1.52E-05	2.7E-07	1.01E-06	0.000262	1.2E-06	1.47E-06	0.007248	0.000011	1.47E-05	1.22E-05	2.5E-06
Q1t	0.000013	2.6E-07	1.01E-06	0.000258	1.1E-06	1.39E-06	0.007266	9.9E-06	1.39E-05	0.000113	0.000012
Q2t	1.28E-05	2.1E-07	1.19E-06	0.000258	0.000001	1.1E-06	0.007254	0.000014	1.63E-05	0.00314	0.0003
Q2t_Fe	1.28E-05	2.5E-07	1.19E-06	0.000259	1.2E-06	1.29E-06	0.007257	0.000011	1.38E-05	0.00455	0.00035
Q3t	4.23E-05	4E-07	1.24E-06	0.00021	8.4E-07	9.61E-07	0.007253	0.000011	1.38E-05	0.000044	0.000004
Q7b	0.00004	4.9E-07	1.09E-06	0.00021	1.1E-06	1.39E-06	0.007257	0.000013	1.63E-05	0.00363	0.00022
Q7t	4.05E-05	3.7E-07	1.04E-06	0.00021	8.8E-07	1.23E-06	0.007258	0.000013	1.63E-05	3.94E-05	6.1E-06
Q9b	3.93E-05	4.2E-07	1.06E-06	0.000209	9.7E-07	1.29E-06	0.00725	0.000011	1.47E-05	0.00117	0.000098
Q9t	3.97E-05	4.1E-07	1.06E-06	0.00021	9.6E-07	1.29E-06	0.007249	0.000012	1.55E-05	3.41E-05	3.6E-06
R1b	4.35E-05	3.5E-07	1.22E-06	0.000355	0.000001	1.1E-06	0.007252	0.000011	1.38E-05	0.000255	7.3E-06
R1t	4.23E-05	5.5E-07	1.86E-06	0.000353	1.8E-06	1.97E-06	0.007251	0.000027	2.76E-05	0.00131	0.00011
R1t	4.36E-05	4.8E-07	1.84E-06	0.000353	1.3E-06	1.53E-06	0.007232	0.000019	1.99E-05	0.00279	0.00011
R1t	4.36E-05	5.6E-07	1.87E-06	0.000352	1.7E-06	1.88E-06	0.00725	0.000029	2.96E-05	0.00241	0.00016
R4b	4.54E-05	3.8E-07	1.23E-06	0.000354	1.1E-06	1.19E-06	0.007255	0.000013	1.54E-05	0.000195	0.000017
S1b	4.35E-06	1.8E-07	1.18E-06	0.000194	1.1E-06	1.19E-06	0.00726	0.000011	1.38E-05	1.16E-05	2.7E-06
S2b	4.08E-06	2.9E-07	1.8E-06	0.000191	1.6E-06	1.79E-06	0.007259	0.000016	1.7E-05	0.001239	0.000084
S2b	3.94E-06	2.6E-07	1.8E-06	0.000189	1.6E-06	1.79E-06	0.007246	0.000015	1.61E-05	0.001074	0.000064
S2b	3.9E-06	2.9E-07	1.8E-06	0.000191	1.6E-06	1.79E-06	0.007244	0.000016	1.7E-05	0.001038	0.00008

Table B.5 LA U-Th calculated ages

Name	Date uncorr (ka)	±2s (abs)	±2s + ε (abs)	Date corr (ka)	Date corr (ka BP)	±2s (abs)	±2s + ε (abs)	$\left[^{234}U/^{238}U\right]_i$	±2s (abs)	±2s + ε (abs)	Rho T-g0	Rho T-g0
A_b	115.129	2.474	2.800	115.129	115.179	2.474	2.800	6.394	0.042	0.047	0.487	0.516
A2b	122.087	1.857	2.302	122.086	122.136	1.857	2.302	6.601	0.031	0.038	0.483	0.540
A2t	108.848	1.708	2.080	108.848	108.898	1.708	2.080	6.633	0.032	0.038	0.407	0.469
A3b	114.484	2.354	2.691	114.484	114.534	2.354	2.691	6.386	0.039	0.045	0.561	0.574
A3t	122.760	2.373	2.740	122.759	122.809	2.373	2.740	6.596	0.040	0.046	0.500	0.537
A4t	117.582	3.773	5.914	117.581	117.631	3.773	5.914	6.469	0.062	0.094	0.644	0.834
A4t	127.267	3.803	6.176	127.266	127.316	3.803	6.176	6.621	0.062	0.099	0.599	0.831
A4t	122.502	4.247	6.340	122.502	122.552	4.247	6.340	6.551	0.069	0.101	0.653	0.827
A4t	112.909	2.171	3.149	112.907	112.957	2.171	3.148	6.125	0.035	0.048	0.523	0.760
A5t	137.350	3.105	3.452	137.350	137.400	3.105	3.452	6.935	0.051	0.057	0.608	0.626
A6b	128.913	2.902	3.245	128.910	128.960	2.902	3.245	6.619	0.047	0.052	0.542	0.568
A6t	106.666	2.196	2.487	106.666	106.716	2.196	2.487	6.603	0.040	0.045	0.458	0.487
A7t	123.745	2.972	3.287	123.743	123.793	2.972	3.287	6.503	0.048	0.053	0.519	0.543
A8t	118.391	2.629	2.942	118.389	118.439	2.629	2.942	6.558	0.045	0.050	0.496	0.523
A9b	118.435	2.255	2.622	118.433	118.483	2.255	2.622	6.475	0.038	0.044	0.519	0.549
A9t	83.883	0.493	1.155	83.883	83.933	0.493	1.155	5.872	0.010	0.021	0.247	0.457
B10t	66.114	1.082	1.761	66.114	66.164	1.082	1.761	6.545	0.029	0.036	0.205	0.571
B1t	70.953	4.916	5.841	70.951	71.001	4.916	5.841	6.075	0.105	0.115	0.372	0.494
B1t	74.238	4.285	5.314	74.238	74.288	4.284	5.314	6.284	0.093	0.105	0.365	0.519
B1t	76.087	5.042	5.974	76.086	76.136	5.042	5.974	6.271	0.109	0.120	0.355	0.483
C1t	93.675	1.564	2.282	93.675	93.725	1.564	2.282	7.046	0.035	0.045	0.281	0.605
C2t	93.480	1.582	2.293	93.480	93.530	1.582	2.293	7.038	0.036	0.046	0.294	0.608
C3t	94.670	1.919	2.541	94.666	94.716	1.919	2.541	7.095	0.043	0.052	0.316	0.562
D	26.417	1.365	1.972	26.413	26.463	1.365	1.972	4.439	0.055	0.056	-0.038	0.151

Name	Date uncorr (ka)	±2s (abs)	±2s + ε (abs)	Date corr (ka)	Date corr (ka BP)	±2s (abs)	±2s + ε (abs)	$\left[^{234}U/^{238}U\right]_i$	±2s (abs)	±2s + ε (abs)	Rho T-g0	Rho T-g0
F4b	27.094	0.408	0.629	27.093	27.143	0.408	0.629	7.326	0.025	0.029	0.034	0.197
F4t	29.279	0.625	0.792	29.279	29.329	0.625	0.792	7.359	0.033	0.036	0.101	0.189
F5bb	29.686	1.144	1.551	29.539	29.589	1.146	1.551	6.275	0.108	0.109	-0.394	-0.192
F5bt	18.323	0.324	0.853	18.320	18.370	0.324	0.853	7.435	0.023	0.027	0.071	0.517
F5tt	30.795	0.649	1.937	30.795	30.845	0.649	1.937	7.252	0.036	0.050	0.033	0.607
F5tt	30.483	0.620	1.928	30.483	30.533	0.620	1.928	7.232	0.040	0.052	-0.053	0.560
F5tt	31.791	0.649	1.949	31.791	31.841	0.649	1.949	7.271	0.040	0.053	-0.039	0.564
FB	118.194	1.141	2.246	118.194	118.244	1.141	2.246	7.578	0.023	0.042	0.538	0.875
G15t	15.777	0.199	0.808	15.777	15.827	0.199	0.808	7.317	0.020	0.025	-0.070	0.534
G1b	21.014	0.243	0.861	21.014	21.064	0.243	0.861	7.281	0.018	0.023	-0.003	0.604
G1t	24.416	0.232	0.886	24.416	24.466	0.232	0.886	7.256	0.018	0.023	-0.066	0.615
G6t	25.298	0.386	0.977	25.298	25.348	0.386	0.977	6.972	0.025	0.029	-0.003	0.481
G7t	21.100	0.225	0.857	21.100	21.150	0.225	0.857	7.276	0.020	0.025	-0.110	0.539
H0t	74.960	0.787	1.719	74.960	75.010	0.787	1.719	6.451	0.020	0.031	0.145	0.717
H1t	59.998	0.599	0.944	59.998	60.048	0.599	0.944	6.634	0.019	0.025	0.105	0.292
H3b	61.245	0.576	0.959	61.244	61.294	0.576	0.959	6.388	0.018	0.025	0.079	0.294
H3t	73.643	0.918	1.267	73.643	73.693	0.918	1.267	6.349	0.022	0.028	0.276	0.371
I2t	48.507	0.604	1.724	48.507	48.557	0.604	1.724	4.792	0.016	0.024	0.026	0.684
I4t	44.597	0.671	1.707	44.596	44.646	0.671	1.707	4.756	0.019	0.026	0.012	0.601
J10t	121.580	2.001	4.692	121.576	121.626	2.001	4.692	3.563	0.017	0.035	0.467	0.890
J17t	125.090	1.980	4.597	125.088	125.138	1.980	4.597	3.764	0.017	0.037	0.460	0.889
J1t	105.402	1.806	3.089	105.402	105.452	1.806	3.089	5.201	0.025	0.039	0.464	0.793
J2t	107.223	1.626	3.082	107.223	107.273	1.626	3.082	5.064	0.022	0.037	0.478	0.835
J3b	104.521	2.674	6.315	104.521	104.571	2.674	6.315	4.566	0.033	0.067	0.447	0.852
J3b	107.323	2.770	6.507	107.323	107.373	2.770	6.507	4.552	0.032	0.068	0.593	0.888
J3b	112.531	2.736	6.692	112.531	112.581	2.736	6.692	4.605	0.031	0.070	0.574	0.893

Name	Date uncorr (ka)	±2s (abs)	±2s + ε (abs)	Date corr (ka)	Date corr (ka BP)	±2s (abs)	±2s + ε (abs)	$\left[^{234}U/^{238}U\right]_i$	±2s (abs)	±2s + ε (abs)	Rho T-g0	Rho T-g0
J3t	114.990	1.591	3.244	114.990	115.040	1.591	3.244	5.036	0.020	0.038	0.556	0.883
J5b	127.274	2.047	3.054	127.273	127.323	2.047	3.054	4.173	0.020	0.029	0.493	0.553
J5t	118.804	1.882	2.774	118.804	118.854	1.882	2.773	4.267	0.020	0.029	0.474	0.529
J6ab	121.091	1.890	3.979	121.091	121.141	1.890	3.979	4.299	0.020	0.038	0.423	0.856
J6at	113.454	1.846	3.989	113.453	113.503	1.846	3.989	3.969	0.019	0.035	0.362	0.838
J6b	118.615	2.050	2.964	118.615	118.665	2.050	2.964	4.051	0.020	0.029	0.422	0.496
J6t	112.694	1.911	2.808	112.692	112.742	1.911	2.808	3.976	0.019	0.028	0.404	0.476
K3t	120.070	2.080	4.148	120.062	120.112	2.080	4.148	4.156	0.021	0.038	0.434	0.842
K4b	130.716	2.212	4.669	130.711	130.761	2.212	4.669	4.000	0.020	0.040	0.498	0.881
K4t	122.431	2.201	4.258	122.422	122.472	2.201	4.258	4.183	0.022	0.040	0.391	0.820
L1b	84.883	1.323	1.762	84.883	84.933	1.323	1.762	5.325	0.022	0.029	0.380	0.431
L1t	91.194	1.507	1.957	91.193	91.243	1.507	1.957	5.284	0.025	0.031	0.313	0.392
L2t	85.370	1.372	1.798	85.370	85.420	1.372	1.798	5.362	0.024	0.031	0.283	0.369
L3b	86.527	2.315	2.577	86.527	86.577	2.315	2.577	5.564	0.042	0.046	0.292	0.331
L3t	91.130	1.512	2.680	91.129	91.179	1.512	2.680	5.170	0.025	0.036	0.292	0.712
L4t	89.256	1.501	2.520	89.256	89.306	1.501	2.520	5.555	0.026	0.037	0.378	0.729
M1t	76.805	1.152	2.381	76.804	76.854	1.152	2.381	4.814	0.021	0.031	0.167	0.696
M3b	79.541	1.329	2.543	79.536	79.586	1.329	2.543	4.744	0.021	0.031	0.290	0.727
M3t	78.494	1.423	2.564	78.493	78.543	1.423	2.564	4.774	0.027	0.035	0.079	0.574
M5t	76.615	1.252	2.404	76.615	76.665	1.252	2.404	4.878	0.023	0.032	0.162	0.656
N-b	67.439	0.858	1.977	67.439	67.489	0.858	1.977	5.167	0.019	0.028	0.093	0.690
N-t	67.226	0.989	2.031	67.226	67.276	0.989	2.031	5.179	0.021	0.030	0.179	0.680
O3b	51.628	0.887	2.065	51.628	51.678	0.887	2.065	4.270	0.018	0.025	0.165	0.683
O3t	66.793	2.035	5.158	66.793	66.843	2.035	5.158	3.891	0.030	0.050	0.223	0.743
O3t	67.176	1.910	5.180	67.175	67.225	1.910	5.180	3.844	0.031	0.051	0.095	0.712
O3t	67.920	1.915	5.201	67.918	67.968	1.915	5.200	3.854	0.028	0.049	0.216	0.763

Name	Date uncorr (ka)	±2s (abs)	±2s + ε (abs)	Date corr (ka)	Date corr (ka BP)	±2s (abs)	±2s + ε (abs)	$\left[^{234}U/^{238}U\right]_i$	±2s (abs)	±2s + ε (abs)	Rho T-g0	Rho T-g0
O4t	54.918	0.997	2.195	54.918	54.968	0.997	2.195	4.198	0.020	0.027	0.095	0.620
P14b	21.302	0.443	0.829	21.302	21.352	0.443	0.829	4.727	0.021	0.026	-0.012	0.194
P17t	22.786	0.326	1.322	22.786	22.836	0.326	1.322	4.772	0.015	0.020	-0.016	0.652
P2t	25.168	0.423	1.373	25.168	25.218	0.423	1.373	4.780	0.019	0.023	-0.034	0.557
Q1b	22.149	0.440	0.799	22.149	22.199	0.440	0.799	5.005	0.023	0.027	-0.038	0.172
Q1t	19.038	0.416	0.781	19.038	19.088	0.416	0.781	4.903	0.021	0.026	0.008	0.206
Q2t	18.710	0.337	1.248	18.691	18.741	0.337	1.248	4.903	0.019	0.023	-0.040	0.546
Q2t_Fe	18.726	0.401	1.266	18.699	18.749	0.402	1.266	4.908	0.023	0.026	-0.044	0.468
Q3t	98.871	1.471	2.983	98.871	98.921	1.471	2.983	4.733	0.020	0.034	0.373	0.811
Q7b	91.532	1.717	2.230	91.510	91.560	1.717	2.230	4.657	0.025	0.031	0.292	0.372
Q7t	93.487	1.333	1.967	93.487	93.537	1.333	1.967	4.666	0.019	0.027	0.250	0.381
Q9b	89.741	1.463	2.032	89.734	89.784	1.463	2.031	4.616	0.022	0.028	0.263	0.367
Q9t	90.912	1.441	2.022	90.912	90.962	1.441	2.022	4.640	0.021	0.028	0.256	0.368
R1b	51.529	0.526	1.210	51.528	51.578	0.526	1.210	7.302	0.020	0.028	0.116	0.663
R1t	50.102	0.834	2.338	50.097	50.147	0.834	2.338	7.241	0.035	0.053	0.022	0.666
R1t	51.883	0.722	2.322	51.872	51.922	0.722	2.322	7.287	0.026	0.049	0.153	0.777
R1t	52.043	0.856	2.375	52.033	52.083	0.856	2.375	7.271	0.034	0.053	0.072	0.694
R4b	54.255	0.586	1.257	54.254	54.304	0.586	1.257	7.338	0.022	0.030	0.105	0.630
S1b	8.184	0.352	1.531	8.184	8.234	0.352	1.531	3.587	0.020	0.023	-0.011	0.458
S2b	7.770	0.572	3.084	7.759	7.809	0.572	3.084	3.536	0.030	0.039	0.020	0.552
S2b	7.581	0.518	3.104	7.573	7.623	0.518	3.103	3.495	0.030	0.038	-0.005	0.549
S2b	7.446	0.572	3.088	7.437	7.487	0.572	3.088	3.520	0.030	0.039	0.025	0.551

B.4 Spring fluid chemistry data

Table B.6 Spring fluid compositions from Kampman et al. (2009), and Ismay brine composition from Spangler et al. (1996).

Spring/ sample name	Temp. °C	pH field	Al µmol/l	Ba µmol/l	Ca mmol/l	Fe µmol/l	K mmol/l	Mg mmol/l	Mn µmol/l	Na mmol/l	Si mmol/l	Sr mmol/l	Cl mmol/l	SO_4 mmol/l	Alk. mEq/l	TDIC mmol/l	$\delta^{18}O$ ‰ SMOW	$\delta^{13}C$ CO_2(g) ‰ PDB	^3He TU	$^{87}Sr/^{86}Sr$	PCO_2 atm	$SI_{calcite}$	Brine %
Green River Airport Well	27	6.18	3.61	0.14	19.75	4.63	2.15	7.95	22.65	18.11	0.92	112.67	2.59	19.06	37.08	75.59	-14.53	-6.61	0.5	0.713327	1.21	0.51	0.06
Crystal Geyser	18	6.46	4.85	0.1	21.78	44.41	7.98	9.02	25.12	159.02	0.19	142.9	137.94	26.46	68.86	107.37	-14.39	-7.31	0.3	0.71266	0.96	0.83	4.43
Small Bubbling Spring	17.2	6.17	3.24	0.12	18.24	2.31	7.35	8.88	19.01	160.27	0.14	137.98	128.63	26.65	56.54	118.89	-14.25	-7.02	NA	0.712554	1.53	0.38	4.13
Big Bubbling Spring	17.5	6.3	5.1	0.1	21.55	2.66	9.36	8.55	7.23	212.87	0.14	157.44	178.29	32.17	66.04	116.33	-13.88	-6.97	0.3	0.71272	1.33	0.64	5.73
Side Seep, Big Bubbling	16.5	6.21	4.97	0.11	19.09	4.03	9.23	8.65	7.54	211.26	0.13	131.03	170.47	30.12	59.69	118.75	-13.77	-7.18	NA	0.712663	1.43	0.43	5.47
Pseudo-Tenmile Geyser	15	6.52	4.35	0.08	19.26	19.24	9.55	8.09	2.15	228.04	0.14	164.24	177.98	31.2	62.06	93.33	-13.76	-7.28	0.7	0.712798	0.71	0.73	5.72
Torrey's Spring	15.8	6.59	4.8	0.13	23.51	47.96	11.02	7.93	19.1	251.29	0.15	145.03	193.14	30.16	78.72	111.63	-13.86	-6.79	0.7	0.712588	0.76	0.98	6.21
Tenmile Geyser	15.7	6.58	5.02	0.14	22.16	83.1	6.79	9.44	18.46	219.01	0.16	236.25	165.19	14.3	58.21	83.19	-13.21	-7.55	0.3	0.711755	0.58	0.88	4.98
Tumble Weed Geyser	15.9	6.46	5	0.12	18.81	5.23	8.11	8.9	12.06	189.25	0.14	153.53	132.88	19.74	62.12	97.94	-13.82	-6.72	0.4	0.712581	0.82	0.72	3.31
Chaffin Ranch Geyser	14.7	6.73	4.99	0.08	26.01	67.61	7.58	9.78	17.37	193.54	0.13	165.45	128.39	14.54	76.12	100.15	-13.76	-7.25	0.5	0.713053	0.53	1.19	3.03
Ismay Brine	24	6.8		1.28	192.13	25.07	28.13	65.83	9.28	2261.85	0.18	2282.58	3102.7	11.45	1.23	1.31	2.19			0.708448			

B.5 Trace metal data

Table B.7 Measured isotopes on iCapQ for metal/calcium ratios

Element	Measured isotope
Na	^{23}Na
Al	^{27}Al
P	^{31}P
S	^{32}S
Cl	^{35}Cl
K	^{39}K
Ca	^{43}Ca
V	^{51}V
Mn	^{55}Mn
Fe	^{56}Fe
Zn	^{66}Zn
Sr	^{86}Sr
Y	^{89}Y
Zr	^{94}Zr
Ba	^{137}Ba
U	^{238}U

B.6 Detrital contamination on laser ablation

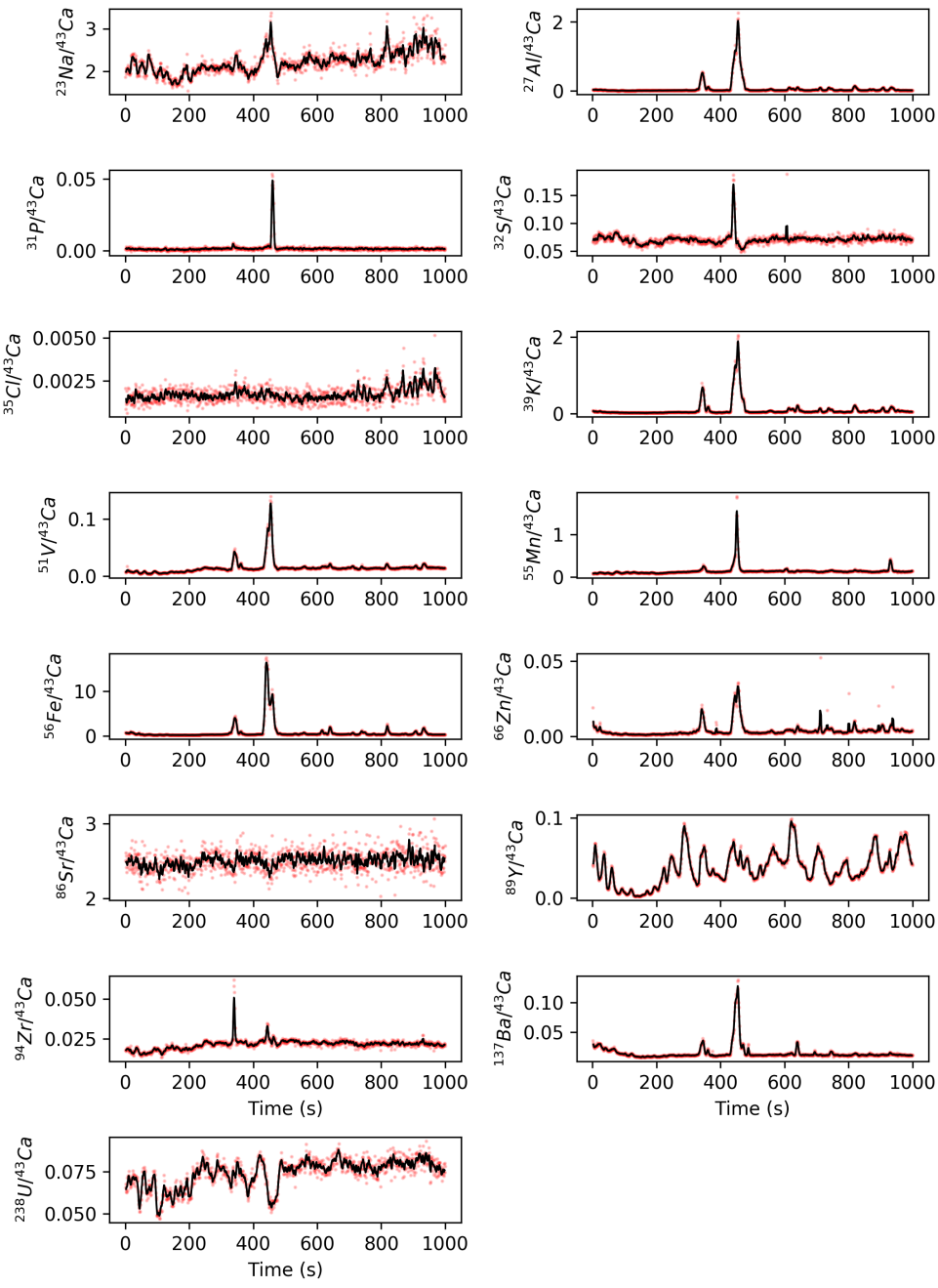

Fig. B.2 Trace metals at beginning of vein, inclusion with Ba, Fe, Al in middle of section around 400-450. Sampling of such an inclusion will look like impure carbonate with much higher ratios to Ca than are true.

B.7 Laser ablation repeat transects

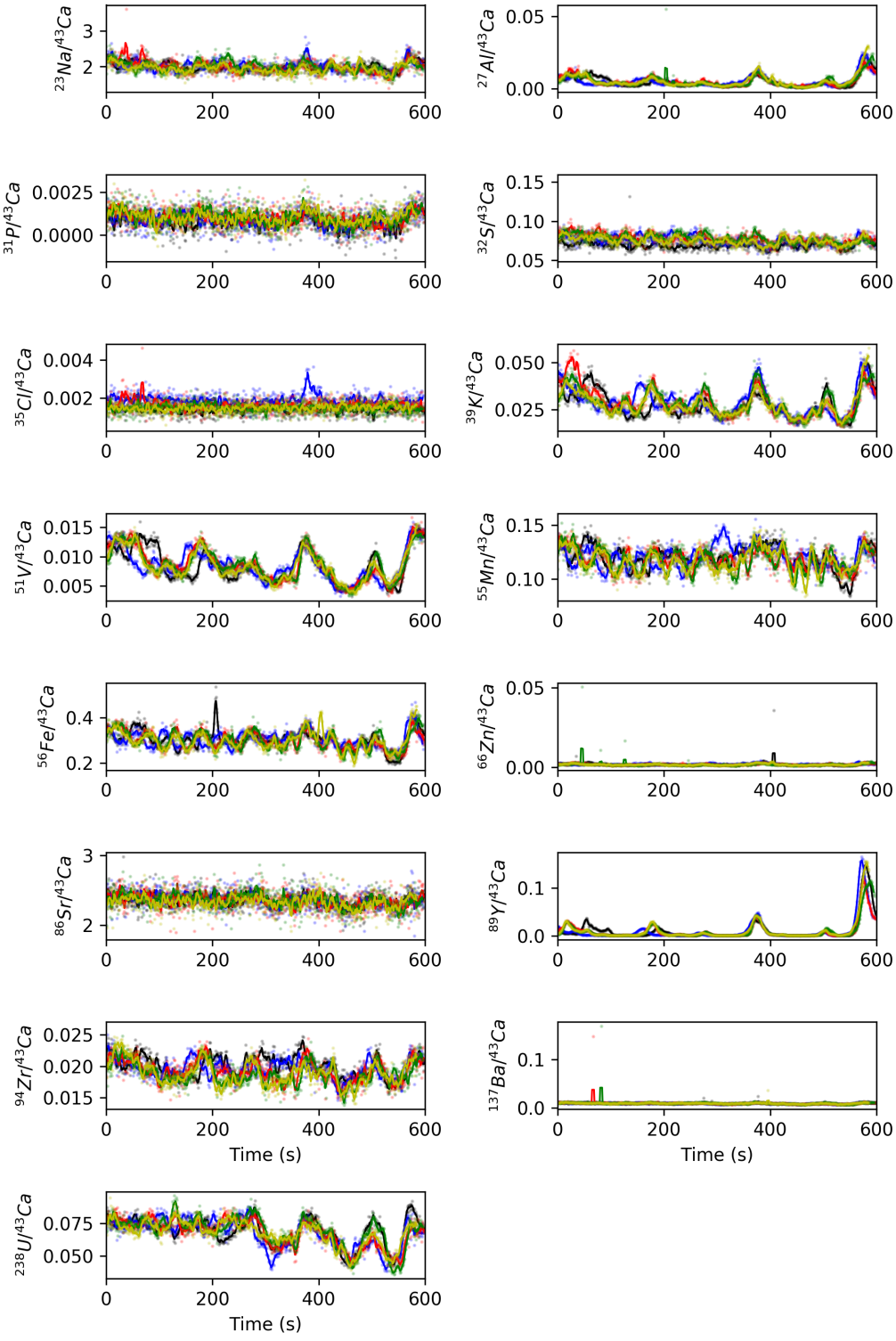

Fig. B.3 Repeat parallel rasters on LG/03/50B

B.8 Full trace metal data: SW/02/36J and SW/06/14E

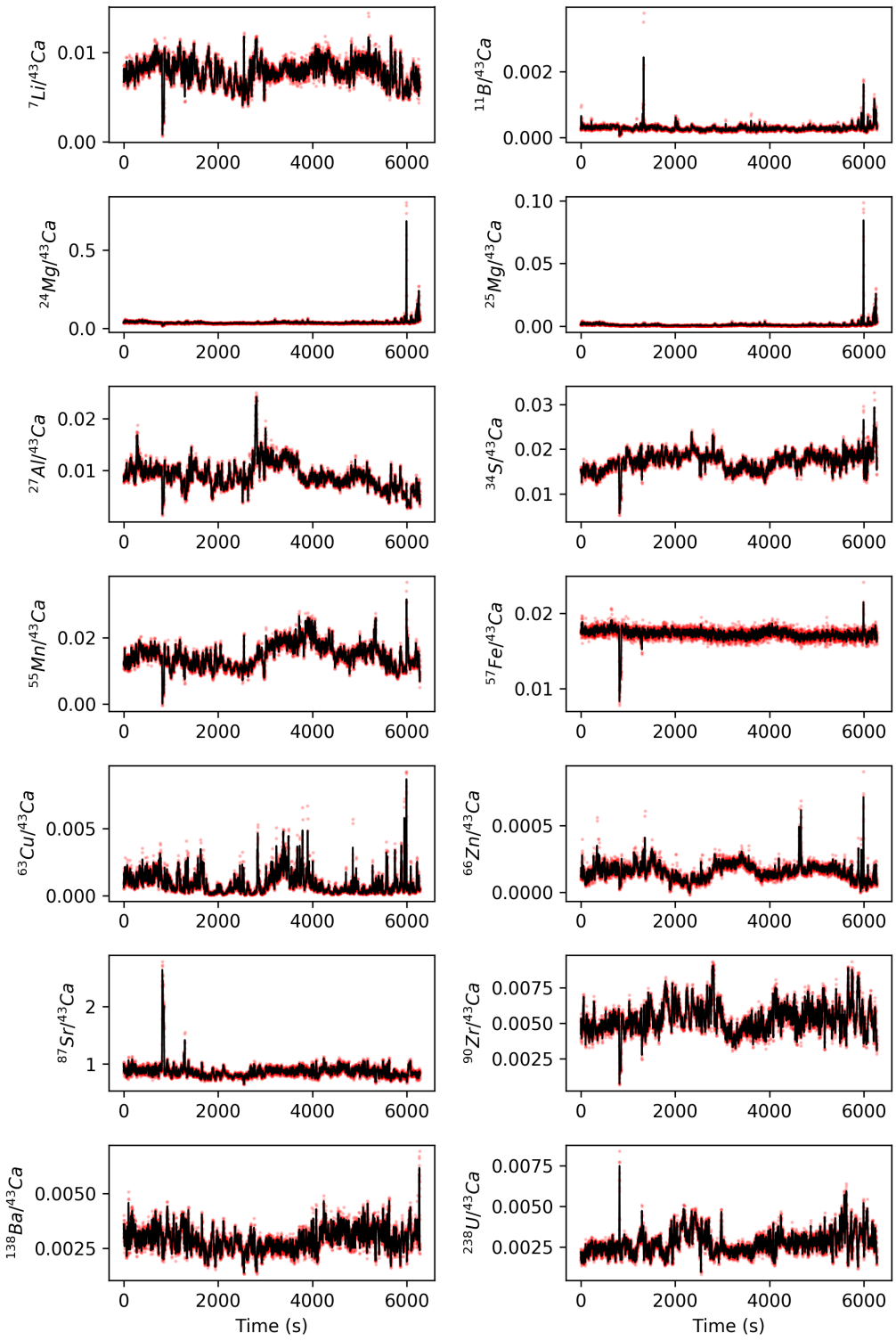

Fig. B.4 Trace metals, measured by laser ablation in sample SW/02/36J

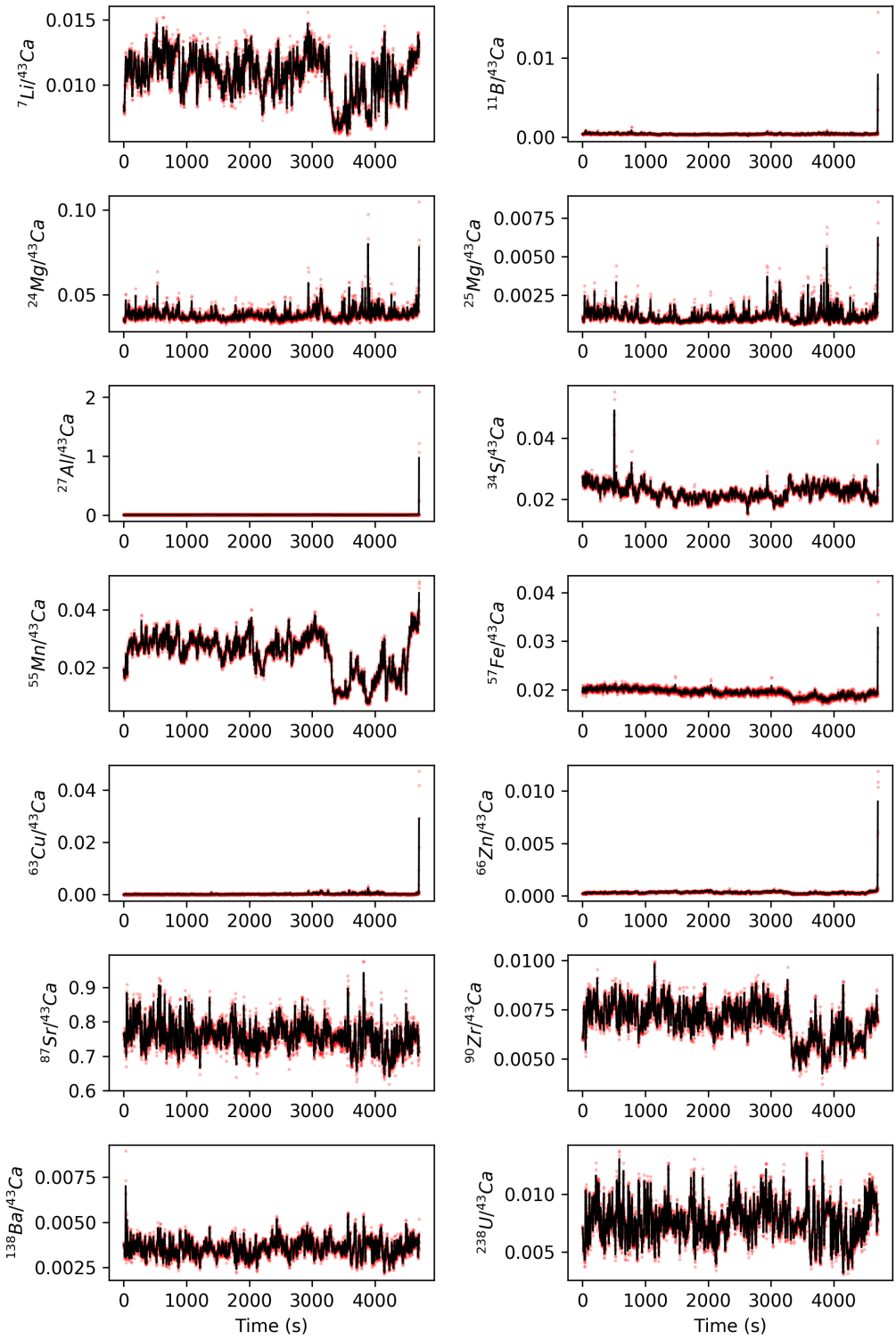

Fig. B.5 Trace metals, measured by laser ablation in sample SW/06/14E

B.9 Fault zone drilling log

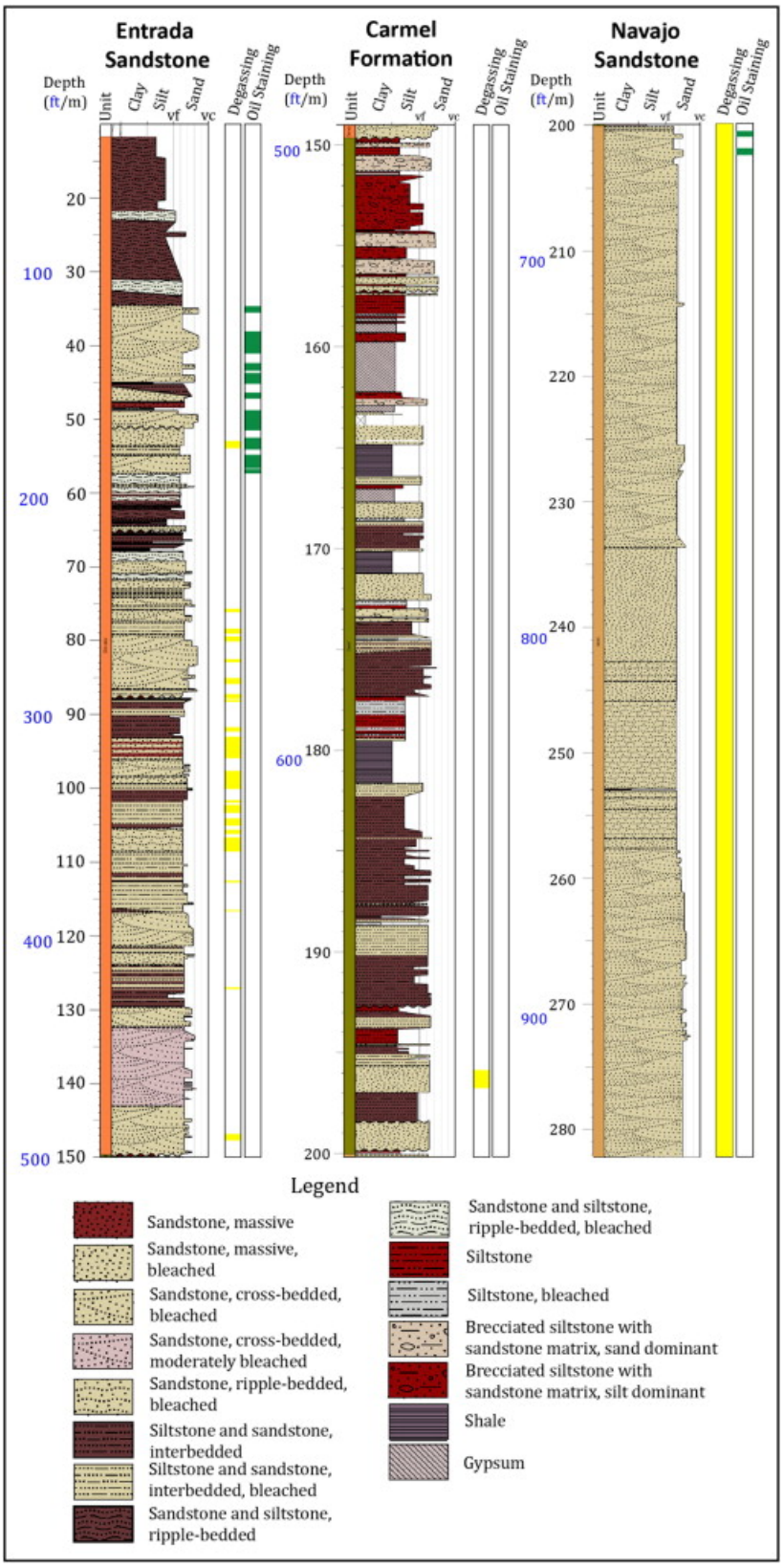

Fig. B.6 Drillcore log from (Kampman et al., 2014b)

B.10 Geyser eruption time-series data and fluid mixing

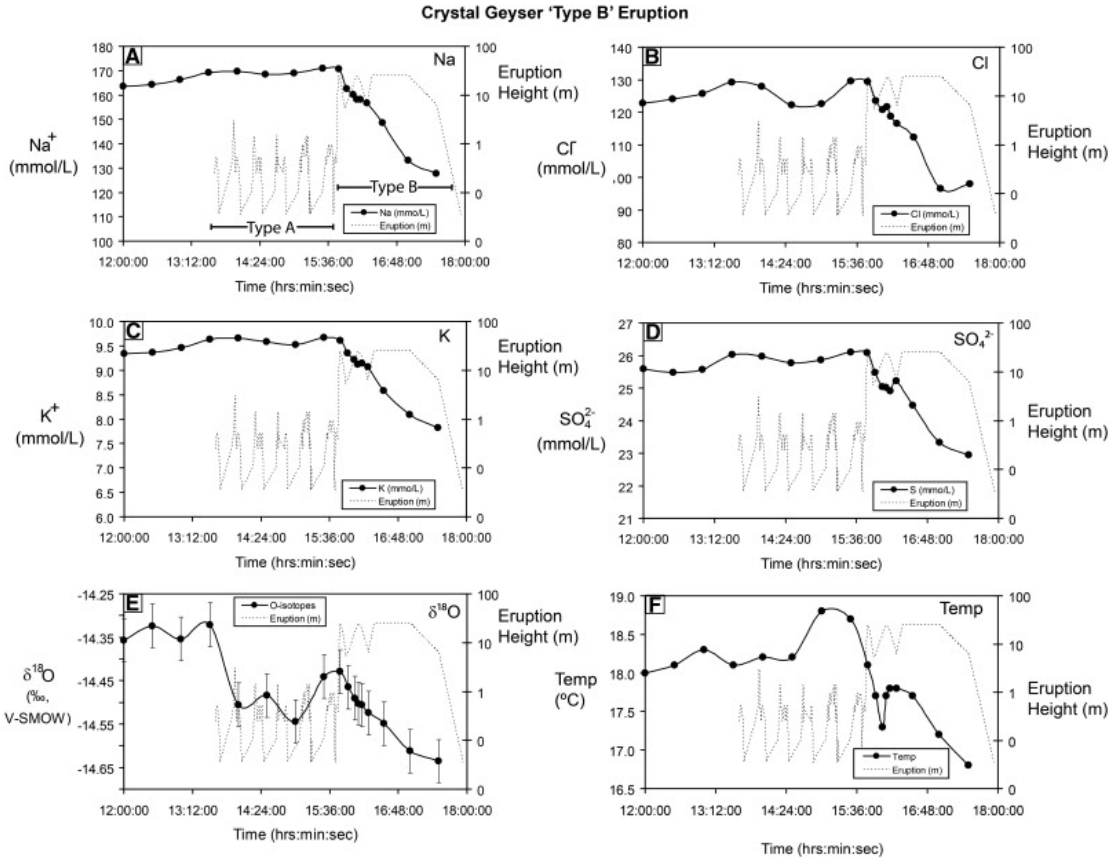

Fig. B.7 Crystal Geyser eruption time series 1; from Kampman et al. (2014b).

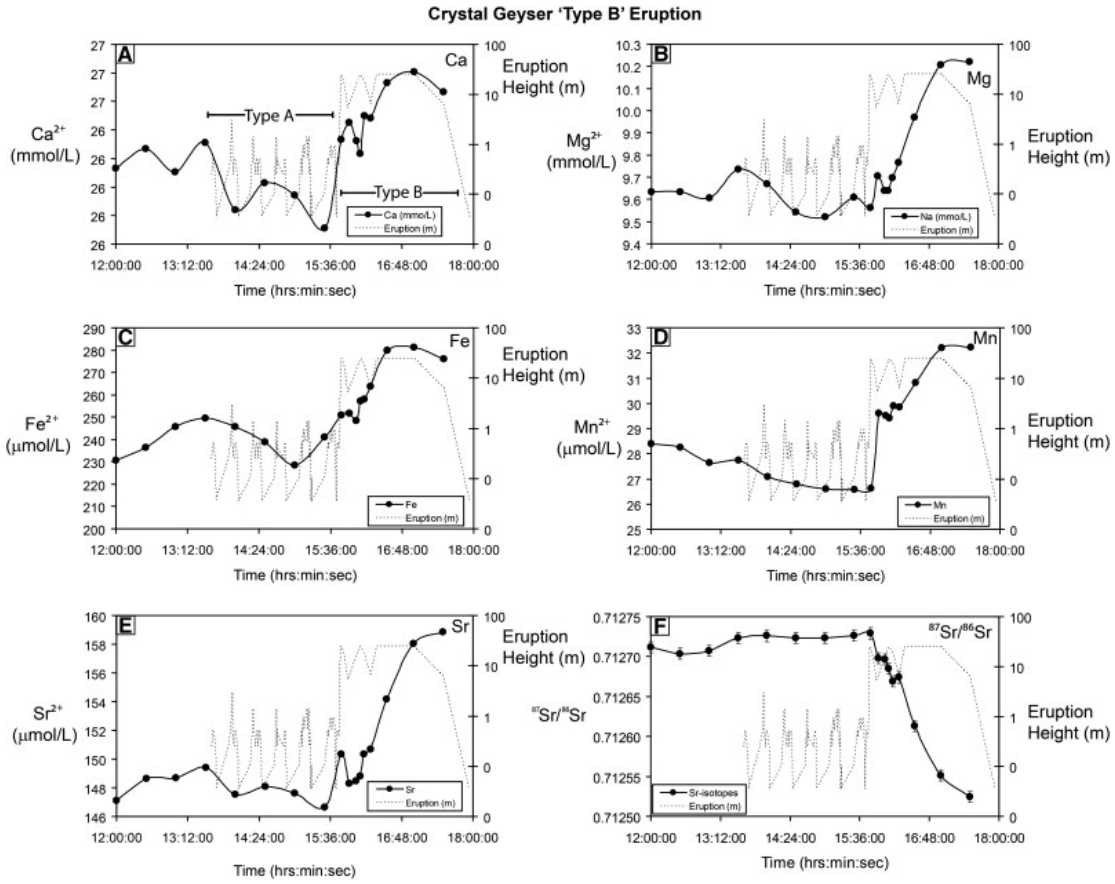

Fig. B.8 Crystal Geyser eruption time series 2; from Kampman et al. (2014b).

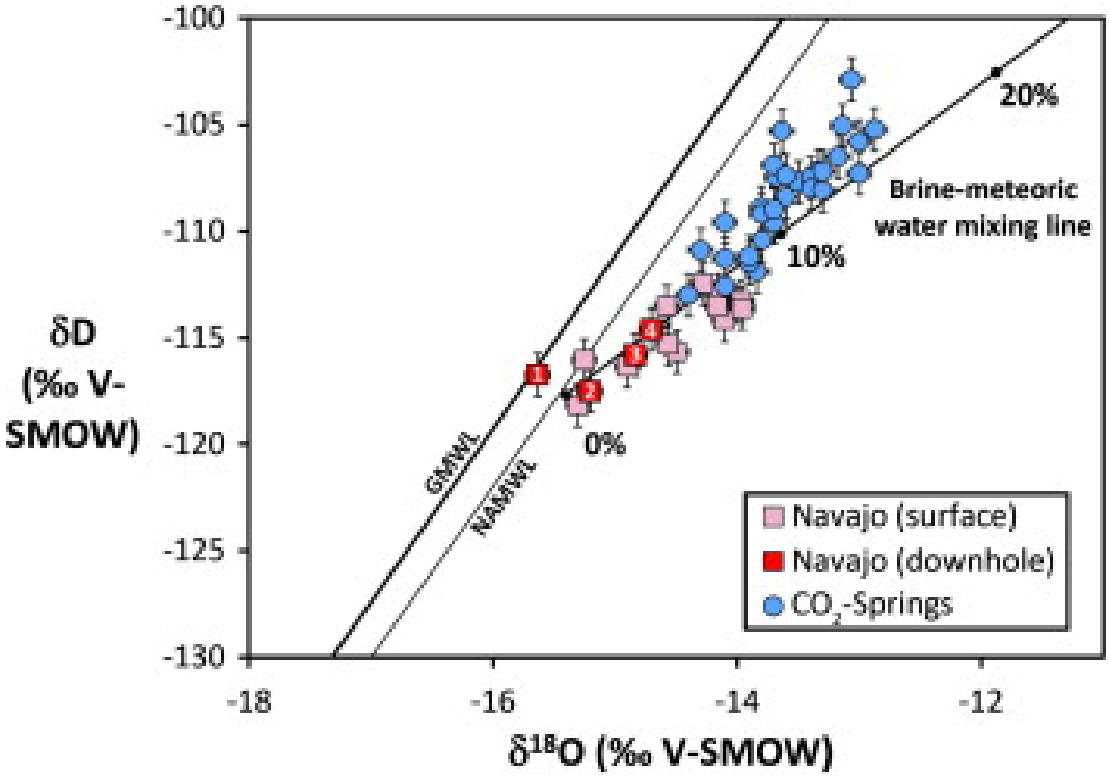

Fig. B.9 Meteoric mixing: δ^{18}O vs. δD; from Kampman et al. (2014b).

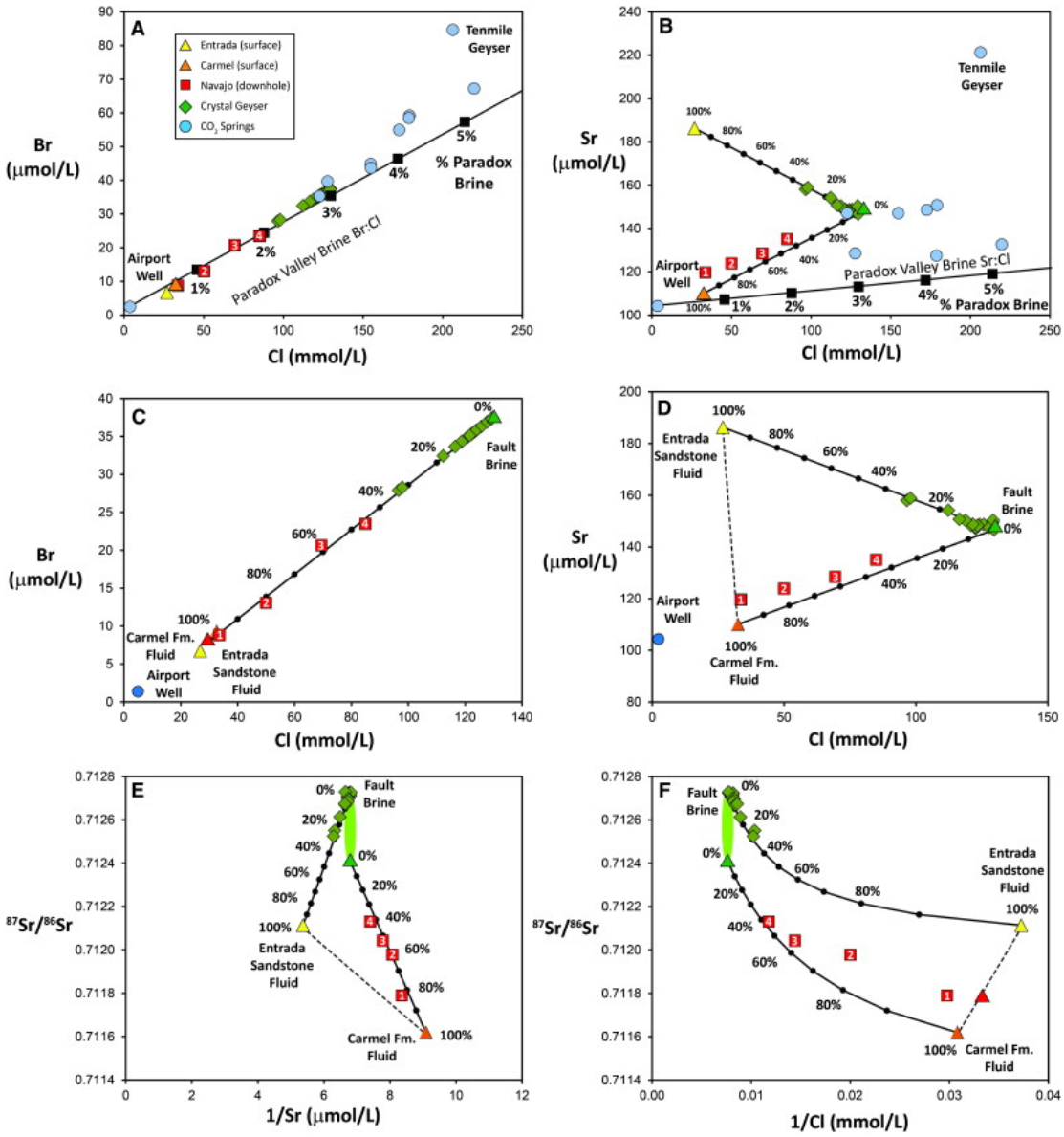

Fig. B.10 3 component mixing 1; from Kampman et al. (2014b).

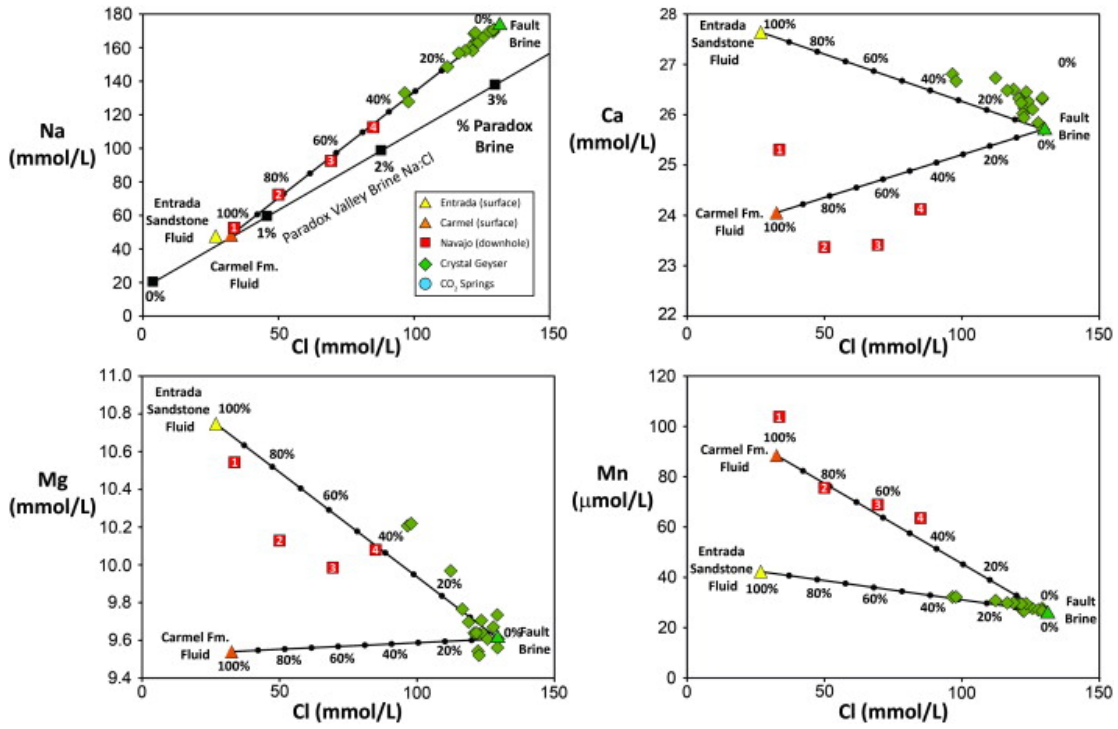

Fig. B.11 3 component mixing 2; from Kampman et al. (2014b).

Table B.8 Estimated and calculated composition of fluid end-members from Table 8 of Kampman et al. (2014b).

	Na	K	Ca	Mg	Sr	Fe	Mn	SO_4	Br	Cl	HCO_3	$^{87}Sr/^{86}Sr$
Entrada Sandstone												
Predicted	41.2	3.7	28.8	11.6	186.2	354.6	44.9	16.4	7.8	26.8	44.9	0.712168
Measured	47.6	3.3	27.6	10.7	186.3	348.9	42.3	17.9	6.7	26.8	45	0.712114
% offset	-14.0	13.4	4.2	7.8	0	1.6	6.2	-8.1	15.3	0	-0.3	
Fault Brine												
predicted	164.7	8.9	23.1	9.7	148.4	45.1	28.6	24.2	36.2	129.6	75.2	0.71237
measured	170.8	9.7	25.7	9.6	146.7	241	26.6	25.5	37.4	129.6	68.3	0.712726
% offset	-3.6	-7.4	-10.2	0.7	1.2	-81.3	7.4	-5.0	-3.2	0	10	
Carmel Formation												
Predicted	51.3	5.1	25.3	10.6	119.4	26.7	104.7	16.5	8.5	32.5	50.3	0.711782
Measured	48.3	4.8	24.1	9.5	110.1	126.8	88.5	16.8	9.3	32.5	56.7	0.71162
% offset	6.1	6.1	5.3	10.6	8.5	-78.9	18.3	-2.1	-8.6	0	-11.2	

Appendix C

Reactive transport: solutions to analytical expressions

Sr-isotopes

The change in $^{87}Sr/^{86}Sr$ in the fluid (r_f) can be written as:

$$K_r \frac{\partial r_f}{\partial t} = D_e \frac{\partial^2 r_f}{\partial z^2} - v \frac{\partial r_f}{\partial z} + MR_d W_d \frac{C_d}{C_f}(r_s - r_f)$$

using terms as defined in the text. Assuming that dispersion is negligible and making a quasi-steady state assumption ($\frac{\partial C}{\partial t} \approx 0$) means that $\frac{\partial r_f}{\partial t}$ can be neglected, this may be rearranged for $\frac{\partial r_f}{\partial z}$:

$$\frac{\partial r_f}{\partial z} = \frac{MR_d W_d C_d}{vC_f}(r_s - r_f)$$

Substitute $a = \frac{MR_d W_d C_d}{vC_f}$, as all terms are constants (this contains the Damköhler number and dimensionless concentrations):

$$\frac{\partial r_f}{\partial z} = a(r_s - r_f)$$

Substitute $b = ar_s$, as r_s is also a constant

$$\frac{\partial r_f}{\partial z} = b - ar_f$$

$$f'(z) = b - af(z)$$

The solution of which is:

$$f(z) = \frac{b}{a} + ce^{-az} = r_s + ce^{-az}$$

Then a can be substituted, and c solved using the boundary conditions ($z = 0, f(0) = r_f$) which are the starting fluid composition.

U-isotopes

Is similar to the Sr isotope case, but with additional substitutions.

$$K_r \frac{\partial A_f}{\partial t} = D_e \frac{\partial^2 A_f}{\partial z^2} - v\frac{\partial A_f}{\partial z} + \sum_i \frac{M_s C_s k_f S_i}{C_f}(A_s - A_f) + \frac{M_s f_\alpha \lambda_{234} C_s}{C_f} + K_r \lambda_{234}(1 - A_f)$$

Assume dispersion is negligible, that there is a single U-bearing phase (or a weighted sum of U-bearing phases), quasi steady state ($\frac{\partial A_f}{\partial t} \approx 0$) and rearrange for $\frac{\partial A_f}{\partial z}$:

$$\frac{\partial A_f}{\partial z} = \frac{M_s C_s k_f S_i}{v C_f}(A_s - A_f) + \frac{M_s f_\alpha \lambda_{234} C_s}{v C_f} + \frac{K_r \lambda_{234}}{v}(1 - A_f)$$

Substitute $a = \frac{M_s C_s k_f S_i}{v C_f}$, $b = \frac{M_s f_\alpha \lambda_{234} C_s}{v C_f}$ and $c = \frac{K_r \lambda_{234}}{v}$, as these terms are all constants. a and b contain the dimensionless ratio of concentrations, a contains the Damköhler number and c is essentially residence time

$$\begin{aligned} \frac{\partial A_f}{\partial z} &= a(A_s - A_f) + b + c(1 - A_f) \\ f'(z) &= aA_s - af(z) + b + c - cf(z) \\ f'(z) &= d + b + c - af(z) - cf(z) \end{aligned} \tag{C.1}$$

Using the substitution, $d = A_s$. The solution of this equation for $f(z)$ is:

$$f(z) = ke^{-az-cz} + \frac{b + c + d}{a + c} \tag{C.2}$$

Terms can be substituted back in, and k can be solved for using the starting fluid composition as boundary conditions (i.e. $z = 0, f(0) = A_{fi}$).